DYE-SENSITIZED SOLAR CELLS BASED ON PERYLENE DERIVATIVES

Dissertation

for Obtaining the Degree Doctor of Natural Sciences
"Doctor rerum naturalium (Dr. rer. nat.)"

zur Erlangung des akademischen Grades des
Doktors der Naturwissenschaften (Dr. rer. nat.)

Presented at the Faculty of Science, University of Kassel
"Fachbereich 18 Universität Kassel"

by

Chérubin, NOUMISSING SAO
from Bafoussam, Cameroon

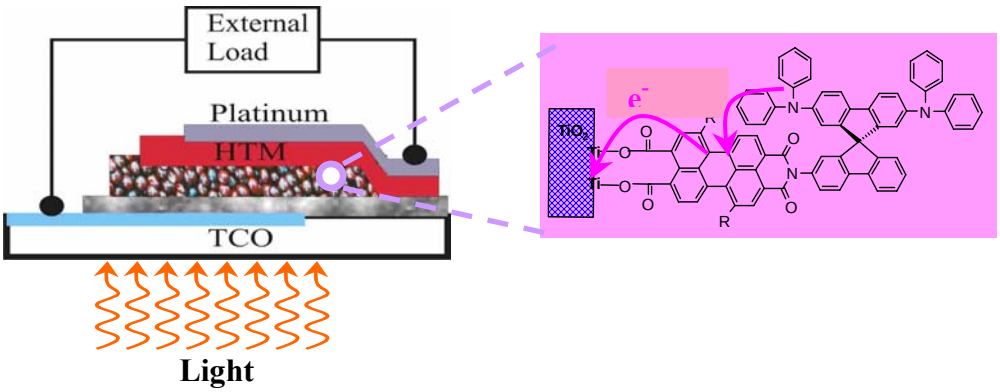

UNIKASSEL VERSITÄT

Kassel, 2009

The present work has been conducted under the supervision of

Prof. Dr. Josef SALBECK

at the Faculty of Sciences

Kassel University

Germany

"I hereby certify that I made this thesis independently, without any disallowed assistance and I did not use others than the aid as indicated in this thesis. I marked all place, which are literally or in a general manner taken out of published or unpublished books or articles. No part of this thesis has been previously submitted in support of an application for any other degree or qualification in this or other university."

"Hiermit versichere ich, dass ich die vorliegende Dissertation selbständig und ohne unerlaubte Hilfe angefertigt und andere als die in der Dissertation angegebenen Hilfsmittel nicht benutzt habe. Alle Stellen, die wörtlich oder sinngemäß aus veröffentlichten oder unveröffentlichten Schriften entnommen sind, habe ich als solche kenntlich gemacht. Kein Teil dieser Arbeit ist in einem anderen Promotions- oder Habilitationsverfahren verwendet worden."

Accepted as dissertation by the Faculty of Sciences, University of Kassel, Germany

Advisor	: Prof. Dr. Josef. Salbeck
First referee	: Prof. Dr. Josef. Salbeck
Second referee	: PD Dr. habil. Daniel Ayuk Mbi Egbe (Linz, Austria)

Day of the oral examination: 09 October 2009

Committee:

Prof. Dr. Josef. Salbeck
PD Dr. habil. Daniel Ayuk Mbi Egbe
Prof. Dr. Harmut Hillmer
PD Dr. Thomas Fuhrmann-Lieker

Cover:

Schematic representation of a solid-state dye-sensitized solar cell. Illustration of the mechanism of the charge transfer occurring by a *through space* process in a bipolar spiro compound used as sensitizer.

"Gedruckt mit Unterstützung des Deutschen Akademischen Austauschdienstes"

ABSTRACT

The oil price rises more and more, and the world energy consumption is projected to expand by 50 percent from 2005 to 2030. Nowadays intensive research is focused on the development of alternative energies. Among them, there are dye-sensitized nanocrystalline solar cells (DSSCs) "*the third generation solar cells*". The latter have gained attention during the last decade and are currently subject of intense research in the framework of renewable energies as a low-cost photovoltaic. At present DSSCs with ruthenium based dyes exhibit highest efficiencies (ca 11%). The objective of the present work is to fabricate, characterize and improve the performance of DSSCs based on metal free dyes as sensitizers, especially on perylene derivatives.

The work begins by a general introduction to the photovoltaics and dye-sensitized solar cells, such as the operating principles and the characteristics of the DSSCs.

Chapter 2 and 3 discuss the state of the art of sensitizers used in DSSCs, present the compounds used as sensitizer in the present work and illustrate practical issues of experimental techniques and device preparation.

A comparative study of electrolyte-DSSCs based on P1, P4, P7, P8, P9, and P10 are presented in chapter 4. Experimental results show that the dye structure plays a crucial role in the performance of the devices. The dye based on the spiro-concept (*bipolar spiro compound*) exhibited a higher efficiency than the non-spiro compounds. The presence of *tert*-butylpyridine as additive in the electrolyte was found to increase the open circuit voltage and simultaneously decrease the efficiency. The presence of lithium ions in the electrolyte increases both output current and the efficiency.

The sensitivity of the dye to cations contained in the electrolyte was investigated in the chapter 5. FT-IR and UV-Vis were used to investigate the in-situ coordination of the cation to the adsorbed dye in the working devices. The open-circuit voltage was found to depend on the number of coordination sites in the dye. P1 with most coordination sites has shown the lowest potential drop, opposite to P7, which is less sensitive to cations in the working cells.

A strategy to improve the dye adsorption onto the TiO_2 surface, and thus the light harvesting efficiency of the photoanode by UV treatment, is presented in chapter 6. The treatment of the TiO_2 film with UV light generates hydroxyl groups and renders the TiO_2 surface more and more hydrophilic. The treated TiO_2 surface reacts readily with the acid anhydride group of the dye that acts as an anchoring group and improves the dye adsorption.

The short-circuit current density and the efficiency of the electrolyte-based dye cells was considerably improved by the UV treatment of the TiO_2 film.

Solid-state dye-sensitized solar cells (SSDs) based on spiro-MeOTAD (used as hole transport material) are studied in chapter 7. The efficiency of SSDs was globally found to be lower than that of electrolyte-based solar cells. That was due to poor pore filling of the dye-loaded TiO_2 film by the spin-coated spiro-MeOTAD and to the significantly slower charge transport in the spiro-MeOTAD compared to the electrolyte redox mediator. However, the presence of the donor moieties in P1 that are structurally similar to spiro-MeOTAD was found to improve the wettability of the P1-loaded TiO_2 film. As a consequence the performance of the P1-based solid-state cells is better compared to the cells based on non-spiro compounds.

ABSTRACT

Der Ölpreis erhöht sich immer weiter, und der weltweite Energieverbrauch wird zwischen 2005 und 2030 voraussichtlich um 50% steigen. Daher gibt es derzeit intensive Bemühungen um die Erforschungen und Entwicklung alternativer Energiequellen, unter anderem auch in Richtung farbstoffsensibilisierter nanokristalliner Solarzellen (DSSCs) "*Solarzellen der dritten Generation*". Letztere haben während der letzten zehn Jahre Aufmerksamkeit erregt und werden derzeit im Zusammenhang mit erneuerbaren Energien als Niedrigpreis-Solaranlagen erforscht. Derzeit zeigen DSSCs auf Basis von Ruthenium-Farbstoffen den höchsten Wirkungsgrad (ca. 11%). Das Ziel der vorliegenden Arbeit ist es, DSSCs auf Basis metallfreier Farbstoffe (insbesondere Perylenderivate) als Sensibilisatoren herzustellen, zu charakterisieren und deren Leistungsfähigkeit zu verbessern.

Diese Arbeit beginnt mit einer allgemeinen Einführung in die Photovoltaik und über farbstoffsensibilisierte Solarzellen, das Funktionsprinzip und die Kennlinien der DSSCs.
Kapitel 2 und 3 diskutieren den Stand der Technik von Sensibilisatoren, die in DSSCs verwendet werden, stellen die für die vorliegenden Arbeit als Sensibilisatoren benutzten Verbindungen vor und erörtert praktische Fragen zu experimentellen Techniken und der Solarzellenherstellung.

Eine vergleichende Studie der Elektrolyt-DSSCs basierend auf den Farbstoffen P1, P4, P7, P8, P9 und P10 wird in Kapitel 4 vorgestellt. Die experimentellen Ergebnisse zeigen, dass die Struktur des Farbstoffes eine entscheidende Rolle für die Leistung der Solarzellen spielt. Der auf dem Spiro-Konzept basierende Farbstoff (*bipolare Spiroverbindung*) zeigte einen höheren Wirkungsgrad als Verbindungen ohne Spiroverknüpfung. Es wurde festgestellt, dass die Anwesenheit von *tert*-Butylpyridin als Zusatzstoff im Elektrolyt die Leerlaufspannung erhöht und gleichzeitig den Wirkungsgrad senkt, während die Gegenwart von Lithium-Ionen sowohl Kursschlussstromdichte als auch Wirkungsgrad erhöht.

Die Empfindlichkeit des adsorbierten Farbstoffes auf im Elektrolyten enthaltene Kationen wird in Kapitel 5 untersucht. Um die Koordination von Kationen am adsorbierten Farbstoff in-situ in den Solarzellen zu überprüfen, wurde FT-IR und UV-Vis-Spektroskopie angewendet. Es wurde festgestellt, dass die Leerlaufspannung von der Anzahl der Koordinationsstellen am Farbstoffmolekül abhängt. P1 mit den meisten Koordinationsstellen zeigte im Gegensatz zu Farbstoff P7 den niedrigsten Spannungsabfall, während P7 weniger empfindlich auf Kation in den Zellen reagierte.

Eine Strategie, um die Adsorption der Farbstoffe an der TiO_2-Oberfläche und somit die Lichtsammeleffizienz der Photoanode durch UV-Behandlung zu verbessern, wird in Kapitel 6 vorgestellt. Die Behandlung des TiO_2-Films mit UV-Licht erzeugt Hydroxylgruppen auf der TiO_2-Oberfläche und macht sie dadurch hydrophiler. Die behandelte TiO_2-Oberfläche reagiert leicht mit Säureanhydriden als Ankergruppen und verbessert die Farbstoffadsorption. Die Kurzschluss-Stromdichte und der Wirkungsgrad der Elektrolyt-basierte Zellen mit UV-Behandlung des TiO_2-Films zeigen eine erhebliche Verbesserung.

In Kapitel 7 werden Festkörper farbstoffsensibilisierte Solarzellen (SSDs) auf Basis von spiro-MeOTAD als Lochtransportmaterial untersucht. Die Effizienz der SSDs ist geringer als die der Elektrolyt-Zellen. Der Grund hierfür ist die schlechte Porenfüllung der Photoanode mit dem aufgeschleuderten spiro-MeOTAD und der dadurch deutlich langsamere Ladungstransport in der spiro-MeOTAD-Schicht verglichen mit dem Elektrolyten als Redoxmediator. Allerdings führte die strukturelle Ähnlichkeit der Donorgruppen in P1 mit spiro-MeOTAD zu einer besseren Benetzungbarkeit des farbstoffbeladenen TiO_2-Films. Als Folge davon ist die Leistung der P1 enthaltenden SSDs besser als die von Solarzellen, die auf Verbindungen ohne Spiroverknüpfung basieren.

TABLE OF CONTENTS

1. INTRODUCTION 1

1.1. Photovoltaic: From the beginning to real application 3

1.2. Photoelectrochemistry, photography and Sensitisation 4

1.3. Dye Sensitized Solar Cells 5

1.3.1. Basic principle of DSSCs 6

1.3.2. Photoelectrode 9

1.3.3. Electron Transfer dynamics 10

1.3.3.1. Electron injection process 12

1.3.3.2. Electron Recombination and back reaction 13

1.3.3.3. Dye regeneration 13

1.3.4. Electrolyte and Organic hole conductor material 14

1.3.5. Counter Electrode 15

1.4. Objective of the work 16

2. MATERIALS INVESTIGATED 17

2.1. Chromophores 17

2.1.1. Classical chromophores 17

2.1.1.1. Ruthenium based chromophores 17

2.1.1.2. Organic chromophores 19

2.1.2. Dye based on spiro concept 21

2.2. Electrochemical and Spectroscopy properties 25

2.3. Organic hole transport materials 29

3. EXPERIMENTAL SECTION

3.1. Device preparation 32

3.1.1. Structure of Dye Solar Cells 32

3.1.2. Fabrication of dye-sensitized solar cells 33

3.1.3. Materials 36

3.1.4. Transparent conducting oxide (TCO) Substrates 37

3.1.5. Preparation of compact TiO_2 layer 39

3.1.6. Nanocrystalline TiO_2 Layer 40

3.1.7. Sensitization 42
3.1.8. Deposition of the spiro-MeOTAD 42
3.1.9. Deposition of the Counter Electrode 42
3.1.10. Sealing of Device 44
3.2. Photovoltaic Device Characterisation 44
3.2.1. Dye solar cells parameters 44
3.2.2. The solar source and Air Mass 47
3.2.3. Incident photon-to-electron conversion efficiency (IPCE) 49
3.2.4. Experimental set-up 50
3.3. Absorption and Fluorescence Spectroscopy 51
3.4. FTIR-Spectroscopy 51
3.5. UV-Pretreatment of TiO_2 film 53
3.6. UV-Vis treatment of Device 54

4. CHARACTERISATION OF ELECTROLYTE BASED CELLS 55
4.1. Determination of optimal preparation conditions of DSSCs 55
4.1.1. The influence of the thickness of TiO_2 film on the performance of DSSCs 55
4.1.2. The choice of the electrolyte: The influence of tBP and Lithium on the performance of DSSCs 60
4.1.3 Influence of the Br^-/Br_3^- redox mediator on the performance of DSSCs 64
4.2. Performance of DSSCs based on non spiro compounds 68
4.2.1. General characteristic of the DSSCs 68
4.2.2. Photo action spectra of DSSCs based on non spiro compounds 75
4.2.3. The influence of incident light intensity on the performance of DSSCs 78
4.2.3.1. Influence on the short circuit current density (J_{sc}), Fill Factor (FF) and efficiency (η) 78
4.2.3.2. Influence of incident light intensity on the open-circuit voltage 81
4.3. Performances of DSSC based on a spiro-linked compound 83
4.3.1. *N*-[2′,7′-Bis-(*N,N*-diphenylamino)-9,9′-spirobifluoren-2-yl]-1,7-bis-(4-*t*-butylphenoxy)-perylene-3,4-dicarboxylic acid anhydride-9,10-imide (P1) 83

4.3.2. Long -Term Stability of P1-based dye solar cell 87
4.4. The effect of the dye structure on the dark current 90
4.5. Conclusion 92

5. CATION COORDINATION 94
5.1. Adsorption behaviour of perylene derivatives onto TiO_2 94
5.1.1. Langmuir Isotherm: Formation of self assemble monolayer 94
5.1.2. Characterisation of the adsorbate–surface binding configuration 97
5.2. Experimental evidence for lithium coordination 101
5.2.1. Characterisation of Li^+ ion coordination 101
5.3. In situ lithium ions coordination in DSSCs 107
5.3.1. Impact of lithium ion coordination on the performance of DSSCs 108
5.3.2. Influence on Li-coordination on the open-circuit photovoltage drop 110
5.4. Further investigation of others cations 112
5.4.1. FTIR spectroscopy 112
5.4.2. UV-Vis absorption spectroscopy 113
5.4.3. Impact on the performance of DSSCs 114
5.4.4. Investigation of Potential drop devices 117
5.4.5. Conclusion 120

6. UV PRETREATMENT 121
6.1. Light harvesting (LH) in DSSCs 121
6.2. Generation of hydroxyl group on the surface of TiO_2 by the UV light 122
6.3. Strategy to improve the LH of thin TiO_2 films 124
6.4. Impact of UV pretreatment TiO_2 on the performance of DSSCs 128
6.5. Conclusion 130

7. CHARACTERISATION OF SOLID-STATE DYE SENSITIZED SOLAR CELLS (SSD) 131
7.1. Solid-State Dye-Sensitized Solar Cells based on non spiro compound 131
7.1.1. Current voltage characteristics of SSD based on P4, P7, P8, P9, P10 131
7.1.2. The influence of incident light intensity on the performance of SSDs 136

7.1.2.1. Influence on the short circuit current density, fill factor and efficiency 136
7.1.2.2. Influence of the incident light intensity on the open circuit voltage 138
7.2. Solid-State Dye-Sensitized Solar Cells based on spiro-linked compound 140
7.2.1. *N*-[2′,7′-Bis-(*N,N*-diphenylamino)-9,9′-spirobifluoren-2-yl]-1,7-bis-(4-*t*-butylphenoxy)-perylene-3,4-dicarboxylic acid anhydride-9,10-imide(P1) 141
7.2.2. Long time stability of P1-based cell 144
7.3. Influence of TiO_2 thickness on solid-state dye sensitized solar cells 146
7.4. Conclusion 150

8. GENERAL CONCLUSIONS 152

REFERENCES 154

Acknowledgement
Curriculum Vitae

Chapter 1
INTRODUCTION

Mankind needs energy for living. Besides the energy in our food necessary to sustain our body and its function (100W), 30 times more energy is used on average to make our life more comfortable. Electrical energy is one of the most useful forms of energy, since it can be used for almost everything. As the world is becoming advanced in technology and economy, more energy is being consumed to keep up the development and the demand on energy boomed over the past years. World energy consumption is projected to expand by 50 percent from 2005 to 2030 [1]. In 2007, the world primary energy consumption was increased by 2.4% – down from 2.7% in 2006, but still the fifth consecutive year of above-average growth. [2]. The energy economy is still highly dependent on three forms: fossil fuel-oil, natural gases and coal with percentages of 37%, 20% and 27%, respectively [1]. With a daily consumption of 82.5 million barrels, oil might run out in around 40 years at current reserves-to-production (R/P) ratio. Meanwhile, the increasing awareness that the unpleasant environmental pollution arising from the combustion of these feedstocks necessitates urgent promotion of alternatives in renewable energy sources to cover the substantial deficit left by fossil fuels.

The photovoltaic effect discovered by the French scientist Edmond Bequerel in 1839 [3] after observing electric potential between two electrodes attached to a solid or liquid system upon light irradiation has been the base for a variety of concept to convert solar radiation into electricity. This concept has opened a new road for alternative energy generation and is actually a hot topic in current research. One simple reason is that the Earth receives 1.2×10^{17} W insolation or 3×10^{24} Joule energy per year from the Sun and this means covering only 0.13% of the Earth's surface with solar cells with an efficiency of 10% would satisfy our present needs [4]. Apart from the abundance of potentially exploitable solar energy, photovoltaic cells also have other competitive advantages such as little need for maintenance, off-grid operation and silence, which are ideal for usage in remote sites or mobile applications.

Today the photovoltaic market is dominated by silicon in its multicrystalline and monocrystalline form. Further silicon research is concentrated on thin-film crystalline silicon (about 5–30 μm active layer thickness), which avoids the costly crystal growing and sawing processes. The problems arising for this material are: assuring adequate light absorption, assuring good crystal quality and purity of the films, and finding a substrate that fulfils all

requirements. Genuine thin-film materials are characterised by a direct band structure, which gives them very high light absorption. Therefore, these materials have a thickness of only 1 µm or less. Other inorganic materials used for photovoltaic devices belong to the group of chalcogenides such as copper indium diselenide (CIS) and cadmium telluride. The interest has expanded from $CuInSe_2$ to $CuGaSe_2$, $CuInS_2$ and their multinary alloys $Cu(In,Ga)(S,Se)_2$. All belong to the so called *second generation* solar cells. The two deposition techniques are either separate deposition of the components followed by annealing or co-evaporation. Laboratory efficiencies for small area devices are approaching 19 % and large area modules have reached 12 %. Cadmium telluride solar cells, which show only slightly lower efficiency, also offer great promise.

From a solid-state physics point of view silicon is not an ideal material for photovoltaic conversion for two reasons: There is a small spectral mismatch between absorption of the semiconductor and the sunlight spectrum, approximated by a black body of 5900 K. A much more serious point is that silicon is an indirect semiconductor, meaning that valence band maximum and conduction band minimum are not opposite to each other in k-space. Light absorption is much weaker in an indirect gap semiconductor than in a direct semiconductor. This has serious consequences from a materials point of view: for a 90 % light absorption it takes only 1 µm of GaAs (a direct semiconductor) versus 100 µm of Si. The photogenerated carriers have to reach the p-n junction, which is near the front surface. The diffusion length of minority carriers has to be 200 µm or at least twice the silicon thickness. Thus, the material has to be of very high purity and of high crystalline perfection. In view of these physical limitations a lot of effort has been invested into the search for new materials. Consequently requirements for the ideal solar cell material are a band gap between 1.1 and 1.7 eV and a direct band structure. Furthermore the material should be readily available, non-toxic, reproducible deposition techniques, which are suitable for large area production. Alternatively to the search of new inorganic semiconductor materials other device geometries have been developed for the purpose of light to electron conversion, such as various concentrating systems including III/V-tandem cells.

In the last years, new concepts of solar cells were conceived and realized. These technologies mainly include dye-sensitized solar cells (DSSCs), polymer solar cells, and nanocrystalline solar cells, all of which are now known as *third generation* photovoltaics since they are very different from the previous semiconductor devices as they do not rely on a traditional *p-n* heterojunction to separate photogenerated charge carriers. Instead, they form a ‘bulky’ junction where charge separation takes place. Because of the low-cost materials and

easy fabrication, these technologies are expected to take a significant share in the fast growing photovoltaic areas.

Although organic solar cells can still not compete with conventional photovoltaic cells in terms of commercial application, the prospective to develop a long-term technology based on environmentally safer materials with almost unlimited availability justifies the intensive research in this domain.

1.1. Photovoltaic: From the beginning to real application

The life on the ground has been always governed by solar power. As early as in the 7th century B.C., magnifying glass was already used to concentrate sun's rays to make fire. Later on, the Roman people built the famous bathhouses (in the first to fourth centuries A.D) with large south facing windows to employ the sun's warmth. They named these sunspaces *heliocamini* (sun furnaces) [5]. However, it was until the 19th century that the photovoltaic effect was discovered. In 1839, Edmund Becquerel, a French experimental physicist of nineteen years old, noticed the generation of an electric current while experimenting with a silver coated platinum electrode placed in the electrolyte [3]. Since this discovery many effort have been made in this field. In 1883, an American inventor [6] developed the first large area solar cells from selenium wafers. However, since the selenium cells converted far less than 1% of all incident sunlight into electric power and deteriorated very rapidly when exposed to strong light, these pioneers in photoelectricity failed to build the solar devices that they had hoped to. These preliminary results opened the road in this technology, which is nowadays amongst hot research topics.

The spectral distribution of the solar spectrum was described by Max Planck in 1901 through his Planck's law [7]. Four years later, Albert Einstein published a simple description of "light quanta" (later called "photons" as suggested by Gilbert Lewis in 1926) and showed how they could be used to explain the photoelectric effect [8], which won him the Nobel Prize in 1921. This is the theoretical basis for all photovoltaic devices and in common semiconductors, photons excite electrons out of the valence band and into the higher-energy conduction band, where they are collected and transported to the outer circuit.

In 1904, Wilhelm Hallwachs made a semiconductor-junction solar cell from copper and copper oxide, a prototype of thin-film Schottky barrier devices. This barrier layer at the semiconductor-metal interface was confirmed by Goldmann and Brodsky in 1914 [9] and later studied in more details by Walter Schottky, Neville Mott and others in the 1930s [10,11].

In 1932, Audubert and Stora discovered the photovoltaic effect in cadmium sulfide (CdS), opening up a way to II-VI solar cells [12]. In the 1950s with the development of silicon electronic, Fuller[13], intuitively made near-surface *p-n* junctions by boron trichloride treatment of *n* type silicon wafer which greatly favoured charge separation of the device, and with these substrates, Chapin got near 6% conversion efficiency - 50 times more efficient than the selenium cells in the 1930s [14]. After this findings, many kinds of *p-n* junction with CdS, GaAs, InP and CdTe were developed, however the cost of the photoelectricity was so high (several hundred $ per watt) and was exclusively used in space application. In the 1970s after the work of Dr. Berman's, the cost of single crystal module is cut down to 10-20 $ per Watt [15]. In the mid 1970s after the political crisis in the Middle East, the embargo and the realization of the limitations in fossil fuel resources, a great interest in the solar cell as an alternative energy source for terrestrial application, awoke. It was during this period that *second generation* solar cells were developed, such as polycrystalline and amorphous silicon, thin-film deposits of silicon, CdTe, CuInSe2, (CIS) and Cu(In,Ga)Se2 (CIGS), as well as multijunction cell technology. This generation of device turned out to be advantageous in production cost with respect to silicon device. In the 1990s new concepts were introduced and developed. The type called *third generation* includes dye-sensitized solar cells, polymers solar cells, and nanocrystalline solar cells. These are different to classical *p-n* heterojunction since they consist of bulk junctions where charge separation takes place. This approach offers a new alternative for low-cost solar cells.

1.2. Photoelectrochemistry, photography and Sensitisation

Becquerel's pioneered photoelectric experiment in 1839. The choice of silver halide as the electrode material in his experiments reflects the rapid growth in knowledge of photochemical effect at that time. Biot [16] was aware of the use of paper sensitized by silver chloride, being contemporary with the introduction of photography by Daguerre and Fox-Talbot. Although the art of formulating photography emulsions only became a science a century later with the theoretical analysis of the process by Gurney and Mott in 1938 [17], there was constant empirical progress extending the overall sensitivity of photography emulsion, which had been particularly deficient for mid-spectral visible light and towards the red. The early "orthochromic" materials had limited capability to register scenes observed in colour realistically on a grey scale due to the semiconductor nature of the silver halides with their band gap between 2.7 and 3.2 eV and for which the photoresponse is negligible for

wavelengths longer than 460 nm. It was noted, for example, that the origin of the gelatine used as the support medium for the alkali halide grains significantly modified the film sensitivity. Only in the twentieth century it was demonstrated that the origin of an organosulfur compound present in calf-skin gelatine was responsible [18], and which is now known to have its effect by inducing a superficial nanostructure of silver sulphide on each grain. This can now be recognised as the first sensitisation at a semiconductor heterojunction, silver sulphide to halide. Even more significant was the work of Vogel, Professor of "photochemistry, spectroscopy and photography" in Berlin. In 1873 [19] he established empirically that the silver halide emulsions could be sensitized to red and even infrared light by suitably chosen dyes, thereby making possible the modern "panchromatic" broad – spectrum black and white film, and the more recently colour photography with the use of spectrally-selected dyes.

1.3. Dye-sensitized Solar Cells

Sensitisation of wide band gap semiconductors using dyes has a long history, dating back to early days of photography of the 19th century: Moser observed that the photoelectric effect on silver plates was enhanced in the presence of erythrosine dye [20] and confirmed by Rigollot in 1893 [21]. Systematic mechanistic studies started only in the late 1960's with the work of dye-sensitisation process on ZnO [22-24] and SnO_2 [25-27] electrodes carried out by Gerischer and Memming. Most of these early studies were fundamental in nature, aimed to understand electron–transfer processes involving valence and conduction bands of a semiconductor immersed in a redox electrolyte. Gerischer combined the stability of large band gap semiconductors with the photosensitivity to light in the visible region by dye adsorption onto semiconductor surface. Though, these works were still on their preliminary stage, the dye sensitized cells obtained were characterised with poor dye anchorage (mostly physisorbed) on the semiconductor surface and low conversion efficiencies restricted by the limited, weak light absorption (in the order of 1 to 2%) of the dye monolayer on the planar surface. Incremental improvements were then achieved both in the chemisorption of sensitizers [28-30], electrolyte redox chemistry and the judicious selection of photoelectrode materials [30-37]. Most semiconductors such as CdS, CdSe, GaP and Si underwent serious photocorrosion or even normal corrosion in the dark, thus a stable, wide band-gap semiconductor, TiO_2, became the material of choice. The breakthrough of dye-sensitized devices as solar cell was then achieved with the used of TiO_2 having a mesoporous structures with high surface area, which allowed a drastic enhancement of the amount of adsorbed dye.

Furthermore the development of metal organic sensitizers N3 and the later panchromatic "black dye" bearing attachment groups which allow the chemical bonding of the sensitizer to the surface of the TiO_2 lead to a drastic improvement in charge injection efficiency. Based on these innovations overall efficiencies of over 10 % were obtained for dye-sensitised mesoporous TiO_2 electrodes in contact with an electrolyte containing an iodide based redox system for dye regeneration [38-42]. A variety of dyes are used in the third generation photovoltaic technology, especially metal free dyes exhibiting high extinction coefficients. Since metal organic sensitizer performed well with a thick TiO_2 film, which increases the cell resistance and reduces the photovoltage, metal-free dye with high extinction coefficient could overcome that problem.

1.3.1. Basic principle of DSSCs

The process describing the conversion of light into electrons in dye-sensitized solar cells is shown in Figure 1.1. Consisting of an electron-conducting phase (*n*-type semiconductor) and a hole conducting phase considered as "mediator" (redox species or hole conductors) forming a "bulky" heterojunction, DSSCs are majority carrier devices where electrons and holes are separated in two chemical phases. In these cells, light is absorbed by the surface anchored dye, leading to a photoexcited state. This mode of carrier generation is also observed in organic bulk junction solar cells where a light-absorbing organic polymer works as the sensitizer and a fullerene derivative as the electron acceptor. According to Gregg classification, these devices belong to "excitonic solar cells". The term refers to the creation (by light absorption) of a molecular excited-state or Frenkel exciton* as the first step in the series of events that lead to charge separation and collection in the devices [43,44]. In the bulk heterojunction cell, the exciton must first diffuse several nm to the polymer/fullerene interface for example, where it can dissociate to form an electron-hole pair, with the hole in the polymer phase and the electron in the fullerene network. In the DSSC by contrast, the exciton is created by excitation of the dye at the interface so that it can dissociate readily to create an electron-hole pair, with the electron injected in the conduction band of the semiconductor and the hole located, initially at least, on the dye molecule [44]. The dye is then regenerated by the

* An exciton in an organic semiconductor (usually a Frenkel exciton) is sometimes considered to be a bound electron-hole pair. However, because of its electroneutrality and the strong binding between the electron and the hole, it is often better characterized as a mobile excited state [43].

mediator, which ensures the transfer of the hole to the counter electrode either in a diffusion or hopping mechanism depending on the mediator nature.

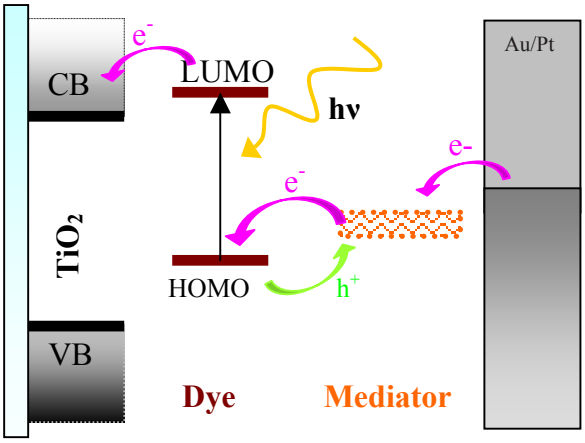

Figure 1.1 Working principle in a illuminated dye-sensitized solar cells under open circuit conditions. VB and CB stand for valence band and conduction band.

Charge separation in a *conventional* photovoltaic built on *p-n* junction is fundamentally different from the one in the DSSCs. Figure 1.2a shows energy band diagram of a conventional *p-n* junction after thermal equilibration of positive and negative charge carriers. Due to the concentration difference between the *p* and the *n* type semiconductor, holes move to the *n* region and electrons to *p* region. The uncompensated charges induced by this diffusion generate a built-in electric field at the junction and impair further percolation of charge carriers since the orientation of the electric field is contrary to the direction of the carrier diffusion. At equilibrium, no net charge diffusion occurs and a depletion region is formed, which is also referred to as a space charge layer. Upon illumination as shown in Figure 1.2b, absorption of photons with an energy higher than a threshold, the band gap, results in generation of excitons which interact via columbic forces. Considering that excitons will recombine after a certain time with emission of photons or phonons (heat), therefore only those created in or close to the space charge layer can be separated by the built-in electric field and contribute to the photocurrent. Since both electrons and holes coexist in the same chemical phase, these cells are called minority carriers devices and their efficiencies are highly dependent on the ability of photogenerated minority carriers (for example, electrons in a *p*-type material) to be collected out of devices before recombining with the majority carriers (holes, in this case) [45].

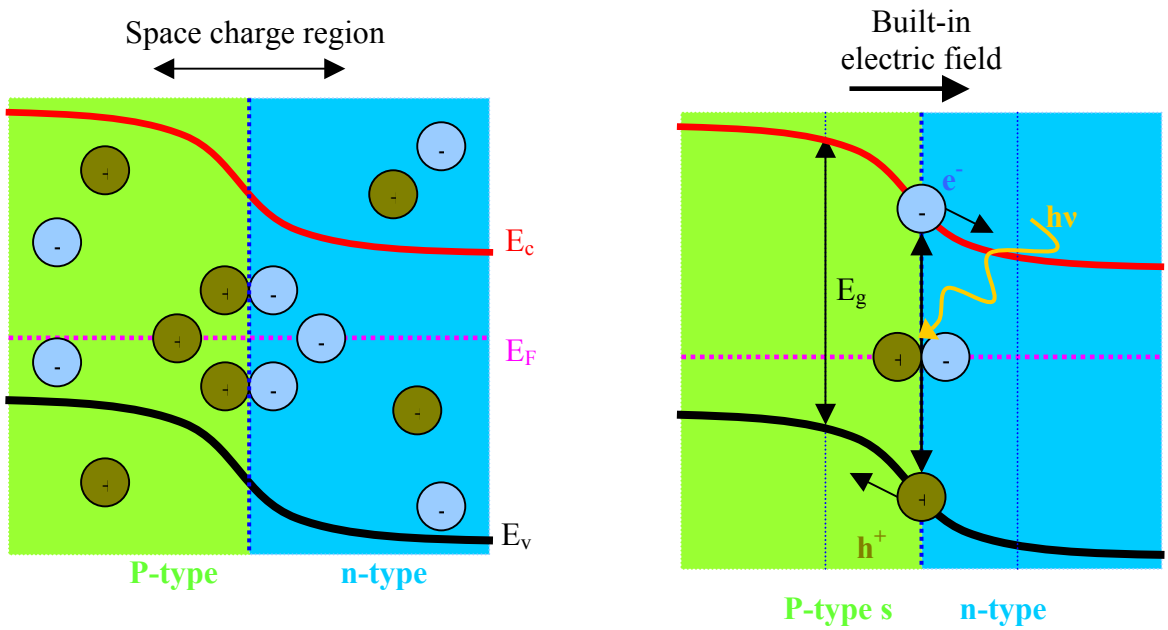

Figure 1.2 a) Energy band diagram of conventional p-n junction under short circuit conditions; b) Charge separation under illumination

Following the above description, the difference between the conventional solar cells and dye-sensitized solar cells can be summarized as follows:

- Upon illumination, light absorption and charge carrier transport are separated in dye-sensitized solar cell, whereas both processes are established in the semiconductor in the conventional solar cell.
- In the DSSCs, the nanoparticles of oxide semiconductor are simply too small to sustain a build-in electric field and thereby the charge transport occurs via diffusion. In a conventional *p-n* junction the presence of an electric field is necessary for an efficient charge separation.
- DSSCs are majority charges carrier devices in which the electron transport occurs in the TiO_2 and the hole by the mediator. Thereby, the recombination processes can be only confined at the interface. Inside a *p-n* junction minority and majority charge carriers coexist in the same bulk volume. Hence these cells are very sensitive to the presence of the trace impurities or defects, which can act as recombination centers.

1.3.2. Photoelectrode

The photoelectrode consists of a wide band gap, porous semiconductor of high surface area, that is sensitized for the visible spectrum by a dye adsorbed on its surface. Titanium dioxide (TiO_2) offers some unique properties making it the preferred semiconductor for dye sensitized solar cells. Its conduction band edge lies slightly below the excited state energy level of many dyes, which is one condition for efficient electron injection. The high dielectric constant of TiO_2 (ε = 80 for anatase) provides good electrostatic shielding of the injected electrons from the oxidized dye molecule attached to the TiO_2 surface, thus preventing their recombination before reduction of the dye by the redox electrolyte.

Due to the presence of band gap, semiconductors only absorbs light below a threshold wavelength λ_g, the fundamental absorption edge, which is related to the band gap energy, E_g, by Eq. 1.8

$$\lambda_g(\text{nm}) = 1240 / E_g(\text{eV}) \qquad 1.8$$

TiO_2 occurs in three crystal modifications, namely rutile, anatase and brookite. While rutile is the thermodynamically stable phase, anatase is preferred for dye sensitized solar cells, due to its larger band gap (E_g = 3.2 eV for anatase compared to E_g = 3.0 eV for rutile, corresponding to an absorption edge of λ_g ~390 nm and λ_g ~410 nm, respectively). The capability of anatase phase to absorb only ultraviolet light, leaving the rest of the visible until the near infrared of the solar spectrum to the surface anchored dyes, depending on the property of the sensitizers.

The hereto related high refractive index of TiO_2 (n = 2.5 for anatase) results in efficient diffuse scattering of the light inside the porous photoelectrode, which significantly enhances the light absorption. So with a rigorous control of the TiO_2 surface one can enhance light absorption and therefore light harvesting efficiency of the photoanode. The light harvesting efficiency (LHE) is given by Eq. 1.9

$$\text{LHE}(\lambda) = 1 - 10^{-A} = 1 - 10^{-\Gamma\sigma} \qquad 1.9$$

where Γ is dye coverage [mol cm^{-2}] and σ is the absorption cross section [cm^2 mol^{-1}] (neglecting the scattering by the film). The cross section σ is related to the molar extinction coefficient ε by Eq. 1.10

$$\sigma = \frac{\varepsilon \cdot 1000}{N_A} \qquad 1.10$$

Typical ε values for dyes lie between 10^4 and 5×10^5 M^{-1} cm^{-1} yielding light-capture cross-section values between 0.0016 and 0.08 nm^2 [41,46,47]. However, the area of the sensitizer molecule occupying the surface of TiO_2 is much larger, about 1-2 nm^2 for Ru-complexes [41]. If we suppose a simple planar electrode TiO_2 surface covered with a monolayer of sensitizer, according to Eq. 1.9 and 1.10 just a few percent of incident light can be absorbed, which is detrimental for device performance. To solve this problem, a porous film consisting of 10 - 20 nm TiO_2 particles was turned out to increase the surface area and light capture by the photoelectrode [48]. Depending on the film thickness, the real surface area can be enhanced 1000-fold than the apparent one. With this strategy LHE can be considerably enhanced despite the fact that TiO_2 surface is recovered by a monolayer of dye. Since TiO_2 has high refractive index, the incoming photon can penetrate deeper and deeper within the mesoporous structure and crosses hundreds of adsorbed dye monolayers. In fact this process mimics the light absorption by green leaves. As the chlorophyll-containing thylakoids are stacked, visible light is absorbed completely by traversing many superimposed vesicles containing the dye.

TiO_2 is known to be a stable photoelectrode in photoelectrochemical cells, even under extreme conditions. Last not least TiO_2 is a cheap, easily available and non toxic compound, that is already widely employed as white pigment in paints and tooth pastes.

1.3.3. Electron Transfer dynamics

DSSCs are photoelectrochemical devices where several electron transfer processes are in parallel and in competition. The presence of a local electrostatic field is not required to achieve good collection efficiencies as it is the case for conventional *p-n* junction cells. Figure 1.3 summarises the electron transfer processes occurring at the dye-sensitized heterojunction. Recent studies of the *electron injection* dynamics from the electronically excited state of [perylene dye] and [Ru(II)polypyridyl complexes] into the conduction band of the TiO_2 demonstrated that the electron injection rate constant (k_{inj}) are relatively similar. k_{inj} was reported to be 5×10^{13} s^{-1} for perylene derivatives [49] and $k_{inj} > 4\times10^{14}$ s^{-1} for Ru-complexes [50]. Assuming, that the injection kinetics do not significantly change upon replacement of the electrolyte mediator by the solid-state charge transport material [51], the injection of electrons by the sensitizer in both the electrolyte cell and solid-state solar cell is expected to show similar characteristics.

Upon illumination, the sensitizer is photoexcited in a few femtoseconds (Eq. 1.1) and electron injection is ultrafast from excited dye S* to TiO_2 CB (Eq 1.2) on the subpicosecond time scale (intramolecular relaxation of dye excited states might complicate the injection

process and change the timescale), where they are rapidly (less than 10 fs) thermalized by lattice collisions and phonon emissions. The relaxation of the excited dye S* occurring in the range of nanosecond (Eq 1.3) is rather slow compared to injection, ensuring the injection efficiency to be unity. The ground state of the sensitizer is then regenerated by I^- in the microsecond domain (Eq. 1.4), effectively annihilating S^+ and intercepting the recombination of electrons in TiO_2 with S^+ (Eq. 1.5) that happens in the millisecond time range. This is followed by the two most important processes – electron percolation across the nanocrystalline film and the redox capture of the electron by the oxidized relay (back reaction, Eq. 1.6), I_3^-, within milliseconds or even seconds.

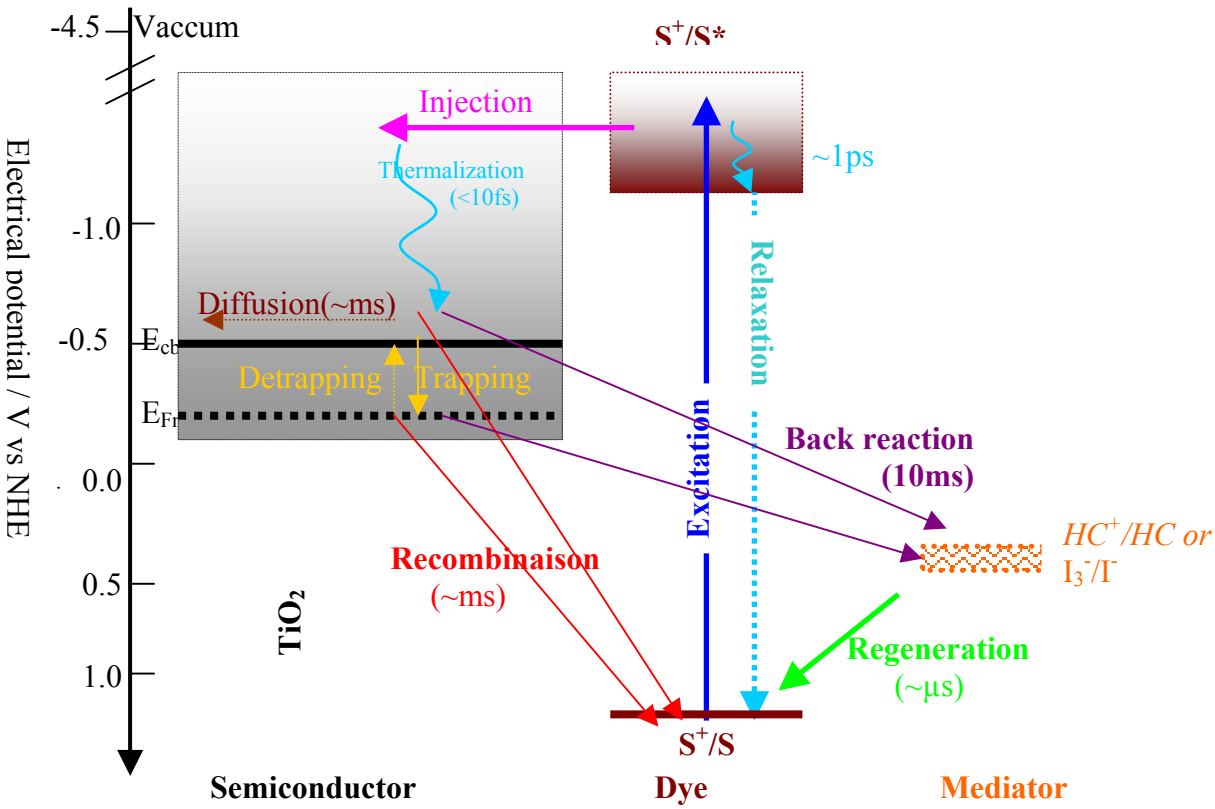

Figure 1.3 Schematic diagram of electron-transfer processes at the dye-sensitized heterojunction

$S\|TiO_2 + h\nu \rightarrow S^*\|TiO_2$	Photoexcitation	1.1
$S^*\|TiO_2 \rightarrow S^+\|TiO_2 + e\text{-}CB(TiO_2)$	Charge injection	1.2
$S^*\|TiO_2 \rightarrow S\|TiO_2 + h\nu' + \Delta$	Relaxation	1.3
$S^+\|TiO_2 + 2\,I^- \rightarrow S\|TiO_2 + I_2^{\bullet}$	Regeneration	1.4
$S^+\|TiO_2 + MeOTAD \rightarrow S\|TiO_2 + MeOTAD^+$	Regeneration (in solid-state DSSC)	
$S^+\|TiO_2 + e\text{-}(TiO_2) \rightarrow S\|TiO_2$	Recombination	1.5
$e\text{-}(TiO_2) + I_2 \rightarrow I_2^{-\bullet}$	Back reaction	1.6

1.3.3.1 Electron injection process

The rate of electron injection has been shown to depend on a variety of parameters, such as the length of the spacer between electron donor and acceptor [52], the density of acceptor states [53], and the electronic coupling between the dye and the semiconductor [54]. According to Marcus and Gerischer's theory [55-57], the total ET rate, k_{ET}, depends on the energetic overlap of donor (S*) and acceptor (semiconductor) states which are related to the density of states (DOS) at energy E relative to the conduction band edge, ρ(E), reorganization energy, λ, and temperature, T. At a given temperature, the overlap increases with a higher ρ(E) and a smaller λ and reaches a maximum when the entire donor distribution function lies above the conduction band edge, E_{cb}. Significant overlap is associated with a fast k_{ET}. In the DSSC, the sensitizer is strongly adsorbed on the semiconductor surface with carboxyl groups as the anchor, resulting in a very large electronic coupling between the π^* orbital of the excited state of the sensitizer and the conduction band of TiO_2, which consists of the unoccupied 3d orbital of Ti^{4+}. In addition, the conduction band of the semiconductor has a continuous and relatively large density-of-states. Thus, electron injection from the photosensitizer to the semiconductor occurs at a higher rate [58] than does the relaxation from the excited state to the ground state (i.e. relaxation via emission)[59]. It has been observed that electron injection from N3 dye into TiO_2 occurs on the order of femtoseconds as measured by the time-resolved laser spectroscopy [50,60]. This ultra-fast rate of electron injection contributes to the high energy-conversion efficiencies of the DSSC. Ultra-fast electron injection ~13fs from perylene to TiO_2 CB was reported.

The ultrafast electron injection is followed by the diffusion of injected electrons in TiO_2 particles. The electron movement in the nanocrystalline TiO_2 to the back contact (*percolation*) is significantly slower than in the TiO_2 single crystal using Ru-complex as sentizer. This has been demonstrated by photocurrent transient measurements after UV

illumination of TiO_2 particles, which showed decay times of milliseconds to seconds for film of ~10μm thickness [58,61-65]. Although electron transport is widely agreed to proceed by diffusion, the observed dynamics are not representative of simple diffusional processes, but contain evidence for charge trapping and trap filling [66,67].

1.3.3.2 Electron recombination and back reaction

Charge recombination between dye cations and photoinjected electrons occurs non-exponentially over picosecond–millisecond time scales. The wide range of time scales is usually attributed to the trapping of electrons by localized states on the semiconductor surface [65-76]. Nanocrystalline materials, possessing a high surface area, have a high density of such intra-band-gap trap states [58]. The distribution of trap energies results in the distribution of electron de-trapping times leading to dispersive transport. Some experiments results reveal strong sensitivity of the recombination rate to the occupancy of trap levels, which can be controlled by different parameters. By increasing the intensity of the light source it was found that the quasi Fermi level moves toward the conduction band leading to the fill of deep traps so that they no longer retard electron transport [77]. The surrounding electrolyte composition [77] and the applying of an external bias [68,70,78] were reported to influence the recombination process. It is known that the nature of dye plays a critical role in the recombination process. Clifford et al. [79,80] shown that by modifying the dye structure one can switch between electron transport-limited dispersive recombination dynamics and interfacial electron transfer-limited exponential recombination dynamics. This means that, large physical separation of the dye cation state from the film surface contributes to reducing the recombination process [79-81].

1.3.3.3 Dye regeneration

In DSSC dye regeneration is the determining step for the performance of the device. The life time of dye cation can be as long as milliseconds in the presence of pure solvent. In the presence of the most widely used I^-/I^{3-} redox system, dye cation quenching of down to microseconds [82,83] characterising dye regeneration. Dye regeneration is faster with increasing I^- concentrations and the lifetime of excited dye (S^+) follows the Stern-Volmer law [84]. However, in the solid state version where organic compounds namely spiro- MeOTAD are used as hole conductor [85], the regeneration of the oxidised dye by the hole conductor

have been found to proceed with a broad range of time constants from 3 ps to 1 ns [86]. Contrary to the case of the oxidation of I^- to I_3^-, which requires the transfer of two electrons, the dye regeneration process in this case is a single electron process and is characterised by a must faster kinetic [85,87].

Multiple phases of injection process were assigned to the heterogeneous nature of the heterojunction, incomplete pore filling and thereby resulting lateral hole migration between neighbouring dye molecules [88] not in contact with the regeneration material. This phenomenon can be suppressed if the dye architecture is defined in such a way that the wettability of mesoporous TiO_2/dye hybrid system by organic hole conductor is improved although this aspect could be really difficult to clarify.

1.3.4 Electrolyte and Organic hole conductor material

In a DSSC the hole conductors regenerate the dye after electron injection into the conduction band of oxide semiconductor. However, for an efficient reduction of oxidised dye the redox potential of the mediator must be more negative than that of the oxidised dye:

$$\Phi\left(D^+/D\right) < \Phi^0\left(S^+/S\right) \qquad 1.7$$

With a good choice of mediator one can have a gain in the open circuit voltage since the maximum voltage obtainable is related to the position of the mediator redox potential, $\Phi\left(D^+/D\right)$ should be as positive as possible. However, the difference in the potential should be high enough to provide a driving force for the dye reduction and therefore an optimal regeneration rate.

Up to now I^-/I_3^- system is still the best electrolyte for DSSCs. Efficiency of more than 11% with acetonitrile-based electrolyte and 8% long-term stability at 80 °C with low volatile electrolyte have been achieved [89-92]. Some new low volatile electrolyte types namely, room temperature ionic liquids have attracted considerable interests as a potential candidate for replacing the volatile organic solvents due to their negligible vapor pressure and high ionic conductivity [93-96]. Stable DSSCs devices were obtained by using binary mixtures of the viscous, pure imidazolium I^-/I_3^- ionic liquid with a low viscosity, highly stable ionic liquid [97]. Following similar logics, quasi-solid electrolytes have been designed by gelating the electrolytes with aliphatic gels [98,99], polymers [82,100,101] or even nanoparticles [102]. Other strategies for solidifying the electrolyte include introducing polymer cations [103,104]

or plastic crystal [105]. Beside these, Br_2/Br^- redox system was also reported as mediator [106].

Hole conductors are also a focus of current research since the majority of them are solids or nonvolatile liquids. Inorganic hole conductors of CuSCN [107-109], CuI [110-112], organic hole conductors such as triarylamines [113] and polymer hole conductors such as poly(3-alkyl thiophene) [114], polyaniline [115] have already been tested in DSCs. Among all the candidates, spiro-OMeTAD remains the best to date [77,85,116]. The electron life time can be increased by reducing the doping level in the OMeTAD, but this also decreases its conductivity. Meanwhile, pore filling is still the most serious problem for increasing the efficiency and stability of the OMeTAD system. However, the structure of dye can help to overcome this problem.

1.3.5 Counter Electrode

The counter electrode is an important component in DSSC where the mediator is reduced. It consists of fluorine-doped tin oxide (FTO) glass coated with platinum to afford more reversible electron transfer. Material like graphite [117-119], carbon black [117-119], activated carbon on FTO-glass and organic-ion doped conducting polymere of poly(3,4-ethylenedioxythiophene)(PEDOT) on both indium tin oxide (ITO) and FTO-glass [120,121] have been used as counter electrode in DSSCs.

In the typical case of solid-state dye-sensitized solar cells, noble metal with high work function, such as gold and platinum as well as carbon and conducting polythiophene polymers were found to form ohmic contact with spiro-MeOTAD [122]. Gold and platinum are typically applied by thermal evaporation in UHV or by sputtering in the case of platinum which is a very controllable technique and reproducible [123]. Metal counter electrode have the advantage of reflecting the light transmitted by the photoanode which cause a second transversal of the dye-sensitized film, thus enhancing light absorption for a given amount of dye. Inert metals, which do not chemically react with organic semiconductor, are, however, known for their diffusion on the surface and into the interior of the organic even at room temperature [124-126]. This effect depends strongly on the evaporation parameters such has evaporation rate and temperature [127]. Carbon and organic polymers have low conductivity and are generally applied in form of a paste by screen-printing or tape casting. In such case the definition of the small active area is difficult although these methods are easy to realize.

Carbon can be also applied in form of pressed graphite [108]. In the present work platinum was used as counter electrode for the sake of availability and reproducibility.

1.4. Objective of this work

The present work focuses on the liquid and solid state DSSCs based on some metal-free dyes namely, perylene derivatives. Since actually the dyes exhibiting better performance in this research field are Ru-complexes characterised by low extinction coefficient and low stability, it is suitable time to explore other dye types. In this logic, some metal-free dye types namely small molecule dyes and dye based on spiro concept also called "spiro bipolar dye" are used as sensitizer in DSSCs. Both electrolyte and solid-sate dye-sensitized solar cells are realized. The effect of the adsorption mode of these dyes (containing acid anhydride as anchor group) onto TiO_2 surface and the influence of cation coordination sites in the sensitizer on the performance of electrolyte-based cells are examined and interpreted. A new strategy to improve dye adsorption onto TiO_2 is presented and the influence on the performance of electrolyte-based cells is discussed. This work is of experimental nature supported by optical and electrochemical analytical technique.

The thesis is subdivided into four main parts: the first part (chapter 2 and 3) discusses the state-of the art of sensitizers in DSSCs, presents the material used as sensitizer in the present work and practical issues of experimental techniques and device preparation. The second part consists of chapter 4, 5 and 6 were devices are mainly based on liquid electrolytes. Chapter 4 shows a comparative study of DSSCs based on two families of dye type. The influence of the nature of the electrolyte on the performance of devices is scrutinized. Chapter 5 addresses the influence of the cation coordination site in the dyes on some parameters of devices. Chapter 6 introduces a new strategy to improve dye adsorption and light harvesting of photoanode by UV pre-treatment of TiO_2 film prior sensitization. The third part, chapter 7 presents the solid-state dye-sensitized solar cell where hole conductor electrolyte is replaced by amorphous film consisted of spiro-MeOTAD. The concept is not new [85], however, the study is motivated by the fact that the presence of donor moieties structurally similar to spiro-MeOTAD improve wettability of dye sensitized mesoporous films. The fourth part (Chapter 8) is the chapter of general conclusion, which is the summary of all previous chapters.

Chapter 2
INVESTIGATED MATERIALS

In this chapter the dyes used in my experiment are described. Then the physical and (electro)chemical properties of well-known chromophores used generally in dye solar cells is compared to metal-free dye based on bipolar spiro compound.

2.1. Chromophores

The efficiencies of the sensitizers used in dye-sensitized solar cells (DSSCs) are related to some basic criteria [128]. The highest occupied molecular orbital (HOMO) energy potential of the dye should be sufficiently positive with respect to the HTM/electrolyte redox potential for an efficient dye regeneration [129]. On the other hand, the lowest unoccupied molecular orbital (LUMO) energy potential of the dye should be sufficiently negative to match the potential of the conduction band edge of the TiO_2. It is also worth to mention that the light absorption in the visible region should be efficient [130]. However, by broadening the absorption spectra the difference in the energy levels of the HOMO and the LUMO is decreased. If the HOMO and LUMO energy levels are too close in potential, the driving force for electron injection into the semiconductor or regeneration of the dye from the electrolyte could be hindered. The sensitizer should also exhibit small reorganization energy for excited- and ground-state redox processes, in order to minimize free energy losses in primary and secondary electron transfer steps.

2.1.1. Classical chromophores

2.1.1.1. Ruthenium Based Chromophores

Chromophores of ruthenium complexes such as the N3/N719 [41,131] dyes and the black dye [132] have been intensively investigated and showed record solar energy-to-electricity conversion efficiencies (η) of 11% (figure 2.1).

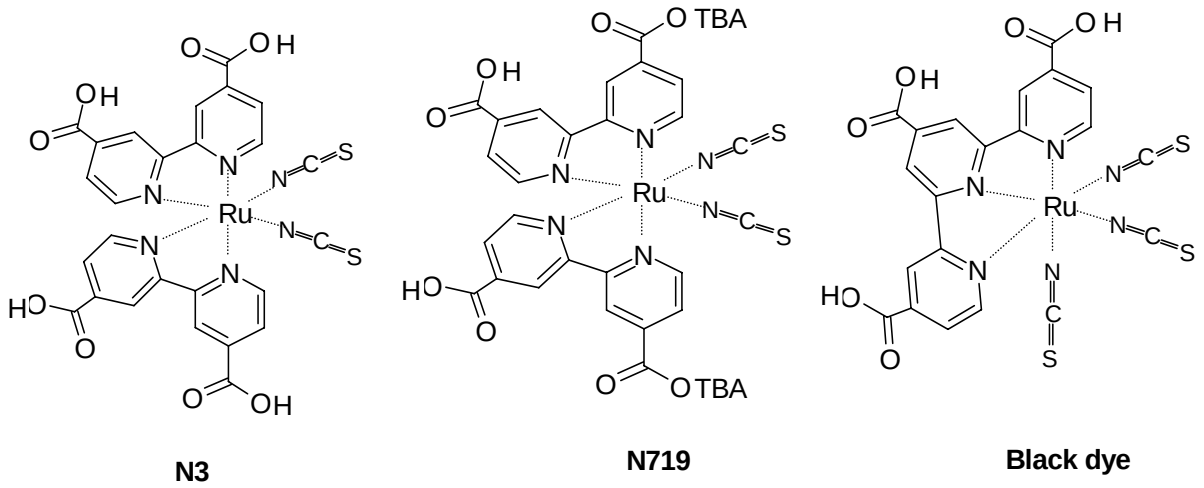

Figure 2.1. The chemical structures of the Ruthenium based sensitizers

A large number of ruthenium based sensitizers have been investigated in order to improve the photovoltaic performance and the stability of the DSSCs [133-136]. Recently, K19 and K77 attract more attention in research because they have shown an excellent device performance and have higher molar extinction coefficients with respect to N3, N179 and Black dye [89,137]. The enhanced absorption properties of those molecules is expected to be come from more extended conjugated system with respect to the former molecules, as shown in Fig. 2.1. [138].

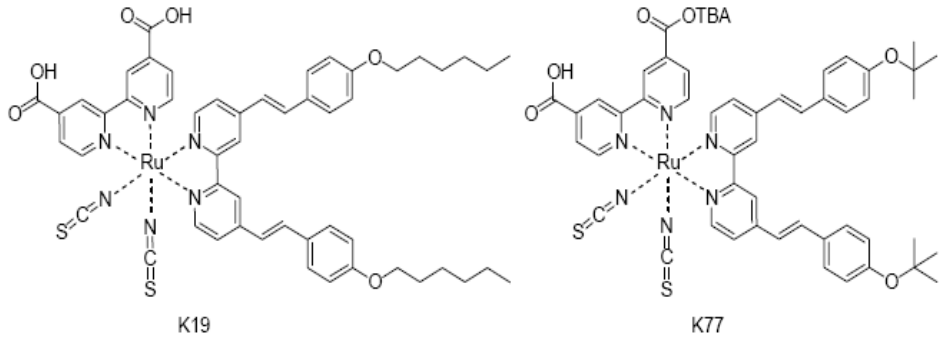

Figure 2.2. The new compound of Ruthenium based sensitizers

However, because of the extinction coefficient lying in the range of 10^4 $M^{-1}cm^{-1}$ thick TiO_2 layers for light harvesting are required, which is not advantageous since the series resistance in the corresponding device becomes more dominant. Thus, the use of metal free dyes with high molar extinction coefficients could probably overcome this problem, especially for solid-state dye sensitized solar cells in which a thin layer of TiO_2 is required.

2.1.1.2 Organic Chromophores

The interest in metal-free organic sensitizers has grown in the last few years. In 2000 Sayama et al. published a merocyanine dye (Mb(18)-N) (Fig. 2.3), which gave an efficiency of 4.2% [139]. Before this milestone, the organic dyes for DSCs performed relatively low efficiencies ($\eta < 1.3\%$) [28,140-143].

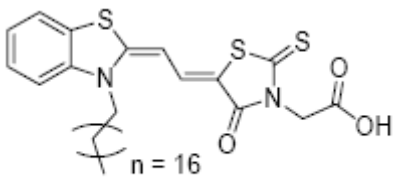

Mb(18)-N

Figure 2.3. Merocyanine dye Mb(18)-N

Organic dyes have some advantages over conventional ruthenium based chromophores as photosensitizers. For instance, they exhibit high molar extinction coefficients and are easily modified due to relatively short synthetic routes and especially low cost starting materials. The high extinction coefficients of the organic dyes are suitable for thin TiO_2 films required in solid-state devices where mass transport and insufficiently pore filling limit the photovoltaic performance [144]. This finding opens new roads for exploring new dye types.

In recent years, a great deal of research aimed at finding highly efficient and stable organic sensitizers has been carried out. A number of coumarin [145-147], indoline [148,149], and triphenylamine [150-153]-based organic sensitizers (Fig. 2.4) have been intensively investigated and some of them have reached efficiencies in the range of 3-8% [128,143-149,151-154]. All these sensitizers are efficient and represent one strategy in developing new chromophores, namely, reaching as high efficiency as possible and dealing with possible stability issues of the chromophore at a later stage.

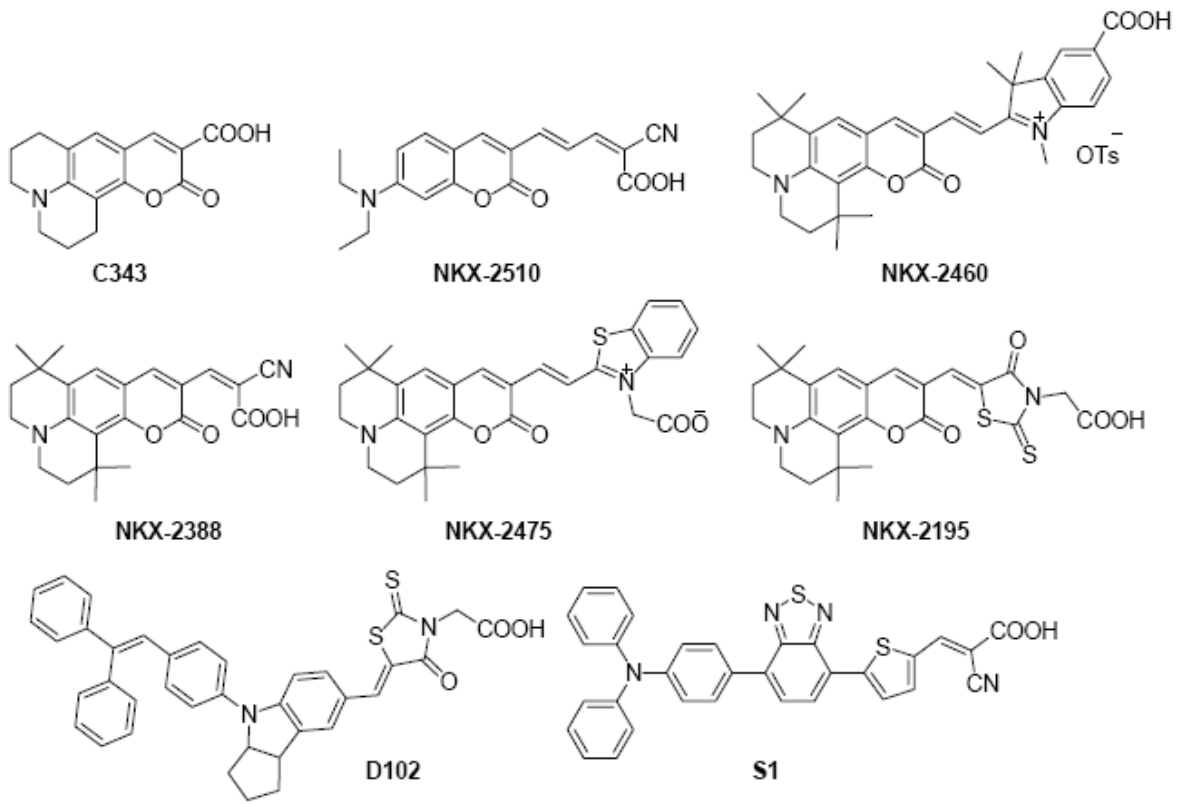

Figure 2.4. Examples of organic dyes.

Perylenes represent the second strategy, starting from highly photo-stable sensitizers, dealing with the efficiency issue by introducing different substituents on the perylene framework. This class of dye has high absorption coefficients in the visible region ($\varepsilon \sim 10^5$ M^{-1} cm^{-1}), and the fluorescence quantum yields of the singlet state are near unity [47]. Electron injection from dye singlet states into the conduction band of a semiconductor is generally faster than that from triplet [81] and it conserves more potential from the light capture. Some perylene compounds have been used as sensitizer in DSSC but their efficiency was low. Recently, the perylene compounds-based dye-sensitized solar cells have reached efficiencies around 1.9% [142,155-157]. After bonding in bay position of perylene core an electron-donating substituent such as pyrrolindone (Figure 2.5. iPr-PMI), which increases the electron density in the perylene moiety and, thus, in TiO_2 CB an efficiency of 2.6% was obtained [158]. However, adding a diphenylamine substituent (Figure 2.5. ID28) at the 3 or 4-position of perylene core turned out to be beneficial (an efficiency of ~4% was obtained) [159]. This continuous development in this category of dye shows how this class of dye is actually in intensive investigation.

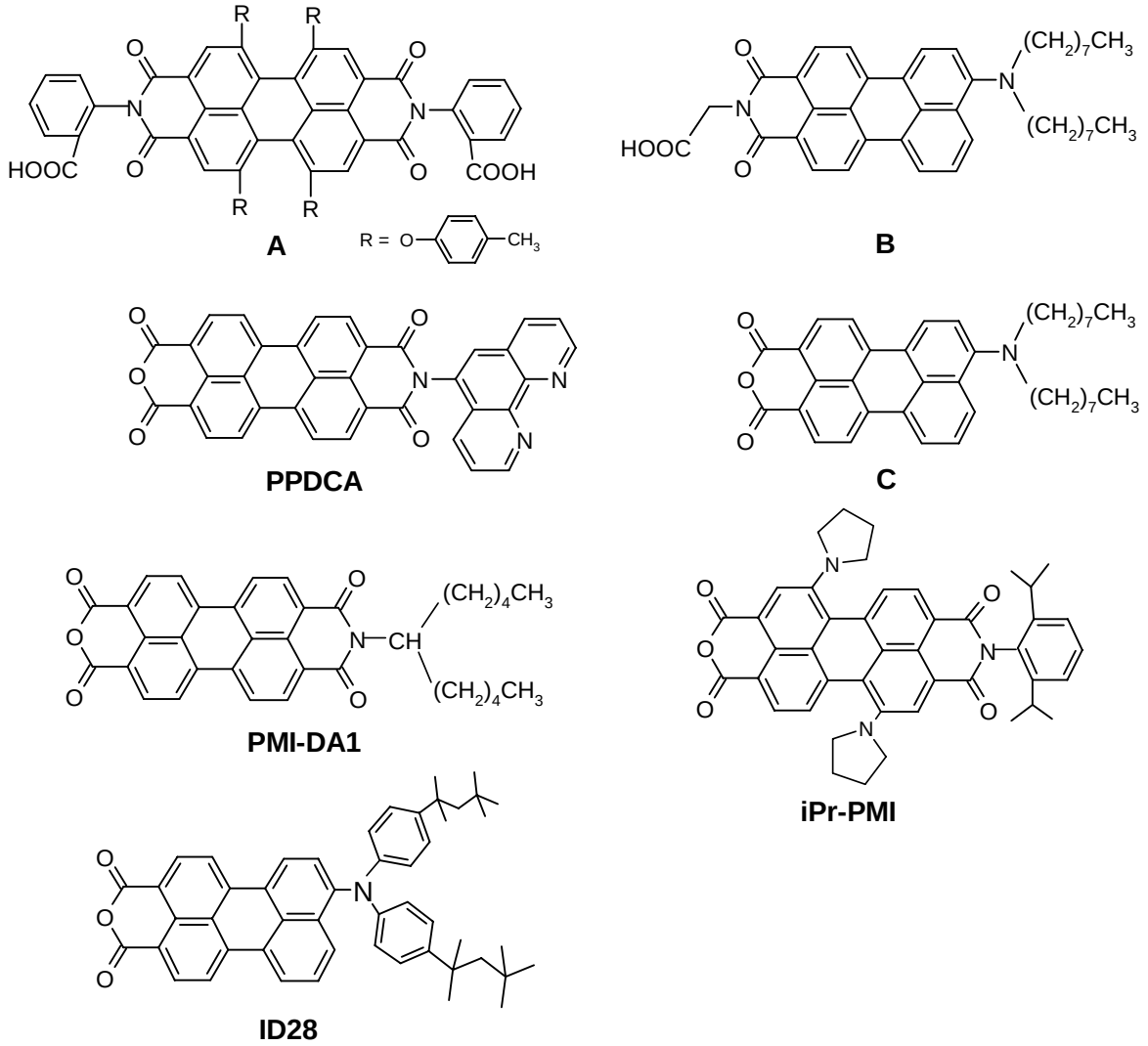

Figure 2.5. Chemical structure of some perylene derivatives used as sensitizer in DSSCs.

2.1.2. Dye based on the spiro concept

Generally, most organic dyes used as sensitizer consist of a conjugated system in which the dye donor moieties are molecularly bonded to acceptor moieties. The diphenylamine is a well-known electron donating group [81]. Edvinsson et al. [159] synthesized some perylene derivatives in which the donating moieties are bonded to the perylene core at 4-position. The overall solar-to-electrical energy conversion efficiency of the corresponding DSSCs was improved to almost 4%. However, in these compounds the intramolecular charge transfer occurs by push-pull process because of the conjugation of the π-system between the donor and acceptor. Such a configuration polarizes the dye and, thus increases its excited-state lifetime, which is useful for an efficient electron transfer to TiO_2 in

competition with excited dye to dye recombination. In order to separate two different moieties (donor and acceptor) without changing their electronic properties, Salbeck introduced the spiro concept in 1996 [160] and many compounds based on this concept have been synthesized and characterized [46,161]. In this concept, different chromophores are connected by the spiro atom. The schematic view of the spiro concept is presented in Figure 2.6(a). Joining two π-systems (in the case of compounds **22**) with a spiro center achieves the task of raising glass transition temperature T_g as has been observed in some spiro-compound [162], because of the steric demand which effectively hinders crystallisation. On the other hand, the spiro atoms links two different charge transport molecules in which the electronic properties are retained. The chemical structure of 2′,7′-bis(N-N-diphenylamino)-9,9′-spirobifluoren-2-yl-amine (**7**), *N*-(di-*t*-butylphenyl)-3,4:9,10-perylene tetracarboxylic acid-3,4-anhydrid-9,10-imid (**P10**) and N-[2′,7′-bis(N,N-diphenylamino)-9,9′-spirobifluoren-2-yl]-N′-(2,5-di-tert-butylphenyl)-3,4,9,10-perylentetracarboxylicdimide (**22**) are shown in Fig. 2.6(b), 2.6(c) and 2.6(d), respectively. The absorption maxima of these compounds are shown in Table 2.1. As it can be observed, the absorption maxima of the spiro-compound are quite similar to those of its parent compounds. This indicates that the spiro atom does not significantly influence the electronic and optical properties of donor and acceptor moieties. However, this behaviour cannot be only attributed to the spiro atom. The frontier orbital of the perylene moiety has a node at the imide nitrogen and the anhydride oxygen atoms. Thus, the spirobifluorene spacer does not affect the electronic structure of π-systeme in the perylene tetracarboxylic [163,164].

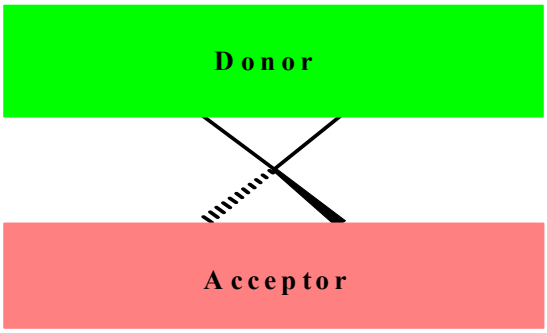

(a)

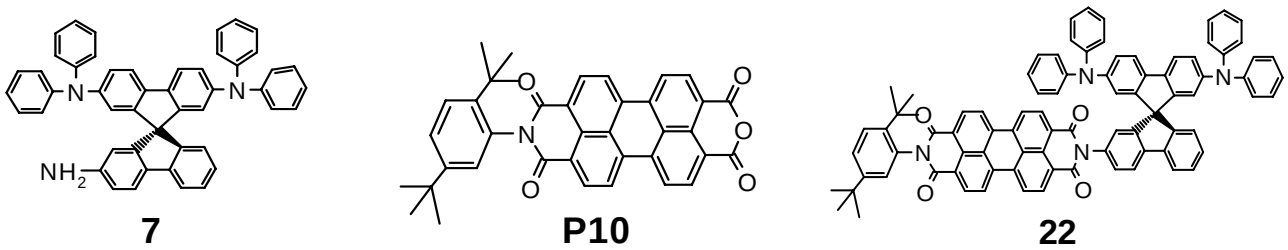

(b) **(c)** **(d)**

Figure 2.6. Schematic view of the active materials using the spiro concept

Table 2.1. Absorption spectra of spiro-compounds and the corresponding parent compounds. (λ/nm; ε/$M^{-1}cm^{-1}$). Concentration = 1×10^{-5} M; Solvent = Dichloromethane

Material	λ_{max} (ε)	Ref.	Material	λ_{max} (ε)	Ref.
7	380 (/)	[46]	**22**	381 (46000)	[46]
P10	522 (70000)	In this work		527 (97000)	

Through this concept, some particular points useful for a dye in DSSC are expected:

- by keeping the donor moieties far from TiO_2 surface we expect that the spirobifluorene-bridge can effectively prevent the recombination of injected electrons from TiO_2 conduction band with the oxidised dye, one of the key problems limiting the performance of Grätzel cells.
- On the other hand, the spirobifluorene-bridge keeps oxidised donors close to the redox electrolyte or organic HTM where interception can easily take place.
- The presence of donor moieties structurally similar to spiro-MeOTAD could improve the wettability of sensitized TiO_2 film by the organic HTM and could thus facilitate hole transfer reaction from the dye cation to HTM in the solid state version.

The actives materials used in this study can divided in two classes, namely spiro-linked compound and those considered as small molecules:

The small molecules are listed below

- Perylene dicarboxylic acid-3,4-anhydride (P7)
- *N*-(Pentafluorphenyl)-perylen-3,4:9,10-tetracarboxylicacid-3,4-anhydrid-9,10- imide (P4)

- *N*-(Diisopropylphenyl)-3,4:9,10-perylene tetracarboxylic acid-3,4-anhydrid-9,10-imide (P8)
- *N*-(Di-*t*-butylphenyl)-3,4:9,10-perylene tetracarboxylic acid-3,4-anhydrid-9,10-imide (P10)
- 1,7-(4´-*t*-butylphenoxy)-3,4:9,10-perylene tetracarboxylic dianhydride (P9)

The bipolar spiro-linked compound used as sensitzer

- *N*-[2´,7´-Bis-(*N,N*-diphenylamino)-9,9´-spirobifluoren-2-yl]-1,7-bis-(4-*t*-butylphenoxy)-perylene-3,4-dicarboxylic acid anhydride-9,10-imide (P1)

The spiro-compound used as hole transport material in solid state solar cell was

- 2,2´,7,7´-tetrakis(N,N-di-p-methoxyphenyl-amine)-9,9´-spirobifluorene (Spiro-MeOTAD)

All these active materials are shown in Figure 2.7.

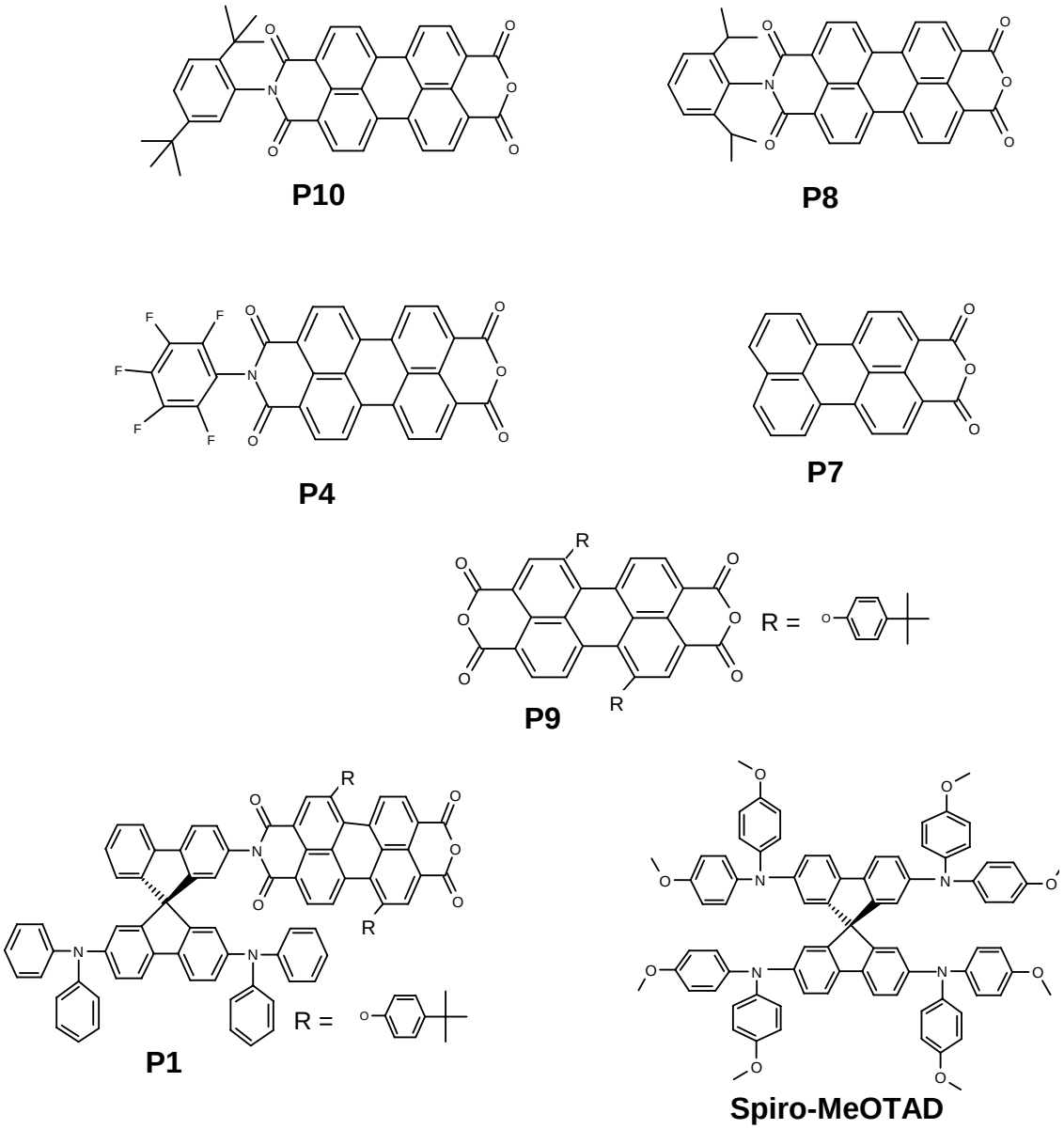

Figure 2.7 The chemical structures of small molecules (P4, P7, P8, P9 and P10) and molecules based on spiro-concept (P1 and spiro-MeOTAD) used in this study.

2.2. Electrochemical and Spectroscopy properties

As already mentioned, the charge injection from the LUMO of the dye and the TiO_2 conduction band as well as dye regeneration are crucial points in dye sensitized solar cells. Thus, energy-level matching is crucial in designing sensitizer. The energy level of active materials can be investigated by utilizing photoelectron spectroscopy (PES) [165] or by absorption spectroscopy. However, the organic materials are usually characterized by cyclic voltammetry [166]. From this point, the values can be extrapolated to the glass phase by

choosing an appropriate reference and neglecting the influence of the polarity of the solvent in which the measurement are taken [167]. The ionisation energy of ferrocene is assumed to be 4.8 eV, thus linking the electrochemical potential to the work function scale of the electrode [168]. Therefore, the energy of the molecular orbital is the negative value, that is,

$$E_{MO} = -(4.8 + E_{1/2}) \qquad 2.1$$

$E_{1/2}$ being the reversible half-wave potential of the electron-transfer reaction with respect to ferrocene. The LUMO level of active material is extracted by substituting the value of $E_{1/2}$ in equation 2.1, which is obtained by voltammetry measurements. The electrochemical measurements of the compounds P4, P7, P8, P9, P10 has enabled to access their LUMO levels. Their HOMO was obtained by subtracting from the LUMO the zero-zero energy ($E_{0\text{-}0}$) estimated from absorption onset (λ_{onset}) of the dye in solution at 10% of the full amplitude at the absorption maximum. Thus, energy of HOMO can be expressed as,

$$E_{\mathrm{HOMO}} = E_{0\text{-}0} - E_{\mathrm{redox}} \qquad 2.2$$

$E_{0\text{-}0}$ being the gap between the HOMO and LUMO of the material (and is obtained by the ratio of $1240/\lambda_{onset}$). This method is widely used [158,159,169] to determine the energy level of some materials. All potentials were obtained vs Fc/Fc^+ and were recalculated with respect to NHE. The measured potentials were recorded with respect to the Ag/AgCl reference electrode. Ferrocene/ferrocenium (Fc/Fc^+, 0.577 V vs NHE). From this investigation the energy levels of materials match perfectly the conduction band edge of TiO_2 and the redox potential of HTM or I^-/I_3^- as shown in the Figure 2.8. (summarized in Table 2.2.).

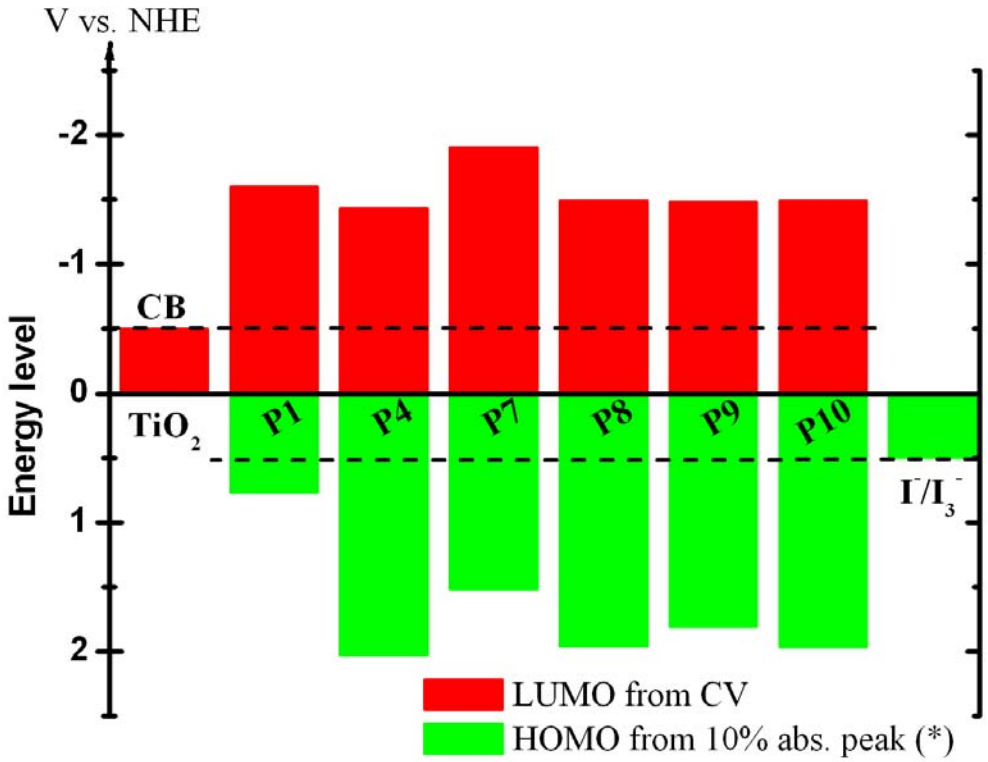

Figure 2.8. Energy level of the conduction band edge of TiO_2 and the LUMO and HOMO level of the active materials. The LUMO level were obtained by CV and the HOMO by absorption onset. (*) CV was used to access HOMO and LUMO of P1. All potentials were obtained vs. Fc/Fc^+ and were recalculated with respect to NHE. Dotted lines represent the energies level of conduction band of TiO_2 and Fermi level of redox electrolyte.

The UV-vis absorption spectra of P1, P4, P7, P8, P10 in CH_2Cl_2 and adsorbed onto TiO_2 are shown in Figure 2.7. All dyes show absorption bands in the visible region except P1, which shows an absorption band in the Ultra-violet region. The absorption maxima of P4, P8 and P10 are centred at 522 nm whereas the absorption band of P7 showing a maximum at 494 nm is hypsochromically shifted towards the blue region of visible spectrum. This change is likely due to the lack of the imide function in P7 compound. However, the absorption bands of P1 and P9 are slightly shifted towards the red region. This is due to the electron donating effect of the phenoxy group, which is directly bonded to the perylene core increasing the electron density in the perylene core and thus modifying the gap between HOMO and LUMO.

This diminution of gap (increase of the HOMO level) induces a bathochromic shift of the absorption maxima, compared to the spectra of compound lacking substituents in the bay position. It is also accompanied by a loss of the vibration fine structure. Both naphthyl halves of perylene structure are twisted against each other in an angle of 15° [170]. The absorption bands in the visible region depicted by all dyes correspond to π-π^* transition in perylene tetracarboxylic moieties. In contrast to other dyes as already mentioned, P1 shows an absorption band in the ultra-violet region at 382 nm. This band is attributed to diphenylamine connected to spirobifluorene spacer. In solution, the fingerprints corresponding to the maximum of the S1 transition are the same for both P1 and P9 dyes and just a slight decrease in extinction coefficient is observed in P9. This suggests that the bipolar nature of P1 and the donor strength of the diphenylamine units do not affect the electronic structure of the perylene tetracarboxylic core.

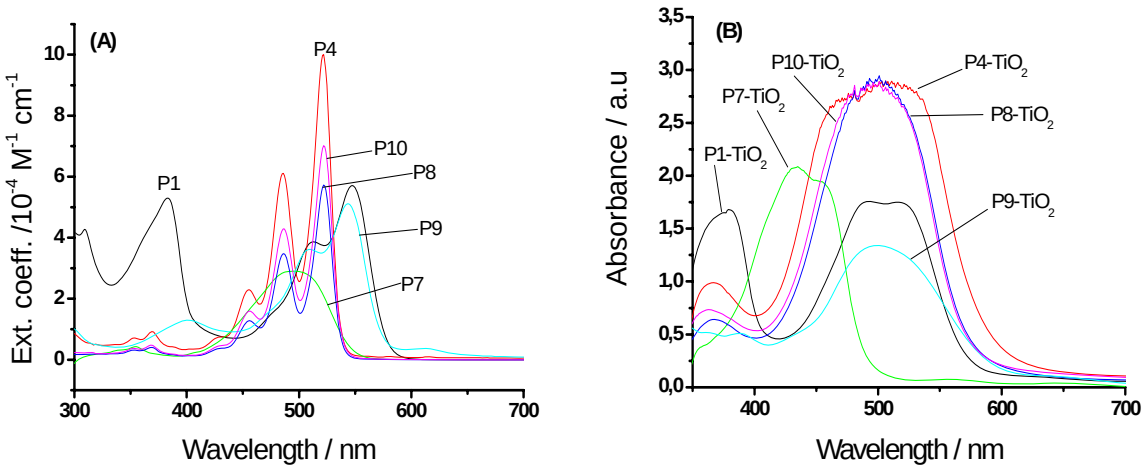

Figure 2.9. The UV-vis absorption spectra of P1, P4, P8; P9, P10 in DCM and P7 in NMP (A) and adsorbed onto TiO_2 film(B). A bare TiO_2 was used as background.

Figure 2.9(b) shows the UV-vis absorption spectra of dye loaded TiO_2 electrodes. When the dyes are attached onto TiO_2, a blue shift of absorption maxima (corresponding to π-π^* transition) with respect to dye in solution is observed. The peaks corresponding to S1 transition are shifted from 546 nm to 517 nm, from 522 nm to 501 nm, from 494 nm to 435 nm, from 522 nm to 501, from 544 nm to 500 nm and from 522 nm to 497 nm corresponding to P1, P4, P7, P8, P9 and P10, respectively. The change can be assigned to the bond opening

of the acid anhydride groups and electron withdrawing character of titanium, which is a lewis acid [155,158,171].

Table 2.2: Electrochemical and spectroscopic data for the perylene dyes in dichloromethane solution and adsorbed on TiO_2 (*). [a)] Values estimated from absorption onset of dyes in Dichloromethane at 10% of the full amplitude at the adsorption maximum. [b)] Values obtained from voltammetry measurements. [c)] Obtained as the sum of experimental E_{redox} and E_{0-0} for the dye in Dichloromethane.

	$\lambda_{max}(\varepsilon_{max})$ nm($M^{-1}cm^{-1}$)	λ_{max}^{*} [nm]	E_{0-0}^{a} [eV]	LUMO[b] [eV]	HOMO[c] [eV]	HOMO [V vs NHE]	LUMO [V vs NHE]	**Ref.**
P1	546 (57000) 382 (53000)	517	/	-3.78	-4.99	0.767	-1.60	
P4	522 (99000)	501	2.31	-3.94	-6.25	2.03	-1.44	
P7	494 (29000)	458	2.26	-3.48	-5.74	1.52	-1.91	
P8	522 (57000)	501	2.30	-3.88	-6.18	1.96	1.50	
P9	544 (51000)	500	2.14	-3.89	-6.03	1.81	-1.49	
P10	522 (70000)	497	2.31	-3.88	-6.19	1.97	-1.50	
TiO_2	/	/	/	/	/	/	-0.50	[158]
I^-/I_3^-	/	/	/	/	/	0.40		[159]
Spiro-MeOTAD	/	/	/	/	-4.77	0.82		[172, 173]

2.3. Organic hole transport materials

One of the most efficient organic material used as hole transport material in DSSC is the well-known 2,2',7,7'-tetrakis(N,N-di-*p*-methoxyphenyl-amine)-9,9'-spirobifluorene (spiro-MeOTAD), as shown in Fig. 2.5. Spiro-MeOTAD was designed for the application in organic devices based on the standard hole transport material N,N'-diphenyl-N,N'-bis(3-methylphenyl)-1,1'-biphenyl-4,4'diamine (TPD). The thermal stability of the glassy state could be drastically improved by connecting two TPD units via a spiro centre [174-176]. Due to the increased steric demand of the spiro molecule, solution and crystallisation properties are changed without significant change of the electronic properties of the base molecule.

Compared to TPD, spiro-MeOTAD has a much higher glass transition temperature, which enables the formation of stable amorphous films. While films of TPD are more or less crystallised after two months, pure spiro-MeOTAD film will stay in the amorphous state for years. That is the reason why Spiro-MeOTAD was successfully used as HTM in solid-state dye sensitized solar cells [85] and in light- emitting diodes [174]. However, the introduction of the spiro center also increases the melting point to 246 °C, which makes it impossible to produce layers of spiro-MeOTAD by thermal evaporation in UHV. The standard deposition technique is, therefore, spin-coating of a solution of spiro-MeOTAD in chlorobenzene.
The substitution of TPD with two methoxy-substituents leads to a seven times higher hole mobility of the material [177]. TPD molecules containing methoxy substituents show an improved stability of the corresponding radical cation, which has been assigned to increased electronic overlap of the molecular orbitals caused by the electron withdrawing methoxy groups. Spiro-MeOTAD contains 8 methoxy substituents and shows a 100 mV higher oxidation potential with respect to the unsubstituted structure.

The neutral form of the hole conductor is pale yellow and absorbs in the UV (λ_{max} = 372 nm). Its four oxidation states can be obtained via chemical oxidation with [N(p-C_6H_4Br)][$SbCl_6$] [122]. The spectrum of spiro-MeOTAD$^+$ shows an intense band at 511 nm and a shoulder at 700 nm. The spiro center connects two identical molecule units in a perpendicular arrangement and acts as an electronic barrier. Therefore the spectrum of the spiro-MeOTAD^{2+} is similar to the mono cation but with a doubled extinction coefficient.
According to Weissörtel [176] the di(radical cation) of spiro-MeOTAD shows absorption maxima in $CHCl_3$ at 511 nm (ε = 40100 M^{-1} cm^{-1}) and 1400 nm (ε = 32200 M^{-1} cm^{-1}), while spiro-MeOTAD^{4+} exhibits an absorption maximum at 865 nm (ε = 118000 M^{-1} cm^{-1}).

The mobility of the spin-coated spiro-MeOTAD has been studied by Poplavsky et al. [178] by means of time-of-flight (TOF) measurements, dark-injection space-charge-limited current transients and steady-state current-voltage characteristics. The voltage dependent room temperature mobilities for film thickness ranging 4000 nm to 135 nm were determined to be in the around of 10^{-4} cm^2/Vs. Contrary to earlier results published by Bach [179] employing smaller molecules of the same structural type as spiro-MeOTAD, the charge transport has been found to be a non-dispersive process. Analysis of the temperature behaviour of the time-of-flight mobility based on the Gaussian Disorder Model developed by Bässler et al. [180] revealed higher energetic disorder for the methoxy-substituted compound (spiro-MeOTAD) than for the non-substituted analogue. The comparison of similar molecules

with and without spiro center revealed that the spiro-concept leads to high morphologic stability, without deteriorating its electronic properties [179].

The conductivity of a pure, 1 μm thick film spiro-MeOTAD film is in the range of $M\Omega/cm^2$. The relative low charge mobility has been compensated by doping of the hole conductor film using tris(p-bromophenyl)ammoniumyl hexachloroantimonate $[N(p\text{-}C_6H_4Br)_3][SbCl_6]$ [122,181]. This oxidative doping of spiro-MeOTAD via a one-electron transfer leads to a dark conductivity that is increased by many orders of magnitude.

Chapter 3
EXPERIMENTAL SECTION

In this chapter, the details of the experimental procedures are described. The materials and techniques that I used for the preparation and characterisation of dye solar cells (both dye sensitized solar cells "DSSCs" and solid-state dye-sensitized solar cells "SSD") are presented as well. Furthermore, a design of dye-sensitized-solar cells, fabrication of the photoanode (working electrode) are shown. The TiO_2 surface pretreatment techniques and spectroscopic methods are described as well.

3.1 Device preparation

3.1.1 Structure of dye solar cells

The dye solar cells contrary to conventional solar cells consist of the two distinct phases, namely solid and liquid phases for electrolyte based dye-sensitized solar cells (DSSC) and crystalline and amorphous phases for solid-state dye-sensitized solar cells (SSC), the latter being monolithic design. The schematic view of the DSCs structure developed in this study is shown in Fig. 3.1 and the details of device fabrication processes are described in section 3.1.2.

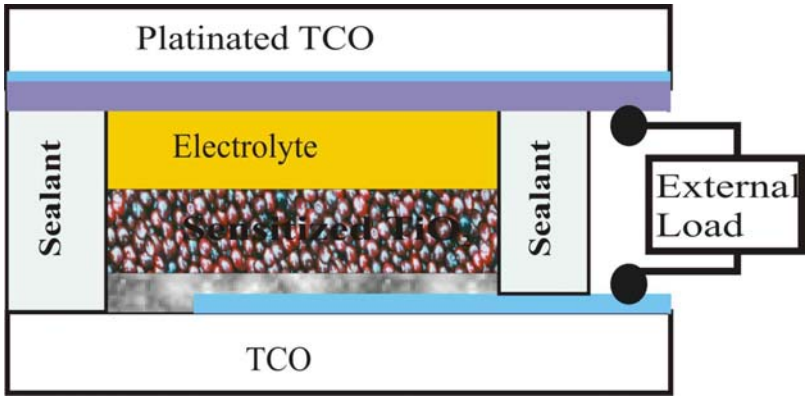

(a)

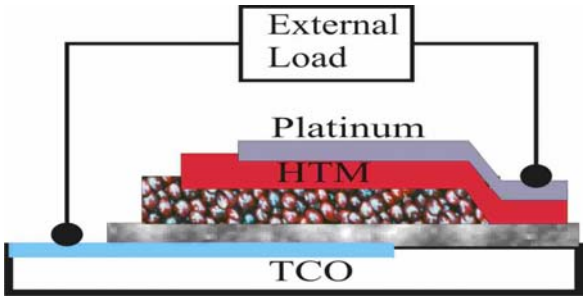

(b)

Figure 3.1. Schematic view of dye-sensitized solar cells: (a) dye sensitized solar cell; (b) Solid-State dye-sensitized solar cell.

3.1.2. Fabrication of dye-sensitized solar cells

This section presents the details of the fabrication of dye-sensitized solar cells. The step by step procedures are displayed in Fig. 3.2. Each picture depicts one step in the fabrication process from the structuring of TCO to complete assembly of the devices.

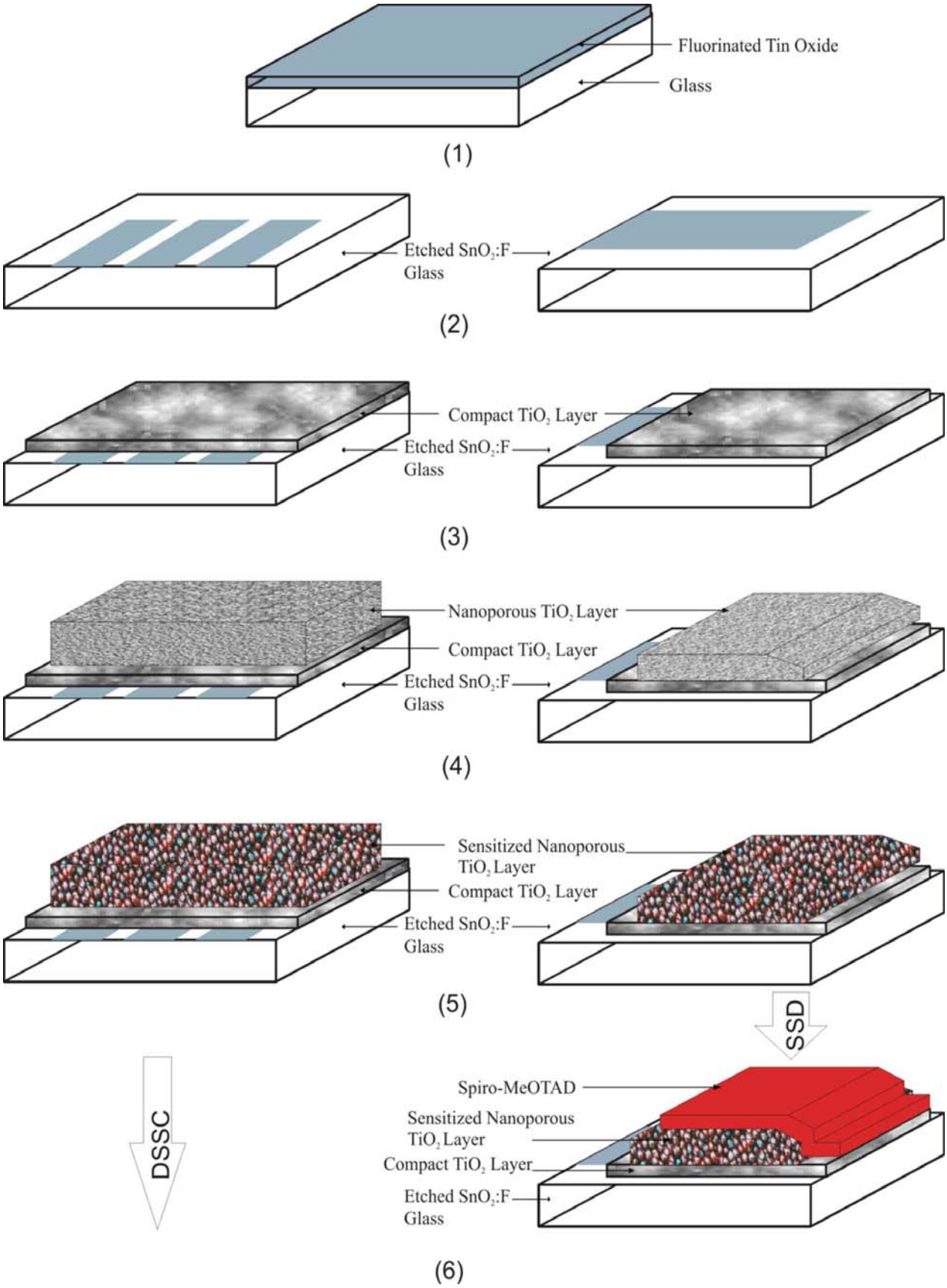
Fluorinated Tin Oxide
Glass
(1)
Etched SnO_2:F
Glass
(2)
Compact TiO_2 Layer
Etched SnO_2:F
Glass
(3)
Nanoporous TiO_2 Layer
Compact TiO_2 Layer
Etched SnO_2:F
Glass
(4)
Sensitized Nanoporous TiO_2 Layer
Compact TiO_2 Layer
Etched SnO_2:F
Glass
(5)
SSD
DSSC
Spiro-MeOTAD
Sensitized Nanoporous TiO_2 Layer
Compact TiO_2 Layer
Etched SnO_2:F
Glass
(6)

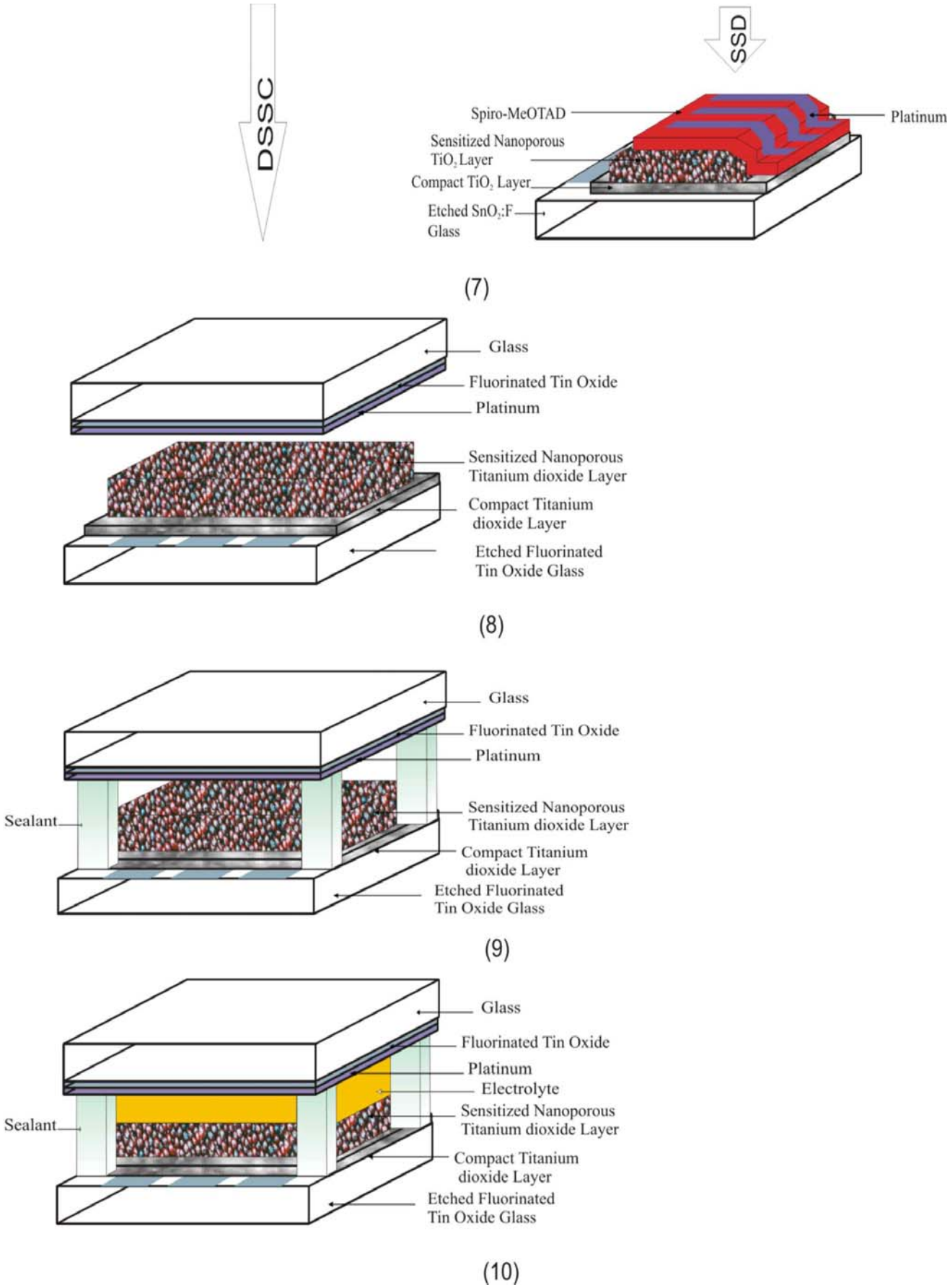

Figure 3.2. The details of dye-sensitized solar cells fabrication

Each step in the device fabrication is briefly mentioned below and the details of DSSC fabrication will be described in depth in section 3.1.3:

(1) and (2) present the non-structurated and structurated fluorine-doped SnO_2 (F-SnO_2) glass

(3). Deposition of compact TiO_2 (~130 nm) on F-SnO_2

(4). Deposition of nanoporous TiO_2 film by tape casting method

(5). Dye sensitization of nanoporous TiO_2 film by soaking TiO_2 film in concentrated dye solution

(6). Deposition of organic hole transport material (HTM) by spin-coating (for solid-state dye sensitized solar cells "SSD")

(7). Deposition of platinum on (HTM) of SSD by thermal evaporation

(8), (9) Counter electrode (platinum coated F-SnO_2 glass) and sealing of both photoanode and counter electrode with surlyn film

(10). Filling of sandwich cell with electrolyte solution

3.1.3. Materials

All chemicals used in this work were of commercial grade.
Chemical additives used in my experiment were: $NaClO_4$ (98%, Fluka) $TBAClO_4$ (98%, Fluka), KClO4 (99%, Aldrich), $LiClO_4$ (95%, Lancaster), I_2 (99.5%, Lancaster) and 1-butyl-3-methylimidazolium iodide (Merck). These materials were used without further purification.
Tert-butylpyridine (*t*BP) (98%) was purchased from Fluka and stored in dry atmosphere until use.

The solvent used in this work were: Acetonitrile (99%,) and 3-methoxypropionitrile (99%, Lancaster) used for preparation of the electrolyte were dried and stored under inert atmosphere until use. Dichloromethane (99.9%, Roth) and chlorobenzene (99%, Lancaster) were used for the preparation of the spin-coating solution.

Di-iso-propoxytitanium bis(acetylacetonate) (TAA) used as precursor for the spray-pyrolitic deposition of compact TiO_2 layer was synthesized according to the procedure proposed by Kavan et Al. [182]. The TAA was synthesised by stoichiometric addition of acetyl acetone ($C_5H_8O_2$) to a stirred solution of titanium isopropoxide [Ti(i-$C_3H_7O)_4$](molar ratio 2:1). This fresh TAA solution (2 M) was immediately diluted with ethanol to a final

concentration of 0.2 M before each coating. The color of the diluted precursor was orange. The synthesis reaction of TAA is the following.

$$[Ti\ (i\text{-}C_3H_7O)_4] + 2\ C_5H_8O_2 \longrightarrow [Ti\ (acac)_2(i\text{-}C_3H_7O_2)] + CH_3CH\ (OH)\ CH_3 \qquad 3.1$$

2,2´,7,7´-tetrakis(N,N-di-p-methoxyphenyl-amine)9,9´-spirobifluorene (Spiro-MeOTAD) was synthesized in our group following the method described by Weissörtel [176].

The TiO_2 paste used in the preparation of nanoporous layers was prepared following the procedure describes by Barbe et al. [48].

This method can be summarized as follow:

- Precipitation (hydrolysis of Ti-alkoxides using 0.1 M HNO_3)
- Peptisation (heating at 80 °C for 8 h) followed by filtration
- Hydrothermal growth/autoclaving (at 200-230 °C to prevent aggregation of rutile at T > 240 °C)
- Sonification (ultrasonic bath at 200 W for 15 × 2 min)
- Concentration (35-45 °C, 30 mbar)
- Binder addition (carbowax / PEG 20.000 g/mol) (0-50 % weigth of TiO_2)

3.1.4 Transparent conducting oxide (TCO) substrates

The choice of TCO is fundamental for the fabrication of DSSCs. TCO should show high electrical conductivity and low absorption of the visible light. However, the decrease of the resistivity is correlated with a decreased transmission for a given material. Correspondingly the two parameters have to be optimised for the application of interest.

The TCO, which works as current collector should pass the demanding processing conditions for the device preparation without changing its physical properties. The TCO typically remains stable up to temperatures slightly above the optimised deposition temperature. Some types of TCO show an increase in resistivity after heating at high temperature and for a long time. Indium tin oxide (ITO) films used in particularly for the preparation of OLED [183] show significant losses of conductivity upon heating over 200°C. Yoshikawa et al. [184] noticed that the resistivity of ITO is increased by 71% and 162% when they are heated to 450°C and 500°C for one hour, respectively. The decrease in conductivity can be attributed to the fact that oxygen bonded to a portion of the oxygen-vacant structure within the ITO film leading to the loss of the oxygen vacancies, which act as electron supplier [184]. In contrast,

fluorine doped SnO_2 film are generally very stable so that the softening of the glass substrate is more limiting than any thermal decomposition of the conducting layer.

According to the so called "figure of merit" enabling to determine the performance of TCO the ratio of the resistance to the transmission of 550 nm radiation has been used [123]. A small value indicated better performance of the TCO. The TCO10-10 glassed used in this work were purchased from Solaronix. Their performances are presented in Table 3.1 and are compared to other glass types. Table 3.1 shows that TCO10-10 is thermally stable with respect to Asahi glass but less than Solaronix [123]. TCO10-10 was preferred because of its availability. On the other hand its chemical patterning is easy leading to straight and more defined active areas.

Table 3.1. Comparison of TCO10-10 substrate with some commonly used TCO subtracts for the preparation of DSSC and SSD

Glass type	**T_{550}[a] [%]**	**R_0[b] [Ω/□]**	**R_1[c] [Ω/□]**	**R_2[d] [Ω/□]**	**R_0/T_{550}[e] [Ω/□]**	**Ref.**
Solaronix (9 Ω/□, 1mm thick)	85	8.4	8.6	8.8	0.10	[123]
TCO10-10 (10 Ω/□, 1.1mm thick)	85	12	15.8	15.7	0.14	This work
Asahi (10 Ω/□, 1mm thick)	82	13.5	12.5	60.2	0.16	[123]

[a] T_{550} = Transmittance at 550 nm, [b] R_0 = initial resistance, [c] R_1 = resistance after first sintering (500 °C, 10 minutes), [d] R_2 = resistance after second sintering (500 °C, 10 minutes), [e] R_0/T_{550} = figure of merit. In parenthesis behind the glass type the nominal resistance of the glass is given as well as the thickness of the glass. Resistance measurements have been performed using the four-point technique.

Structuring of Fluorinated Tin Oxide glass

The chemical structuring of FTO as shown in Figure 3.2(2) was done using Zn granulate (20mg/cm²) in combination with 2 M citric acid (1ml/cm²). A mixture of HCl and HNO_3 was also tested, but it showed a poor etching capability. Scotch tape was used as a mask for TCO area which acted as the back contact in the final device. After 45 min of

treatment in acid medium (HCl and HNO_3) some islands of conductive oxide were observed leading to very irregular etching borders. The use of Zn granulates and citric acid in the same time scale enabled a more exact structuring. The structured TCO layers were purified by subsequent sonification in various solvents (1 × acetone, 2 × ethanol, 1 × Hellmanex (2 % in H_2O), 3 × H_2O, 2 × ethanol) for 15 min in each solvent. Cleaned substrates were stored in pure ethanol. Prior to the deposition of TiO_2 layers, the substrates were additionally cleaned by an Ozone plasma treatment for 15 min (250 W, Tepla 200 plasma system).

3.1.5 Preparation of compact TiO_2 layer

Fig. 3.3 shows the setting up of our spray pyrolysis system. Compact layer of TiO_2 were deposited by aerosol pyrolysis of the precursor TAA according to the procedure described by Kavan et al.[182]. The samples were heated by using a temperature-controlled hotplate at (430°C ± 0.1) °C (StörkTronic, Präzitherm, GmbH) and the precursor solution was sprayed from a distance of 20 cm (vertical). For layers of about 130 nm thickness 20 to 25 spray processes of roughly ~ 110 µl precursor solution with and interval of ~10 sec were performed, which corresponds to an overall consumption of 0.35 mL/cm². The interval between each process (10 s) allows the complete pyrolysis of the previous layer and to restore the original substrate temperature. Thin film float glass was used as the mask to cover lines of FTO for later contact formation. After deposition, the prepared TCO/TiO_2 was annealed at 500 °C for 1 hour in air with a programmable Laboratory Oven (Controller P 320(Mb 1), Nabertherm, GmbH) to achieve complete pyrolysis of organic species. The thickness of the deposited TiO_2 blocking layer was measured by mean of a profilometer (Dektak II A, Sloan Technology Corporation, USA). The resulting TiO_2 layer posses mainly anatase character [182] and is presumably n-doped.

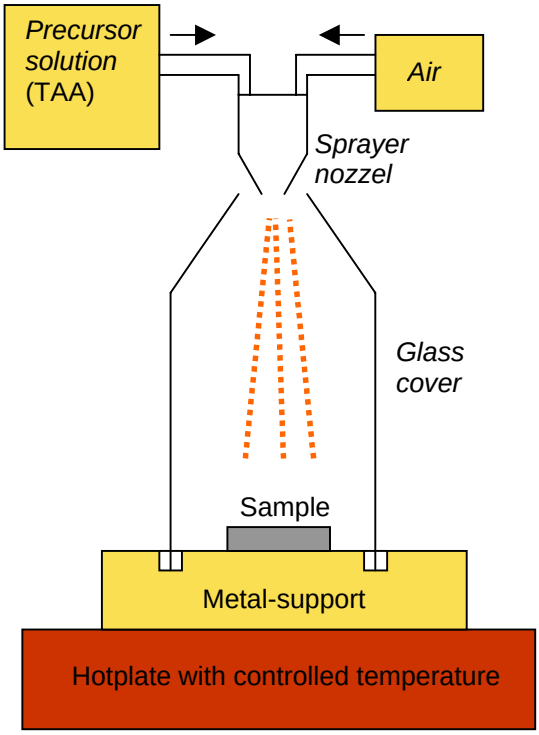

Figure 3.3. Spray pyrolysis set-up

3.1.6 Nanocrystalline TiO_2 layer

The TiO_2 layer was deposited on the FTO substrate by Tape-Casting method as illustrated in Figure 3.2(4). Prior the deposition of TiO_2 colloid, Scotch tape was used to mask a TCO area for the back contact in the final device. A small portion of the colloid is deposited on the substrate and by the mean of rod glass the drop is spread over the structured FTO glass. Around 2 × 1.5 cm² of the substrate surface was covered by broad stripes of TiO_2 paste. After the paste was spread, the films were left to dry for ~5 minutes before the tape was removed and, then, left to dry for 30 minutes at room temperature under normal atmospheric conditions in a dust free environment. The thickness of the film was adjusted by the amount of the paste (using a small spoon) and also by the pressure on the glass rod. The pressure on the glass can be controlled after some practice and due to the high viscosity and slow drying of the paste, it can be applied several times until satisfactory quality of the film is reached. The layers were then baked to remove organic additives and sinter the particles to a mechanically adhering and electrically conducting film. A special sintering program (see Figure 3.4) was proposed by Bach [122] and also used by Krüger [123] and enabled to obtain reproducible grain growth and phase transformation during the sintering. That temperature program consists of heat ramps and isotherms that are chosen to separate the combustion of the additives and the sintering in time. This was done in order to avoid contamination due to carbon inclusions, a

problem, which may occur if organics are trapped in pores, which close during calcinations before they can burn off. The upper sintering temperature, which is typically 450-500 °C, is determined by the physical properties of the substrate (compare section 3.1.4). The firing atmosphere is affecting the doping of the TiO_2. Firing an oxide in a reducing atmosphere such as hydrogen for example may create oxygen vacancies, which leads to n-type doping. Previous work by Kay [185] has shown that best results for the TiO_2 colloids are obtained for sintering in dry air or under a constant flux of oxygen. In this work no scattering particles were added to the TiO_2 pastes and the films obtained where highly transparent. The thickness of the deposited TiO_2 film was measured by profilometry.

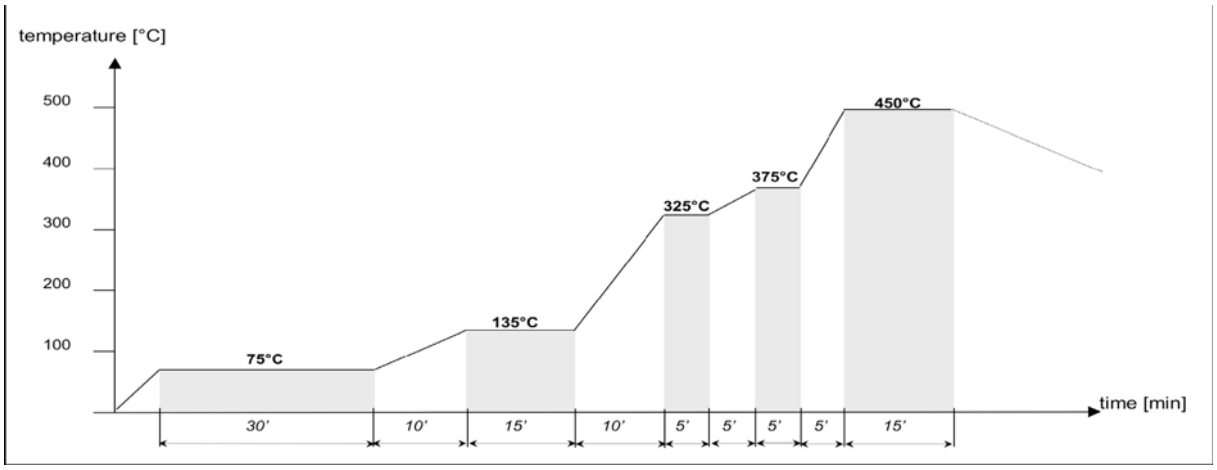

Figure 3.4. Temperature program for sintering of tape-coasted films

TiO_2 film post-treatment

The obtained TiO_2 film (see Figure 3.2(4)) is submitted to $TiCl_4$ post-treatment. Such a treatment was turned out to be advantageous on the performance of the devices. This pre-treament increases the surface area of the dye adsorption and the formation of native surface TiO_2 layer of high purity. Furhermore Ti complexes in $TiCl_4$ are believed to condense at interparticle necks, thereby increasing the interparticle connection and the electron percolation. However, the treatment causes a decrease of the average pore size and the porosity [123]. Therefore the $TiCl_4$ concentration and time of treatment needs to be optimised regarding the required pore size. 50 µl/cm^2 of a 0.02 M $TiCl_4$ solution were applied to the nanocrystalline film for 12 h at room temperature in a dust free environment. Contact areas were protected with adhesive tape. Afterwards the samples were washed with a large amount of distilled water and sintered for a second time for 30 min at 450 °C (ramp: 10 min).

3.1.7 Sensitization

After preparing nanoporous TiO_2 films they were stored in a desiccator over silica gel until the final assembly of the solar cell. Before dye loading, the film is heated at 450 °C for 20 min and cooled to ca. 80 °C before immersing in the dye solution. This operation enables to remove condensed water since the latter blocks the dye solution from reaching all parts of the film, thus reducing dye adsorption. On the other hand baking leads to a partially dehydroxylated, highly activated surface for dye adsorption. The film was soaked in concentrated dye solution (~10^{-4} mol l^{-1}) for a night in the dark. The dye adsorption was found to follow the Langmuir formalism. However, a typical time for dye uptake was 24 h, which is long enough to achieve equilibrium between dye adsorption and desorption. After dye-loading the electrode is rinsed with the solvent used for each dye to remove excess of dye. After that the electrode is dried under an argon flow and directly used for the assembly of the photovoltaic cells (Figure 3.2(5)). The sensitized film is also known as photoanode or working electrode.

3.1.8 Deposition of the spiro-MeOTAD

After perfectly preparing the photoanode, it is spin-coated with the hole transport material (HTM) for solid state device. The hole conductor composition was 0.2 M in spiro-MeOTAD, 0.13 mM in $Li(CF_3SO_2)_2N$, 0.18 M in tBP and 0.76 mM in $N(p\text{-}C_6H_4Br)_3SbCl_6$ dissolved in chlorobenzene. 100 (150) µl of spin-coating solution were applied to the immobilized sample and a thin film was formed by rotating the sample at 1500 rpm for 30 s with an acceleration of 200 rpm. The samples were then dried in argon for 45 min and in vacuum for a night at (0.1 mbar), and were kept in a desiccator before being transferred into a vacuum chamber to apply a thin platinum contact layer via thermal evaporation. The configuration of the prepared cell is symbolised by Figure 3.2(6).

3.1.9 Deposition of the Counter Electrode

The metal contact electrode was deposited by thermal evaporation in UHV (5×10^{-6} mbar) using a Pfeiffer evaporator (Pfeiffer PLS 500s, Laborsystem). Evaporation rates were 0.28 nm/s. The thickness of the layer was monitored by an integrated quartz

balance setup. A metal mask was used to define the contact areas on the sample. The corresponding device is shown in Figure 3.2(7).

Thicker gold layers have been reported to be advantageous due to their higher reflectance and conductivity [123]. But due to the fact that the apparatus for evaporating gold was not completely set up during the period of our experiment, platinum was used as counter electrode, although it seems less advantageous than gold. Platinum films of about 30 nm were deposited and seemed to be less opaque. However, the deposition of thicker films was avoided since it requires longer evaporation time and thus longer thermal stress for the devices. On addition thicker films are mechanically instable and tend to peal off. That is why platinum counter electrode of 30 nm was definitively retained for solid-state devices in this work. Concerning the counter electrode used in DSSCs a 20 nm thin layer of platinum was deposited on FTO substrate. The thus prepared electrode was slightly transparent and turned out advantageous since the corresponding device perfoms well when it is illuminated from its front side (through photoanode) or its back side (through the counter electrode). Comparative study of the performance of DSSCs illuminated on front side and on the back side were realised and the results are presented in the Figure 3.5. This result shows that using thin platinum film enables DSSCs to be sensitive to reflected light, which is one of the limiting factors in classical solar cells.

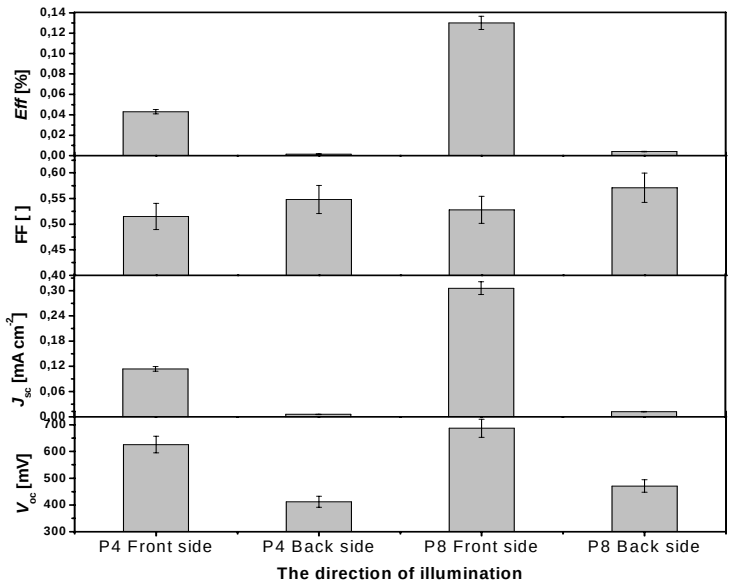

Figure 3.5. The influence of illumination side on the performance of P4 and P8 based cells with 20 nm platinum deposed FTO substrate as counter electrode. The electrolyte used in these cells consisted of 0.5M LiBr, 0.05M Br_2 and 0.2M *tert*-butylpyridine in acetonitrile. The incident light intensity was 86 mW cm^{-2}.

3.1.10 Sealing of Device

In this work SSD versions were not completely sealed. However, electrolyte based cells DSSC were completely sealed to avoid rapid evaporation of the electrolyte during the time to collect data and to prevent water molecules from diffusing from the atmosphere into the cells. Surlyn 1601 (Jura Plast Company, Germany) with melting point 90 °C and 65 µm thickness was used as sealant. A slip of surlyn 1 mm wide was cut from large foil and were subsequent washed in various solvent (1 × acetone, 1 × ethanol) for five minute in each solvent. Afterwards they were dried in argon flow environment and were ready to use. Each piece of sealant was then layed onto the border of the photoanode. The sandwich-type cells were completely prepared by placing the platinum-coated FTO glass (counter electrode) on the top of FTO-TiO_2-dye (working electrode) as indicated by the Figure 3.2(8) and Figure 3.2(9). With the help of a laboratory dryer, a flux of warm air was generated which enabled the both photoanode and counter electrode to bond each to other. During this operation two holes were left on opposite side of the cell, which enable to fill the sandwich cell with the redox electrolyte. After injecting redox electrolyte in the cell the hole were completely closed with two components epoxide glue (UHU GmbH & Co.KG, Germany) as shown in Figure 3.2(10).

3.2. Photovoltaic Device Charaterisation

3.2.1. Dye solar cells parameters

The standard characterisation techniques of solar cells include the determination of the DC current-voltage characteristic under white light illumination of different intensities and the determination of the photocurrent under low intensity monochromatic light.

Current-voltage characteristics of solar cells are described based on the Schottky equation for thermionic emission:

$$I(V) = I_{ph} - I_O.\exp\left[\frac{q\cdot(V+I\cdot R_S)}{n\cdot k\cdot T} - 1\right] - \frac{V+I\cdot R_S}{R_p} \qquad 3.2$$

where R_S is the series resistance, R_p the shunt resistance, n the ideality factor, I_0 the saturation current of the diode, and I_{ph} the photocurrent. The Shottky equation models the dark current in a one-diode system and offers only a simplified representation of the present system. The real

structure of the device is much more complicated corresponding to multidiode model that takes into account different charge transport processes in the cell. However, already the simple Shottky approach yields reasonable good fits for most of the devices and is useful for general discussion of the shape of the I-V curves. Analysis of the photocurrent-voltage curves includes the determination of the following parameters:

Short-circuit current density (J_{SC}): J_{SC} is measured at the condition where the applied potential, V, equals zero volt. J_{SC} increases linearly with the illumination intensity.

Open-circuit potential (V_{OC}): Cell potential measured when current in the cell is zero, corresponding to almost flat valence and conduction bands. V_{OC} is obtained from Equation 3.2 by setting the current to zero:

$$V_{oc} = \frac{n \cdot k \cdot T}{q} \ln\left(\frac{I_{ph}}{I_o} + 1 - \frac{V_{oc}}{I_o \cdot R_p}\right) \approx \frac{n \cdot k \cdot T}{q} \ln\left(\frac{I_{ph}}{I_o} + 1\right) \qquad 3.3$$

Maximal power output (P_{max}): For a given bias voltage the power output of the cell is the product of the measured cell current and the voltage P(V)=I·U. I_{max} and V_{max} are the coordinates of the maximum in the P(V) curve (maximum power point). The maximum power corresponds visually to the area of the largest rectangle, that can fit inside the current voltage curve (Figure 3.6).

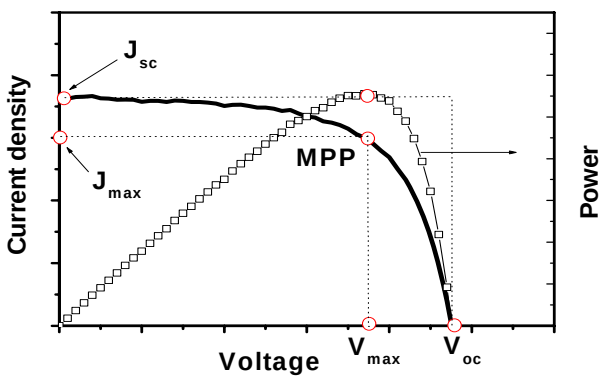

Figure 3.6. A typical I-V curve in the experiment. The empty squares line at different bias shows the power output and red circle explains maximum power point.

The fill factor (FF) is the ratio of the maximum power to the external short and open circuit values:

$$FF = \frac{J_{max} \cdot V_{max}}{I_{sc} \cdot V_{oc}} \qquad 3.4$$

This parameter indicates the deflection of the current-voltage characteristic from a square like curve and depends therefore on series and shunt resistance. Figure 3.7 illustrates the influence of series resistance R_s and shunt resistance R_p on the current-voltage characteristic. It can be seen that a low shunt resistance mainly influences the FF through a shift of the maximum power point, but it also influences the open circuit voltage if it leads to real shunting of the device. To obtain high fill factors R_s has to be as small as possible while R_p needs to be as high as possible. The influence of R_p on J_{sc} is typically negligible. The influence of the series resistance on the FF is generally more dramatic since it tilts the whole I-V curve around the V_{oc} point. V_{oc} remains unchanged if the series resistance becomes large enough, even J_{sc} will be lowered. Typical FF of dye cells range from 0.6 to 0.8 depending on the individual device and usually increase with the decreasing light intensity.

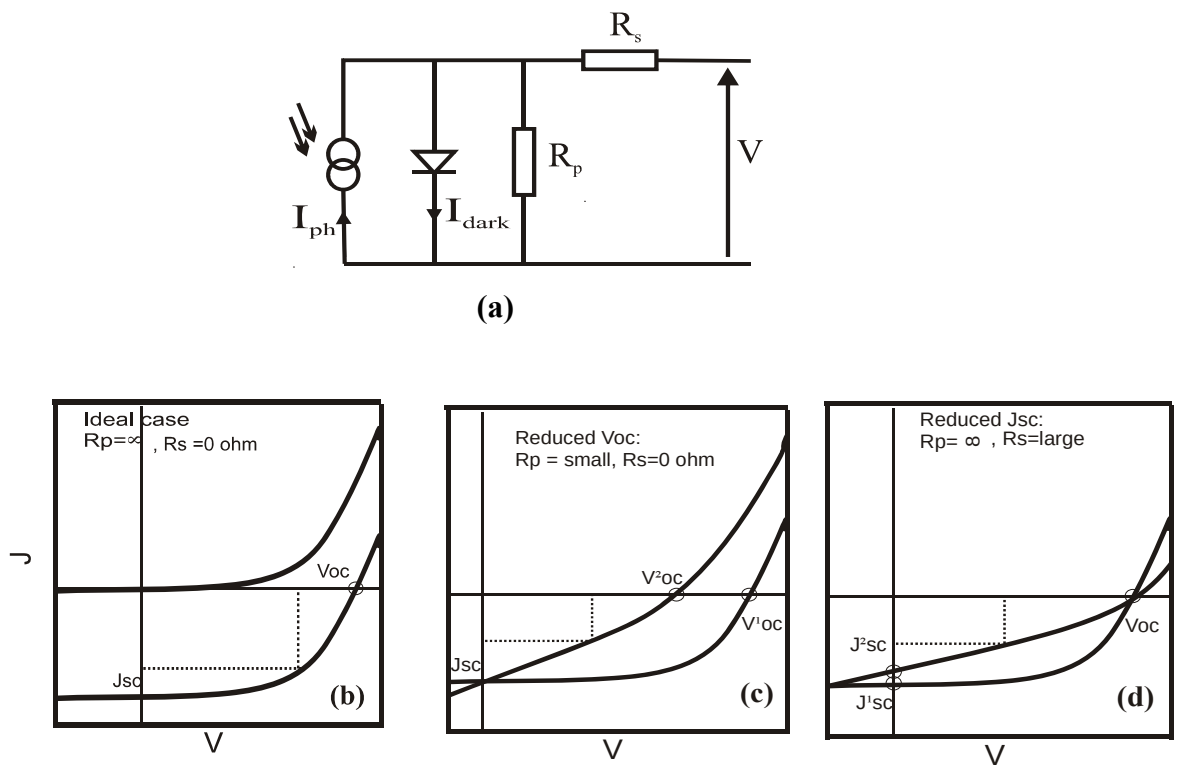

Figure 3.7. **(a)** Equivalent circuit for a DSC. The parallel resistivity R_p resembles all shunts while the serial resistivity resembles the bulk resistivity of the active area, contact resistivity and circuit resistivity**. (b)** ideal I-V characteristics in the 4th quadrant for a solar cell with a negligible R_s and infinite R_p.**(c)** I-V characteristics in the 4th quadrant for a solar cell with a small R_p and a negligible R_s. **(d)** I-V characteristics in the 4th quadrant for a solar cell with an infinite R_p and large R_s.(J_{sc}=short-circuit current density, V= potential)

The **efficiency (η)** expresses the performance of solar cell and is defined as the ratio of the maximum electrical power extracted to the radiation power incident on the solar cell surface.

$$\eta = \frac{P_{max}}{P_{in}} = \frac{J_{sc} \cdot V_{oc} \cdot FF}{P_{in}} \qquad 3.5$$

The efficiency is a function of the V_{oc}, the J_{sc} and the FF of the cell. Accordingly improvement of the photovoltaic yield is the result of the optimisation of these three parameters. These three parameters depend on the measurement condition and strongly on light intensity.

3.2.2. The solar source and Air Mass

The solar spectrum is a mixture of light with different wavelengths, ranging from ultraviolet, visible and infrared region of the electromagnetic spectrum. According to the black-body radiation, the energy density per wavelength de_γ/λ can be expressed as a function of λ by eq.3.6

$$\frac{de_\gamma(\lambda)}{d\lambda} = \frac{2hc_0 d\Omega}{\lambda^5} \frac{1}{\exp(hc_0/\lambda k_B T) - 1} \qquad 3.6$$

where dΩ is solid angle element, C_0 is the velocity of the light in the medium, k_B and h are the Boltzmann constant and Planck constant, respectively. By taking $d^2e_\gamma/d\lambda^2=0$, the maximum value of $de_\gamma/d\lambda$ is at the wavelength

$$\lambda_{max} = \frac{hc_0}{4.965 k_B T} = 0.2497 \frac{\mu m\ eV}{k_B T} \qquad 3.7$$

The power density at the sun's surface is 62 MWm^{-2} and it reduces to 1353 W m^{-2} at the point just outside the Earth's atmosphere since the solid angle subtended by the sun, Ω_s, is as small as 6.8 x 10^{-5} sr. On passing through the atmosphere, the spectrum is partially attenuated by the absorption of oxygen, ozone in the ultraviolet region and water vapour, carbon dioxide, methane in the infrared. This attenuation is described by the 'Air Mass' factor since the absorption increases with the mass of air through which the radiation passes. For a thickness

of ZO of the atmosphere, the path length SO through the atmosphere for radiation at an incident angle θ relative to the normal to the earth's surface is given by

$$SO=ZO/\cos\theta \qquad 3.8$$

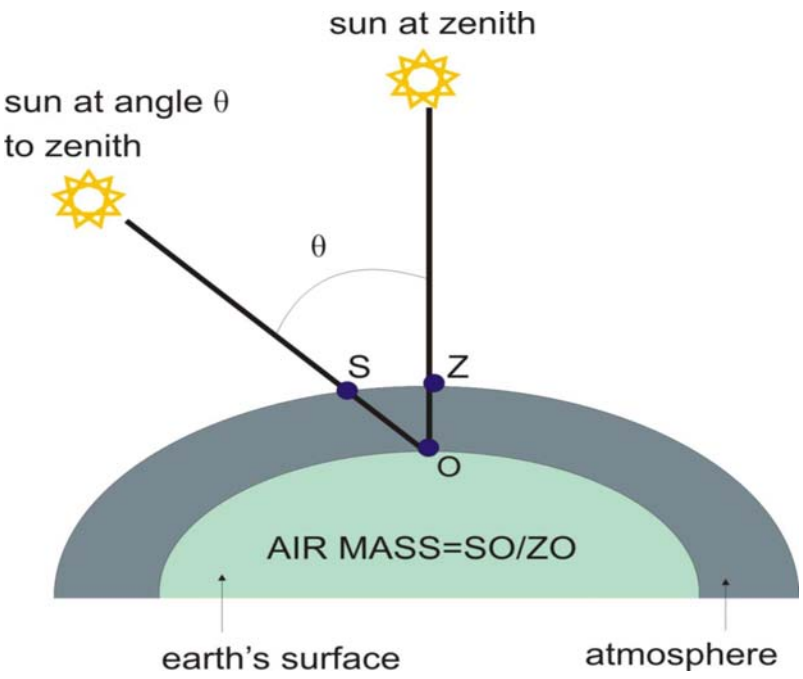

Figure 3.8. Illustration scheme of the "air mass" concept.

The ratio SO/ZO is called the Air Mass factor. The spectrum outside the atmosphere is denoted as AM0 and that on the surface of the earth for perpendicular incidence as AM1. The standard spectrum for moderate weather is AM 1.5, which corresponds to a solar incident angle of 48° relative to the surface normal and gives a mean irradiance of 1000 W m^{-2}. Figure 3.9 shows the comparison between the spectrum of AM0 and AM1.5. The actual irradiation varies with seasons, climates, day time and the position of the sun. Averaged over the year, the global mean energy density ranges from less than 100 W m^{-2} at high latitude areas to around 300 W m^{-2} in Saudi Arabia. It is a little more than 100 W m^{-2} in central Europe, where the amount of energy incident to the surface in a year is about 1000 kWh m^{-2} and also known as 1000 sun hours per year.

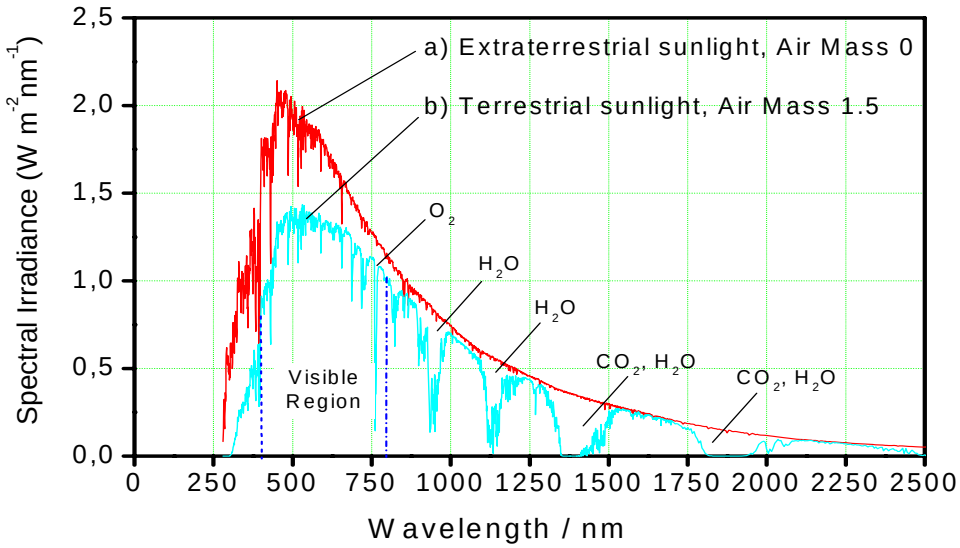

Figure 3.9 Solar irradiance spectra of:a) AM0 and b) AM1.5.

The standard test conditions have been defined by American Society for Testing and Materials (ASTM) for comparing the solar cell characteristics in different laboratories all over the world. These specify that the temperature of the cell should be 25°C and that the solar radiation incident on the cell should have a total power density of 100 mW/cm^2, with a spectral power distribution characterised as AM1.5.

3.2.3 Incident photon-to-electron conversion efficency (IPCE)

The incident photo-to-electron conversion efficency (IPCE) is defined as the number of photo-generated electrons in the external circuit divided by the number of incident photons at a certain wavelength.

$$\mathrm{IPCE}(\lambda) = \frac{\mathrm{n}_{\mathrm{electron}}(\lambda)}{\mathrm{n}_{\mathrm{photon}}(\lambda)} = \frac{q\mathrm{N}_{\mathrm{electron}}/\mathrm{S}}{q\mathrm{N}_{\mathrm{photon}}/\mathrm{S}} = \frac{\mathrm{I}(\lambda)}{q\mathrm{N}_{\mathrm{photon}}/\mathrm{S}} \qquad 3.9$$

The incident power

$$\mathrm{P}_{\mathrm{in}}(\lambda)(Watt) = \mathrm{P}_{\mathrm{in}}(\lambda)\left(\frac{Joule}{\mathrm{S}}\right) = \frac{\mathrm{N}_{\mathrm{photon}}}{\mathrm{S}} h\upsilon = \frac{\mathrm{N}_{\mathrm{photon}}}{\mathrm{S}} \frac{hC_0}{\lambda} \qquad 3.10$$

With Eq.3.10, Eq. 3.9 can be written as

$$\mathrm{IPCE}(\lambda)=\frac{\mathrm{I}(\lambda)}{\frac{q\cdot \mathrm{P_{in}}(\lambda)\cdot\lambda}{hC_0}}=\frac{\mathrm{I}(\lambda)}{\mathrm{P_{in}}(\lambda)}\frac{hC_0}{q}\frac{1}{\lambda}\approx\frac{\mathrm{I}(\lambda)}{\mathrm{P_{in}}(\lambda)}\times\frac{1240}{\lambda(nm)} \qquad 3.11$$

I(λ) corresponds to the measured current in μA/cm^2, $P_{in}(\lambda)$ is the output optical power in W/m^2, and λ the wavelength of the incident irradiation in nm. In general the IPCE is measured under short-circuit conditions and is graphically displayed versus the corresponding wavelength in a photovoltaic action spectra. The IPCE corresponds to the photoresponse or external quantum efficiency. Correcting the IPCE for the number of photons, which are not absorbed by the test cells lead to the internal quantum efficiency or:

Absorbed-photo-to-electron conversion efficency (APCE), which is defined by the ratio of the number of electron-hole pairs generated in the solar cell to the number of photons absorbed by the photoactive surface of the device at a given wavelength. The APCE is calculated dividing the IPCE by the light harvesting of the test device:

$$\mathrm{APCE}(\lambda)=\frac{\mathrm{IPCE}(\lambda)}{1\text{-}\mathrm{T}} \qquad 3.12$$

3.2.4. Experimental set-up

The current-voltage (*J-V*) characteristics and the incident photon to electron conversion efficiency (IPCE) were monitored and measured by using a Keithley 276 source measurement unit. J-V measurements were generated using self-written LabVIEW program. A solar simulator equipped with xenon lamp (AM 1.5, Solar light Company, Model 16S-300, USA) was used as light source and light intensity was measured with a pyranometer (solar light company, PMA2144, USA). The ultraviolet and infrared portion of the spectrum was eliminated by using a filter. The incident light intensity was tuned using neutral density filters (Eastman Kodak Company, USA).

For the IPCE measurement light of a 300 W Xe arc lamp were spectrally narrowed to a monochromatic light using monochromator (Jobin Yvon Instrument SA, France). The intensity of incident monochromatic light was calibrated with Si power meter (Vector H410, Scientech). No corrections for surface and interface reflection losses were made for standard characterization. The Figure 3.10 shows the set up of our measurement system.

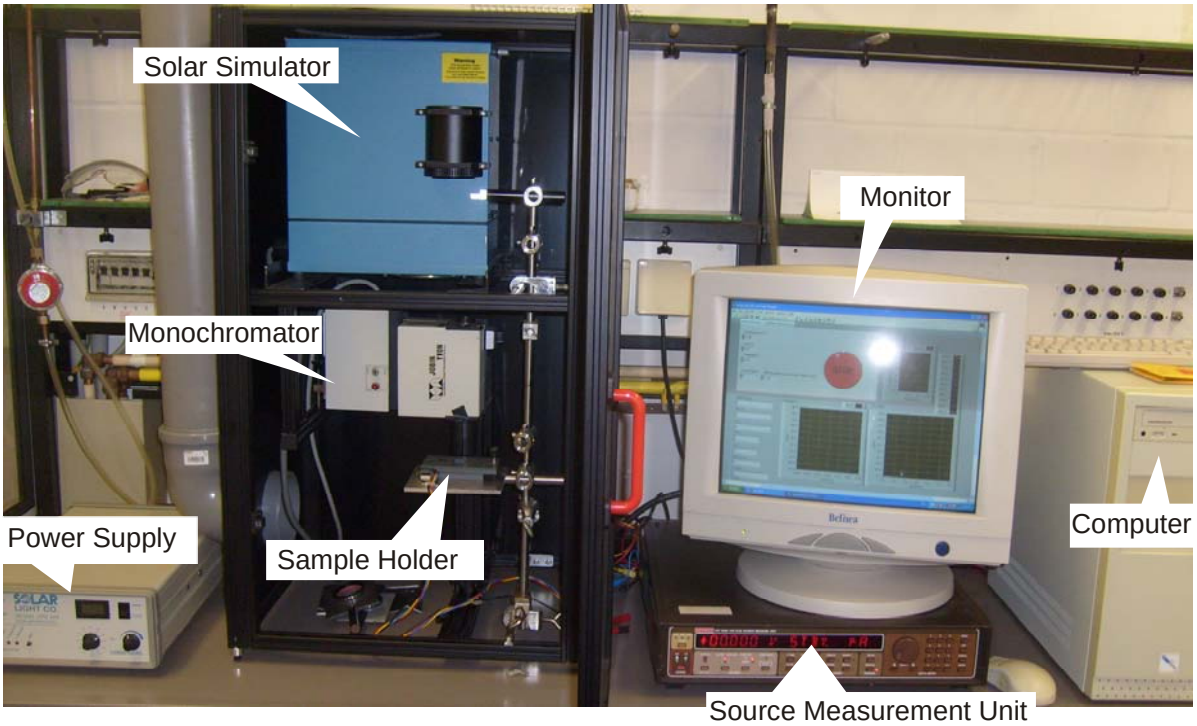

Figure 3.10. Set-up of measurement system with dark chamber.

3.3. Absorption Spectroscopy

Absorption spectra in solution were measured in a 1 cm path length quartz cell (Firma Helma) on a Perkin-Elmer, Model Lambda 900 UV/Vis/NIR spectrometer. For measuring the absorption of the dye-sensitized TiO_2 films, the samples were attached to a central aperture sample holder with double-side tapes. The beam was then incident from the glass side.

3.4. FTIR-spectroscopy

Vibrational spectroscopy provides the most definitive means of identifying surface species generated upon molecular adsorption and the species generated by surface reactions. It is based on the fact that infrared illumination stimulates molecular vibration. Energy will only be absorbed if there is a net change of dipole moments due to the vibrational motion of the molecule, i.e. a transition dipole moment. This energy adsorption can be monitored making use of several different techniques, from which Fourier Transform Infrared (FTIR) spectroscopy has become the standard technique for chemical characterisation. With the development of attenuated total reflection (ATR) or internal reflection spectroscopy FTIR gained importance as a straightforward and non-destructive tool for surface characterisation. The ATR technique is based on the fact that a material will reflect much of the incident

radiation depending upon its actual reflectivity, when the angle of the incident light is different from zero degree. If an IR transparent crystal such as diamond is placed behind and in good optical contact with the sample, light passing into the diamond can be made to emerge on the opposite side having made multiple reflections at the diamond-sample interface. The number of reflections N the light will undergo as it propagates down a crystal with the thickness W and the length L before emerging at the other end is given by:

$$N=\frac{L}{W}\cot an(\phi) \qquad 3.13$$

At each reflection, an evanescent electric field (E) is generated in the sampled medium, the intensity of which decays exponentially with distance (z) from the surface:

$$E=E_0 \cdot \exp\left[\frac{-Z}{d_p}\right] \qquad 3.14$$

where E_0 is the intensity of the incident radiation and d_p the penetration depth, which is a function of the refractive index η_1 of the ATR crystal, refractive index η_2 of the sample medium, and the angle of incidence θ:

$$d_p=\frac{\lambda}{2\cdot\pi\cdot\eta_{12}\sqrt{\sin^2\theta-\eta_{12}}} \text{ with } \eta_{12}=\frac{\eta_2}{\eta_1} \qquad 3.15$$

Considering the refractive index of type-IIa-diamond and a typical organic material to be 2.4 and 1.5 respectively, the top 2 μm of the surface will be sampled at 45º incidence [123,186]. The intensity of the reflected light at each reflection point will be reduced by the presence of infrared absorbing material in the sample medium. The emerging light contains important absorbance information about the sample. The quality of ATR spectrum is dependent on sample contact rather than sample thickness.

Experiment set-up

Attenuated Total Reflection (ATR) infrared spectroscopy was used for the analysis of the surface of TiO_2 films. The sampling surface was pressed into intimate optical contact with the top surface of the crystal with a high refractive index, through which the infrared radiation passed and got reflected within the ATR element several times before it was collected at the output end of the crystal. Fourier-Transform (FT) was used to increase the sensitivity and

resolution of data acquisition. The ATR-FTIR spectra were measured using a FTS 7000 FTIR spectrometer (Firma Biorad, Model FTS 40A). Spectra were derived from 64 scans at a resolution of 2 cm^{-1}. All samples were measured under quasi identical mechanical force used to push the mesoscopic TiO_2 films in contact with the diamond window. The dye-loaded electrodes were rinsed in acetonitrile and dried prior to measuring the spectra. No ATR correction was applied to the data. The obtained data were further processed with Biorad Win-IR-sofware in ATR-mode.

3.5 UV-Pretreatment of TiO_2

For the UV pretreatment, the nanoporous films of TiO_2 were exposed to mercury lamp (254 nm, 365 nm, Oriel, Model 6035) in laboratory ambient conditions. The preparation chamber is shown in figure 3.11. The sample holder maintained the sample at 2 cm distance to the UV lamp and the UV light intensity on the surface of the sample was estimated to be ~2 mW cm^{-2}. Before switching the lamp on, the preparation chamber is totally covered with a black cloth to avoid any skin contact with the UV radiation. After UV irradiation of the TiO_2 film, it was rapidly heated in furnace at 250°C for 5 min, followed by cooling until 80 °C and soaked in dye solution for sensitization.

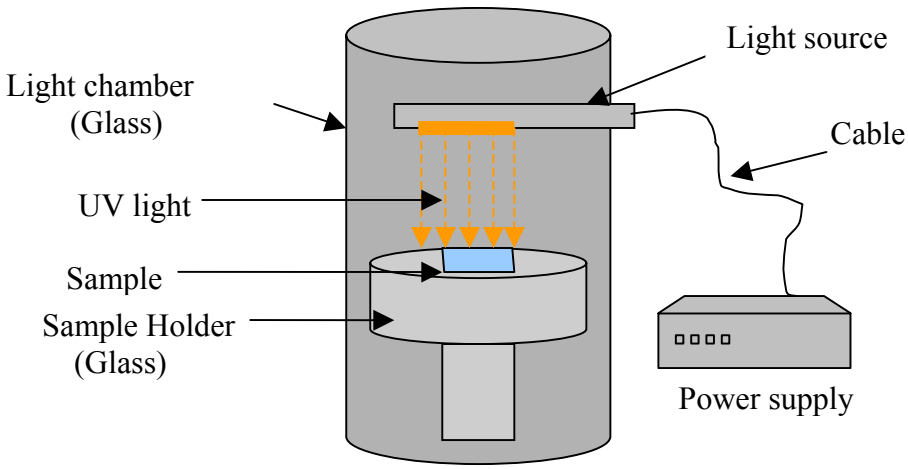

Figure 3.11 Set-up of TiO_2 UV pre-treatment system.

3.6 UV-vis treatment of Device

The treatment of the DSC with UV-Vis light was turned out to be beneficial since it increases the performance of the dye-cell [142,187]. In this experiment, the solar cells were illuminated for 20 min with 300 W Xe Lamp. The infrared part of the light spectrum was eliminated by passing the light through a water filter in a 1 cm path length quartz cell. The intensity of the incident light on the device surface was kept constant at 190 mW cm^{-2}.

CHAPTER 4
CHARACTERIZATION OF ELECTROLYTE-BASED CELLS

In this chapter, the device performance of electrolyte-based dye-sensitized solar cells (DSSCs) are presented and discussed. The optimal TiO_2 film thickness is also discussed. The influence of some additives in the electrolyte such as *tert*-butylpyridine (tBP) and lithium ions on the performance of a device is investigated. In addition, the physical characteristics of DSSCs based on different molecular dyes are discussed. The long term stability of the device based on P1dye is also addressed.

4.1. Determination of optimal preparation conditions of DSSCs

4.1.1. The influence of the thickness of TiO_2 film on the performance of DSSCs

It is well known that the dye cells performance largely depends on the film thickness [40,188-190]. If *d* is considered as thickness of TiO_2 film, its increase leads to increase dye adsorption and light absorption. This could have as consequence the increase in short-circuit photocurrent J_{sc}. High efficient DSSC require a TiO_2 film thickness of *d* ~10 μm (excluding the scattering layer) with radius of nanoparticle ranging between 2-10 nm since with this thickness the light is entirely absorbed by the sensitzed TiO_2 film [40].

The open-circuit voltage V_{oc} of DSSC behaves complementary to J_{sc}. When the sensitized film thickness is increased a decrease in V_{oc} is generally observed [188-190]. Gómez et al. found that by varying the film thickness between 3 μm and 9.7 μm the open-circuit voltage is decreased by ~0.06 mV. Chappel et al. [190] using SnO_2 as inorganic semiconductor observed a decrease by 0.05V when thickness is changed from 0.1 μm to 4 μm. The open circuit voltage according to Ref. [188] was found to decrease by ~ 0.03 V when the TiO_2 film thickness was increased from 5 μm to 11 μm.

However, it is worth noting that for a given photoelectrode, the optimal thickness depends on the extinction coefficient of the adsorbed dye as well as on the particle properties [40]. Ruthenium complexes dye with extinction coefficients lying in the range $\varepsilon \sim 10^4$ $M^{-1}cm^{-1}$ require thick nanoporous TiO_2 film, whereas with metal free dye having generally high extinction coefficients ($\varepsilon \sim 10^5$ $M^{-1}cm^{-1}$) thin nanoporous TiO_2 is expected. While the optimal

film thickness for N719 was reported [191] to be in the range of 10–15 µm, only 5 µm TiO_2 film was reported to generate the best efficiency for hemicyanine dyes (metal-free dye) [192,193]. From these observations, it can be concluded that the ideal case in DSSC is to employ a dye that has a very high extinction coefficient on a very thin porous film, which can produce both high photocurrent and high photovoltage, resulting in a higher efficiency. Perylene derivatives fit perfectly with these criteria.

In the experiments described here P1 was used as dye and a series of four devices with TiO_2 thicknesses of 4, 7, 13 and 17µm were fabricated and characterized. Each device consisted of three identical cells showing same J-V characteristics. The electrolyte used consisted of 0.6 M 1-Butyl-3-methylimidazolium iodide, 0.1 M I_2, 0.05 M $LiClO_4$ in 3-methoxy-propionitrile. Figure 4.1 shows current-voltage characteristics of the corresponding devices and Figure 4.2 depicts the correlation between the thickness of TiO_2 film and the parameters of the devices.

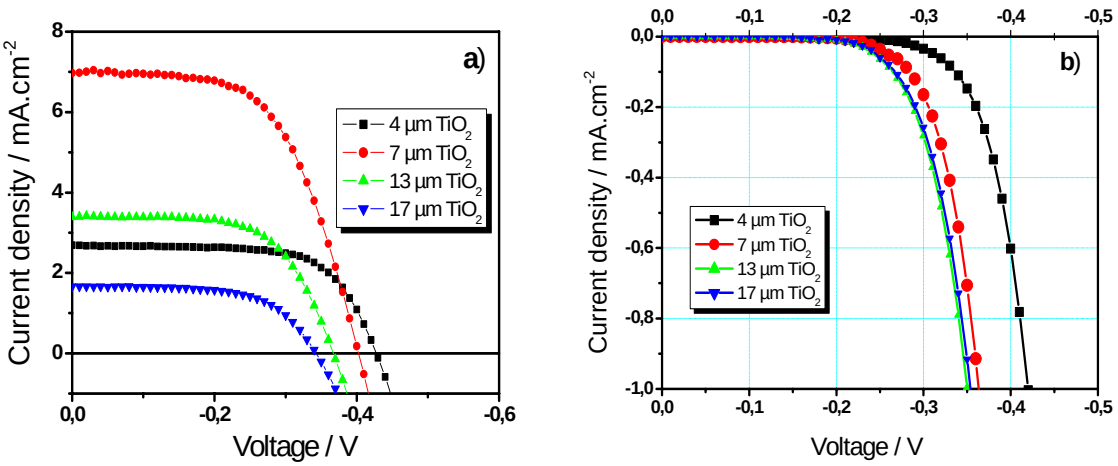

Figure 4.1: Influence of TiO_2 thickness on the performance of DSSC cells based on P1: (a) J-V characteristic of DSSC under simulated solar light AM 1.5 at 1 sun (100 mW cm^{-2}); (b) characteristics of DSSC in the dark.

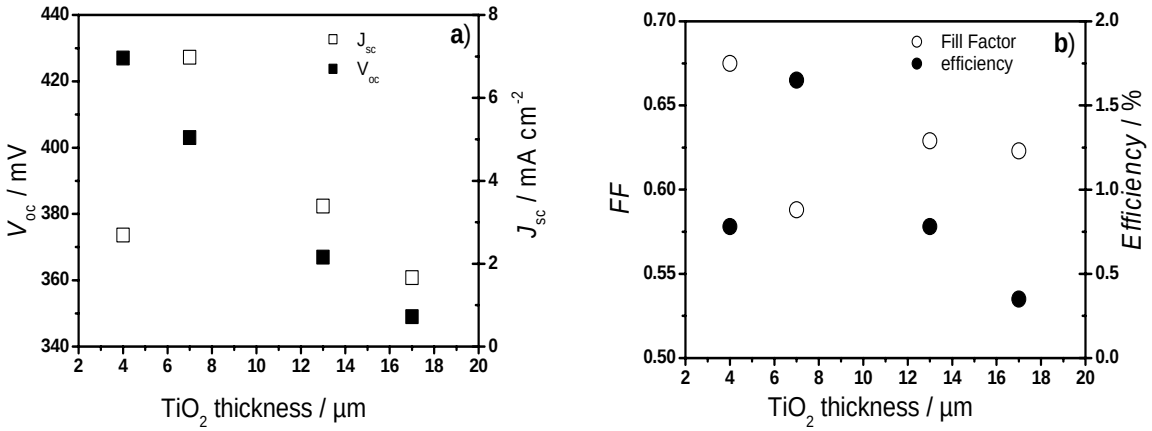

Figure 4.2: Variation of DSSCs parameters with TiO_2 film thickness: (a) The empty (□) and the filled rectangular (■) makers show the J_{sc} and V_{oc}, respectively; (b) The empty (○) and the filled circles (●) makers show the FF and efficiency η, respectively.

In principle, dye in the film will build up with increasing thickness, and an increased J_{sc} would be expected. However, from Figure 4.2(a) it can be seen that in DSSC assumption is valid just for thin TiO_2 film. The short-circuit current density is increased from 2.69 mA cm^{-2} to 6.98 mA cm^{-2} when TiO_2 film thickness is growing from 4 µm to 7 µm, respectively. Beyond 7 µm the short-circuit current density decreases gradually to 3.39 mA cm^{-2} for 13 µm and to 1.66 mA cm^{-2} for 17 µm. This behavior is cleary illucidated in Figure 4.2 (a). That can suggest that, the probability of recombination and the cell resistance beyond 7 µm become large with increasing film thickness, since the electron has an average distance, to be transported across an increasing number of colloidal particles and grain boundaries. On the other hand, since the device is illuminated through the substrate, dye molecule adsorbed in the outer part (i.e part far from TCO glass) of TiO_2 film will absorb less and less light with increasing film thickness as the dye adsorbed in the inner part (i.e the part adjacent to TCO glass) prevent a deeper penetration of the light.

At the same time the V_{oc} decreases gradually from 427 mV to 403, 367 and 349 mV when the TiO_2 film thickness is increased from 4, 7, 13 and 17 µm, respectively.

From Figure 4.2(b), it can be seen that the efficiency increases from 0.78% to 1.65% when the film thickness is changed from 4 µm to 7 µm and decreases gradually to 0.78% and 0.35% for film thickness 13 and 17 µm, repectively. The fill factor decreases from 0.675 to 0.588 when the film is changed from 4 to 7 µm (the minimum value was found at 7 µm), and increases slightly to 0.629 at 13 µm afterwards it remains almost unchanged at 17 µm. The FF of the cells shows about 25% decline as the thickness increases from 4 to 17 µm (Figure 4.2(b)),

which can be attributed to the increase of resistance in the cell [194]. This change in the property of DSSC with increasing thickness of a porous layer followed by the decrease of V_{oc} has already been mentioned in the literature and has been qualitatively discussed [188,190,194]. In fact J_{sc} grows with increasing *d*, but not proportional, since absorption by the Lambert-Beer's absorption law drops exponentially and thus the first few microns of sensitized TiO_2 layer absorb a large part of the incident photons. The recombination process is expected to increase proportionally to *d* since both the TiO_2/electrolyte-interface as well as the absolute number of surface states recombination is promoted proportionally with the increase of the layer thickness. The decrease in open circuit voltage when *d* is increased consequently results from a growing proportion of recombination site [195] contrasting with the slightly weaker increasing electron injection. This increases of electron injection and, thus, J_{sc} with layer thickness of TiO_2 according to our results is observed in the range 4 µm < *d* < 7 µm. For *d* > 7 µm J_{sc} decreases gradually with the increase of *d*.

An expression of V_{oc} describing quite perfectly its relation with the thickness of TiO_2 film in the case of DSSC was reported [69,196] and is expressed by Eq. 4.1

$$V_{oc} = \frac{kT}{qu\alpha} \ln\left(\frac{A\varphi_{ep} I_0}{n_0^{u\alpha} k_{et} c_{ox}^m} \right) \qquad 4.1$$

where α is the electron transfer coefficient, I_0 incident photon flux, n_0 the electron population in conduction band of TiO_2 at the equilibrium, φ_{ep} the ratio of injected electron to I_0 , A the ratio of absorbed photon flux to I_0, k_{et} the rate constant for back reaction transfer. The order of the rate of reaction is expressed as the exponents *m* for the oxidized redox species and *u* for the electron respectively. Equation 4.1 describes a logarithmic dependence of the open circuit voltage on the incident light intensity, no distinction being made between free electrons in the conduction band and the localized electrons in surface states. The dependence of *d* is located in both the numerator and the denominator of the logarithmic expression. Assuming that the incident light I_0 is constant, the absorption of photon increases with increasing film thickness and thus the number of injected electron in relation to the incident photons φ_{ep}. The increase is, however, not linear, but proportional to $(1 - e^{-d})$ and goes at one hundred percent absorption in saturation [197]. In the logarithmic denominator of the Equation 4.1, the rate constant k_r increases proportionally to TiO_2 thickness and, hence, linearly to the surface states with d. Consequently, it is expected a decrease of the absolute value of the logarithmic expression of Equation 4.1 with *d* and hence the open circuit voltage V_{oc}. This TiO_2 thickness

dependence of V_{oc} in DSSCs is quite similar to that reported in inorganic solar cells [198,199] and is therefore considered as "*normal*". The use of thin silicon films was turned out to increase V_{oc} in classical solar cell [200,201]. Queisser [199] gave a simple thermodynamic explanation for this change. He explained this behaviour by an entropy suppression in thin films. In inorganic solar cells, the confinement within a thinner layer of width *W* raises the density of carriers (per unit volume), higher density means reduced entropy, thus better conversion. From Eq. 3.3, considering the case of ideal diode (n = 1)

$$V_{oc} \approx \frac{k \cdot T}{q} \ln\left(\frac{I_{sc}}{I_o} + 1\right) \qquad 4.2$$

where I_{sc} is the short circuit current for V = 0.
The reverse saturation current is expressed as [199],

$$I_0 = \frac{q \cdot n_0 \cdot W}{\tau} \qquad 4.3$$

being depending on carrier densities, n_o, lifetimes, τ, and transport parameters.
From Eq. 4.2 and 4.3 and with $I_{sc} << I_0$, one obtains the derivative**,** which is

$$\frac{dV_{oc}}{dW} = -\frac{k \cdot T}{qW}$$

The entropy S per charge carrier particles in a semiconductor with an effective density of states N_c in the conduction band, having the electron effective mass m* [199,202],
$N_c = 2(2\pi\ m^*kT/h^2)^{3/2}$ is [199,202,203]

$$\frac{S}{k} = \frac{5}{2} - \ln\left(\frac{n}{N_c(T)}\right) \qquad 4.4$$

The entropy *S* is the only physical quantity depending on *W*, since $n(W) = I_{sc}\tau/qW$.
Assuming that lifetime τ remains independent of thickness *W* and assuming non-degeneracy, and taking in account the extending of the Eq. 4.4 to hole *p*, one obtains [198]

$$\frac{dV_{oc}}{dW} = \left(\frac{k \cdot T}{q}\right)\left(\frac{dn}{dW}n^{-1} + \frac{dp}{dW}p^{-1}\right) \qquad 4.5$$

as the explicit formula for the change of output voltage with change of layer thickness W, based on the consideration of the entropy reduction with compression. Since the derivatives of particle densities with respect to thickness, such as dn/dW, are negative, the open-circuit voltage V_{oc} does increase with shrinking W, and so does the efficiency, since the current remains constant.

The charge recombination in DSSC can be estimated by the magnitude and onset of the dark current, which arises from the reduction of I_3^- ions by the electrons in the conduction band. The dark current potential scans for photoelectrodes are plotted in Figure 4.1(b). The dark current onset is shifted to a lower potential with increasing thickness, and a thinner film produces a smaller dark current at the same potential above 0.25 V. These observations reflect a higher recombination rate between transported electrons and I_3^- ions in thicker films. The increase of the dark current with film thickness results in a loss in V_{oc}. Thus, V_{oc} decreases with increasing thickness [41].

From this investigation, a 7 µm thickness of TiO_2 turned out to generate device with good performance. If not otherwise mentioned 7 µm is retained as thickness of TiO_2 in DSCCs in this work, since all dye investigated have an extinction coefficient lying in the same range. In the following sub-section the influence of electrolyte composition on the performance of DSSCs will be scrutinized.

4.1.2. The choice of the electrolyte: The influence of tBP and Lithium on the performance of DSSCs

It is well known that a strategy to suppress charge recombination in Grätzel cell is the use of 4-*tert*-butylpyridine (tBP). Introduction of the latter into the electrolyte modifies some characteristics of device by shifting the CB edge of TiO_2. tBP is widely use in the DSSC and performs well with metal complexes used as dye. Whereas the application of lithium ions was found to be essential in device performance, the presence of tBP in different electrolyte turned out to be disadvantageous for devices based on metal free compound used as dye in this work. However, the introduction of tBP into the electrolyte solution changes the dielectric properties and allows a high amount of lithium salt to be dissolved as observed by Krüger [123]. tBP is expected to assist the dissolution of the lithium ions as a result of interaction of lithium ions

with the amine function of the tBP [123]. The presence of these two additives and their influence on the performance DSSCs were investigated by photovoltaic experiments.

Characterisation of modified devices

In this experiment a series of electrolyte-based cells with electrolyte consisting of lithium on one hand and with tBP on the other hand were compared in terms of their influence on photovoltaic parameters. Table 4.1 compares the photovoltaic output for varying cell types. Electrolyte **A** containing 0.6 M 1-butyl-3-methylimidazolium iodide, 0.1 M I_2 in 3-methoxypropionitrile solvent is considered as the reference electrolyte for this investigation. The lithium ion was introduced by dissolving $LiClO_4$ salt in the electrolyte.

Tableau 4.1. Change in device performance at 100% Sun and 54% Sun light intensity for various cell type.

Electrolyte and Additives	**100% Sun**			
	V_{oc} **[mV]**	J_{sc} **[mA/cm^2]**	**FF [%]**	η **[%]**
A	548	0.247	0.544	0.074
A + 0.5 M **tBP**	569	0.222	0.627	0.079
A + 0.05 M **Li**	403	6.975	0.588	1.653
A + 0.5 M **tBP** + 0.05 M **Li**	508	1.641	0.697	0.581
Electrolyte and Additives	**54% Sun**			
	V_{oc} **[mV]**	J_{sc} **[mA/cm^2]**	**FF [%]**	η **[%]**
A	499	0.137	0.569	0.075
A + 0.5 M **tBP**	534	0.090	0.639	0.057
A + 0.05 M **Li**	390	3.456	0.641	1.599
A + 0.5 M **tBP** + 0.05 M **Li**	481	0.788	0.724	0.508

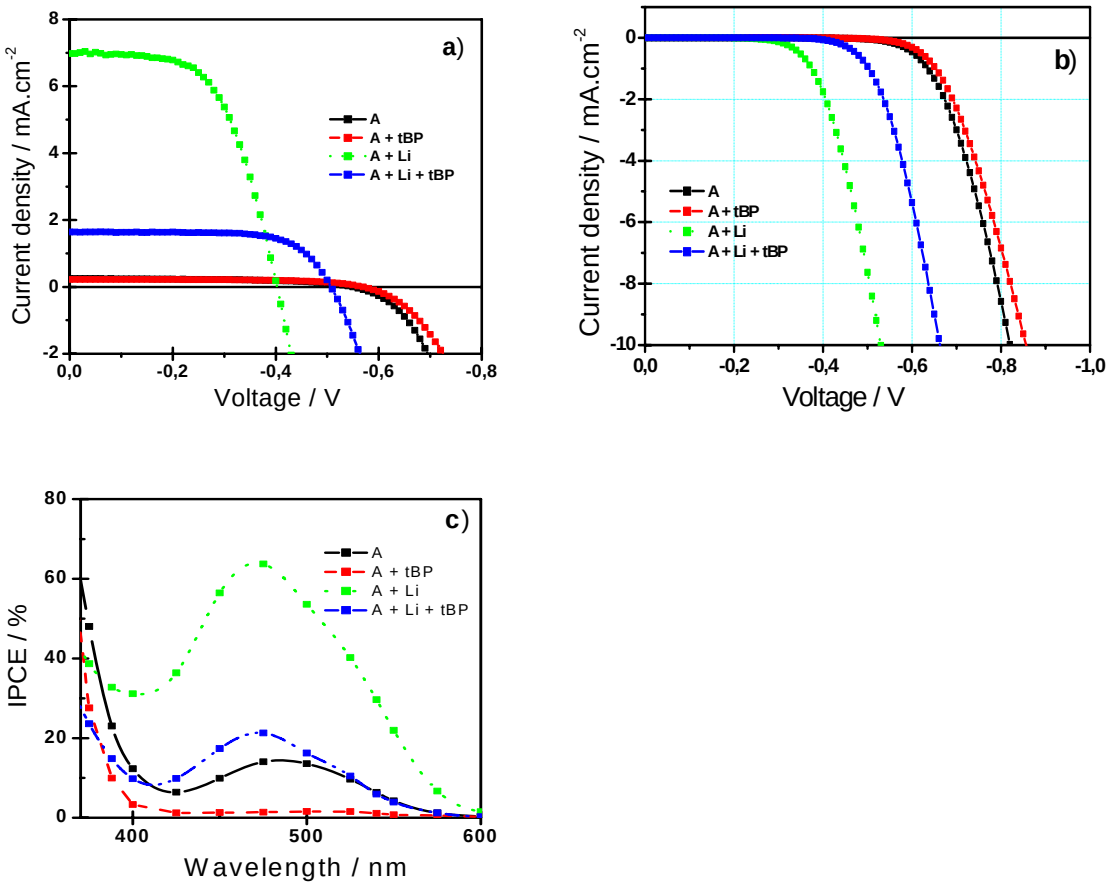

Figure 4.3. Current-voltage characteristics at illumination intensity of 1 Sun (a) and in dark (b); IPCE for different device types (c).

Figure 4.3 shows the current voltage characteristics and the incident photon to current conversion efficienecy (IPCE) of modified cells. While introducing tBP in the electrolyte A results in a clearly enhanced open circuit voltage from 548 to 569 mV, the tendency for the short circuit current is the opposite, it varies from 0.25 to 0.22 mA cm^{-2} at 1 Sun (Table 4.1, Figure 4.3(a)). The same tendency is observed at 0.54 Sun. In the presence of tBP additive the fill factor increases independently of light intensity. This increase of the fill factor and the open circuit voltage is due to the fact that the presence of tBP in the electrolyte shifts the conduction band edge of TiO_2 and thus leads to the suppression of the dark current at the semiconductor electrolyte junction. In fact, triiodide, due to its relatively small size, either crosses the dye layer or has access to nanometer-sized pores [41] into which the P1 cannot penetrate, i.e., where the surface TiO_2 is bare and exposed to the redox electrolyte. The effect of tBP is to decrease the rate of the reduction of triiodide. This is clearly noticeable in Figure 4.3(b), where the onset of the dark current in the presence of tBP is shifted to higher voltage with respect to a device based on electrolyte A. The efficiency is nearly the same at 1 Sun and

tends to decrease at 0.54 Sun. The presence of tBP in the electrolyte turns out to be more beneficial for open circuit voltage and fill factor.

After introducing lithium in the electrolyte A, (A + 0.05 M Li), V_{oc} decreases while the current increases strikingly from 0.25 to 6.98 mA cm^{-2} at 1 sun (Table 4.1, Figure 4.3(a)). A slight increase in fill factor is observed and efficiency increases remarkably from 0.07 to 1.65%. All these parameters behave quite identically independently of low or high incident light intensity except the fill factor that increases at 0.54 Sun in presence of lithium. Noticeable is the striking improvement of efficiency in the presence of lithium.

After combining both tBP and lithium in the electrolyte (A + 0.5 M tBP + 0.05 M Li) a so called co-modified cell is obtained. Its V_{oc}, J_{sc} and η are 508 mV, 1.64 mA cm^{-2} and 0.98%, respectively. All parameters of this co-modified cell lie between those obtained in the presence of tBP and lithium separately (Table 4.1, Figure 4.3(a)). However most remarkable is the decrease in J_{sc} and efficiency with respect to cell containing only lithium ion independently of light intensity. While the fill factor is increased when tBP and lithium are added at 1 Sun, it increases more at low light intensity. The dark current in this co-modified cell is less pronounced with respect to lithium-based cell (Figure 4.3(b)).

Figure 4.3(c) depicts the evolution of IPCE of the modified devices. When tBP is added to the electrolyte A the IPCE decreases from 14.1% to 1.7%. In contrast after adding lithium ions to the electrolyte A the IPCE increases strikingly to 63.7%. Combining both additives leads to IPCE of 21.3% at 475 nm.

Out of this, it can be noticed that in the presence of additives in the corresponding device behaves differently with respect to the unmodified device. The presence of tBP in the electrolyte provokes an increasing V_{oc} and decreasing J_{sc} while the presence of lithium ions leads to higher J_{sc} and lower V_{oc}. The divergent effects of these additives were rationalised in terms of their influence on the energetics of the conduction band/ trap states and therefore on the kinetics of charge recombination: While lithium causes a band edge shift away from the vacuum level, tBP provokes a band edge shift in the other direction by deprotonation of the TiO_2 surface [69,78,204]. The adsorption of tBP respectively pyridine on metal oxides has been studied in detail by FTIR, since pyridine serves as an analytical tool to detect surface states acting as Lewis acids [205-207]. From this study it is known that pyridine can bind physically or chemically via the nitrogen to the oxide surface. While the physical coordination is rather weak and will not stand higher temperatures, the chemical coordination of the pyridine shows high temperature stability [206]. Since all devices where prepared and characterised in standard conditions, the physisorbed tBP could probably less evaporate but

can react with free lithium ions in the cell. The shift of the TiO_2 band edge away from the vacuum level after adding lithium increases the driving force for electron injection from the excited dye while the tBP acts conversely. That is why low J_{sc} is generated by the device containing tBP with respect to the device containing only lithium ions. This observation shows that the presence of lithium in the cell is beneficial, while the presence of tBP seems to be disadvantageous in term of efficiency generated at this level of investigation. The impact of lithium ions on the performance of the device will be discussed in detail in section 6.4.

The investigation of the effect of tBP in DSSC was also extended to other dyes used in this work. The results obtained are shown in Table 2. All dyes exhibit similar behaviour than P1-based cells. V_{oc} and FF generated by all dye types are higher than their corresponding tBP-free cells. The J_{sc} and the efficiency also decrease considerably. These observations suggest that the presence of tBP in electrolyte decreases the performance of device independently of the chemical structure of the dye.

From this study one can observe that device based on electrolyte A + 0.05 M Li exhibits better performance while tBP containing electrolyte turns out to be disadvantageous. Therefore, unless otherwise mentioned electrolyte A + 0.05 M Li will be used as mediator for a comparative study of DSSCs based on various dye type.

4.1.3 Influence of the Br^-/Br_3^- redox mediator on the performance of DSSCs

Iodide triiodide redox couple is revealed to be the most efficient for DSSC as already demonstrated. Its energy level matches perfectly with the HOMO levels of the compounds investigated in this work as sensitizer. It is widely used because of its good reversibility and stability, necessary conditions in Grätzel cells [41]. In the latter, the maximum voltage under illumination corresponds to the difference of the Fermi level of metal oxide semiconductor and the redox potential of the electrolyte. This means that the change in one of these parameters could significantly modify some characteristics of the device. In the aim to have a gain in photovoltage, a choice can be made on the nature of the metal oxide semiconductor or on the redox mediator. While keeping unchanged all additives in the electrolyte, which could interact with TiO_2 surface, another redox mediator was tested. In this experiment the proportion of additives were kept in the same ratio for comparison. With an oxidation potential (1.09 V Vs NHE) more positive than the oxidation potential of iodide triiodide couple (0.4 V) [208], the use of Br^-/Br_3^- is expected to generate high open circuit voltage and reduce the dark current in the device. It should be noted that the HOMOs (calculated vs.

NHE) of all investigated dyes are higher than the oxidation potential of Br^-/Br_3^-, an essential condition for efficient dye regeneration in the cells. In this experiment the electrolytes used consisted of 0.3 M LiBr, 0.03 M Br_2, 0.5 M *tert*-butylpyridine in dried acetonitrile and of 0.3 M LiI, 0.03 M I_2, 0.5 M *tert*-butylpyridine in acetonitrile. (Table 4.2.).

Characteristics of modified devices

Figure 4.4 depicts the current voltage characteristics of P1-based cells measured at incident light intensity of 88 mW cm^{-2} at 25°C. The measurements were performed directly after preparation of devices without complete sealing. It should be noted that Br_2 is a strong electrophile and tends to undergo bromination with unsaturated bonds especially in the presence of catalysis or light irradiation [209]. For this reason measurements were performed directly after assembling the devices. For comparisons, the current voltage characteristics of both Br^-/Br_3^- and I^-/I_3^- type cells are shown in Figure 4.4 and the characteristic are summarised in Table 4.2.

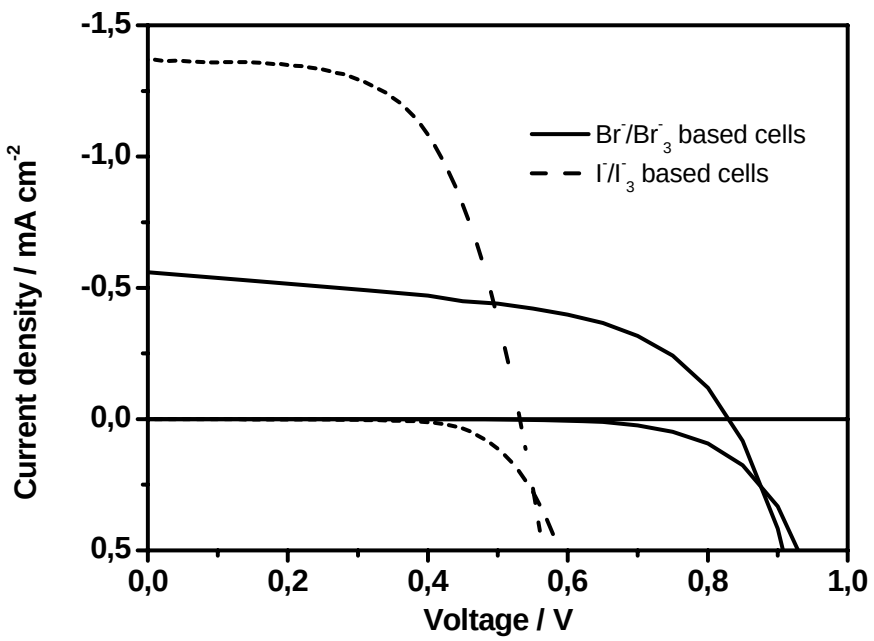

Figure 4.4. Current-voltage characteristics in the dark and at an illumination intensity of 88 mW/cm² for the devices based on Br^-/Br_3^- (solid line) and I^-/I_3^- (dash line). The electrolyte solutions consisted of 0.3 M LiBr, 0.03 M Br_2, 0.5 M *tert*-butylpyridine in acetonitrile of Br^-/Br_3^- -based cell and 0.3 M LiI, 0.03 M I_2, 0.5 M *tert*-butylpyridine in acetonitrile for I^-/I_3^- -based cell.

Table 4.2. Performances of DSSCs based on various dye and electrolyte types

Dyes	Electrolyte: 0.3 M LiBr, 0.03 M Br_2, 0.5 M *t*BP in acetonitrile			
	V_{oc} [mV]	J_{sc} [mA/cm^2]	FF [%]	η [%]
P1	839	0.324	0.519	0.27
P4	626	0.114	0.515	0.04
P7	652	0.153	0.536	0.06
P8	687	0.306	0.528	0.13
P9	647	0.181	0.575	0.07
Dyes	**Electrolyte: 0.3 M LiI, 0.03 M I_2, 0.5 M *t*BP in acetonitrile**			
	V_{oc} [mV]	J_{sc} [mA/cm^2]	FF [%]	η [%]
P1	529	1.260	0.682	0.52
P4	450	0.393	0.609	0.12
P7	477	0.501	0.609	0.17
P8	455	0.511	0.621	0.16
P9	503	0.521	0.621	0.18

From Figure 4.4 and Table 4.2, it can be seen that the open circuit voltage generated by the Br^-/Br_3^- based cell is 839 mV. The J_{sc} and fill factor are 0.324 mA cm^{-2} and 0.513, respectively. This corresponds to an overall efficiency of 0.27%. The device based on the I^-/I_3^- redox couple generates the values of 529 mV, 1.26 mA cm^{-2} and 0.682 corresponding to $V_{oc,}$ J_{sc} and fill factor, respectively. These yield an overall efficiency of 0.52%. When comparing the performance of the two types of cells, V_{oc} increases while J_{sc} decreases when the redox mediator is changed from I^-/I_3^- to Br^-/Br_3^-. The V_{oc} is increased by 310 mV upon replacing the redox couple I^-/I_3^- with Br^-/Br_3^- in P1-based cells. This corresponds to a gain of 57% in V_{oc} and confirms the prediction. The increase in V_{oc} is also observed in DSSCs based on other dye type (Table 4.2). This gain in V_{oc} is due to the enlarged energy level difference between the redox potential of the Br^-/Br_3^- and TiO_2 CB. Similar behaviour has been also reported by other research groups [142,209]. On the other hand, V_{oc} also depends on the dark current that is related to the charge recombination between conduction band electrons and the oxidized half in the electrolyte. The dark current onset potential is related to V_{oc}: the larger the dark current onset potential, the larger V_{oc}. As it can be seen from the dark current-potential plot in Figure 4.4, the dark current onset potential is shifted to larger values when I^-/I_3^- is

replaced by Br^-/Br_3^- in the devices. This observation suggests that the use of Br^-/Br_3^- contributes significantly to the suppression of dark current partly responsible for the V_{oc} enhancement.

The J_{sc} decreases from 1.260 to 0.324 mA cm^{-2} in P1-based cells (see above) upon the mediator changing from I^-/I_3^- to Br^-/Br_3^-. This decreasing in short circuit current density is also observed in devices based on other dye types. J_{sc} decreases from 0.393 to 0.114 mA cm^{-2}, 0.501 to 0.153 mA cm^{-2}, 0.511 to 0.306 mA cm^{-2} and 0.521 to 0.181 mA cm^{-2} in P4, P7, P8 and P9-based cells, respectively (Table 4.2). This substantial decreasing in J_{sc} could have two origins. On one hand it could be attributed to the small driving force for electron injection from bromide to oxidised dye. Since the oxidation potential of Br^-/Br_3^- is more positive than that of I^-/I_3^- the dye regeneration could be kinetically limited. On the other hand, the decreasing in J_{sc} could be attributed to the reduction kinetic of bromine at the counter electrode. Suri et al. [209] have reported that the reduction of bromine is slower than that of iodine at the Pt counter electrode. Furthermore, in the same preparation conditions Suri et al. [209] found that the conductivity of Br^-/Br_3^- (0.6 S/m) is slower than that of I^-/I_3^- (1.0 S/m). These factors could explain the decrease in J_{sc} in cell consisted of Br^-/Br_3^- as redox mediator. However, they have reported relative similar short circuit current density when using both mediators. Their results contrast with those obtained in this work. In their works, ZnO was used as nanoporous semiconductor and Eosin Y (1.15 V vs. NHE) [210] used as dye. Eosin Y was reported [210] to be more stable once adsorbed onto ZnO and hence shrinks the recombination process leading to an improvement of the cell performance. This could explain the relatively similar performance of their devices. The HOMO level of the latter is sufficiently positive for efficient dye regeneration by Br^-/Br_3^-. Although the performances of the cells seem to be limited by the kinetic of the reduction of Br_3^- at the counter electrode and its conductivity [209], it turned out thermodynamically favourable for electron exchange with the family of dyes investigated in this work.

From Table 4.2 one can see that the FF generated by the device decreases when the redox couple I^-/I_3^- is replaced with Br^-/Br_3^-. This could be mainly attributed to the nature of redox couple since the decreasing is independent of the dye structure. All investigated dyes exhibit a loss in fill factor (Table 4.2). At this stage of investigation the decrease of FF could be attributed to the nature of the electrolyte. The fill factor is a phenomenological quantity, which depends on the series resistance of the cell, the resistance of the substrate-TiO_2 interface, the resistance associated with ion transport in the electrolyte, the charge transfer resistance at the counter electrode and the voltage dependence of the recombination rate. The

charge transfer at the counter electrode is affected by the redox activity of the Pt (or graphite) catalyst toward oxidized redox species, the electrolyte, the solvent, and concentration of the oxidized species (e.g. I_3^-) [211]. From this, it can be suggested that the low fill factor Br^-/Br_3^- based cell with respect to I^-/I_3^- is likely due to its low conductivity and the poor charge transfer at the Pt/electrolyte interface, which could increase the series resistance in the device, although a deeper study is required to better understand this phenomenon.

4.2. Performance of DSSC based on non-spiro compounds

In this sub-section is presented a comparative study of DSSCs based on various non-spiro compounds, namely, *N*-(pentafluorphenyl)-perylen-3,4:9,10-tetracarboxylic acid-3,4-anhydrid-9,10-imide (P4), perylene dicarboxylic acid-3,4-anhydride (P7), *N*-(diisopropylphenyl)-3,4:9,10-perylene tetracarboxylic acid-3,4-anhydrid-9,10-imide (P8), 1,7-(4´-*t*-butylphenoxy)-3,4:9,10-perylene tetracarboxylic dianhydride (P9), *N*-(di-*t*-butylphenyl)-3,4:9,10-perylene tetracarboxylic acid-3,4-anhydrid-9,10-imide (P10). The TiO_2 film thickness used is 7 µm and the electrolyte used consists of 0.6 M 1-butyl-3-methylimidazolium iodide, 0.1 M I_2, 0.05 M $LiClO_4$ in 3-methoxy-propionitrile.

4.2.1. General characteristic of the DSSCs

Figure 4.5 (a) shows the current density-voltage (*J-V*) characteristics of DSSC based on P4, P7, P8, P9 and P10, characteristics measured in ambient atmosphere at room temperature (RT) under illumination of 1 sun and the plot of power of the corresponding devices versus voltage Fig. 4.5(b). The chemical structures of the investigated non-spiro compounds are presented in Fig. 4.5(a).

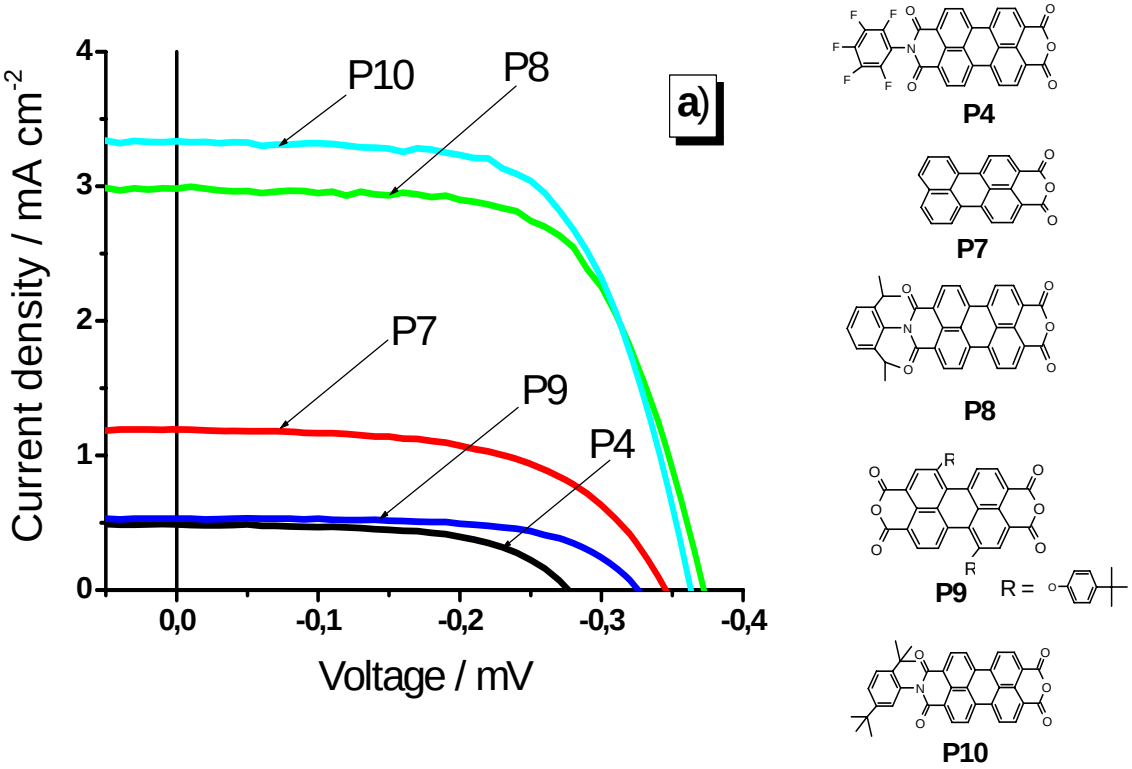

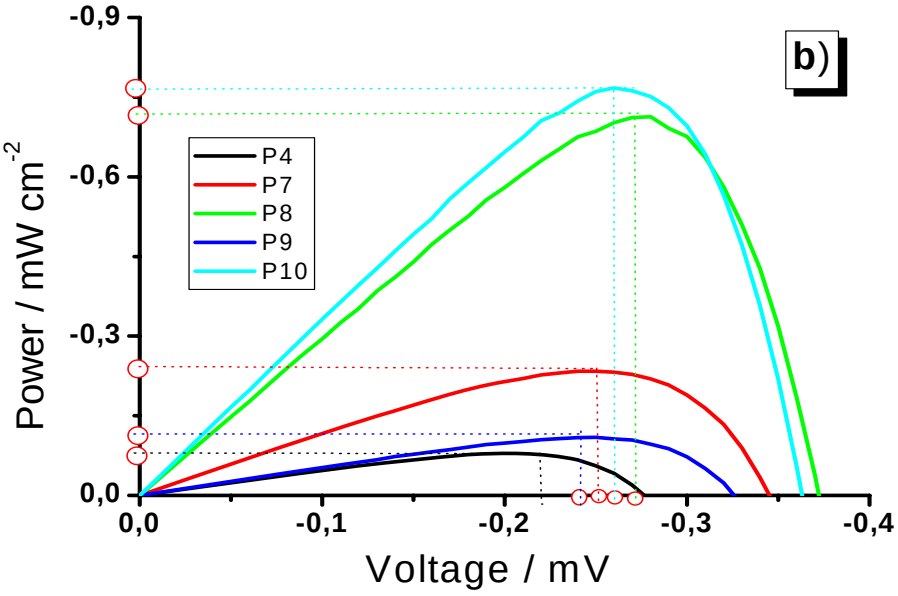

Figure 4.5. (a). Current-Voltage characteristics of devices based on P4, P7, P8, P9, P10 with electrolyte consisted of 0.6 M 1-butyl-3-methylimidazolium iodide, 0.1 M I_2, 0.05 M $LiClO_4$ in 3-methoxy-propionitrile at 1 sun and in dark, TiO_2 film thickness ~7 µm, active area 0.15 cm^2. On the right side the chemical structure of investigated dyes are depicted. (b). The plot of power against voltage at 1 Sun.

The results extracted from the J-V characteristics of DSSC based on P4 measured at room temperature (RT) (Figure 4.5 (a)) are 0.487 mA cm^{-2}, 277 mV and 0.586 for J_{sc}, V_{oc} and FF, respectively. These lead to an overall efficiency (η) is 0.08 %. The voltage and current density at maximum power point are 200 mV, 0.39 mA cm^{-2} for maximum power of 0.08 mW cm^{-2}, respectively (Figure 4.5 (b)). From the (Figure 4.5 (a)), one can see that the J_{sc}, V_{oc} and FF generated by the device based on P7 are 1.195 mA cm^{-2}, 345 mV and 0.567,respectively, leading to an overall efficiency of 0.23 % (calculated at 100 mW cm^{-2}, AM 1.5). The voltage and current density at the maximum power point were found to be 240 mV, 0.974 mA cm^{-2} and 0.233 mW cm^{-2} (Figure 4.5 (b)). It can be observed that both devices perform differently. The J_{sc}, V_{oc} and η are by 0.71 mA cm^{-2}, 68 mV and 0.15 % higher in DSSC containing P7 than device based on P4.

A low performance is also observed with P9. The J_{sc}, V_{oc} and FF generated by the device containing P9 are 0.53 mA cm^{-2}, 325 mV and 0.635 respectively corresponding to an overall efficiency of 0.11 % at one sun (Figure 4.5(a)). This device generates photovoltage, current density and power at the maximum power point of 250 mV, 0.437 mA cm^{-2} and 0.11 mW cm^{-2} respectively (Figure 4.5(b)). These parameters are located between those of P4 and P7. However, devices containing P8 and P10 behave totally differently as showed in Figure 4.5(a), and (b). The performances exhibited by device based on P8 are 2.98 mA cm^{-2}, 372 mV and 0.642, corresponding to J_{sc}, V_{oc} and FF, respectively. The overall efficiency of this device is 0.71 %. DSSC based on P10, exhibits J_{sc}, V_{oc} and FF of 3.34 mA cm^{-2}, 363 mV and 0.633, respectively, which leads to an overall efficiency of 0.77%. The current density and voltage at the maximum power point are 2.95 mA cm^{-2} and 260 mV, respectively, for maximum power of 0.77 mW cm^{-2}. Although the device containing P10 has an efficiency relatively close to that generated by P8-based cell (0.71 %), a slight difference in J_{sc} is observed.

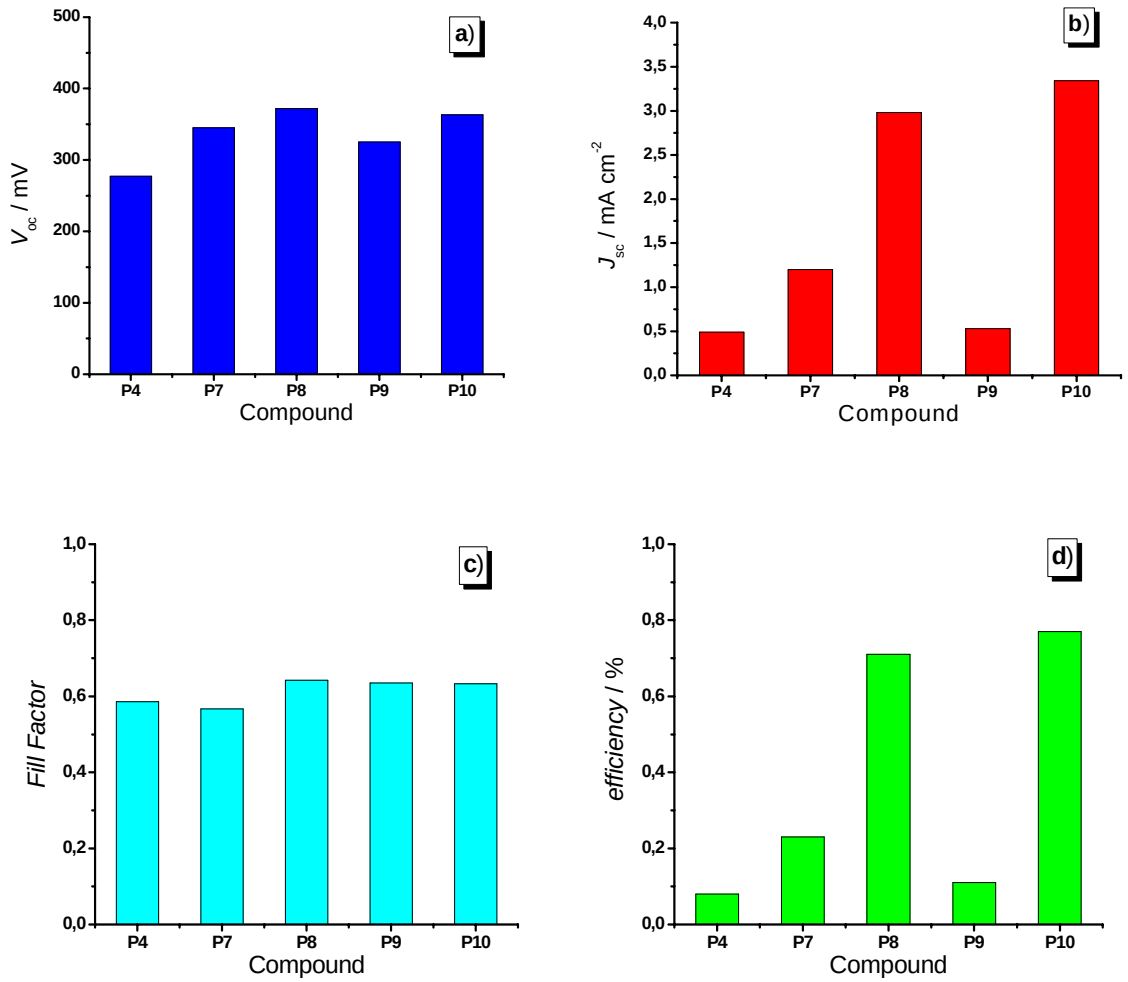

Figure 4.6. Summary of parameter generated by DSSC based on P4, P7, P8, P9, P10: (a) Open circuit voltage (b) Short circuit current density, (c) Fill Factor, (d) Efficiency. Conditions as in Fig. 4.5.

Discussion

Figure 4.6 displays the summary of parameter extracted from J-V characteristic of device investigated, as shown in Fig. 4.5. These results show that the J_{sc} generated by DSSCs containing P4 is ~2.5 times lower than that generated by DSSCs containing P7. The difference between J_{sc} generated by P4 and P7 can be attributed to the low driving force for electron injection from excited P4 dye to the TiO_2 CB with respect to P7. The LUMO level of P4 is –3.94 eV, which is relative close to the conduction band edge of the TiO_2 (– 4.2 eV) [40,43,47,81,133,213]. The low LUMO level exhibited in P4 can be attributed to the presence of the pentafluorophenyle substituent. The Pentafluorophenyle substituent bonded to the perylene core through the nitrogen atom of the imide function behaves as electron

withdrawing group and thus affects the electron donating capability of the perylene core and reduces the electron injection yield from the excited dye to the TiO_2 conduction band. Wang et al. reported that the electron injection yield depends strongly on the driving force whose minimum threshold has been found to be 0.2 eV [214]. However, the HOMO energy level of P4 (-6.25 eV) is more negative with respect to the energy level of the I^-/I_3^- (-4.92 eV) redox couple [215]. This predicts that the regeneration of oxidized P4 could be thermodynamically easier than the reduction of oxidized P7 in operating cells. Moreover, this energy difference between both the oxidized P4 dye and mediator is higher than that in P7-based cell. This means that P4 regeneration could be much faster than P7 regenation in an operating cell. In such system electrons donated by iodide are much easier than recaptured by triiodide. Tributsch [216] suggests that the suppression of the reverse reaction here is not a phenomenon involving the Marcus theory inverted region, since replacement of I^-/I_3^- by redox systems with similar redox potentials ($Fe^{2+/3+}$, $Fe(CN)^{3+/4+}$, quinone/hydroquinone) leads to a significant drop of solar cell efficiency. Thus, HOMO level of P7 (-5.74 eV) lower than the I^-/I_3^- energy level is also sufficient to insure fast dye regeneration. Thereby, electron injection from the dye to the semiconductor conduction band could explain the better performance exhibited by P7-based cell with respect to P4-based cell.

DSSC based on P8 generates J_{sc}, V_{oc} and FF values of 2.98 mA cm^{-2}, 372 mV and 0.642, respectively. The overall efficiency of this device is 0.71%. These values are relative similar to those obtained by Zafer et al. [157]. In their works Zafer et al. have used P8 as dye, although the preparation conditions were different. They obtained 4.1 mA cm^{-2}, 251 mV and 0.58 for J_{sc}, V_{oc} and FF, respectively. The efficiency extracted from their device was 0.60%. The strikingly low open-circuit voltage of their device could be attributed to the high thickness of the TiO_2 film used. In their device, the TiO_2 electrode consisting of a 10 µm mesoporous layer and a light scattering layer consisted of 400 nm anatase TiO_2 particle sizes of 4 µm thicknesses. The layer of TiO_2 thickness is expected to reduce the open-circuit voltage as discussed above. So, the use of thinner TiO_2 enables to have a gain in V_{oc} even though it is not automatically compensated by J_{sc}. However, devices based on P8 perform better than P4 and P7-based cells. The J_{sc} in P8-based cell is higher than in P7-based cell and especially 6 times higher than in P4-based cell. Devices containing P4 seem to be the best choice for comparison because of their similarities in chemical structure. The increase in short circuit density in P8-based cell with respect to P4-based cell could be attributed to the high driving force for electron injection from excited P8 to TiO_2 CB. In fact this difference as already mentioned may be attributed to the difference of the electrochemical potentials. The

aromatic ring in P8 (diisopropylphenyl) is a stronger electron donor than pentafluorophenyl, the latter being less electron donating because of inductive effect of fluor. That is why with a LUMO level of P8 (-3.88 eV) higher than that of P4 (-3.94 eV), P8 could inject more efficiently electron in TiO_2 CB than P4. On the other hand the open circuit voltage is also increased with respect to P4-based cells. Such a change may be due to change of dipole moment at the TiO_2/dye interface which shifts TiO_2 CB edge to a more positive value increasing the photovoltage in the device. Furthermore the dark current is reduced. It is shifted to higher voltage contributing to the enhancement of Voc. This aspect will be discussed in detail in the section 4.4. That is why with the same preparation conditions the P8-based cell generates a strikingly higher efficiency than in P4-based cells. The current density and the photovoltage at the maximum power point extracted from this device are 2.547 mA cm^{-2} and 280 mV respectively leading a power of 0.73 mW cm^{-2} as depicted the Figure 4.5(b). This value is obviously higher than in P4-based cells and could suggest a low recombination or back reaction in the cell as also observed by Cameron [217].

As shown in Figure 4.5(a), J_{sc}, V_{oc} and FF generated by DSSC based on P10 are 3.34 mA cm^{-2}, 363 mV and 0.633, respectively, leading to an overall efficiency of 0.77%. The current density and voltage at the maximum power point are 2.95 mA cm^{-2} and 260 mV, respectively. These lead to a maximum power of 0.767 mW cm^{-2} (Figure 4.5(b)). The efficiency generated by P10-based cell is higher than the performance generated by P4, P7 and P9-based cells. The intriguing fact is that the performance of P10-based cell is similar to P8-based cells (0.71%), but relative better than P7-based cells. This difference could be attributed not only to the geometrical resemblance of their substitutents (Fig.4.7) but also to their redox potential. P8 and P10 have the same electrochemical potentials (LUMO = -3.88 eV and HOMO = -6.19 eV) suggesting same short-circuit currents. However, compound P7 with the lack of substituents and highest LUMO level should perform better. In contrast P7-based cell exhibits lowest J_{sc}. The short-circuit currents generated by P8-based cell (2.98 mA cm^{-2}) is by ΔJsc~0.35 mA cm^{-2} lower than 3.34 mA cm^{-2} obtained with P10-based cell. The same observation was also made on the corresponding solid-state versions and will be discussed in section 7.2.

The difference noted on the performance of P10, P8, and P7-based cells can be mainly attributed to their chemical structure. Both P8 and P10 exhibit the same LUMO energy level, which could predict the same driving force for electrons injection in TiO_2 conduction band. In fact, the lack of rotation of the isopropyl substituents at 2 and 6 position of the aromatic ring in P8 could enable aggregation with respect to *t*-butyl substituent at position 5 where its

360 °C free-rotation could prevent aggregation of P10 and thus, enhancing electron injection. In Figure 4.7 molecular mechanical (MM) calculations of P8 and P10 are shown where it can be observed the positions of isopropyl in P8 and *t*-butyl in P10 all playing a crucial role on aggregation preventing processes. The MM calculations of P7 compound in Figure 4.7 shows that P7 is planar. The lack of alkyl bulky substituent in P7 could induce its aggregation on TiO_2 surface, which is likely responsible of the low J_{sc} generated by P7-based cell with respect to P8 and P10-based cells.

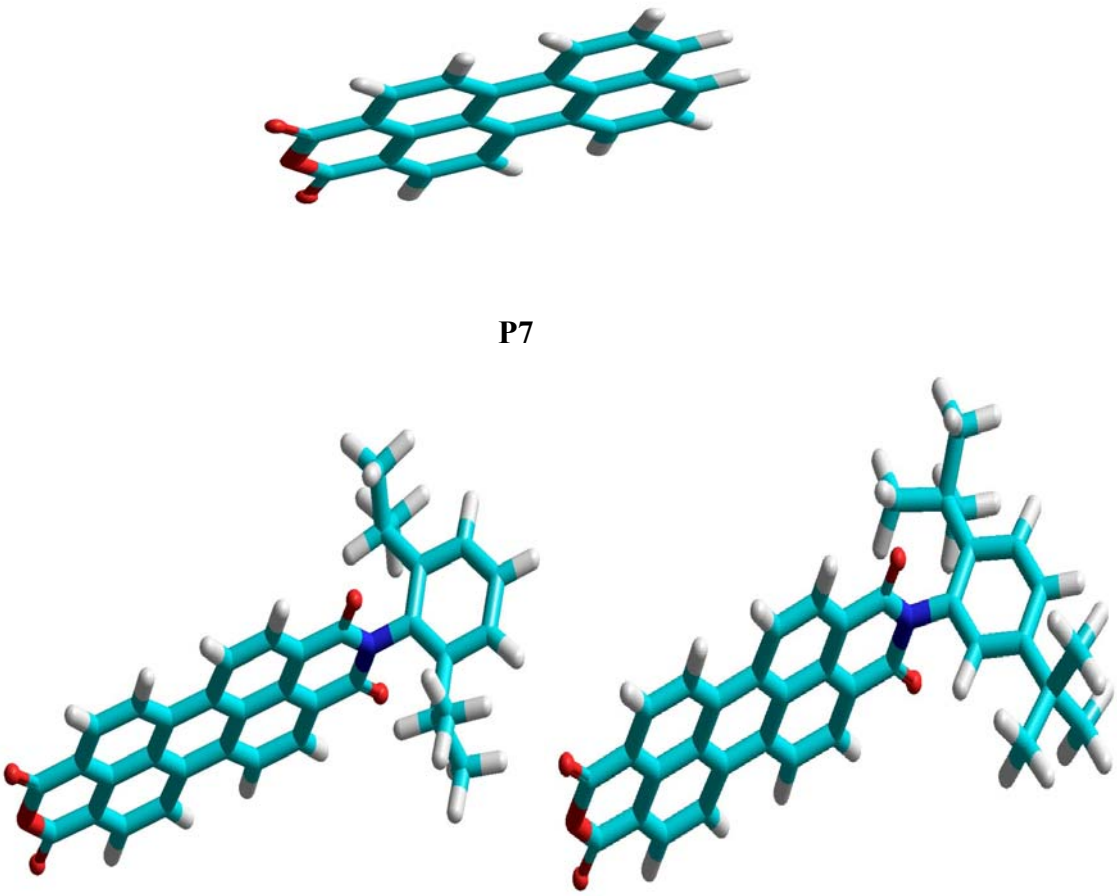

Figure 4.7. Molecule structure of P7, P8 and P10.

In P8 and P10 based cell, V_{oc} are not far one to another and could suggest that the dipole moment of both dyes on the surface of TiO_2 film could act relative identically with respect to P7. Considering morphology aspects, the presence of substituents in P8 and P10

prevents dye aggregation in TiO_2 film and enhances the photoelectron injection from dye to titania.

In Figure 4.5 is shown the I-V characteristics of DSSC based on P9 measured in the standard conditions at 100 mW cm^{-2}. The J_{sc}, V_{oc} and FF collected from this device are 0.53 mA cm^{-2}, 325 mV and 0.635 respectively corresponding to an overall efficiency of 0.11 % at one sun (Figure 4.5(a)). This device generates photovoltage, current density and power at maximal power point of 250 mV, 0.437 mA cm^{-2} and 0.11 mW cm^{-2} respectively (Figure 4.5(b)).

Structurally, P9 is not very comparable to the compounds previously discussed, namely, P4, P7, P8, and P10. Only its electronic properties can enable us to more understand its behaviour in DSSC. It is well known that the substituents in the bay-area have a pronounced effect on the redox potential of perylene derivatives [164]. With two phenoxy electron-donor substituents at the bay position, the HOMO (-6.03 eV.) level of P9 is more positively shifted with respect to P8 and P10. This means that, the former is easy to oxidize and rather difficult to reduce. Taking into account the similarity of their LUMO levels, namely, 3.88 eV for both P8 and P10 and 3.89 eV for P9, their electron injection yield to titania could be the same. However, the kinetics of P9 regeneration by iodide in DSSC can be slower than in P8 and P10-based cells. This can be attributed to the P9 HOMO level lying at 0.15 eV above P8 and P10. Thus, the driving force for regeneration of oxidised P9 is reduced.

4.2.2. Photo action spectra of DSSCs based on non spiro compounds

Figure 4.8 shows action spectra of incident photon-to-current conversion efficiency (IPCEs) for DSSCs based on P4, P7, P8, P9 and P10.

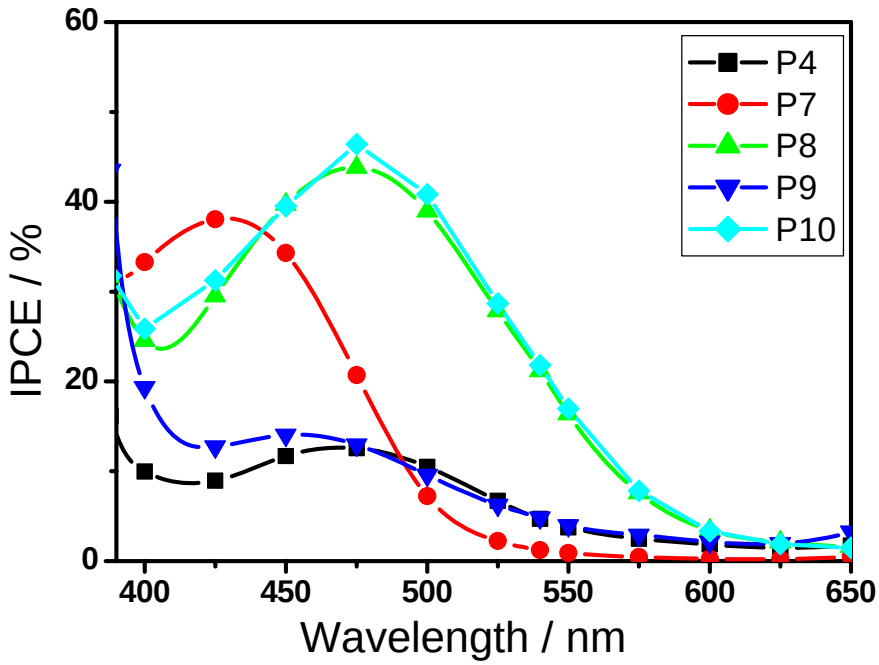

Figure 4.8. Action spectra of incident photon-to-current conversion efficiency (IPCE) for DSSCs based on P4, P7, P8, P9 and P10. Condition as in Fig. 4.5.

From Figure 4.8 one can observe that the onset wavelength of IPCE for these devices is different. The onset wavelength of IPCE for P7-based cell is 550-575 nm, whereas those of P4, P8, P9 and P10 are 600-625 nm. This blue shift of the onset wavelength of IPCE could be due to the lack of electron donating substituent or extension of the conjugation in the perylene core of P7. Introducing electron donating group induces a red-shifting in the visible spectrum of organic chromophore [218]. IPCE values higher than 30% are observed in the range of 388 to 457 nm for P7-based cell, 428 to 517 nm for P8-based cell and 425 to 520 nm for P10-based cell. The maximum values were 38% at 425 nm with a photocurrent density of 57 μA cm^{-2} for the DSSC based on P7, 43.8% at 475 nm with a photocurrent density of 185 μA cm^{-2} for the DSSC based on P8 and 46.4% at 475 nm with a photocurrent density of 156 μA cm^{-2} for the DSSC based on P10. The IPCE values lower than 30% are observed for devices based on P4 and P9. The IPCE of P4 based cell is located in the range of 450 to 500 nm with a maximum value of 12.6% at 475 nm for a current density of 27 μA cm^{-2}. P9-based cells show an IPCE in the range of 400 to 475 nm with a maximum value of 14% at 450 nm where a J_{sc} of 26.4 μA cm^{-2} has been extracted.

The IPCE is the product of light-harvesting efficiency (LHE(λ)), the quantum yield of electron injection ($\varnothing_{inj}(\lambda)$), and the efficiency of collecting the injected charge ($\eta_c(\lambda)$) at the back contact, and it is expressed as [193]

$$\text{IPCE} = \text{LHE}(\lambda)\ \varnothing_{inj}(\lambda)\ \eta_c(\lambda) \qquad 4.2$$

For the same dye loading and TiO_2 film thickness (see Figure 2.7(b)), one might expect the IPCE peak values to follow the trend of LHE, P4 ≈ P8 ≈ P10. Figure 4.8 shows that the order of the IPCE values is in fact P8 > P10 > P4. This could in principle due to different dye coverage, quenching of the excited-state due to dye aggregation, or different degrees of overlap of the LUMO level of the dyes with TiO_2 conduction band. The loading of P4, P7, P8 was determined experimentally using Langmuir formalism and will be discussed later. It was found that the surface concentrations of P4, P7, P8 were 77.3, 66.82 and 80.9 μmol/m^2, respectively. These surfaces coverages are almost in the same order even though P8 seems to have the highest value. The high IPCE of DSSCs based on P8 with respect to P4 could not be really attributed to surface coverage since their LHE on film are relatively the same (see Figure 2.7(b)). However, the reason which could explain the difference in IPCE of P4 and P8-based cells could be the electron injection efficiency $\varnothing_{inj}(\lambda)$. From Eq. 4.2, one can see that an increased electron injection efficiency $\varnothing_{inj}(\lambda)$ contribute to an increasing IPCE. The energy difference between the LUMO of P4, P7, P8, P9 and P10 and TiO_2 CB edge was found to be 0.26, 0.72, 0.38, 0.31 and 0.38 eV, respectively. P4 has lowest TiO_2 CB overlap whereas P7 exhibits highest TiO_2 CB overlapping. The low overlapping may predict a low driving force for electron injection and thus a low quantum yield of electron injection ($\varnothing_{inj}$) from the excited dye to TiO_2 CB Accordingly, the electron injection efficiency of P7 will be higher than P4. The highest IPCE exhibited by P8 and P10 could be due to the hindrance of aggregation by the bulky alkyl substituent. However, the maximum IPCE of these devices is red shifted with respect to devices based on P7. The shift of IPCE towards red region of visible spectrum with respect to P7-based cell is likely due to the electron donating character of the diisopropylphenyl substituent in P8 and P10. Although it is reported that a substituent at the nitrogen of anhydride imide ring does not affect the electronic propertie of perylene π-systems [158,164], the energy levels P4, P7, P8 and P10 extracted by electrochemical and optical methods show a real difference. (See section 2.2). This observation was also made by Zafer et al. [157] which found the LUMO level of PMI-AR and PMI-CH to be -0.73 V and -0.46 V versus Ag/AgCl, respectively, and confirms that the nature of the substituent in

perylenemonoimide (PMIs) derivatives can considerably affect their electrochemical potential and thus their electron injection capability in titania.

4.2.3. The influence of incident light intensity on the performance of DSSCs

4.2.3.1 Influence on the short circuit current density (J_{sc}), Fill Factor (FF) and efficiency (η)

Figure 4.9 displays the characteristics of P4, P7, P8, P9 and P10-based cells at various incident light intensities (P_{inc}). P_{inc}, varying from 0 to 100 mA cm^{-2}. As shown in Figure 4.9(a), the short-circuit photocurrent density, J_{sc}, increased almost linearly with incident light intensity up to 100 mW cm^{-2}. This linearity indicates that the photocurrent generated in my devices is not limited by the diffusion of iodide or triiodide ions within the nanocrystalline network up to J_{sc} of 0.49, 2.98, 0.53 and 3.36 mA cm^{-2} for P4, P8, P9 and P10 based cells at 1 sun, respectively. The linearity is also observed in the device based on P7 up to J_{sc} ~1.195 mA cm^{-2} at 86 mW cm^{-2} [193,209].

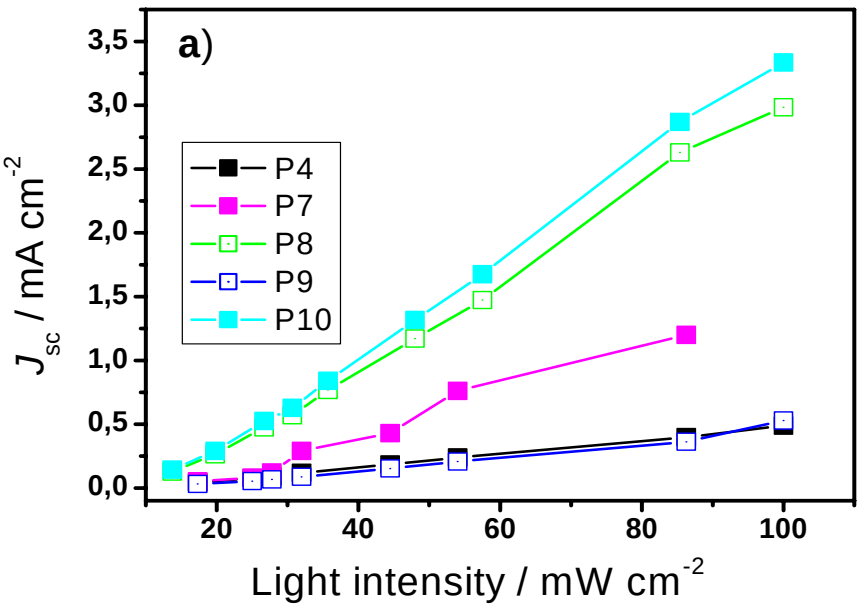

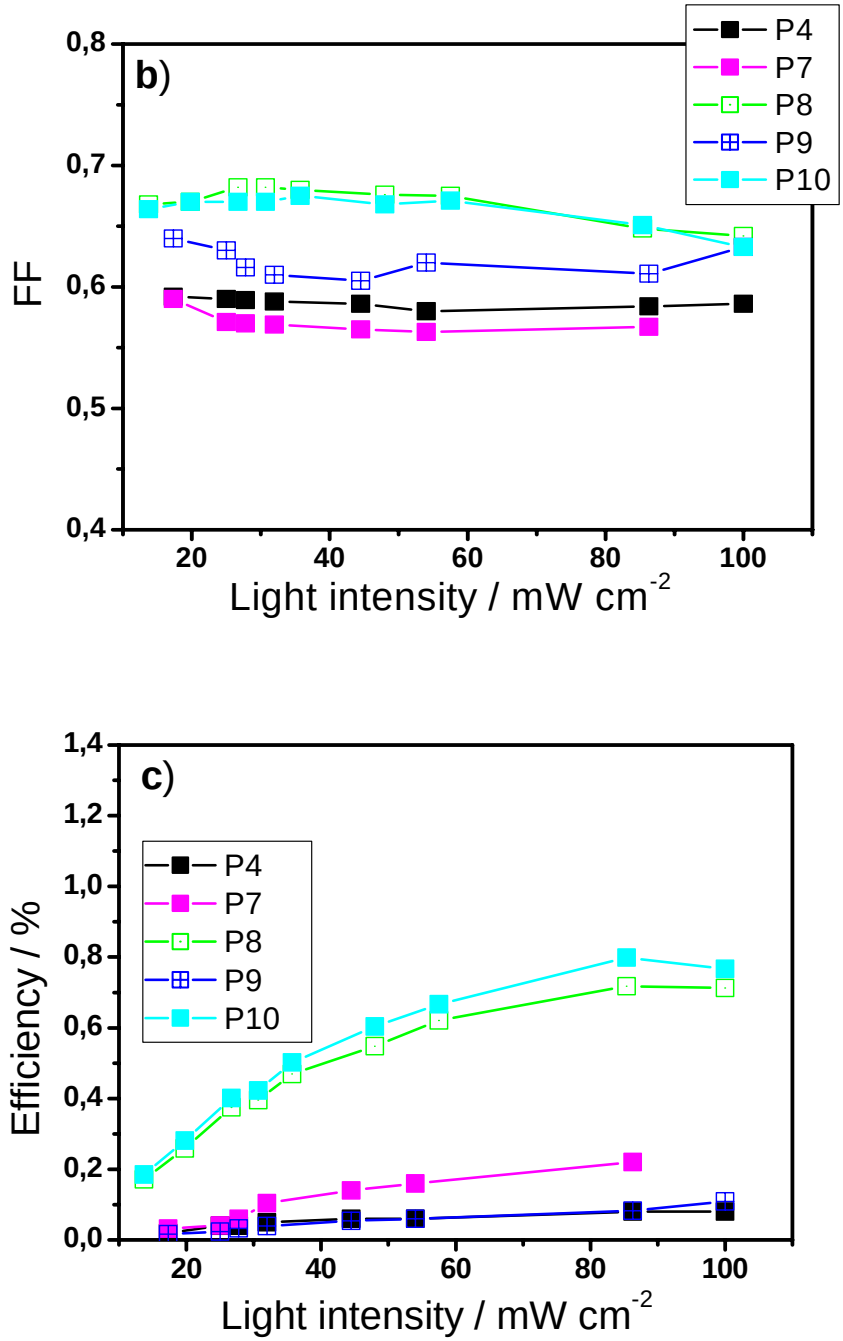

Figure 4.9. Dependence of (a) the short-circuit photocurrent, J_{sc}, (b) Fill factor, FF, (c) efficiency, η, with incident light intensity in DSSCs based on P4, P7, P8, P9, P10 with electrolyte consisting of 0.6 M 1-butyl-3-methylimidazolium iodide, 0.1 M I_2, 0.05 M $LiClO_4$ in 3-methoxy-propionitrile at 1 sun and in dark, TiO_2 film thickness ~7 µm, active area 0.15 cm^2.

This trend of J_{sc} to increase with light intensity is due to the fact that the electron transport in nanoporous titania film can be described by the proposed multiple trapping-detrapping model [72]. Along with the increase of light intensity, deep traps will be filled with

photoinjected electrons and do not retard the electron transport any more. So the detrapping of electrons from shollow traps is much faster when incident light intensity is increased, resulting in a higher electron diffusion in TiO_2 CB and hence J_{sc}. However, the slopes of drop of J_{sc} as a function of incident light intensity are differing. Taking devices individually, devices based on P8 and P10 exhibit slopes higher than other devices. The difference can be attributed to high driving force for electron injection in TiO_2 CB, which lead to increase the population of electron in deep trap at a given incident light intensity and thus their diffusion in TiO_2 CB.

Figure 4.9(b) shows the dependence of fill factor, FF, on incident light intensity. From Fig. 4.9(b) one can see that the FF in P4-based cell decreases from 0.592 to 0.590, 0.589, 0.588, 0.586 when P_{inc} varies from 17.3 to 25, 27.8, 32, 44.5 mW cm^{-2} and remains relative constant until 100 mW cm-2 were a value of 0.586 is obtained. The FF in P7-based cell decreases from 0.590 to 0.571, 0.570, 0.569, 0.565, 0567 when the light intensity is changed from 17.3 to 25, 27.8, 32, 44.5, 86.3 mW cm^{-2}. The same trend is observed in devices based on P9. The FF decreases from 0.640 to 0.605 when light increases from 17.3 to 44.5 mW cm^{-2} and beyond 44.5 mW cm^{-2} FF increases slightly but remains lower than the value obtained at lowest light intensity, 0.611 being obtained at 86.3 mW cm^{-2}. Devices with highest FF are P8 and P10. The FFs extracted from P8 and P10-based cell decrease with light intensity. FF varies from 0.642 to 0.668 in the range of the light intensity studied with a maximum value of 0.682 between 26.7 and 30.7 mW cm^{-2}. It increases from 0.668 to 0.682 and decreases gradually when light intensity is increasing. In the device based on P10 the FF is constant in the light intensity range between 19.8 and 35.7 mW cm^{-2} with a mean value of 0.67 and decrease gradually with light intensity until 0.633 for 100 mWcm^{-2}.

From these results one can observe that device based on P8, P9 and P10 show FF located in the range of an ideal cell. The typical FF of a dye cell is in the range of 0.6 to 0.8. The decrease of FF with increasing light intensity can be attributed to the ohmic losses in conducting glass support [216].

Figure 4.9(c) shows the dependence of efficiency, η, on the incident light intensity. From Figure 4.9(c) one can see that η of device based on P7 increases slightly from 0.03 to 0.16% as the incident light intensity increases from 17.3 to 54 mW cm^{-2}. However, the maximum efficiency is relative low, i.e. 0.23% at 86.3 mW cm^{-2}. Device based on P4 and P9 generate also relative low η. η of P4-based cells varies from 0.02 to 0.08% as incident light is increase from 17.3 to 100 mW cm^{-2}. The maximum value, 0.08% is obtained for incident light intensity range between 86.3 and 100 mW cm^{-2}. The same trend is observed in P9-based cells.

The efficiency of P9-based cell increases slightly from 0.02 to 0.6% when incident light intensity is increased from 17.3 to 54 mW cm^{-2}. The maximum value 0.11% is obtained at 100 mW cm^{-2}. The efficiency of devices based on P8 shows a tendency to increase from 0.17% to 0.71% as light intensity is increased from 13.7 to 85 mW cm^{-2} and remains relative constant between 85 and 100 mW cm^{-2} with a maximum value 0.72 % at 85 mW cm^{-2}. In device based on P10, η increases from 0.2 to 0.5% when incident light intensity is changed from 13.7 to 48 mW cm^{-2} and tends to be constant beyond 57.5 mW cm^{-2} with the highest value 0.80% at 85.4 mW cm^{-2} (Figure 4.9(c)). Globally, η is almost constant for incident light intensity lying between 40 and 100 mW cm-2. This is not the case for inorganic solar cell where η decreases when incident light intensity is reduced [203].

4.2.3.2 Influence of incident light intensity on the open-circuit voltage

The dependence of V_{oc} on incident light intensity was investigated and the results are shown in Figure 4.10.

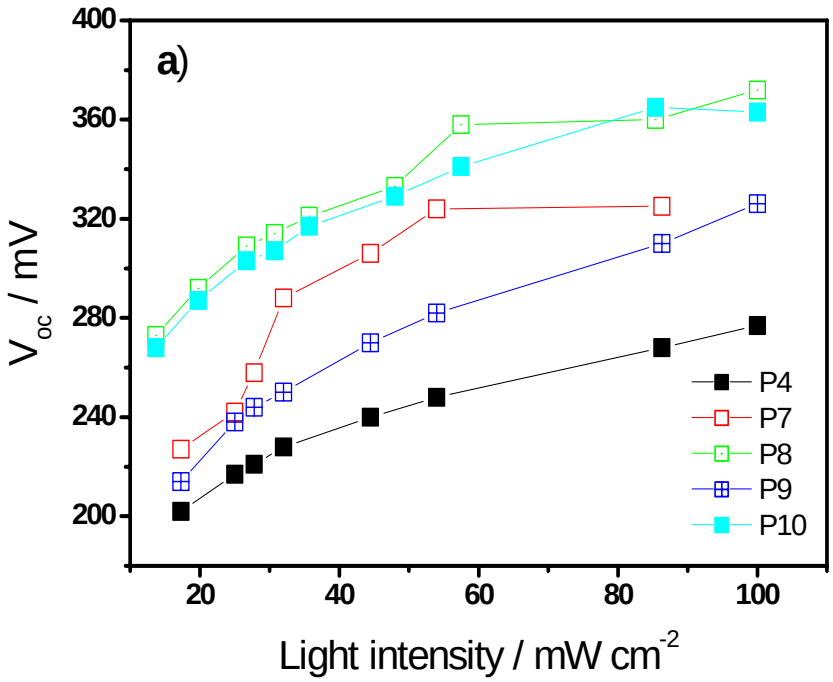

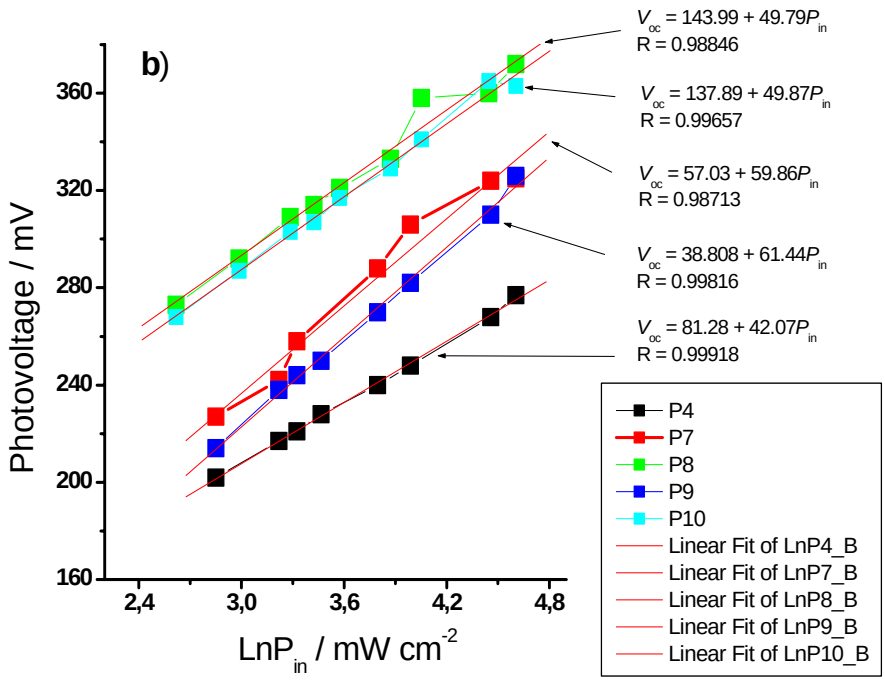

Figure 4.10. Relationship between (a) incident light intensity and the open-circuit voltage, V_{oc}, and (b) the logarithm of the incident light intensity and V_{oc}. The solid red lines denote the linear fit to the experimental data.

Figure 4.10(a) shows the dependence of V_{oc} with incident light intensity. V_{oc} of device based on P7 increases with incident light intensities between 17 mW cm^{-2} and 54 mW cm^{-2} and reached a plateau between 54 and 100 mW cm^{-2}. Like P7-based cell, V_{oc} of P4, P8, P9, P10-based cells increase with incident light intensity and tend to reach a plateau between 80 and 100 mW cm^{-2}. This logarithmic dependence is characteristic of DSSCs. The plateau at high light intensity suggests saturation in the conduction band of TiO_2.

Figure 4.10(b) shows the dependence of V_{oc} on the logarithm of the incident radiant power over a range 0-100 mW cm^{-2}. V_{oc} in DSSCs is generally proportional to the logarithm of incident light intensity [41,193] and, thus, to the logarithm of electrons injected as expressed by Eq. 4.1**.** In that expression 1/ $u\alpha$ represents the diode quality factor or ideality factor [203,219,220] and its typical value is between 1 and 2 [203,219,220]. From Figure 4.10(b), within the range of the measurement a linear relationship is obtained. The slopes found are 42.07, 59.86, 49.79, 61.44, 47.87mV per decade for P4, P7, P8, P9 and P10-electrolyte based cells yielding ideality factors of 0.71, 1.01, 0.84, 1.04 and 0.85, respectively. The calculated values of the product $u\alpha$ were 1.4, 0.99, 1.19, 0.96 and 1.18 for P4, P7, P8, P9 and P10, respectively. P4-based cell has the lowest ideality factor (0.71) whereas P7 and P9

based cells show the highest values. Thereby P7 and P9-based cell show relatively perfect diode behaviour. This is not the case for P8 and P10 based cells, although they exhibit the highest V_{oc} at 1 sun. This near ideal photodiode behaviour is characteristic of DSSC and demontrates that the recombination reaction is indeed first order with respect to electron concentration [219]. For all devices, the values of the product $u\alpha$, obtained from the slope of the linear portion of the plots (figure 4.10(b)) and equation 4.1 are virtually the same, suggesting that the nature of the molecule do not significantly affect the mechanism of the back reaction transfer. It is important to point out, however, that equation 4.1 does not consider the role of surface-state charging or conduction-band edge shifting of TiO_2 due to the dipole moment of dye. The later plays an important role in the reduction of the dark current in DSSCs [69]. For the light intensity of 100 mW cm^{-2} the V_{oc} of the devices are 277, 345, 372, 325, and 363mV for P4, P7, P8, P9 and P10-based cell, respectively. This slight difference in V_{oc} could be attributed to the dipole moment of different dyes at the interface between dye and TiO_2. This aspect will be discussed in section 4.4.

4.3. Performances of DSSCs based on a spiro-linked compound

4.3.1. *N*-[2´,7´-Bis-(*N,N*-diphenylamino)-9,9´-spirobifluoren-2-yl]-1,7-bis-(4-*t*-butylphenoxy)-perylene-3,4-dicarboxylic acid anhydride-9,10-imide (P1)

N-[2´,7´-Bis-(*N,N*-diphenylamino)-9,9´-spirobifluoren-2-yl]-1,7-bis-(4-*t*-butylphenoxy)-perylene-3,4-dicarboxylic acid anhydride-9,10-imide (P1) is a bipolar compound consisting of donor unit and an acceptor both separated by a spirobifluorene bridge. P1 comes from its parent P9, the latter being the most suitable compound for a comparative study. In P1 the biphenylamine moieties are connected to perylene core by spiro-spacer. But here, the electron donating effect of spiro-diphenylamine moiety does not affect the electronic structure of the acceptor unit owing to the frontier orbital node at the imide on one hand. On the other hand, the spiro center inhibits the conjugation between the donor and acceptor. Therefore, intramolecular charge transfer occurs in P1 by a through-space charge transfer process [46,163].

DSSCs based on P1 have been realised. Figure 4.11 shows the current voltage characteristic of devices based on P1 measured in the standard conditions at one sun and in the dark.

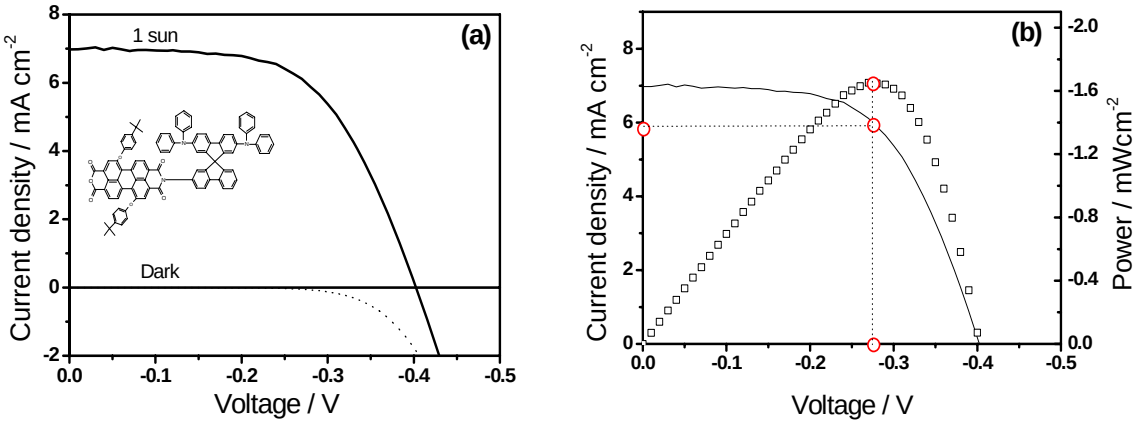

Figure 4.11. (a)**.** Current-Voltage characteristics of devices based on P1 with electrolyte consisted of 0.6 M 1-butyl-3-methylimidazolium iodide, 0.1 M I_2, 0.05 M $LiClO_4$ in 3-methoxy-propionitrile at 1 sun and in dark, TiO_2 film thickness ~7 µm, active area 0.15 cm^2. The inset depicts the chemical structure of P1. (b). The plot of power against voltage.

As it is depicted in Figure 4.11(a), the J_{sc}, V_{oc} and FF generated by this device are 6.975 mA cm^{-2}, 403 mV and 0,588 leading to an efficiency of 1.65% in standard conditions. The current and voltage at the maximum power point extracted from the device are 6.114 mA cm^{-2} and 270 mV for a maximum power of 1.65 mW cm^{-2} (Figure 4.11(b)). Comparing the current density generated by P1-based cell with its parent P9 (0.53 mA cm^{-2}) (Figure 4.4.), the latter is 12 times smaller. This difference is attributed to the molecular structures. The presence of donor moieties in P1 increases electron density in perylene core and thus in TiO_2 CB in the assembled device. Since the donor is separated from the acceptor by a spiro-bridge the intramolecular charge transfer takes place by a through-space charge transfer process as already mentioned. On the other hand, the recombination of injected electron from TiO_2 CB with excited dye is expected to be limited [163,208]. Furtheremore, the oxidized donor moieties embedded in redox electrolyte are more available to undergo the regeneration mechanism. In DSSCs the open circuit voltage is controlled by the difference between the CB edge of TiO_2 and the redox mediator potential. The V_{oc} generated in P1 based cells is by 78 mV higher than that of P9-based cells. This change is likely due to the dipole moment of P1 on the surface of TiO_2 and the suppression of recombination [41,163,172,208] as shown by the shift of dark current to high potential, as it will be discussed in section 4.4.

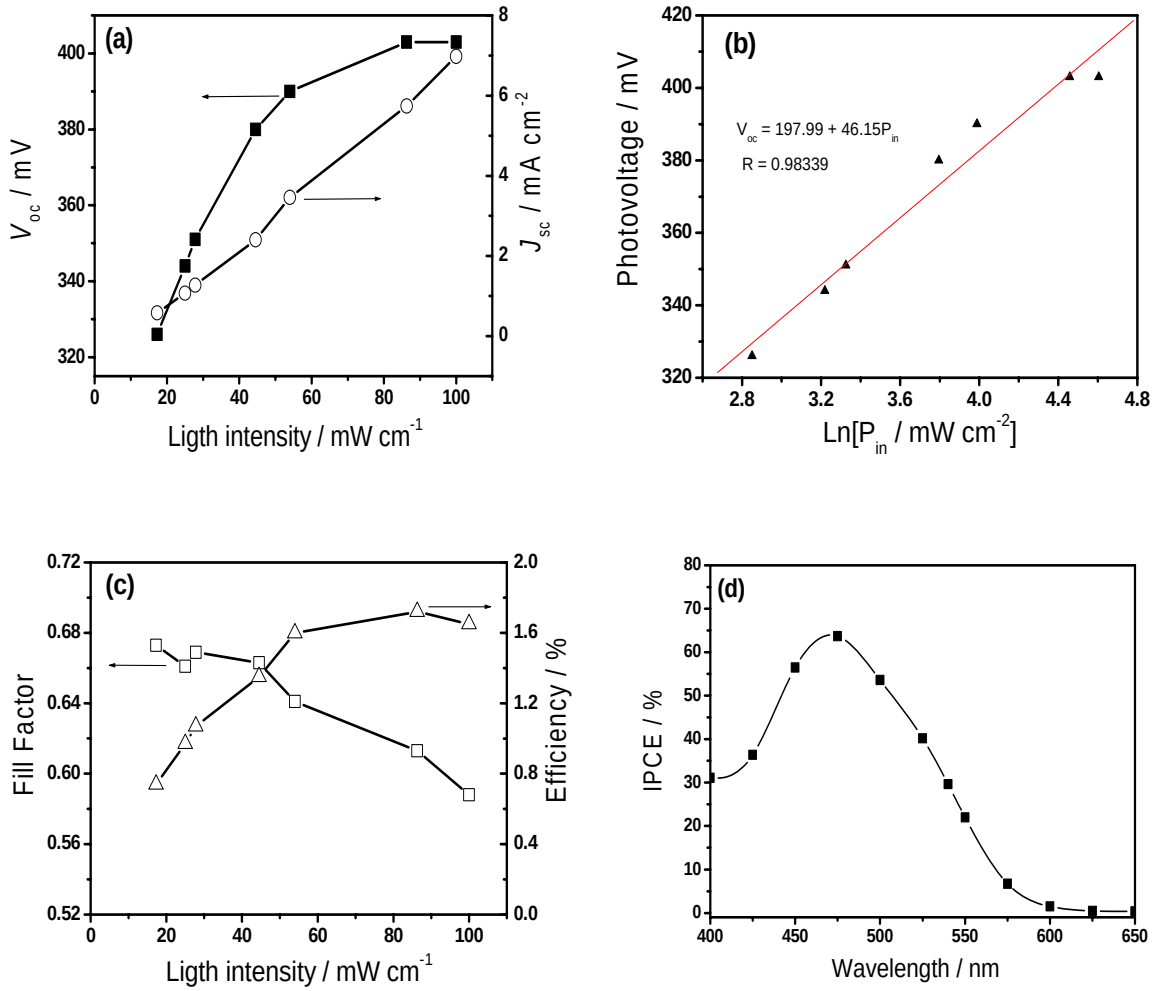

Figure 4.12. Relationship between (a) light intensity and the short-circuit photocurrent and open-circuit photovoltage, (b) the logarithm of light intensity and open-circuit photovoltage, (c) light intensity and fill factor and efficiency. (d) IPCE of the corresponding device. Conditions as in Fig. 4.11.

Figure 4.12 shows the light dependence of parameters in P1-based cells and their photo-action spectra. From Figure 4.12(a) it can be observed that the short-circuit current density increases linearly with light intensity. This linearity observed in the range of light studied suggests that the current density is not limited by the diffusion of iodide in TiO_2 network. A similar behaviour was observed with the reference cell (P9-based cell) as shown in Figure 4.9(a). As shown in Figure 4-12(a) V_{oc} increases with light intensities and reaches a plateau between 83 and 100 mW cm^{-2}. However, the logarithmic relationship shows a linear behaviour (Figure 4.12(b)). The slop extracted from the draw of V_{oc} against logarithm of incident light intensity is 46.15 mV per decade of light intensity. The calculated value of the

ideality factor was found to be 0.78. This value shows the near-ideal photodiode behaviour of P1 based cells. The linear relationship with the logarithm of incident light intensity suggests that the recombination between injected electron and I_3^- ions is quantitatively reduced with increasing light intensity. The fill factor slightly decreases with light intensity as shown in Figure 4.12(c). This increase in V_{oc} with incident light intensity while the fill factor decreases is due to the ohmic losses in the conducting glass support [41]. The efficiency shows slight dependency on light intensity between 17 and 45 mW cm^{-2} and remains unchanged beyond 45 mW cm^{-2}. The highest yield η=1.72% is observed at 86.3 mW cm^{-2}. Globally the P1-based cell shows good behaviour under illumination with respect to the reference. This is likely due to reduction or suppression of back reaction. Moreover, with LUMO located at 0.43 eV above the TiO_2 CB edge the injection of the electron could be facilitated and the presence of spiro-diphenyl moiety could shield the TiO_2 surface thus preventing the recombination of injected electrons in TiO_2 CB with I_3^-. The incident photon-to-electron conversion efficiency of a P1-based cell is shown in Figure 4.12(d). The photo-action spectrum extends from 425 nm to 550 nm with a maximum of 63.4% at 475 nm for a photocurrent density of 135.85 µA cm^{-2}. Unlike the maximum IPCE of 14% between 400 and 475 nm extracted from its parent P9-based cell as illustrated in Figure 4.8, P1-based cells exhibit better performance. Such improvement in P1-based cells could be mainly attributed to a high quantum yield of electron injection as indicated by the equation 4.2. P1 shows considerable high TiO_2 CB overlapping. This predicts a high driving force for electron injection.

Edvisson et al. previously reported high IPCE value with perylene derivatives consisting of donor moieties connected to the perylene core in position 9 [208]. The chemical structures of the corresponding materials 9-(bis-*p-tert*-octylphenyl) amino-1,6-di-(*p-tert*-octyl-phenoxy)-perylene-3,4-dicarboxy anhydride (ID-34) and 9-(diphenylaniline)-1,6-di(*p-tert*-octylphenoxy)-perylene-3,4-dicarboxy anhydride (ID-35) are displayed on the next page. The incident photon-to-current conversion efficiency generated by ID-34 and ID-35 are 69 and 72% respectively. Although, the device preparation (electrolyte composition) is not similar to that used in this work it appears clearly that the presence of donor moiety in perylene core improves the performance of the devices with respect to DSSCs based on donor-free dyes. Furthermore, they found that the short-circuit current densities were 7.96 mA cm^{-2} and 6.13 mA cm^{-2} for ID-34 and ID-35 with a photoanode consisted of 10 µm without scattering layer [208]. Edvisson et al. [208] attributed this improvement in performance in DSSCs to the increase of intramolecular charge separation in the dye, promoting more effective electron injection into TiO_2 in competition with excited dye to dye

recombination (S* → S) and preventing the undesired recombination of electrons from the TiO_2 CB with the oxidised dye. The enhancement in V_{oc} in P1-based cell with respect to P9-based cell is mainly attributed to the dipole moment of P1 on the TiO_2 surface, which shifts the TiO_2 CB, and/or repulsion of species from the TiO_2, resulting less recombination. Such observations have been already done by some authors [172,208]. An attempt of discussion of this dipole moment effect on the cell performance will be slightly approached in section 4.4.

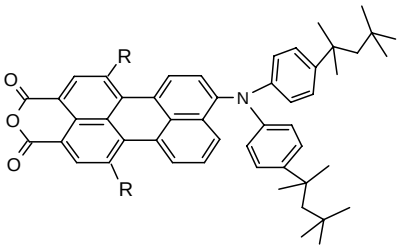

ID34

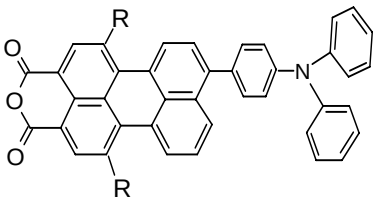

ID35

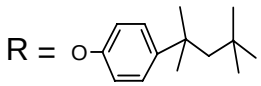

4.3.2. Long -Term Stability of P1-based dye solar cell

High stability under long term exposition on ambient condition is a crutial parameter for sustained cell operation. So the I-V curves of P1 electrolyte solar cells at different time scales were measured. After preparing the device it was kept under ambient condition in summer season. The P1–electrolyte based cell performances were followed during almost two months. Their characteristics were collected and are shown in the Figure 4.13.

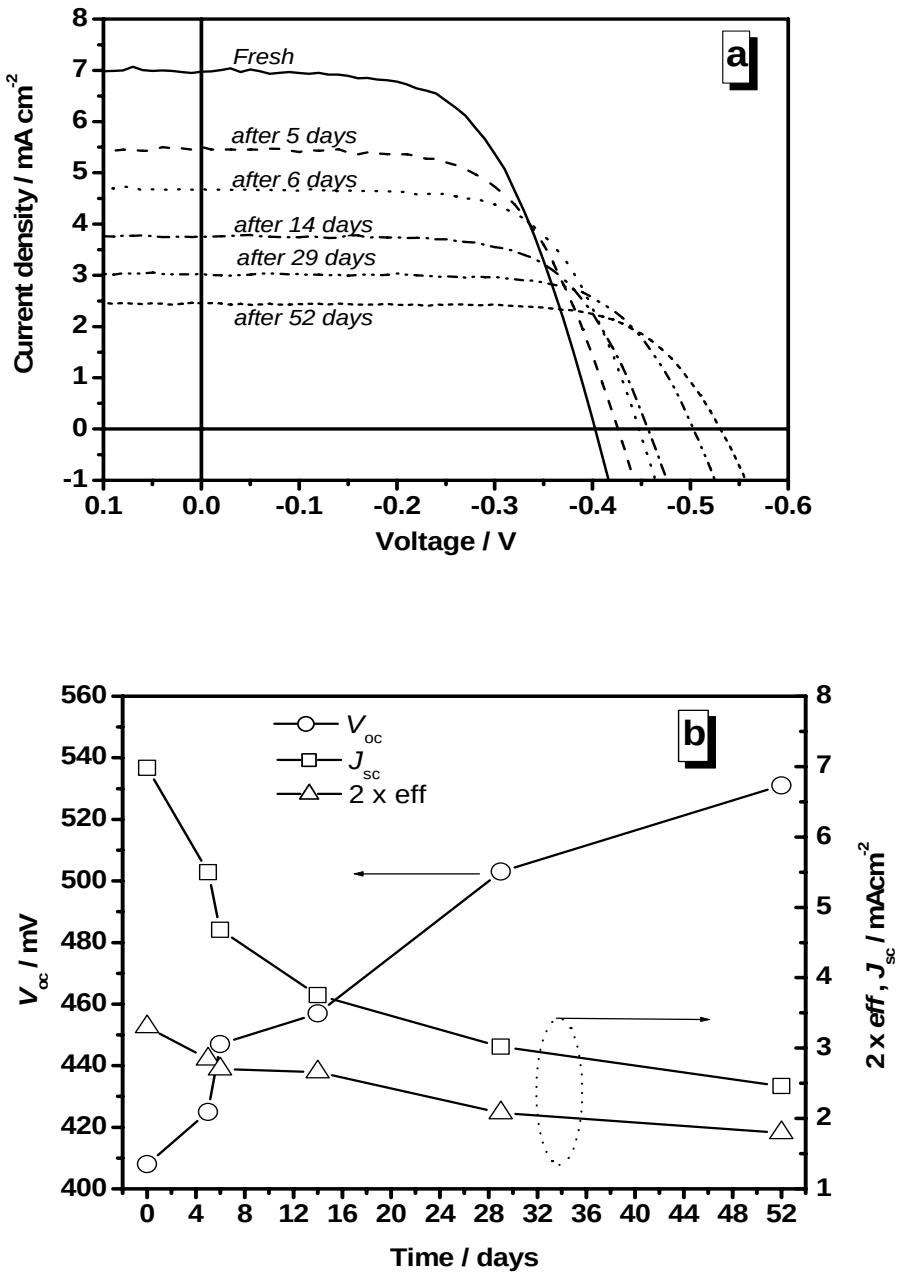

Figure 4.13. Stability of P1-based cell after exposure on ambient condition during summer season: (a) current voltage characteristic of the device (b) evolution of cell parameters with the time.

Figure 4.13(a) depicts the current voltage characteristics of P1 based measured in standard condition after keeping the device on ambient conditions for days. The experiments were carried out in summer season. As shown in Figure 4.13(a) the short circuit current density decreases with the life time whereas the open circuit increases. Moreover, during the

first six days the current drops strikingly from 6.98 to 4.68 mA cm^{-2} afterwards it decreases slowly until the fifty-second day where the J_{sc} generated were found to be 2.459 mA cm^{-2} as shown in Figure 4.13(b), corresponding to an overall J_{sc} losses of 65%. The efficiency also decreases but not noticeable. η decreases slowly after fourteen days where just a slight drop from 1.65 to 1.33% was observed. However after 52 days the efficiency drops to 0.89%. Such a change in J_{sc} and η could be attributed to the sealing techniques [221,222]. Even if the much applied Surlyn sealing technique is used, some recent infrared studies show that gradually water molecules diffuse from the atmosphere into the cell. The consequence is a reaction with triiodide leading to iodate with intermediates of the iodine electrochemistry reacting further with oxygen and water [216,223]. The regeneration of the oxidised sensitizer S^+ by iodide in water- and oxygen-free organic electrolyte (Eq 4.3) [216]

$$2S^+ + 3I^- \rightarrow I_3^- + 2S \qquad 4.3$$

will , with certain probability, change in the presence of water and oxygen, to (Eq 4.4) [164]:

$$2\ S^+ + 3I^- + 4O_2 + H_2O \rightarrow 2S + 3IO_3^- + 2H^+ \qquad 4.4$$

These changes occur in the cell. Water and oxygen access lead to a depletion of iodine (triiodide) so that the electrolyte gets bleached. As consequence J_{sc} decreases, since the regeneration of I^- at the counter electrode becomes more and more impossible because of the crystallisation of iodate [216] or its adsorption onto TiO_2 [223]. The efficiency decreases with time as shown in Figure 4.13(b). The device efficiency drops by 19% after two weeks and 45% after two months. This decrease in efficiency during the first two weeks is lower than that of J_{sc} where 46% loss is observed during the same time period. This could be due to the fact that the decrease in J_{sc} is compensated by the increase of V_{oc}. The open circuit voltage increases with the time as it can be observed in the I-V characteristics curve (Figure 4.13(b)). It tends to increase gradually in time range of the investigation. This behaviour could be attributed to the gradual adsorption of water molecules diffusing from the atmosphere into the cell. The water increases the barrier height between the conduction band of TiO_2 and the redox potential of the mediator after chemisorptions of hydroxyl group. Such a change in V_{oc} was also observed for pre-treated TiO_2 with water [221], pyridine [41,224,225] and ammonia [223]. Although the stability of P1-based cells could be affected by diffused water due to sealing problems, other criteria like the stability of the dye under illumination, the state of

adsorption and its interaction with the surface of TiO_2 was reported to participate to the long-term stability of the DSSC. It has been reported that transition metal complexes are more stable than purely organic dye molecules [216,152]. Combinatorial research on long-term stability realised by Tributsch [216,226] and other groups reveal that organic dyes are much more susceptible to oxidative degradation than Ru metal complexes. To my knowledge no systematic research has been done for perylene anhydride acid derivative except some works of Tributsch [216] at early time of sensitization. It is worth noting that after two weeks the evaporation of organic electrolyte (bubble formation) was observed and became more pronounced after one month due to sealing problems.

4.4. The effect of the dye structure on the dark current

The chemical structure of the dyes has been revealed to play a crucial role in the recombination process. In this section a comparative study of current-voltage characteristics of DSSCs based on various dye type in the dark is presented. The current-voltage characteristics measured in the dark at 25 °C for different devices are shown in the Figure 4.14. For a realistic comparison, the dyes were classified in two groups according to the similarity in their structures. P4, P8 and P10 are in the first class (class I) and P1 and P9 the other second class (class II). It is well known [208] that the dipole moment on the TiO_2 surface hinders the dark current in the device in operating conditions. The dark current is known as the recombination of electron from TiO_2 CB with I_3^-. This charge recombination can be estimated by the magnitude and onset of dark current. Figure 4.14 shows that P4 and P9 give dark currents at low onset potential, whereas P10, P8 and P1 show dark current at successively high potential. This is in excellent agreement with the increased value of open-circuit photovoltage observed in this work and confirmed by other authors [208]. The reduction in dark current at certain potential can originate from (i) higher conduction band in the TiO_2 and less electron population in the CB or (ii) improve electronic blocking between I_3^- species in the electrolyte and the F:SnO_2/dye and TiO_2/dye interface [208]. To attribute this effect to the molecular origin, apart from the dipole effect, we can also notice that for category of dyes containing phenyl derivatives (class I) bonded to perylene core at the nitrogen atom, P8 and P10 give the least dark current. This behaviour is likely due to the fact that the bulky alkyl groups although being little far from TiO_2 surface repulse I_3^- species from TiO_2 and thus contribute to suppressing the dark current. The small dark current exhibited by P1 is likely due to its bipolar character with respect to its parent P9. In this category the dark

current onset shifts to low potential from P1→ P9-based cells and showing that the recombination is likely more pronounced in P9-based cells with respect to P1-based cell. Assuming that the dye is adsorbed in monolayer (as discussed in section 6.1), dye coverage alone cannot explain the observed dark current behaviour. The molecular origin of this effect can in part be explained by a contribution of the dye dipoles to a conduction band shift. The donors moieties polarize the dye to permanent dipoles, which is beneficial in DSSC by the suppression of dark current and the enhancement of open-circuit voltage.

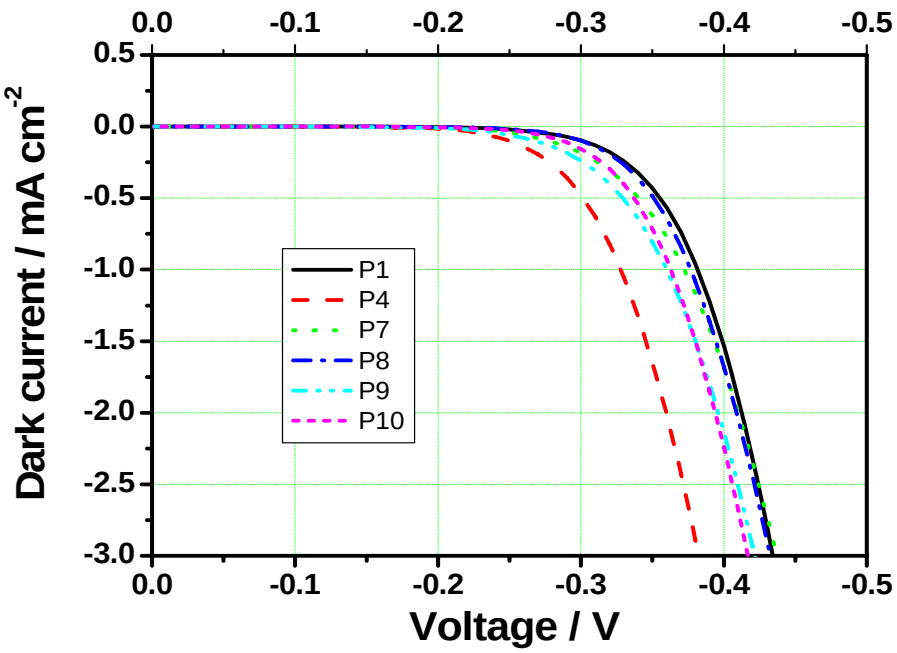

Figure 4.14. Current voltage measurements for devices performed in the dark. The thicknesses of TiO_2 were ~7 µm and the electrolyte consisted of 0.6 M 1-butyl-3-methylimidazolium iodide, 0.1 M I_2, 0.05 M $LiClO_4$ in 3-methoxy-propionitrile. The measurements were performed in the dark at 25°C.

4.5. Conclusion

In this work DSSC based on P1, P4, P7, P8, P9, P10 have been realised and characterised. The measurements were performed under standardized conditions and the results are summarised in Table 4.3. The devices based on small molecules exhibited lower performances than the device based on bipolar spiro compound. P1-based cell gives the best efficiency and shows the striking effect of spiro concept on the performance of perylene-based cells. The presence of the bulky group (alkyl-phenyl) bonded to perylene monoimide (P8 and P10) suppresses dye aggregation and increases electron injection and thereby efficiency when compared with P7. P4 containing an electron withdraw entity namely pentafluorophenyl moiety further depletes the electron density in the perylene core and thereby the electron injection capability. Electron donating groups turn out to reduce the dark current in device. The performance exhibited by P8-based cells was quite similar to results reported by Zafer et al. [157].

The effects of some additive in the electrolyte on the performance of DSSC have been investigated. The results showed that the presence of lithium ion turned out beneficial for DSSC. Short circuit current increased remarkably after adding lithium ion in the electrolyte. In contrast, addition of *t*BP was revealed to be disadvantageous despite the fact that it contributed to suppress dark current by open circuit voltage enhancement.

The use of Br^-/Br_3^- as redox couple enabled to increase considerably the open circuit voltage. However, the low photocurrent generated was likely due to the poor reactivity of the bromine at the interface electrolyte/platinum despite the fact the photocurrent was not limited by the diffusion of the electrolyte in TiO_2 network. Due to the fact that the bromine is a strong electrophile and tends to undergo bromination with unsaturated bonds especially in the presence of catalysis or light irradiation [209] the long-term stability will be limited. The long-term stability of the DSSC based on I^-/I_3^- was controlled after exposure P1-based cells on ambient atmosphere. The open circuit voltage was increasing while the short circuit current was decreasing with the time. These changes were mainly attributed to sealing problemes and for this reason the solid-state versions have been developed (Chapter 7).

Table 4.3. Summary of device performances extracted from IPCE and IV measurement as discussed in section 4.2 and 4.3.

Material	V_{oc} **[mV]**	J_{sc} **[mA/cm²]**	**FF**	V_m **[mV]**	J_m **[mA/cm²]**	**IPCE [%]**	**η [%]**	**Ref.**
P1	403	6.98	0.588	270	6.11	63.7	1.65	this work
P4	277	0.49	0.586	200	0.39	14	0.08	this work
P7	345	1.20	0.567	240	0.97	38	0.23	this work
P8	372	2.98	0.642	280	2.55	43.8	0.71	this work
	251	4.1	0.580	169	3.6	48	0.60	[157]
P9	325	0.53	0.635	250	0.44	14	0.11	this work
P10	363	3.34	0.633	260	2.95	37	0.77	this work
ID34	696	7.96	0.590	–	–	69	3.2	[208]
ID35	651	6.13	0.550	–	–	72	2.2	[208]

Chapter 5
CATION COORDINATION

In this chapter the influence of cation-coordination on the performance of devices based on P1 and P7 is investigated. The adsorption mode of P1 and P7 on TiO_2 surfaces is addressed. The sensitivity of potential ions-coordination sites of hybrid TiO_2/dye electrodes to some cations was studied and their impact in the performance of DSSCs based on P1 and P7 are discussed as well.

5.1. Adsorption behaviour of perylene derivatives onto TiO_2

Investigating the adsorption mode of perylene derivatives with acetic anhydride as anchor group on TiO_2 (101) surface should give information about cation complexation sites in the adsorbed dyes. For this reason, knowing how dyes are bonded onto TiO_2 (101) surface could enable to predict their stable form on the surface of TiO_2 (101) and to know how adsorbed dyes behave towards the electrolytic environment in the working cells.

5.1.1. Langmuir Isotherm: Formation of self-assembled monolayer

Performance of dye-sensitized solar cells is known to be governed by the chemical nature of dye especially that of its anchor group, and its adsorption mode onto the TiO_2 surface [227-229]. Furthermore the formation of a monolayer of an organic dye on the surface of TiO_2 is crucial for the functionality of DSSCs. The performance of DSSCs especially the electron injection efficiency was reported to be hindered by the formation of aggregates [67]. The role of aggregation on the sensitizing properties of dyes has been of great interest for the photographic industry [230,231]. Absorption properties and exciton dynamics in cyanine aggregates were revealed to be crucial parameters for efficient spectral sensitization of silver halides. Formation of H- and J-aggregates of merocyanine dyes has also been studied in a TiO_2 mesoporous network [232]. All these applications were motivated by the change of light absorption properties upon self-assembly of monomers. Furthermore, the investigation of electron and charge transfer in such system was reported to be a multi-step process characterized first by (i) energy transfer from monomers to the J-aggregates follow by (ii)

electron transfer reaction from J-aggregates to the TiO_2 conduction band [232]. However, side-reactions like electron transfer from J-aggregate to dye is not to be excluded. To the best of my knowledge up to now there is no clear explanation of this process, which contributes in decreasing the performance in DSSC. Lian and co-workers [233] studied the charge transfer process in N3-sensitized TiO_2. They found that the amplitude of the slower kinetic phase decreased from 16 % to less than 5 % in aged sample. Wenger [234] showed that the observed kinetic heterogeneity is due to the aggregation of dye molecules on the surface rather than to a dual excited state mechanism as previously suggested. Many metal free dyes namely merocyanine [139,232], indoline [235] were revealed to aggregate on TiO_2 with interesting performance in DSSCs. The formation of monolayer could be important for DSSCs since it could enable to scrutinize how the dye is configured onto the TiO_2 surface, thus enabling to predict ion-coordination sites in the TiO_2/dye hybrid system. To the best of my knowledge there is no study addressing how the adsorption mode of perylene acid anhydride can influence some parameters like V_{oc} and J_{sc} in working DSSCs.

In this study, the adsorption mode of perylene derivatives onto TiO_2 (101)(see section 6.2) surface is investigated. According to the preparation road of TiO_2 the faces of the crystalline particles are predominantly oriented along <101> direction [48]. Nanocrystalline TiO_2 films on glass were used as substrates. In the aim to avoid aggregation of our perylene derivative on the surface TiO_2, the film was soaked in diluted solution (~10^{-6}M) for a short time. The use of TiO_2 powder turned out to be disadvantageous during this experiment because it was difficult to extract all TiO_2 colloids from solution. Such colloids can introduce a significant experimental error due to their strong absorption in the UV. Owing to that, the nanocrystalline TiO_2 substrate was preferred, as the colloids were easily removed from the solution, without leaving traces of impurities.

The formation of self-assembled monolayers upon absorption from solution was verified by recording adsorption isotherms. The amount of substance adsorbed per TiO_2 surface area as a function of the equilibrium concentration of P7 dye is shown in Figure 5.1(a). The absorption isotherm saturates at higher concentrations showing no real tendency to form a double layer. When the ratio of equilibrium concentration to the amount of substance adsorbed is plotted against the equilibrium concentration, as shown in Figure 5.1(b), a linear relation is observed, indicating Langmuir-type adsorption behaviour. Analysing the adsorption isotherms according to the Langmuir formalism (see equations below) [122] yielded values for the adsorption equilibrium constant (K) and the surface concentration of adsorbate (Γ_{max}) at monolayer coverage for perylene dyes.

$$K = \frac{\vartheta}{(1 - \vartheta).C_{eq}} \qquad 5.1$$

$$\vartheta = \frac{n_{ads}}{n_o} = \frac{\Gamma}{\Gamma_{max}} \qquad 5.2$$

$$\frac{C_{eq}}{n_{ads}} = \frac{1}{n_o K} + \frac{1}{n_o} C_{eq} \qquad 5.3$$

ϑ = degree of surface coverage

C_{eq} = equilibrium concentration of the adsorbate in solution

n_{ads} = adsorbed amount of substance per unit surface area

n_0 = adsorbed amount of substance per unit surface area at monolayer coverage

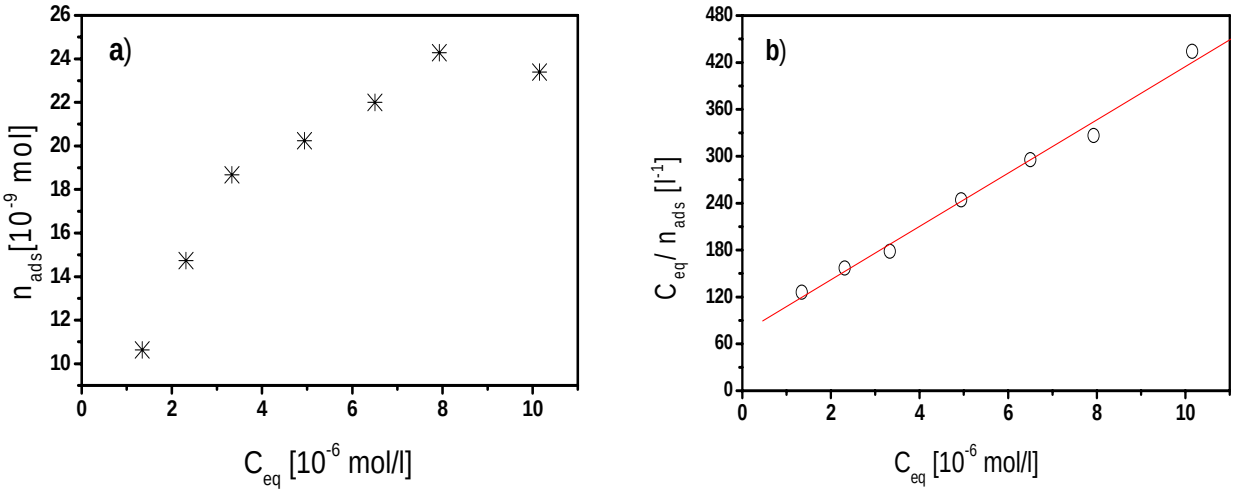

Figure 5.1 **a)** Adsorption isotherm for the adsorption of Perylene dicarboxylic acid-3,4-anhydrid (P7) on nanocrystalline TiO_2 substrates from NMP solutions. The amount of substance adsorbed and the equilibrium concentrations were derived from UV/VIS spectroscopy. **b)** The ratio of the equilibrium concentration to the amount of substance absorbed is plotted against the equilibrium concentration. Adsorption isotherms exhibiting Langmuir behaviour show linear dependencies in this plot.

In the following table the characteristics of different dyes are summarized.

Table 5.1. Adsorption equilibrium constant (K), surface concentration of adsorbate (Γ_{max}) at monolayer coverage for P1, P4, P7 and P8 dyes as extracted from Langmuir plots as shown in Figure 5.1.

Adsorbates	**P1**	**P4**	**P7**	**P8**
K [L/mol]	$4.98*10^5$	$3.32*10^5$	$3.5*10^5$	$3.7*10^5$
Γ_{max} [μmol/m^2]	43.35	77.3	66.82	80.9

From Figure 5.1(a) it can be seen that P7 forms a monolayer on the surface. The tendency of dyes to aggregate on nanoporous TiO_2 is not observed in the time scale of experiment. The binding constants of the dyes do not show obvious deviation (Table 5.1). All values are in the same order of magnitude. Only a difference is noted for the small amount of P1 dye adsorbed per unit surface area at monolayer coverage. It can be due to the steric hindrance of the bulky diphenylamino-spirobifluorene moiety.

5.1.2. Characterisation of the adsorbate–surface binding configuration

Different experimental techniques have been applied to investigate the nature of the binding mode of carboxylic acids to the titanium oxide surface. IR spectroscopy has been performed to study the adsorption of Ru-complexes [237-239]. These molecules show an absorption band at around 1700 cm^{-1} arising from the C=O stretch mode of the un-dissociated carboxylic group. This band disappears when the molecule is linked to nano-structured anatase, rutile or amorphous TiO_2, which has been interpreted as bi-dentate bridge coordination [236-238]. Also formic acid [240-242], which is the anchor group of some chromophores intensively investigated (benzoic acid [243] and bi-isonicotic acid [244]), has been found to adsorb on rutile (110) under dissociation of a proton in a bidentate bridging coordination.

The (101) crystal face is also the most frequent surface in the nano-structured film used in this work. Vittadini et al. [245] studied the adsorption of formic acid on the anatase (101) surface theoretically under consideration of different configurations for both molecular and dissociative adsorption. They found the bi-dentate bridging configuration to be the most stable dissociative adsorption mode for a clean surface. The energetically favoured un-

dissociative configuration is mono-dentate binding through the carbonyl group accompanied by a hydrogen bond between the proton of the anchor group and a surface oxygen atom [245].

Even though more attention is focussed on the adsorption mode of carboxylic acid, some attempt to investigate the adsorption mode of acetic anhydride on metal oxide was done. Puttock and Rochester [246] have demonstrated that the adsorption of acetic anhydride on the surface of anhydrous Vanadyl Pyrophosphate $(VO)_2P_2O_7$ is dissociative. It has been suggested that the dissociation of acetic anhydride would lead to CH_3CO^+ and $CH_3CO_2^-$ ions [247]. However, no infrared band which could be ascribed to discrete CH_3CO^+ ions was observed on the $(VO)_2P_2O_7$ surface [246]. Puttock and Rochester [246] suggested that CH_3CO^+ ions react with surface oxide ions to form a second type of adsorbed acetate (with vibration band at 1655 cm^{-2}), which may be linked to surface sites in a unidentate configuration. Botani et al. [248] have also demonstrated that acetic anhydride adsorbs dissociatively on the surface of zeolites. Ashima et al. [249] studied the adsorption of acetic anhydride (Ac_2O) on a $TiO_2(110)$ surface. They found by the mean of high resolution electron energy loss spectrometry (HREELS) and low energy electron diffractometry (LEED) that the adsorption of Ac_2O is dissociative. In dissociative adsorption, especially on a $TiO_2(110)$ surface, Ac_2O may react with bridging oxygen O_B to convert to two acetate ions ($2CH_3CO_2^-$) [249] as shown in the scheme 5.1, and CH_3CO^+ neutralises the negative O_B atom of $TiO_2(110)$ type II oxide * surface.

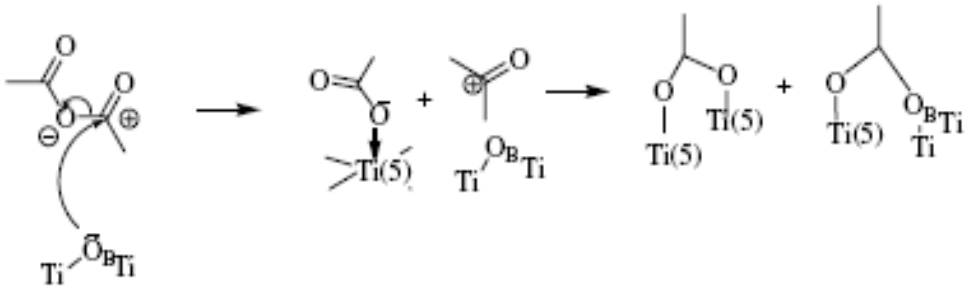

Scheme 5.1 Dissociative adsorption of acetic anhydride on $TiO_2(110)$ surface**[249]**.

However, contrary to Ref. [246], Ashima et al. [249] suggested that $CH_3CO_2^-$ should be adsorbed onto 5-fold coordinated Ti site as an acetate in a bridging form. The other part CH_3CO^+ interacts with the oxygen bridging site O_B. The C=O in adsorbed CH_3CO^+ should

* $TiO_2(110)$ is a type II oxide that has a surface negative charge arising from O_B according to Noguera's classification[250].

also interact with one 5-fold coordinated Ti to form a bridging structure since HREELS showed no evidence for the presence of monodentate acetate species [249]. It was also suggested that this heterolytic adsorption neutralizing the negative O_B is the necessary condition for a stable adsorption of Ac_2O on the TiO_2 (110) surface [249].

Figure 5.2 shows the IR spectra of Perylene dicarboxylic acid-3,4-anhydride (P7) powder in the range of 1000 tom 2000 cm^{-1} and the difference spectrum of P7 sensitized and unsensitized anatase TiO_2. The samples for the latter spectrum have been prepared analogue to the samples for the Langmuir isotherm measurements. To investigate the adsorption mode P7 was selected because it was the ideal adsorbate presenting less infrared sensitive sites especially carbonyl of imide functions, which could interfere with carbonyl of carboxylate. The unsensitized reference sample has been exposed to pure solvent while dye coating the other sample.

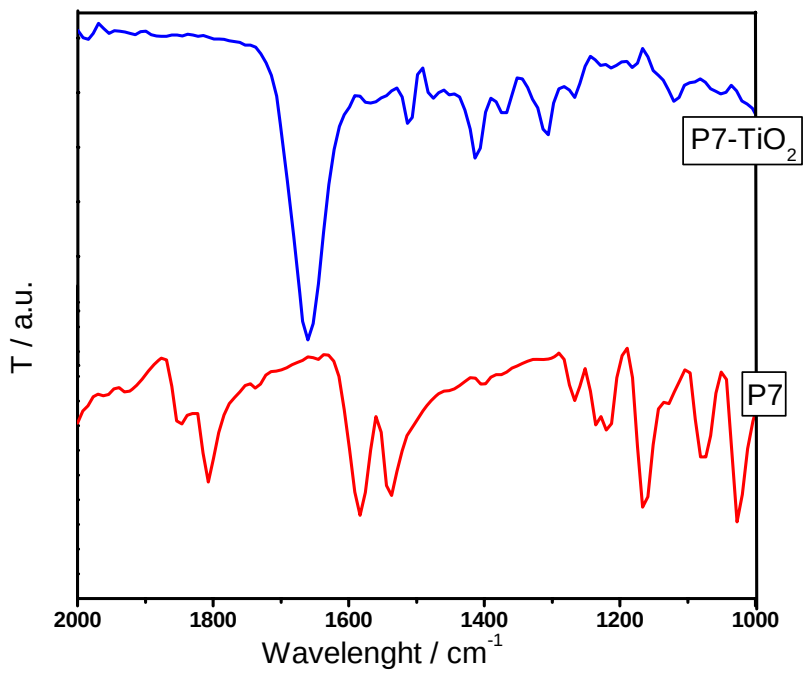

Figure 5.2. FT-IR spectra of Perylene dicarboxylic acid-3,4-anhydrid (P7) and the difference spectrum of P7 sensitized and unsensitized anatase (P7-TiO_2)

Pure perylene shows bands up to 1583 cm^{-1} [251,252], which arise mainly from in-plane vibrational modes [253]. The most obvious difference between the spectra of P7 and P7-TiO_2 is the absence of bands corresponding to the acid anhydride group at 1807-1845 cm^{-1} in the spectrum of P7-TiO_2. The strong signal at 1027 cm^{-1} is attributed to υ (C-O) of the acid anhydride ring of P7. Once adsorbed onto TiO_2 surface it disappears. This IR spectrum suggests that there is an opening of the acid anhydride ring on the surface of TiO_2. It was reported that the C=O stretching mode of the carboxylic group [236-239] appears at 1680 cm^{-1}. A band at 1655 cm^{-1} in the spectrum of acetic anhydride adsorbed on $(VO)_2P_2O_7$ has been ascribed to the carbonyl stretching vibrations of carbonyl group in undissociated acetic anhydride molecules bound to a Lewis-acid site in the $(VO)_2P_2O_7$ surface [246]. However, the behaviour of this band differed significantly from the behaviour of the band at 1680 cm^{-1} ascribed to undissociated adsorbed acetic acid and suggests that the band at 1655 cm^{-1} was the product of dissociative adsorption [246]. It was concluded that the band at 1655 cm^{-1} corresponds to the acetate, which may be linked to the surface site in a unidentate configuration. By analogy the band at 1660 cm^{-1} (Fig. 5.2) could be ascribed to the carbonyl group of the opened (dissociated) acid anhydride group of P7 on the surface of TiO_2(101). According to FT-IR spectra, the adsorption mode of P7 on TiO_2 (101) is likely monodentate as shown in Scheme 5.2(A). The configuration B and C can be excluded since the IR spectrum shows a band at 1660 cm^{-1}, characteristic of C=O. The latter would be absent in configurations (B) and (C) of Scheme 5.2. It is worth noting that flat anatase (101) terraces exhibit a sawtooth-like surface structure. It is characterized by the presence of acidic-basic pairs of coordinative unsaturated ions, that is, 5-fold coordinated Ti^{4+} ions and 2-fold-coordinated bridging oxygen O^{2-} [254]. Because of this lower coordination, Ti and O atoms are more active and bind more strongly with adsorbates. However, the bidentated bridging form as suggested by Ref. [249] is not likely observed with P7 because of the fact that during the opening of acid anhydride ring, both $–COO^-$ and $–CO^+$ remain bonded to the perylene core and are, accordingly, less free to move if we consider that the adsorption of P7 on TiO_2 (101) occurs dissociatively.

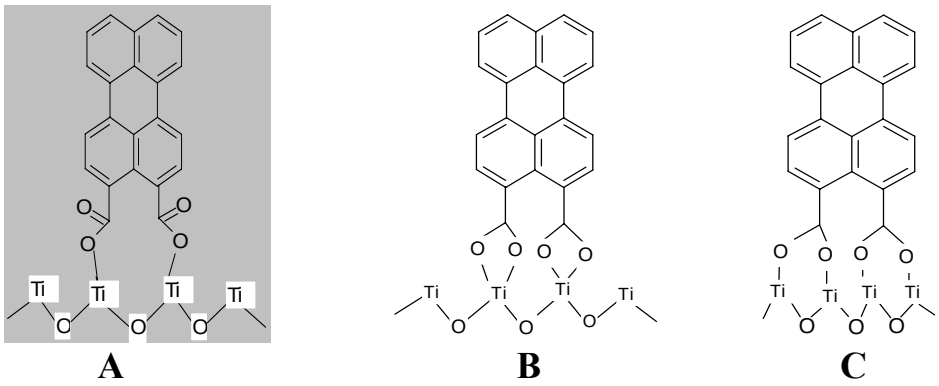

Scheme 5.2. Possible binding configurations of Perylene dicarboxylic acid-3,4-anhydrid (P7) on TiO_2 surface. **A**-Unidentate; **B**- Bidentate chelating; **C**-Bridging bidentate. The most likely binding mode is in the marked box.

5.2. Experimental evidence for lithium coordination

Since FT-IR spectra established that the adsorption of the P7 is monodentate, which was concluded from the presence of free carbonyl in the P7-TiO_2 hybrid system, we can now scrutinize the behaviour of C=O groups towards the ionic environment in a prepared cell and its impact on the performance of the cells.

For the investigation of cation-P7-TiO_2 complexation, sensitized P7-TiO_2 substrate was immersed into the MI (M=Li) solution (0.5M, in dry acetonitrile) for 4 hours. After removing the sample from solution it was directly dried in argon flow atmosphere and was ready for measurements.

5.2.1. Characterisation of Li^+ ion coordination

FT-IR spectroscopy

The lithium ion coordination with C=O of the dye-loaded film was characterised by FTIR measurements. The IR spectra of Lithium-complexed dye-loaded film are shown in Figure 5.3.

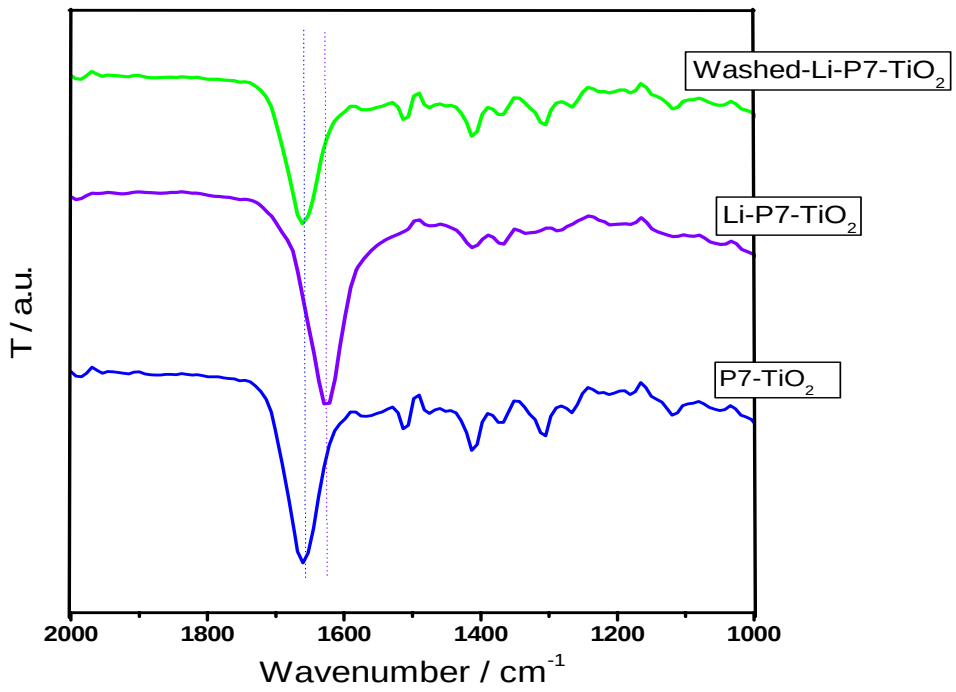

Figure 5.3. The FT-IR spectra of P7-loaded TiO_2 film (P7-TiO_2) (blue), Li-coordinated P7-loaded TiO_2 film (Li-P7- TiO_2) (violet) and Li-coordinated P7-loaded TiO_2 film after washing (green). A bare TiO_2 film previously soaked in acetonitrile was used as background. The blue and violet dotted lines show the position of the bands corresponding to C=O group in untreated and lithium treated dye loaded TiO_2 films, respectively.

From Figure 5.3, it can be observed that the vibration band υ(C=O) 1660 cm^{-1} is shifted to lower energy (1629 cm^{-1}). The shift of the vibrational frequency ($\Delta\upsilon \approx 31$ cm^{-1}) could be due to coordination of lithium ions with the C=O group (-C=O ··· Li^+). After the film is rinsed with pure acetonitrile, the original peaks are restored. This change on IR spectra suggests that lithium ions in solution react with the dye-loaded film. This coordination likely modifies the force constant in C=O bond and shift its vibrational frequency to low frequency.
To extend this investigation and to know how a compound with many coordination sites could behave, *N*-[2′,7′-bis-(*N,N*-diphenylamino)-9,9′-spirobifluoren-2-yl]-1,7-bis-(4-*t*-butylphenoxy)-perylene-3,4-dicarboxylic acid anhydride-9,10-imide (P1) was tested. The samples were prepared similarly to that of precedent experiment. According to the adsorption mode of P7, which give rise to two potential coordination sites (C=O), one could estimate the coordination site number in P1-loaded TiO_2 film to be 3 times higher than in P7 adsorbed

onto TiO_2. Scheme 5.3 shows potential lithium ion coordination sites in the P1-loaded TiO_2. Figure 5.4 shows the IR spectra of P1, a P1-loaded TiO_2 film and a Li-treated P1-loaded TiO_2 film. From Figure 5.4 the peaks at around 1770-1738 cm^{-1} and 1711-1672 are assigned to the symmetric and asymmetric vibration of C=O of acid anhydride and that of imide in P1, respectively [158,255]. The peaks due to acid anhydride disappear after adsorption of the dye on the TiO_2 electrode, while those due to imide remain relative intact. The strong signal at 1014 cm^{-1} is attributed to υ (C-O) of acid anhydride ring in P1. Once adsorbed onto TiO_2 surface it disappears. This implies that there is an opening of the acid anhydride ring on the surface of TiO_2. Besides these, the peak at 1109 cm^{-1} is assigned to υ(Ph-O) stretch of phenoxyl group. It remains quite intact after P1 is adsorbed onto TiO_2 surface, since it doesn't participate in the adsorption process. However, from the spectrum of adsorbed P1 onto TiO_2 (Fig. 5.4. spectrum P1-TiO_2), it is not possible to differentiate the band arising from C=O of the anchor group to that of the imide function. In comparison to IR spectra of compound P7 (Figure 5.3), one can suggest that there is a superposition of vibrational frequencies at 1652 cm^{-1}. If one takes into account the fact that the υ(C=O) of P7-loaded TiO_2 film is observed at 1655 cm^{-1} and that C=O is not implicated in the adsorption process, one could suggest that the sharp band at 1652 cm^{-1} corresponds to the C=O resulting from the opening of the anhydride ring of P1 on the surface of TiO_2. On the other hand, considering that the adsorption mode of P7 onto TiO_2 is monodentate could enable to suggest that the sharp band at 1652 cm^{-1} is that of C=O of anchor group after the opening of the ring in P1.

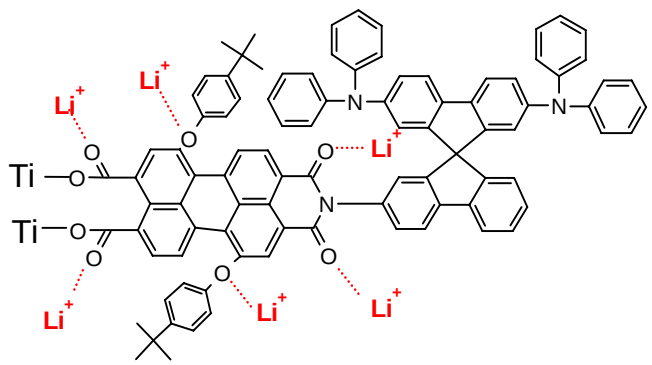

Scheme 5.3. Li-coordination sites in the P1-loaded TiO_2 film.

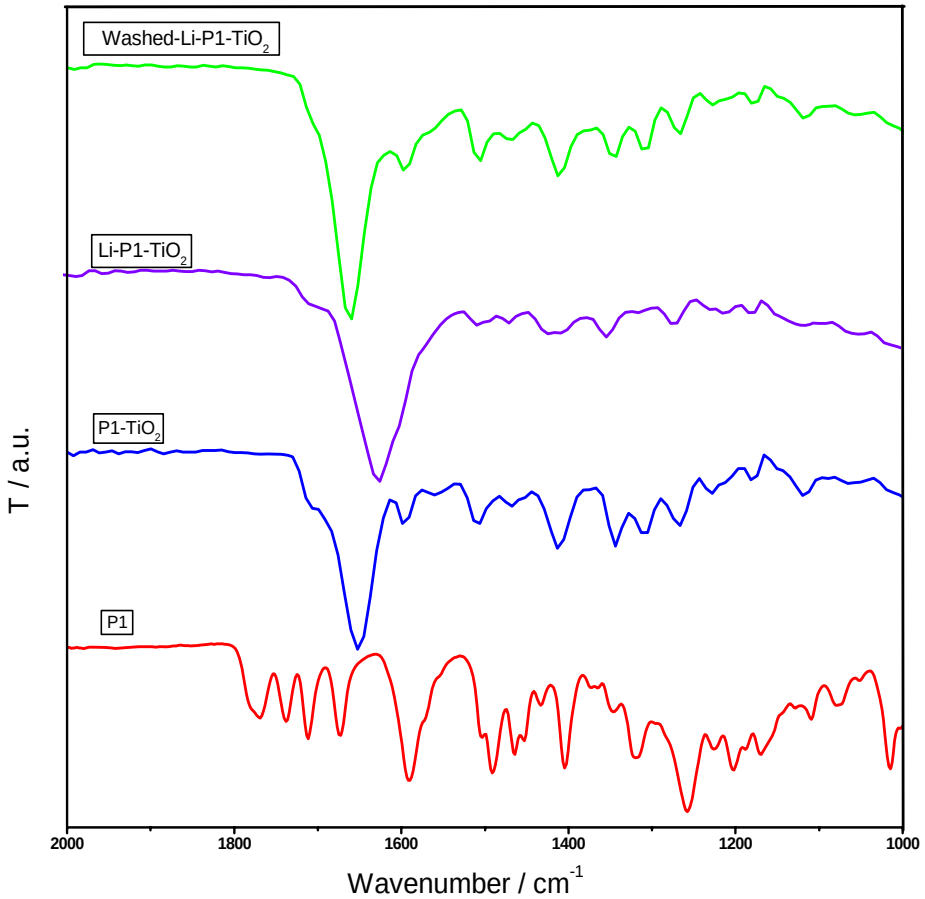

Figure 5.4. The FTIR spectrum of P1 dye (P1), P1-loaded TiO_2 film (P1-TiO_2), Li-coordinated P1-loaded TiO_2 film (Li-P1-TiO_2) and Li-coordinated P1-loaded TiO_2 after rinsing with acetonitrile (washed-Li-P1-TiO_2). A bare TiO_2 was used as background.

From Figure 5.4 it can be observed that after immersing the sensitized electrode into a solution containing lithium ions, a shift to lower frequency of the band corresponding to free C=O spectrum (spectrum Li-P1-TiO_2) is observed, which means that adsorbed dye intereacts chemically with cation species (Scheme 5.3). This behaviour of P1-TiO_2 electrode after lithium ion treatment is almost similar to that observed in P7-TiO_2 electrode. In the region of the symmetric and asymmetric vibration of C=O of imide at 1652 cm^{-1}, there is a shift to lower energy (1621 cm^{-1}) due to coordination with lithium ions (-C=O··· Li^+). The interaction between Li^+ and the carbonyl of some substituted acetophenones was already investigated [256]. It was found that the interaction between Li^+ and carbonyl base is predominantly an ion-dipole attraction and the ion-induced dipole attraction as well rather than a covalent

interaction [256]. However, ion-dipole attractions turned out to shift the C=O stretching frequency. Kappers et al. [257] have investigated the interaction between adsorbed CO and potassium ions in the K-LTL zeolite. They found that the CO stretching frequency is shifted and they explained that by ion-dipole interaction between the adsorbed CO and the potassium ions in the zeolite channels [257]. Direct interaction of the oxygen of linear-CO with an alkali cation increases the adsorption energy and decreases the stretching frequency [257]. For these reasons, by analogy, I think that after copious washing of the lithium treated electrode with dry acetonitrile, the ion-dipole interaction is screened and original IR peaks of free C=O are restored.

Furthermore the band attributed to phenoxy (Ph-O) at 1109 cm^{-1} disappears. This disappearance of the peak at 1109 cm^{-1} from υ(Ph-O) is likely due to lithium ions coordination (Ph-O··· Li^{+}). After the film is rinsed with pure acetonitrile, the original peaks are restored. All those observations suggest that the adsorbed dye molecules interact chemically with lithium ions contained in electrolyte solution. A similar observation was reported by Kuang et al. [92,258]. They used a ruthenium complex coded K51 containing triethylene oxide methyl ether side chain. After immersing the electrode in a solution of LiI the solution, the 1106 cm^{-1} peak attributed to υ(C-O) stretch was diminished by 50% and shifted to lower energy 1078 cm^{-1}. They explained these changes by the coordination of C-O with lithium.

Since we have the proof that lithium ions, as a Lewis acid react with some coordination site of the dyes used in this study, one can now scrutinize the effect of these ion-dipole interactions on the UV-Vis absorption spectrum of adsorbed P1 and P7.

UV-Vis absorption spectroscopy

Figure 5.5 shows the UV-Vis absorption spectra of P1-TiO_2 and P7-TiO_2 before and after lithium ion treatment. From spectrum P1-TiO_2 in Figure 5.5a, the broad band located in the region of 450 -575 nm with its maximum at 520 nm is attributed to π-π* transition in perylene moiety and the broad band 275-400 nm is that of diphenylamine moieties. After treating of P1-loaded electrode with lithium ions the obtained spectrum is denoted Li-P1-TiO_2. One can see that the peak of original P1-loaded absorption (520 nm) is shifted to lower wavelength (515 nm). The blue shift of the broad band at 520 nm is more noticeable with respect to that of diphenylamine moieties. From Figure 5.5b the band corresponding to

perylene at 434 nm is also shifted to lower energy (424 nm) after treating the P7-TiO_2 with lithium containing solution. The blue shift of the maximum absorption peak could result from Li^+ coordination to carbonyl oxygen of dye-loaded TiO_2. The complexation of Li^+ ions by the O-atom of the phenoxy group, and the carbonyl of anchor group and imide group is the main cause of this effect because it modifies the electronic properties of the perylene π-system. The shift of absorption band of the Li-P1-TiO_2 electrode ($\Delta\lambda$~5 nm) is smaller than the Li-P7-TiO_2 electrode ($\Delta\lambda$~10nm). In the P7-TiO_2 electrode the lithium ions are coordinated by C=O of the anchor group. Li^+ ions (Lewis acid), which have electron-withdrawing ability, in principle will push down the energy level of the lowest unoccupied molecular orbital (LUMO) of dye-loaded TiO_2, and the gap to the highest occupied molecular orbital (HOMO) will decrease, which will lead to a red shift of adsorption spectrum [259,260]. The opposite behaviour is observed in this study. The ion-dipole interaction increases the gap between the HOMO and LUMO, which can be seen from the blue shift of the absorption peak. After proton exchange by lithium in N3 Wang et al. [259] found that the maximum absorption peak at ~530 nm (corresponding to Metal to Ligand Charge Transfer) of N3-loaded films is blue shifted by ~20 nm. They attributed this shift to the increase of gap between the LUMO and HOMO, which was due to lower the electron–withdrawing ability of lithium than of proton. It was also found that ex-situ proton exchange in N3 with tetra-butyl ammonium ion (TBA) leads to a blue shift of the absorption peak [259]. At this stage of my investigation, one can suggest that the blue shift observed in Figure 5.5 results from the in-situ lithium coordination.

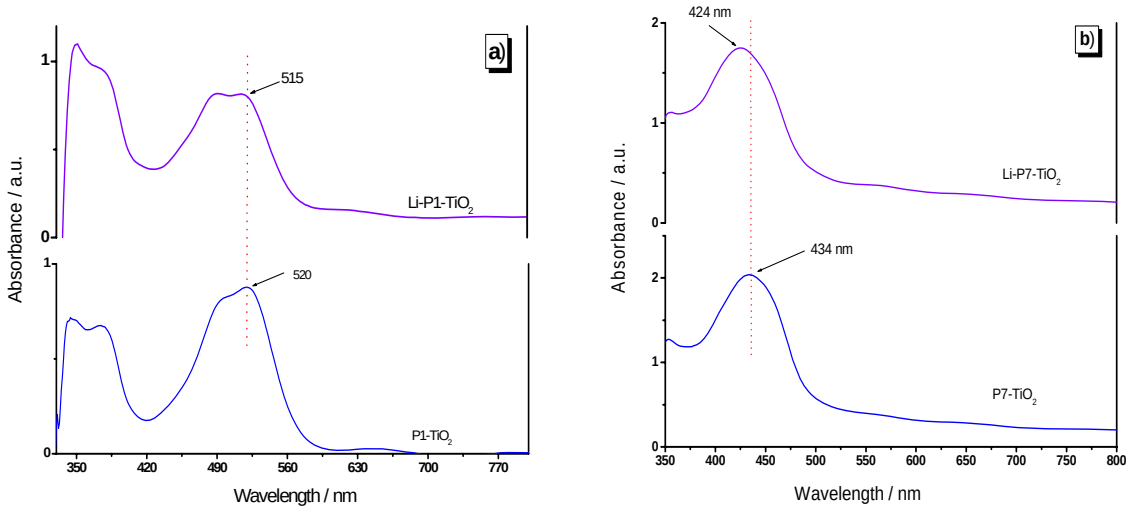

Figure 5.5. Influence of lithium ions coordination on the UV-Vis absorption spectra of sensitized TiO_2 film: **a)** UV-Vis absorption spectra of P1-loaded TiO_2 (curve P1-TiO_2) and Li-coordinated P1-loaded TiO_2 film (Li-P1-TiO_2); **b)** absorption spectra of P7-loaded TiO_2 (curve P7-TiO_2) and Li-coordinated P7-loaded TiO_2 film (Li-P7-TiO_2).

5.3. In situ lithium ions coordination in DSSCs

In this section the influence of the coordination site on the performance of DSSCs based on P1 and P7 will be discussed. P1 and P7 are used as sensitizer in this work because the former presents more metal ions coordination sites than the latter. Both have the same adsorption mode on the surface of TiO_2, which could predict the same behaviour of anchored groups towards cations contained in the electrolyte. To carry out this investigation solutions with different lithium concentrations were used. The electrolyte composition is described as follows: Electrolyte **A** contains 0.6 M 1-butyl-3-methylimidazolium iodide, 0.1 M I_2 in 3-methoxypropionitrile solvent. Electrolyte **B**, **C** and **D** contain 0.05, 0.125, and 0.25 M $LiClO_4$, respectively in electrolyte **A**. The current voltage characteristics of the devices was measured under standard conditions (AM1.5 100mW cm^{-2} at 25°C)

5.3.1. Impact of lithium ion coordination on the performance of DSSCs

The influence of lithium ions coordination sites on the performances of DSSCs based on P1 and P7 is investigated and their J-V characteristics is measured under standard

conditions. It is known that the dipole moment of organic molecule [122,159,173,261] on the surface of TiO_2 and the nature of the electrolyte cations [262-264] change the conduction band energy level considerably. Since in this section we aim to scrutinize the TiO_2 CB shifting through the generated V_{oc} of each device, the effect of the dipole moment of each dye on TiO_2 has to be avoided. The J-V characteristics of modified devices are shown in Figure 5.6.

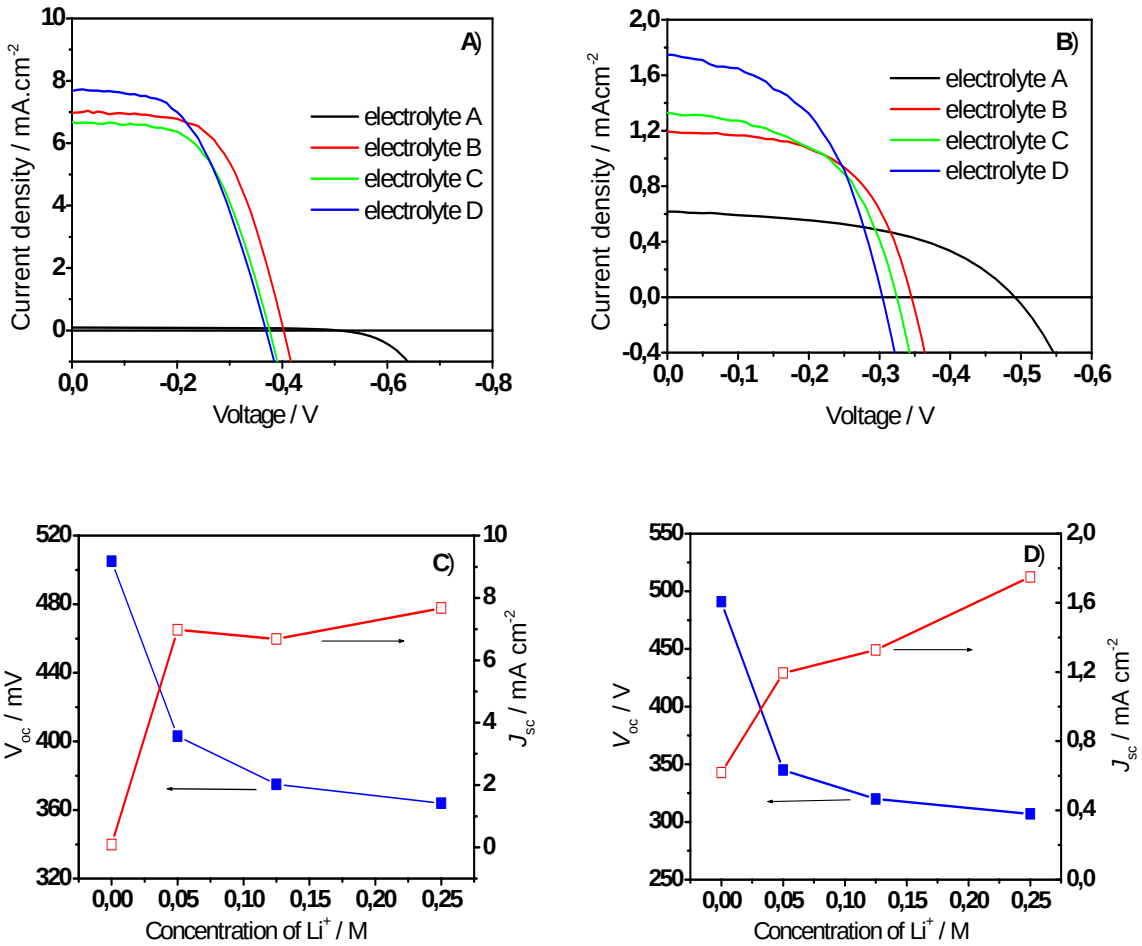

Figure 5.6. Current-voltage characteristics of devices based on P1 dye **(A)** and P7 dye **(B)** at different concentrations of lithium ions; the variations in J_{sc} and V_{oc} of P1-based cells **(C)**, P7-based cells **(D)** with electrolytes containing different Li^+ concentrations in mol/L.

Table 5.2. Photovoltaic parameters of DSSCs based on P1 and P7 dyes with different electrolytes A, B (A + 0.05 M Li^+), C (A + 0.125 M Li^+) and D (A + 0.25 M Li^+) under AM 1.5 sunlight (100 $mWcm^{-2}$).

Sensitizer	Electrolyte	V_{oc}/mV	J_{sc}/$mAcm^{-2}$	FF	V_{max}/mV	J_{max}/$mAcm^{-2}$	IPCE/ %	η/ %
P1	A	505	0.09	0.587	390	0.07	14.5	0.03
	B	403	6.98	0.588	270	6.11	63.7	1.65
	C	375	6.68	0.566	260	5.18	53.7	1.42
	D	369	7.68	0.521	240	6.17	63.3	1.48
P7	A	491	0.62	0.489	330	0.450	22.1	0.15
	B	345	1.20	0.567	240	0.974	38	0.23
	C	324	1.33	0.529	230	0.990	34.7	0.23
	D	304	1.75	0.498	200	0.264	43.7	0.27

From Figure 5.6, one can see that the device characteristics depend on the Li^+ ion concentration. The parameters of modified cells are summarized in Table 5.2. For cells incorporating P7, J_{sc} increases gradually from 0.62 mA cm^{-2} to 1.20, 1.33 and 1.75 mA cm^{-2} when the concentration of Li^+ ions is changed from 0 M to 0.05 M, 0.125 M and 0.25 M, respectively. However, this is counterbalanced by a decrease in V_{oc} from 491, 345, 324 and 304 mV, respectively.

Beside P7-based cells, P1-based cells show the same tendency. J_{sc} increases strikingly from 0.09 to 6.98 mA cm^{-2} when the Li^+ ion concentration is changed in the device from 0 to 0.05 M after what it increases slightly until 7.68 mA cm^{-2} with a Li^+ ion concentration of 0.25 M. In contrast, V_{oc} decreases from 505 to 403, 375 and 369 mV when the Li^+ ion concentration is increased from 0 M to 0.05 M, 0.125 M and 0.25 M, respectively. The increase in J_{sc} with Li^+ ions concentration is likely due to a high screen effect generated by lithium to the photogenerated electron-hole pair (oxidized dye and injected electron).

Kelly et al. attributed such cation dependence electron injection yield to a thermodynamic effect, in which cation adsorption induce a positive shift of TiO_2 acceptor states, resulting in more favourable energetics for electron injection [146]. Many authors have done the same remark. By increasing lithium concentration in electrolyte Kuang et al.

[92,258] observed an increase in J_{sc} followed by a decrease in V_{oc}. They attributed the change in J_{sc} and V_{oc} to the lowering of the TiO_2 conduction band level in the presence of Li^+ ions.

However, surface adsorption of Li^+ ions on TiO_2 has been revealed to reduce the recombination of injected electrons and the mediator [92]. In fact, the electron injected into the TiO_2 network and the negative charges of the mediator are screened effectively over a diameter of the ionic cloud due to Li^+ ions. This could explain the increase of J_{sc} with Li^+ ion concentration.

5.3.2. Influence on Li-coordination on the open-circuit photovoltage drop

In the aim to investigate the influence of the coordination site of dye molecules on the performance of DSSCs, the potential drop* for both P1 and P7-based cells at different lithium concentration were measured. P1 and P7-based cells show a drop in V_{oc} when the lithium concentration increases (Fig.5.6c,d). Figure 5.7 shows the difference in V_{oc} plotted against lithium-ion concentration for devices containing P1 and P7.

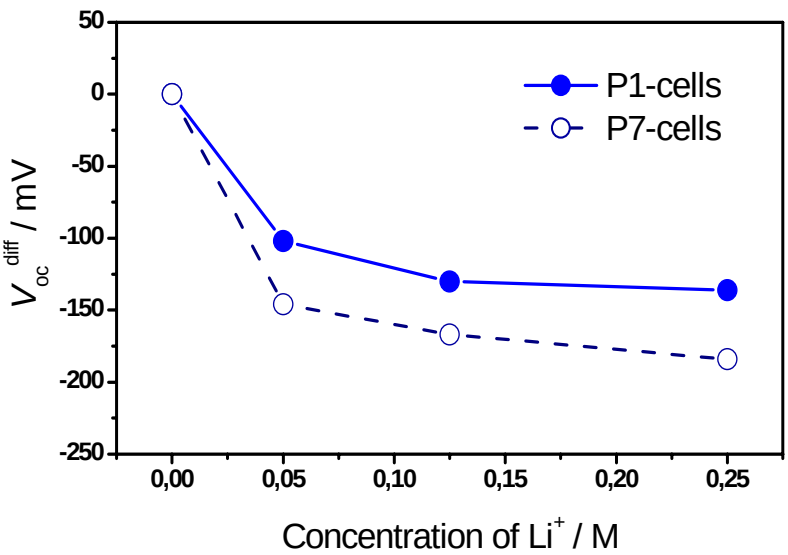

Figure 5.7. The potential drop in P1 and P7-based cells at different Li^+ concentration in M.*

∗ The potential difference has been calculated by making the difference between the V_{oc} value at each $[Li^+]$ and V_{oc} obtained with electrolyte A considered as the electrolyte without lithium (where $[Li^+]=0$).

$$V_{oc}^{diff} = V_{oc}\left(\left[M^+\right]=0\right) - V_{oc}\left(\left[M^+\right]=a\right)$$

From Figure 5.7, it can be seen that P1 and P7-based cells show the same behaviour. V_{oc} drops from 0, -146, -0.167 to -0.184 mV in P7-based cells and from 0, -0.102, -0.130 to -0.136 mV in P1-based cells when [Li^+] is changed from 0, 0.05, 0.125 to 0.25 M, respectively. Globally, V_{oc} drops with lithium ion concentration and exhibits a plateau at high lithium ion concentration. However, the V_{oc} drop in P7-based cells is higher than that of P1-based cells. This strongly suggests that the lithium in P7-based cell is free to access the TiO_2 surface. Hence, its adsorption onto TiO_2 induces a positive shift of the TiO_2 CB. In P1-based cells a real difference is observed. A kind of in-situ Li complexation is observed in device based on P1with respect to devices based on P7. In P1 based cells, a high concentration of ions is held by the dye molecules and thus causes an increasingly strong "*charge screening*" effect [258]. Moreover, at [Li^+]=0.25M a considerable drop of Voc is observed because the coordinating capacity of the P1 sensitizer has been exceeded and Li^+ remains free to adsorb to the TiO_2 surface lowering the conduction-band level and hence the V_{oc}.

Kuang et al. [92] have investigated the consequence of surface adsorption of Li ions on the charge recombination rate and the position of the quasi-Fermi level. By using a transient-voltage-decay technique, they found that in the presence of low concentrations of Li^+ no real impact is observed but at [Li^+]=250mM the recombination lifetime was 13 ms for the dye K60 containing lithium-coordination sites. Comparing this finding to that obtained with Z907Na (non-ion-coordinating sensitizer) [258] where in the presence of only 50 mM Li ions the transient lifetime is changed from 5.5 ms to 10.4 ms), they concluded that the complexation by an ion-coordinating sensitizer influences the recombination process. However, at high concentrations of Li ions the charge recombination process is slower leading to high J_{sc}. This suggests that in P1 the charge recombination rate is reduced [92] and the open-circuit voltage is increased since the coordinated ions are prevented from adsorbing to the TiO_2 surface and the potential is positively shifted. According to these observations, it is confirmed that, the O-atom of phenoxy group, the carbonyl groups of anchor and amide groups are likely to coordinate to Li^+ present in the electrolyte, preventing Li^+ from contacting TiO_2. This explains the fact that the decrease in V_{oc} is smaller for P1-based cells with respect to P7-based cells. Li^+ scavenging by coordination to P1 dye is corroborated by the FTIR spectroscopy data shown above.

5.4. Further investigation of others cations

The experiment has been extended to other ions with different size like Na^+, K^+ and TBA^+. The electrodes were prepared as described above and were immersed in the different electrolyte types.

5.4.1. FTIR spectroscopy

FTIR spectra of modified electrodes based on P1 dye were recorded and the results are shown in the Figure 5.8. From Figure 5.8, it can be seen that in the region of asymmetric and symmetric vibration of -C=O of imide, the peaks are shifted to lower energies. The peak at 1652 cm^{-1} is shifted to 1610 cm^{-1} after treating the electrode with Na^+ ions and Ka^+ ions respectively whereas for electrodes treated with TBA^+ the peak corresponding to C=O is not intense enough.

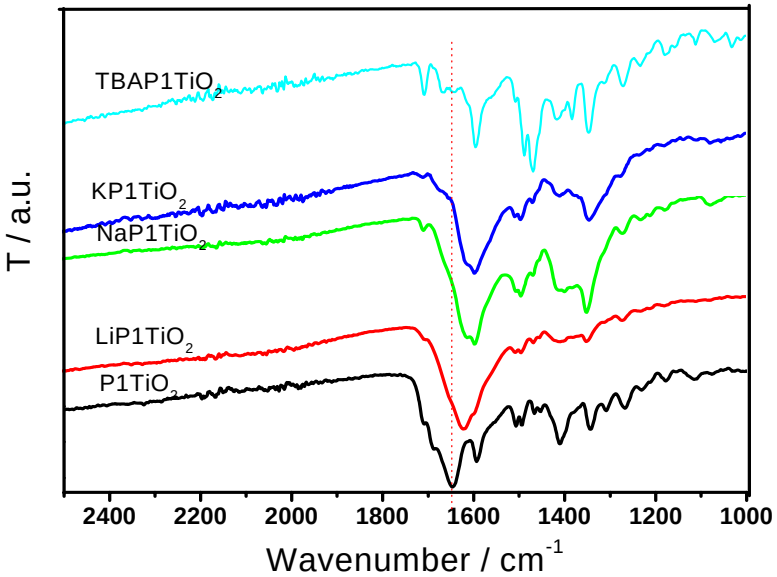

Figure 5.8. The FTIR spectra of P1-loaded TiO_2 film ($P1TiO_2$)(black-line), Li-coordinated P1-loaded TiO_2 films ($LiP1TiO_2$)(red-line), Na-coordinated P1-loaded TiO_2 film ($NaP1TiO_2$)(green-line), K-coordinated P1-loaded TiO_2 film ($KP1TiO_2$)(blue-line) and TBA-coordinated P1-loaded TiO_2 film ($TBAP1TiO_2$)(cyan-line). A bare TiO_2 was used as background.

From Figure 5.8 a strong shift towards lower energy with respect to the original peak is observed. It leads to the confirmation that the smaller cation size, the stronger its coordination strength and the higher is the vibration energy. This observation enables thus to establish the following order: K = Na > Li > TBA.

5.4.2. UV-Vis absorption spectroscopy

The UV-Vis absorption behaviour of cation-complexed dye-loaded TiO_2 was also investigated and the results are shown in Figure 5.9. As Figure 5.9 depicts, after complexation of cations by dye-loaded TiO_2, a slight shift of the original P1-loaded absorption peak is observed. The blue shift of the broad band located in the region of 450-575 nm corresponding to perylene moiety is more pronounced than the diphenylamine band (broad band 275-400 nm). The peak at 520 nm shifts to 515, 510 and 510 nm once treated with Li^+, Na^+ and K^+ ions respectively. In contrast, a relatively unchanged peak (to 521nm) is observed after treating the photoelectrode with TBA^+ containing solution. This could suggest that the bulky TBA^+ can hardly coordinate to the O-atom of the complexation site in P1. The blue shift of the maximum absorption peak increased in the order: K > Na > Li > TBA = cation free. Such behaviour can be explained by the affinity of complexation site with cations. The cations (Lewis acid), which have electron-withdrawing ability, increase the energy level of the lowest unoccupied molecular orbital (LUMO) of P1-loaded TiO_2 and hence the gap between the highest occupied molecular orbital (HOMO), thus resulting in a blue shift of the absorption peak. The complexation of cations by the O-atom of phenoxy, and carbonyl of the anchor and the imide group is probably the main cause of this effect because it modifies the electronic structure of the perylene π-system, though the peak shift was not very significant. Therefore, the blue shift observation supports the in-situ complexation of P1-loaded TiO_2 with the used cations.

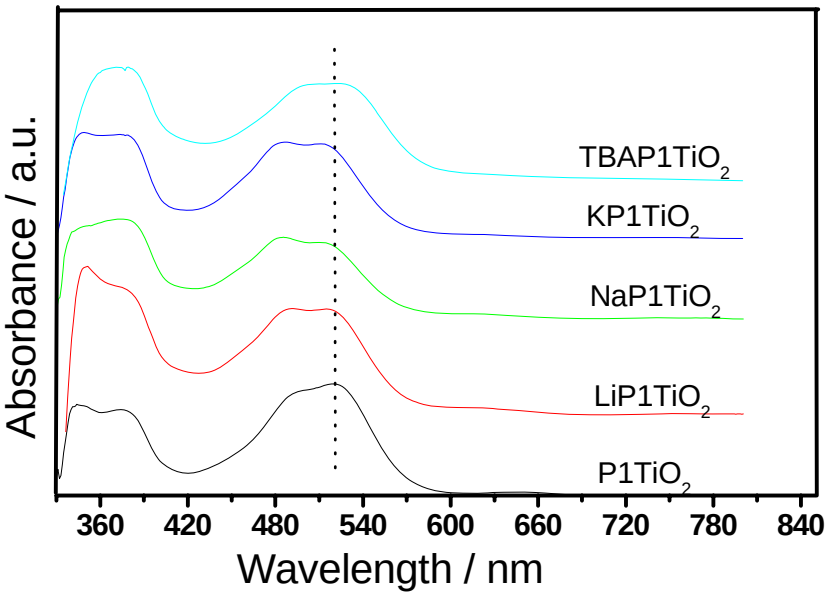

Figure 5.9 Comparison of UV-Vis absorption spectra between P1-loaded TiO_2 and various Metal-coordinated P1-loaded transparent TiO_2 films: P1 adsorbed onto TiO_2 film ($P1TiO_2$), Li-coordinated P1-loaded TiO_2 film ($LiP1TiO_2$), Na-coordinated P1-loaded TiO_2 film ($NaP1TiO_2$), K-coordinated P1-loaded TiO_2 film ($KP1TiO_2$) and TBA-coordinated P1-loaded TiO_2 film ($TBAP1TiO_2$). A bare TiO_2 was used as background.

5.4.3. Impact on the performance of DSSCs

The influence of the complexation Na^+ K^+ and TBA^+ on the performance DSSC based P1 and P7 was investigated and the parameter extracted from the corresponding devices are shown in Figure 5.10. The preparation and characterisation of these devices were similar to devices based on Li-containing electrolyte described above. Electrolyte A consists of 0.6 M 1-butyl-3-methylimidazolium iodide, 0.1 M I_2 in 3-methoxypropionitrile solvent. Electrolyte B_M, C_M and D_M contain 0.05, 0.125, and 0.25 M $MClO_4$ (with M= Na, K, TBA), respectively in electrolyte A. The current voltage characteristics of the devices was measured in the standard condition (AM1.5 100 mW cm^{-2} at 25°C)

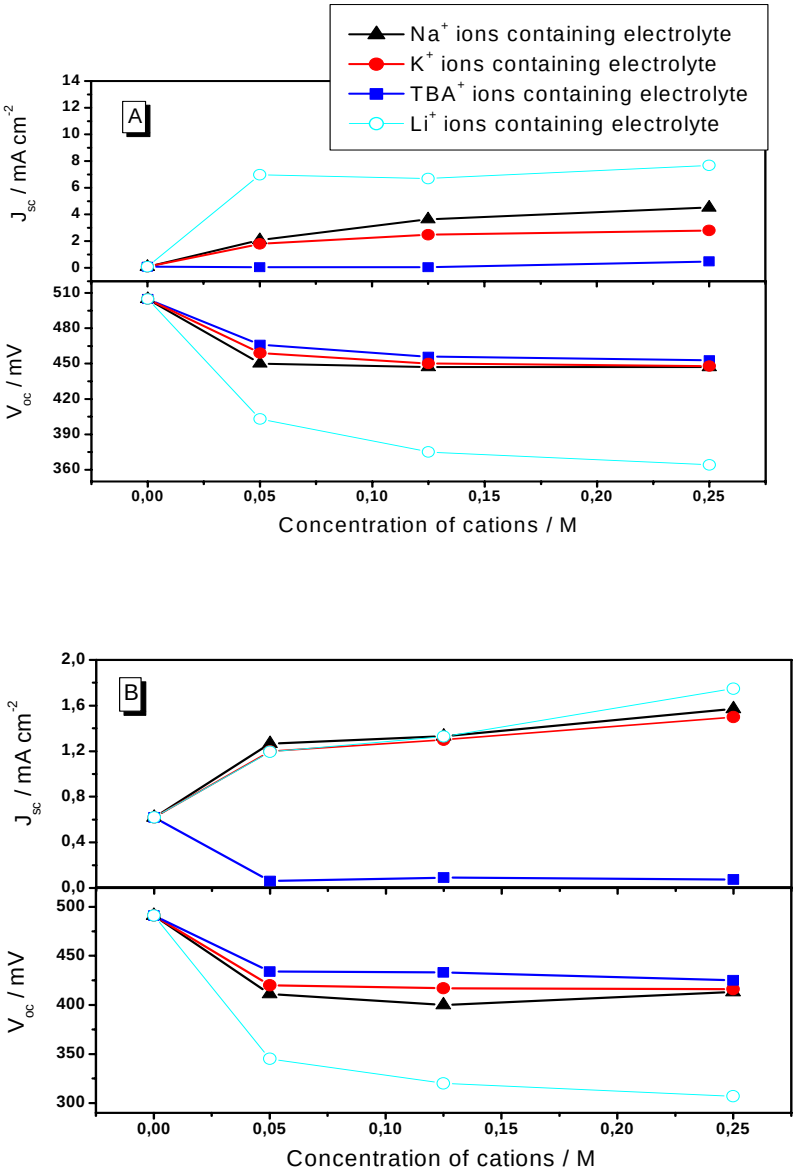

Figure 5.10. Variations in J_{sc} and V_{oc} of: (a) P1-based cells; (b) P7-based cells for different electrolyte type and concentrations.

Figure 5.10, shows that J_{sc} and V_{oc} depend strongly on the nature and concentration of cations. For devices based on P1, J_{sc} increases but not linearly from 0.10 mA cm^{-2} to 4.52 mA cm^{-2} in Na^+ ions containing electrolyte, from 0.10 mA cm^{-2} to 2.80 mA cm^{-2} in K^+ ions containing electrolyte, and increase slightly from 0.10 mA cm^{-2} to 0.49 mA cm^{-2} in TBA^+ ions containing electrolyte when the concentration of each cations types are changed from 0 to 0.25 M (Figure 5.10a). In contrast V_{oc} decreases from 505 mV to 447 mV in Na^+ ions containing electrolyte, from 505 mV to 448 mV in K^+ ions containing electrolyte and from

505 mV to 470 mV in TBA^+ ions containing electrolyte when the concentration in each cation types is changed from 0 to 0.25 M (Figure 5.10a).

Figure 5.10b shows the variation of J_{sc} and V_{oc} in cells based on P7. From Figure 5.10b it can be seen that the variation of J_{sc} and V_{oc} is similar to that observed in P1-based cells with different electrolyte type and concentration except the TBA-modified cell where J_{sc} decreases when [TBA^+] is changed from 0 to 0.05M. J_{sc} generated by P7 based cells increases from 0.62, 1.27, 1.33 and to 1.57 mA cm^{-2} with [Na^+] and from 0.62, 1.00, 1.20 and 1.49 mA cm^{-2} with [K^+] when their concentration are varied from 0 to 0.05, to 0.125 and to 0.25 M, respectively. However, J_{sc} drops from 0.62 to 0.06, 0.09, 0.08 mA cm^{-2} with TBA^+ containing electrolyte when the concentration is changed from 0, 0.05, 0.125 and 0.25 M respectively. V_{oc} decreases in the different cell types as the concentration of the cation is increased. V_{oc} decreases from 505 to 447 mV in Na^+ ions containing electrolyte, from 505 to 448 mV in K^+ ions containing electrolyte and from 505 to 470 mV in Na^+ ions containing electrolyte when the concentration of each cation in the electrolyte is varied from 0 to 0.25 M.

One can remark from the data (Fig.10a,b) that the parameters extracted from P1 and P7-based cells varied identically but not in the same order of magnitude. Devices based on Na^+ and K^+ containing electrolytes show considerable increase in J_{sc} with respect to devices based on TBA^+ ions when the concentrations are increased. Globally, this enables the classification of the increase in J_{sc} in the order $Li^+ < Na^+ < K^+ < TBA^+$ at each concentration. It can be remarked that the smaller is cation size the higher is the photogenerated current. This is due to the fact that small cation can be adsorbed or intercalated easily on the TiO_2 surface forming an thin electric double layer [265] resulting in higher concentration of I^- at the interface between TiO_2 /dye where regeneration of the oxidized dye cation can be facilitated. On the order hand intercalated small size cations screen well the injected electron and improve $J_{sc.}$ It is worth noting that the essential advantage of the electrolytic screening process is its independence from recombination events. For example the redox potential of the Li^+ ions [266,267] lies at -3 V (NHE), about 2 eV higher than the redox potential in the range of > -1 V (NHE) of the electrons in the TiO_2 network [262,267]. So Li^+ like other cation types used in this work cannot react with injected electrons.

There have been a great number of studies involving the influence of the deposition and adsorption of various ions on the performance of dye-sensitized solar cells as well as the photocatalytic activity [262,263,268-274]. It is known that several cations existing in the electrolyte solution as the counteraction of I^- and I_3^- play important roles in the high-energy conversion efficiency. For example, the interaction of Li^+ with the TiO_2 surface enhances the

electron transfer from the adsorbed sensitized dye to the conduction band in TiO_2 and also the electron transfer from I^- to the oxidized dye, leading to a high photocurrent. Kelly et al. [146], after studying the effect of various cations types on the charge separation in a hybrid TiO_2/dye system found that the quantum yield for interfacial charge injection from vibrationally hot molecular excited states to TiO_2 is decreases in the order $Ca^{2+} > Sr^{2+} \sim Ba^{2+} > Li^+ > Na^+ > K^+ \geq Rb^+ \sim C^{s+} \sim TBA^+ >$ neat CH_3CN. Grätzel et al. [273] also reported an increased of photocurrent in the order of $Mg^{2+} > Li^+ > Na^+$ and attributed that to the charge density of the metal ions which are found to be potential-determining. Some evidence was found that the adsorption of metal ions is responsible for the positive shift of the flat band potential [146,262,263,273] at low concentrations, while intercalation close to the electrode surface may be important at higher concentrations [262,264].

While J_{sc} is increased in devices when the concentration of cations in the electrolyte is augmented, the open circuit voltage, V_{oc}, in contrast decreases but not linearly. As observed in devices based on Li^+ ions containing electrolyte (Figure 5.6c,d and Table 5.2) V_{oc} decreases in each cell type but tend to reach a plateau at high cation concentration. For each type of cation V_{oc} decreases when the concentration is increased in DSSCs in the order $Li^+ > Na^+ > K^+ > TBA^+$. Such decrease in V_{oc} as a function of cation size is due to the fact that small sized cations are easily intercalated into the nanoporous hybrid TiO_2/dye system, wherease bulky cations like TBA^+ hardly penetrates the space between the adsorbed dye molecule and the surface of TiO_2. This adsorption of cation shifts the conduction band edge of TiO_2 resulting in the decrease of V_{oc}. Fitzmaurice et al. [262,263] reported that the addition of 1 mM $NaClO_4$, $LiClO_4$, and $Mg(ClO_4)_2$ lead to slight *positive* shifts vs NHE of 0.07, 0.06, and 0.02 V in the flat band potential. As observed in this work each device type show decrease in V_{oc} when the concentration of cation is increased. However, the amplitude of the decrease in P7-based cells cell is not similar than in P1-based cells. In the following sub-section the difference in potential drop in both devices types will be scrutinized.

5.4.4. Investigation of the potential drop in the devices

The potential drop in DSSCs based on P1 and P7 turned out to be different when using an electrolyte containing Li^+ ions as discussed above. Here the experiment is extended to other cations. The potential drop in devices based Na^+, K^+ and TBA^+ containing electrolyte was calculated and the result are show in Figure 5.11.

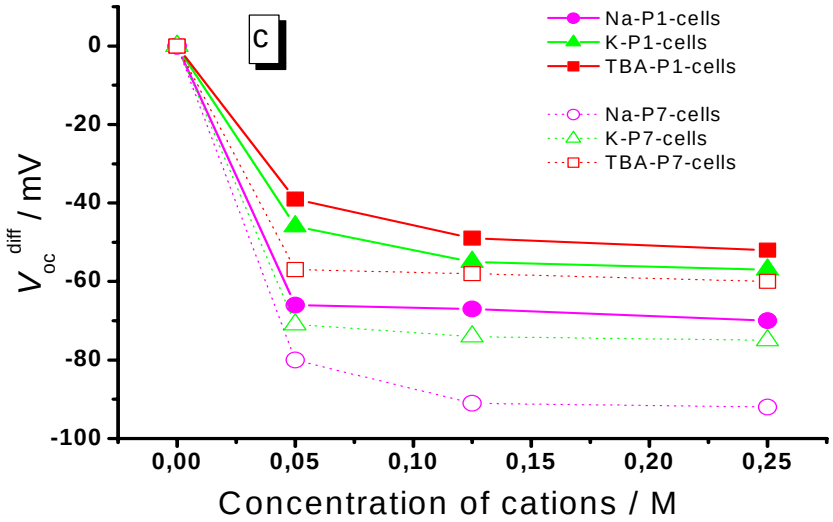

Figure 5.11. The potential drop (V_{oc}^{diff}) in P1 and P7-based cells at different concentration of Na^+ K^+ TBA^+ in M.*

* The potential difference has been calculated following the same calculation route as described in the case of Li^+ containing electrolyte.

Table 5.3. Summary of the values of potential drop V_{oc}^{diff} for P1 and P7-based cell at each cations concentration

$[M^+]$/M	Potential drop (V_{oc}^{diff})					
	Na^+-P1-cell	**Na^+-P7-cell**	**K^+-P1-cell**	**K^+-P7-cell**	**TBA^+-P1-cell**	**TBA^+-P7-cell**
0	0	0	0	0	0	0
0.05	- 66	- 80	- 46	- 71	- 39	- 57
0.125	- 67	- 91	- 55	- 74	- 49	- 58
0.25	- 70	- 92	- 57	- 75	- 52	- 60

From Figure 5.11 and Table 5.3, it can be seen that the potential drop in each device decreases and reaches a plateau at a cation concentration lying between 0.125 M and 0.25 M. However, the amplitude of drop differs in each case. For example, in P1 cells in conjunction with Na^+, K^+ and TBA^+, V_{oc}^{diff} drops in the order $Na^+ > K^+ > TBA^+$ for a given cation concentration. The same tendency is observed in P7-based cells where V_{oc}^{diff} drops in the same order $Na^+ > K^+ > TBA^+$ for a given cation concentration. Globally, one can remark that the

drops are less pronounced in P7-based cells (using Na^+, K^+, TBA^+)(Fig. 5.10b) with respect to the devices containing Li^+ ions. As already mentioned the reason is simple. The small cations are more readily adsorbed than the cation having larger size, and in return the TiO_2 CB is shifted to the more positive side, which reduces the V_{oc}.

However, when one looks closely how the drop in potential varies in each modified cell type, one remarks that for each cation concentration the drop in potential is more pronounced in P7-based cells than in P1-based cells. For example for [Na^+] = 0.25 M, the potential drop in P1-based cells is V_{oc}^{diff} = -70 mV whereas in P7-based it is -92 mV. Moreover, for [K^+] = 0.25 M, the potential drop in P1-based cells V_{oc}^{diff} = -57 mV whereas in P7-based it is -75 mV. The difference could be attributed to the cation complexation sites existing in dye P1. Like it was observed in the lithium modified cells discussed above, in P7 based cells, Na^+ and K^+ ions are free to access the TiO_2 surface with respect to P1-based cells. In fact, oxygen in P1 is likely to coordinate to Na^+ and K^+ present in the electrolyte, inhibiting them from contacting the surface of TiO_2. This explains that the decrease in the V_{oc} is smaller for P1 as compared to P7.

Kuang et al. [92,258] reported a similar observation. By using dye K51 containing triethylene oxide methyl ether (TEOME) the latter behaving like potential ion coordination sites, they found an invariance in the potential of their device. They attributed the potential invariance of the cell to the inhibition of Li^+ adsorption to the TiO_2 surface by the coordination of Li^+ to the TEOME groups of the K51 sensitizer.

However, the drop of the potential in devices containing TBA^+ though behaving qualitatively like other cation types is quantitatively different. The decrease in V_{oc} in P1 and P7-based cells is smaller than in devices based on other cations. At [TBA^+]=0.25 M, V_{oc}^{diff} = -52 mV in P1-based cells whereas V_{oc}^{diff} = -60 mV in P7-based ones. These values are the lowest with respect to that obtained with other cation types. The difference could be due to the fact that bulky TBA^+ can hardly coordinate to oxygen of complexation site in P1 and P7 sensitizer. Moreover, TBA^+ hardly penetrates the space between the adsorbed dye molecule and the surface of TiO_2. It could remain only at a certain distance of the TiO_2 surface forming some cloud of positive charges, inducing just a slight positive shift of the TiO_2 CB. This could have as consequence a poor electron injection because of the poor overlap between dye excited level and TiO_2 CB [146].

5.5. Conclusion

The adsorption behaviour of perylene derivatives with acid anhydride as anchoring groups on the surface of TiO_2 was investigated. The results show that the adsorption mode is dissociative with an unidentate configuration, giving rise to free C=O at the carboxylate anchoring group. This free C=O was found to be sensitive to electrolyte nature and was found to contribute significantly to the change in V_{oc} in the devices, due to an in-situ cation coordination. P1 containing many coordination sites with respect to P7 has shown a slight invariance in the potential owing to the inhibition of cations to reach the TiO_2 surface. Small sized cations turned out to generate high J_{sc} and low V_{oc}.

Chapter 6
UV PRETREATMENT

In this chapter a strategy to improve the light harvesting efficiency of the photoanode for DSSCs is presented. The method consists of UV irradiation of the TiO_2 films before sensitization. The impact of such treatment on the performance of DSSCs is discussed as well.

6.1. Light harvesting (LH) in DSSCs

The performance of dye solar cells depends on the capability of the sensitized TiO_2 film to absorb enough light in a wide range of the visible spectrum. One method for improving DSC efficiency is to modify the surface of a semiconductor photoelectrode. The light harvesting efficiency of the photoanode of DSSCs has been improved by diverse approaches.

Recently Krüger et al. [275] reported a road to improve light harvesting of the photoanode in DSSCs by performing the dye adsorption in the presence of silver ions in the dye solution. From spectroscopic evidence it was inferred that the silver was mainly binding to the sensitizer N3 via the amphidentate thiocyanate, allowing the formation of ligand-bridged dye complexes. However, in their approach, the TiO_2 surface was not directly involved, since the improvement of light harvesting was the fact of an intermolecular reaction (adsorbed molecule and free molecule). Some attempts to improve light absorption by modifying the TiO_2 surface have been realised. Many works have been done regarding the TiO_2 fabrication method to achieve a large surface area for dye adsorption with a nanoparticle TiO_2 film [40,276,277], nanoparticles mixed with relative large sized TiO_2 particles [278], TiO_2 particle with high density of pores [279] and nanotubes [280]. However, these studies have not dealt with the adsorption mechanism of the dye on the TiO_2 electrodes.

After treating the TiO_2 film with HCl Wang et al. [214] found a considerable increase of light absorption of the photoanode using black dye as sensitizer. The HCl pretreatment resulted in a significant increase of the dye adsorption, a positive shift of the flat band of TiO_2, a reduced dark current, and an increased resistance at the TiO_2/dye/ electrolyte interface. Jung et al. [281] by following the same route as described by Wang, treated TiO_2 with HNO_3 and HCl before N3 dye sensitization and observed an improvement in dye adsorption at the TiO_2 surface.

It was reported that the adsorption of methanol molecules onto TiO_2 films is improved after pretreating the TiO_2 surface with UV light [282-284]. The explanation given about this phenomenon was the generation of hydroxyl group on the surface of TiO_2 film. However, the mechanism of TiO_2 surface modification is at present controversial [285]. The most widely accepted explanation consists of the hydroxylation of the surface induced by a photocatalytic process [284,286,287]. By the use of this approach, Hirose et al. [288] recently found that the J_{sc} of DSSC based on N719 was improved when the TiO_2 was exposed to UV light. They explained the improvement by the generation of OH sited on the TiO_2 surface where N719 is dissociatively adsorbed. With the use of multiple-internal-reflection geometry infrared absorption spectroscopy (MIR-IRAS) they observed that the adsorption of N719 on TiO_2 is dissociative consuming surface OH sites [288]. However, to the best of my knowledge there is no work addressed on the influence of such UV pretreatment on the adsorption of perylene derivatives containing acid anhydride as anchor group. It is known that acid anhydrides readily react with active hydrogen compounds such as alcohols and amines [289]. By this UV pretreatment process, one can expect that titanol (Ti-OH) generated could improve or catalyse the adsorption kinetic of perylene acid anhydride derivatives on the TiO_2 surface and thus improve the LH efficiency of photoanode in DSSCs. In this chapter will be shown how the UV pretreatment improves the adsorption of perylene derivative on the TiO_2 and the performance of devices.

6.2. Generation of hydroxyl group on the surface of TiO_2 by the UV light

Previous mechanistic studies show that TiO_2 photoexcitation induces the formation of surface defects (oxygen vacancies) at which ambient H_2O could favorably compete with O_2 for dissociative adsorption [283,287,290-295]. The specific surface atom arrangements are known to be responsible for the crystallographic-facet-dependence of light-activated wettability changes [292]. In commonly used anatase TiO_2 films for solar cells as it is the case in this work, the surfaces that are in contact with the dye solution are mainly crystallographically equivalent (101)/(011) facets, whereas (001) basal facets represent the minority [296]. The respective features are illustrated of Figure 6.1a and b.

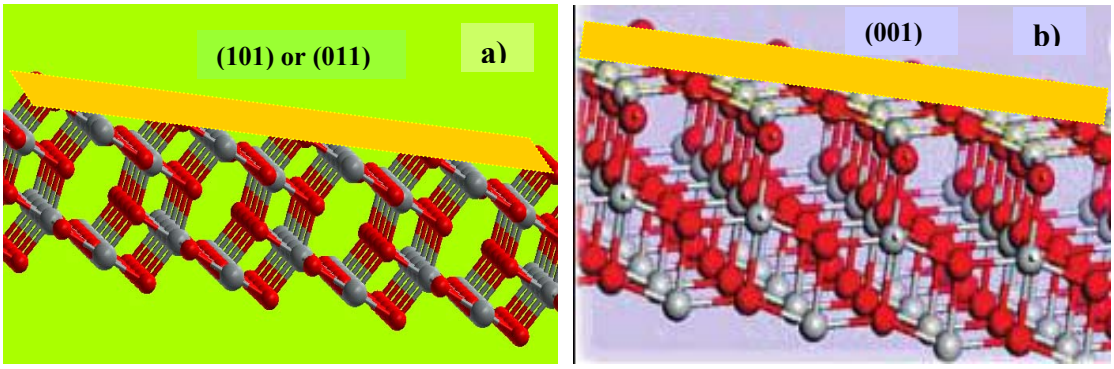

Figure 6.1. (a) Atomic model for (101)/(011) types surfaces and (001) bare surfaces (b) in the TiO_2 anatase structure. Oxygen atome are in red, titanium atoms are gray. The planes identified by the yellow grid intercept bridging-type oxygen atoms on the outermost exposed atom planes. (Source of the Fig.6.1(b) ref.[296])

In the anatase structure, low-energy bare (101) and (011) surfaces exhibit a strongly corrugated profile (Fig.6.1a), in which the outmost 2-fold-coordinated O anions (2c-O) are bound to 5-fold-cordinated Ti cations (5c-Ti) (the rest of the structure is made up of lowered 6c-Ti cations and 3c-O anions). On (001) surfaces (Fig.6.1b), only 5c-Ti atoms are present, which interconnect raised 2c-O and lowered 3c-O anions. So, H_2O could be adsorbed differently depending on the surface of TiO_2 [297,298].

Mechanism of hydroxyl formation under UV irradiation

TiO_2 has an amphoteric character. The unsaturated titanium surface atoms work as Lewis acids while oxygen sites act as Lewis bases. In unirradiated films, H_2O could adsorb dissociatively only at 5c-Ti sites on (001) surfaces, but according to literature it would mainly retain a molecular state on (101)/(011) surfaces [297,298]. Under UV irradiation there is a band gap photoexcitation of electron-hole pairs (Eq. 6.1), thus bridging 2c-O sites may be easily removable by the photogenerated holes, in turn leading to highly unstable 4c-Ti^{3+} atoms (i.e., oxygen vacancies) (Eq. 6.2 and 6.3). Such defect sites are known to possess a strong propensity to be reconstructed by dissociative H_2O adsorption, resulting in two adjacent TiO-H groups per each healed vacancy (Eq. 6.5 and scheme 6.1) [299,300]. The dominance of (101)/(011) facets in our TiO_2 films can be thus expected to be a favourable condition for light-induced surface hydroxylation proceeding to a significant extent.

$$TiO_2 + h\nu \longrightarrow h^+ + e^- \quad 6.1$$

$$TiO^{2-} + h^+ \longrightarrow Ti\text{-}O^- \quad 6.2$$

$$Ti\text{-}O^- + h^+ \longrightarrow 1/2O_2 + Ti\text{-}\square\text{-} \quad \text{(oxygen vacancy)} \quad 6.3$$

$$Ti^{4+} + e^- \longrightarrow Ti^{3+} \quad \text{(surface trapped)} \quad 6.4$$

$$Ti\text{-}\square\text{-} + H_2O \longrightarrow Ti\text{-}OH_2 \longrightarrow Ti\text{-}OH + H^+ \quad \text{(dissociative adsorption)} \quad 6.5$$

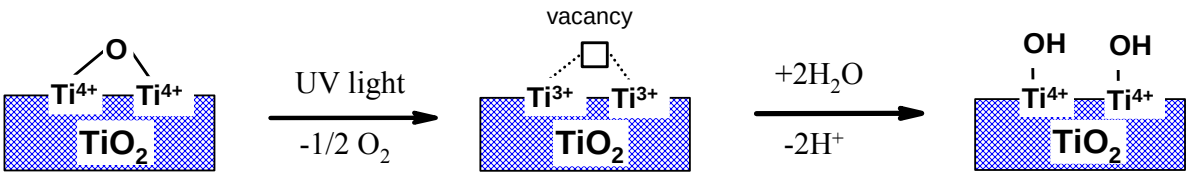

Scheme 6.1. Sketch of the mechanism of UV–induced hydroxylation of TiO_2 surface

6.3. Strategy to improve the LH of thin TiO_2 films

The strategy to improve LH consists in UV irradiation of TiO_2 surface prior sensitization. For the UV pretreatment, the bare nanoporous films were exposed to the entire emission of a mercury lamp in laboratory ambient conditions. The sample holder maintained the sample at ~2 cm distance from the UV lamp. The UV light intensity on the surface of the sample was estimated at ~2 mW cm^{-2}. After UV pre-treatment the TiO_2 was soaked in the dye solution for sensitization. The light harvesting efficiency at the maximum absorption wavelength can be estimated using the following Eq. 1.9

The light harvest of pretreated sensitized films was measured by absorption spectroscopy. The figure 6.2 depicts the absorption spectra of pretreated TiO_2 film sensitized with P1 and P7 dye as a function of UV irradiation time. The UV light intensity on the surface of TiO_2 film (4µm thickness) was estimated to ~2 $mWcm^{-2}$

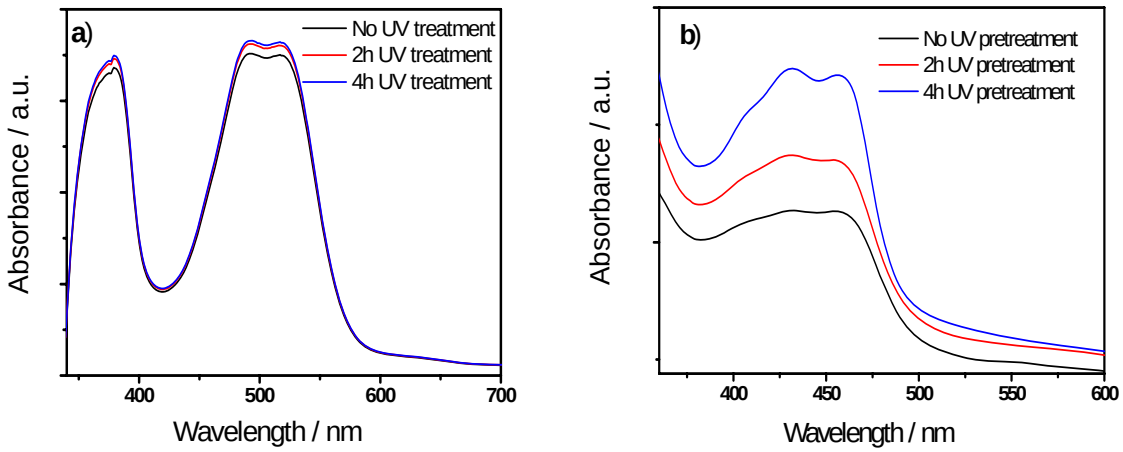

Figure 6.2 Influence of UV pretreatment time of the TiO_2 film on the UV-Vis absorption spectra of (a) P1-loaded and (b) P7-loaded pretreated TiO_2 film.

As it is clearly illustrated in figure 6.2, the absorbance increases with exposure time until 4 hours, where the maximum absorbance was observed. From Figure 6.2, one can see that the absorbance maximum (corresponding to π-π^* transition) is increased for both sensitized film from 1.74, 1.80 and 1.81 at 513 nm upon UV pre-treatment of 0, 2 and 4 h respectively. This leads to an improvement of LHE of 3.0 and 4% at the maximum absorption according to Eq 6.6, after 2 and 4h of treatment. For the same UV treatment time (2 hours and 4 hours) the LHE of P7 loaded electrode at 458 nm is enhanced by 24 and 59%, respectively. No real shift is observed for peak maxima, which implies the stability of different adsorbed dyes. Since the immersion of the TiO_2 film in dye solution is done while it is still hot (~ 80 °C), it may be possible that there are still important quantities of OH sites where acid anhydride rings could dissociatively adsorbed. At this stage of investigation, it is difficult to give a clear explanation of this phenomenon, however, it is likely that UV treatment enhances the chemisorption of both P1 and P7 dyes onto the generated *hydrophilic* TiO_2 surface as illustrated in scheme 6.2.

The UV irradiation increases the surface activity of the TiO_2 films. With the help of Sum Frequency Generation (SFG) vibration spectroscopy, Wang et al. [284] found that the chemisorption of methanol onto TiO_2 is enhanced after a previous UV treatment. According to literature, acid anhydrides readily react with active hydrogen compounds [289]. So we believe that, the enhancement in P1 and P7 absorption (figure 2) is likely due to the

improvement of surface activity of TiO_2 by UV pre-treatment, which polarizes more and more the surface atoms and facilitates adsorption.

It is worth noting that a *photocleaning* effect of the UV-treatment can also be considered. It has been reported that naturally adsorbed hydrocarbon is effectively removed with the photocatalytic reaction under UV exposure [301]. Such impurities may cause steric hindrances to the dye adsorption. From these observations, one can suggest that both combined effects of UV treatment (hydrophilicity and photocleaning) increase the chemisorption of dye on the TiO_2 surface.

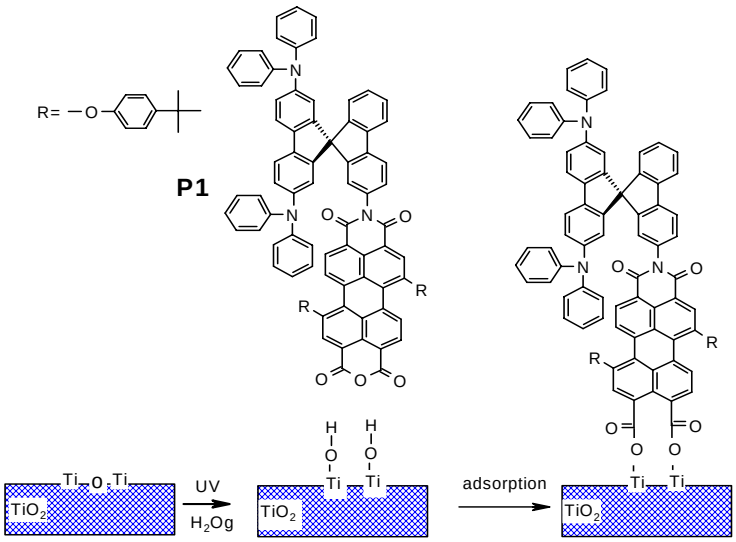

Scheme 6.2. Adsorption model of P1 onto UV pretreated TiO_2 surface

Because of the availability of P7 dye and its small size with respect to P1, an attempt to investigate the quantity of adsorbed dye as a function of irradiation time by Langmuir isotherm measurements was carried out. The results are presented in Figure 6.3

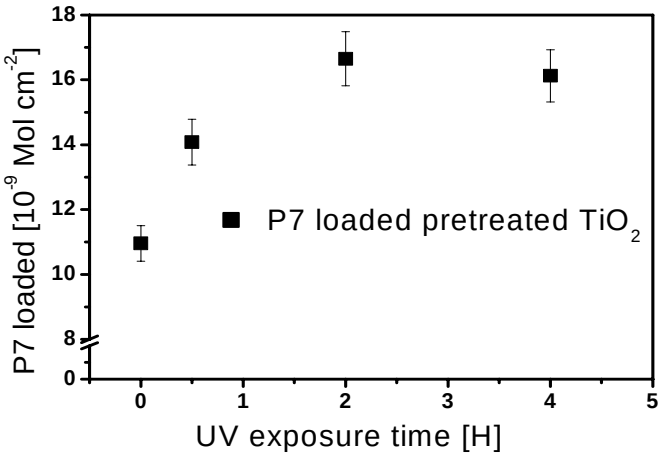

Figure 6.3 Variation of the quantity of P7 dye adsorbed as a function of UV exposure time of TiO_2 film.

The figure 6.3 depicts the evolution of the quantity of adsorbed dyes P7 as a function of UV exposure time of TiO_2. One can see that the quantity of adsorbed dyes increases with the exposure time and tends to reach a plateau at exposure time range between 2 and 4 hours where 16.65×10^{-9} and 16.12×10^{-9} mol/cm² of P7 is chemisorbed, respectively. The increase in adsorption after an exposure time from 0 to 4 hours is like due to the presence of more adsorption sites, which leads to the adsorption of P7 dye. From a thermodynamic point of view, the surfaces consisting of unsaturated atoms are energetically unstable and therefore are surface active sites. In our laboratory, it was really difficult with the help of (ATR-FTIR) to scrutinize the mechanism and the different steps of adsorption of P7 onto the hydrophilic TiO_2 surface, because that technique was not very sensitive to explore the OH group on TiO_2 surface. By using MIR-IRAS, Hirose et al. [288] successfully observed adsorption of N719 on OH site of TiO_2 surface. They observed the disappearance of OH groups after adsorption of N719 and concluded that UV pretreatment of TiO_2 enhances N719 chemisorption.

6.4. Impact of UV pretreatment TiO_2 on the performance of DSSCs

The influence of UV treatment on the performance of DSSC was carried out with dye P1. The current voltage characteristics of DSSCs made with dye P1 untreated and UV-pretreated TiO_2 films are shown in Figure 6.4. The redox electrolyte used consist of 0.3 M LiI, 0.03 M I_2 , 0.5 M tert-butylpyridine (TBP) in dried acetonitrile (ACN) (*electrolyte 1*) and 0.5 M tetra-n-butylammonium iodide (TBAI), 0.05 M I_2 and 0.2 M TBP in dried ACN

(*electrolyte 2*). The devices are characterized under solar simulated white light AM1.5 (86 mW / cm²).

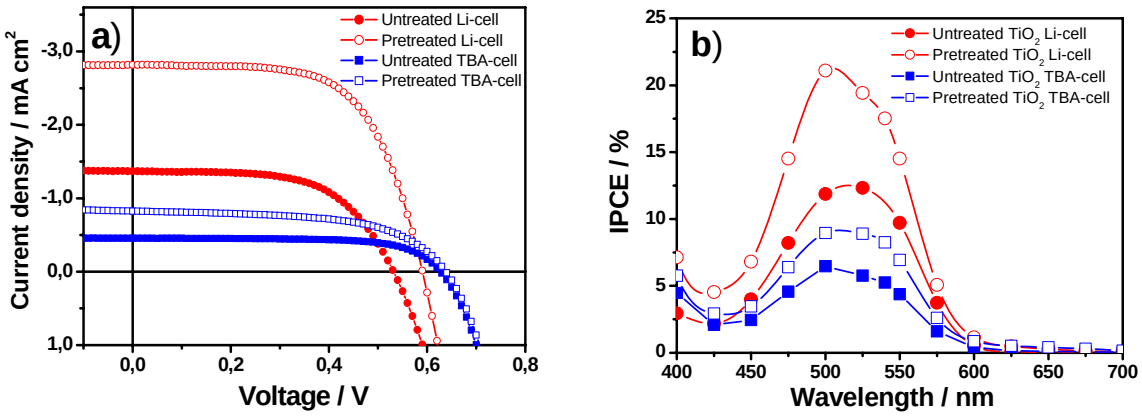

Figure 6.4: a) J-V characteristics of devices based on UV pretreated TiO_2 films and P1: untreated Li-cell (red filled circle); 2h UV pretreated Li-cell (red open circle); untreated TBA-cell (blue filled square) and 2h UV pretreated TiO_2 TBA-cell (blue open square). **b)** corresponding photocurrent action spectra: untreated Li-cell (red filled circle); 2h UV pretreated Li-cell (red opened circle); untreated TBA-cell (blue filled square) and 2h UV pretreated TiO_2 TBA-cell (blue opened square). TiO_2 thickness ~ 4µm; Incident light intensity 86 mW.cm^{-2}

Table 1. Summary of current voltage characteristics before and after UV pretreatment of TiO_2 film for DSSCs based on Li^+ and TBA^+ containing electrolyte

Time (hour)	V_{oc} (mV)		J_{sc} (mA/cm²)		*FF*		η (%)		*IPCE* (%)	
	TBA-Cell	Li-Cell	TBA-Cell	Li-Cell	TBA-Cell	Li-Cell	TBA-Cell	Li-Cell	TBA-Cell	Li-Cell
0	627	531	0.46	1.37	0.63	0.60	0.22	0.5	6.5	12.3
2	638	590	0.84	2.82	0.59	0.63	0.36	1.2	9.0	21.1

The devices made with untreated TiO_2 film in conjunction with *electrolyte 1* have an overall energy-conversion efficiency (η) of 0.5 %. The short circuit current density (J_{sc}), open circuit voltage (V_{oc}) and fill factor (FF) are 1.37 mA cm^{-2}, 531 mV and 0.601 respectively.

Devices made with 2h UV pretreated TiO_2 film generate an efficiency of 1.2 % for J_{sc}, V_{oc} and FF of 2.82 mA cm^{-2}, 590 mV and 0.631 respectively (Fig. 6.4a). This corresponds to more than two times improvement in efficiency after UV-pretreatement of TiO_2. The incident photon to electron conversion efficiencies (IPCE) of the untreated and pretreated titanium oxide devices were 11.9 % and 21 % respectively, which corresponds to an overall improvement of 72 % in quantum efficiency (Fig. 6.4b).

It is well known that Li^+ is a potential-determining ion for TiO_2 because it specifically adsorbs or intercalates into the TiO_2 [302,303]. The additional positive surface charge from adsorbed Li^+ shifts the TiO_2 conduction band (CB) edge to a more positive potential (thereby enabling more facile electron injection from some adsorbed dyes). In the aim to evaluate the Li^+ ions effects and to be sure that the performance of the device is not the consequence of its adsorption but rather of UV pretreatment, *electrolyte 2* was also tested. As depicted in the Figure 6.4a, the short circuit current density increases from 0.46 mA cm^{-2} to 0.84 mA cm^{-2} for untreated and pretreated of TiO_2 films respectively. The complete characteristics are summarized in Table 1. No decrease in the V_{oc} for both Li-cells and TBA-cells is observed which allowed to conclude that the CB edge of TiO_2 is not significantly affected by the treatment and that all the mechanisms occur only on its surface. The improvement in J_{sc} and quantum efficiency is consistent with the fact that UV-pretreatment generates more OH adsorption sites on TiO_2 surface for P1 and increases electron injected density in the TiO_2 conduction band under illumination. Furthermore, V_{oc} in TBA-cells is higher than that of Li-cells. The reason is simple. Because of its large size and the non reactive alkyl groups on its periphery, TBA^+ does not adsorb on the TiO_2 surface nor does it react chemically with it. But the small J_{sc} obtained, with respect to Li^+ containing electrolyte is a direct consequence of interaction of Li^+ with TiO_2, which favours electron injection. Furthermore, both charges, i.e., the electron injected into the TiO_2 network and the positive counter charge left behind on the dye molecule are screened [267] effectively over a diameter of the ionic cloud due to 0.3 M LiI, i.e., over a few nm with respect to TBA^+ ions diameter. On the other hand small size cations by screening efficiently photoinjected electrons in the CB, prevent their recombination with triiodide contained in the electrolyte [258,304]. The weak adsorption of TBA^+ onto TiO_2 surface can be the main cause for the low photocurrents generated by TBA-cells with respect to Li-cells [47,187].

A curious fact is the variation of V_{oc} after treatment (Table1). V_{oc} is increased from 531 to 590 mV for Li-cells with untreated and treated TiO_2, respectively. The same trend is observed in TBA-cells where V_{oc} increased from 627mV and 638 mV for untreated and

treated devices, respectively. This behaviour is particularly strange, since it is known that the exposure of TiO_2 to UV light provokes shifting of the Fermi level to more positive value [187]. One would expect a decrease in potential in the UV pretreated TiO_2 devices but the opposite occurs. This means that the whole process occurs only on the surface of TiO_2. Recently, Hirose et al. [288], also observed an improvement of the performance of DSSCs based on UV pretreated TiO_2 sensitized with N719 dye without significant change in Voc. The possible cause of such improvement in performance of DSSCs has been attributed to the OH generation which enhances the chemisorption of N719 on the TiO_2 surface and to the photocleaning effect by the photocatalytic reaction.

However, a deeper study is required to better understand how bridging O-atom behaves during chemisorption process of acid anhydride onto TiO_2 surface. According to Ref. [296] newly surface-introduced OH species seem to be metastable and tend to disappear in the dark under air and restore the initial surface state hydroxylation. It could be very interesting to know how the generated OH during chemisorption of P1 or P7 really behaves. However, from these preliminaries results, one can say that the UV pretreatment of titanium oxide film improves the performance of DSSCs based on perylene derivatives independently of the nature of counter ions in the electrolyte.

6.5. Conclusion

A strategy for enhancing the adsorption of perylene derivatives by UV treatment of TiO_2 surface was presented. The UV pre-treatment of TiO_2 prior to sensitization turned out to be beneficial for dye adsorption since the light absorption of the treated photoanode is improved by 3% and 24% for P1 and P7, respectively, after 2 hours of UV treatment for example. This leads to an improvement of the performance of DSSCs independently of cation type in the electrolyte.

Chapter 7
CHARACTERIZATION OF SOLID-STATE DYE-SENSITIZED SOLAR CELLS

In this chapter the current voltage characteristic of solid-state dye sensitized solar cells (SSD) based on small molecule perylene derivatives and molecules based on the spiro concept is presented. The long-term stability of SSD based on P1 is discussed. The influence of the TiO_2 film is discussed as well.

7.1. Solid-State Dye-Sensitized Solar Cells based on non spiro compound

7.1.1. Current voltage characteristics of SSD based on P4, P7, P8, P9 and P10.

Unless otherwise mentioned 2 µm was used as TiO_2 film thickness in this work and the effect of the film thickness on the performance of SSD is discussed later. The current-voltage characteristics of solid-state dye-sensitized solar cells (SSD) based on P4, P7, P8, P9 and P10 measured in ambient atmosphere at room temperature in the dark and under illumination of 0.54 sun and 1 sun are shown in Figure 7.1.

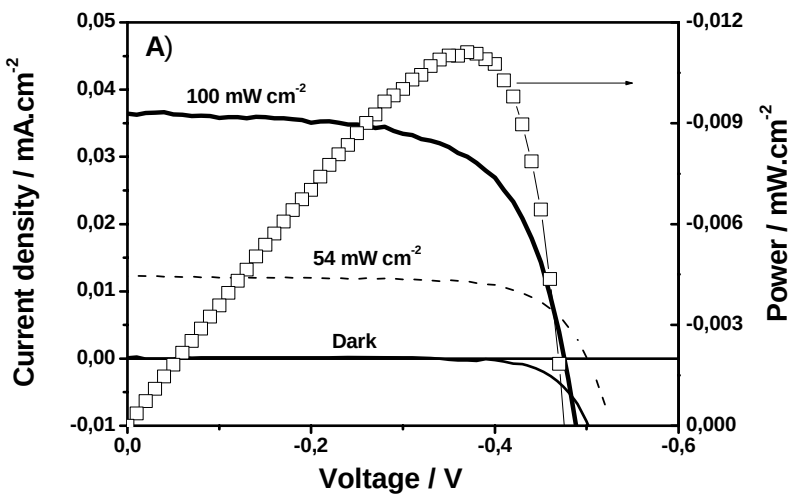

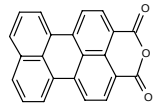

P7

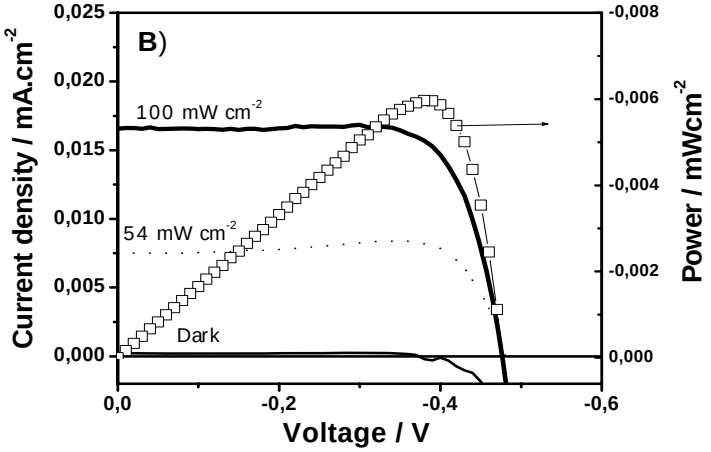
B)
100 mW cm-2
54 mW cm-2
Dark
Current density / mA.cm-2
Power / mWcm-2
Voltage / V
0,025
0,020
0,015
0,010
0,005
0,000
-0,008
-0,006
-0,004
-0,002
0,000
0,0
-0,2
-0,4
-0,6

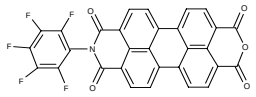

P4

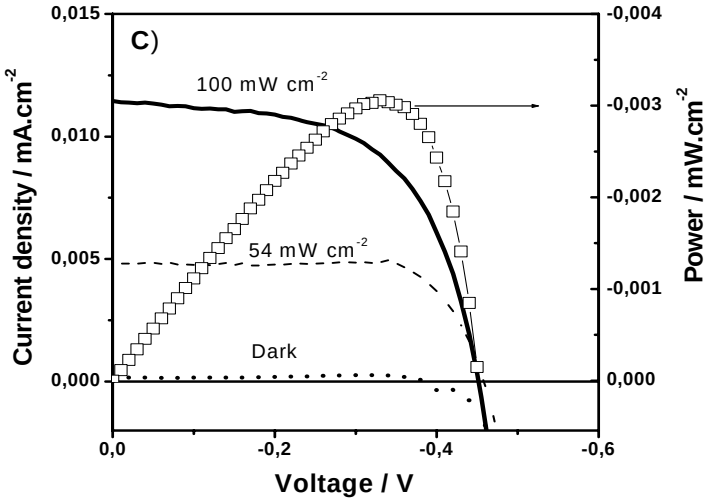
C)
100 mW cm-2
54 mW cm-2
Dark
Current density / mA.cm-2
Power / mW.cm-2
Voltage / V
0,015
0,010
0,005
0,000
-0,004
-0,003
-0,002
-0,001
0,000
0,0
-0,2
-0,4
-0,6

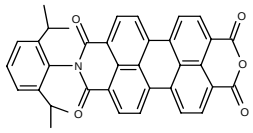

P8

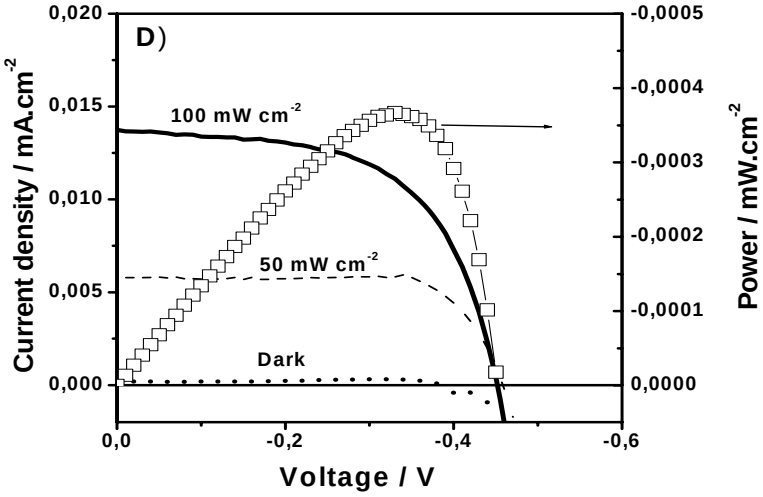
D)
100 mW cm-2
50 mW cm-2
Dark
Current density / mA.cm-2
Power / mW.cm-2
Voltage / V
0,020
0,015
0,010
0,005
0,000
-0,0005
-0,0004
-0,0003
-0,0002
-0,0001
0,0000
0,0
-0,2
-0,4
-0,6

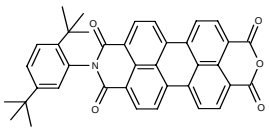

P10

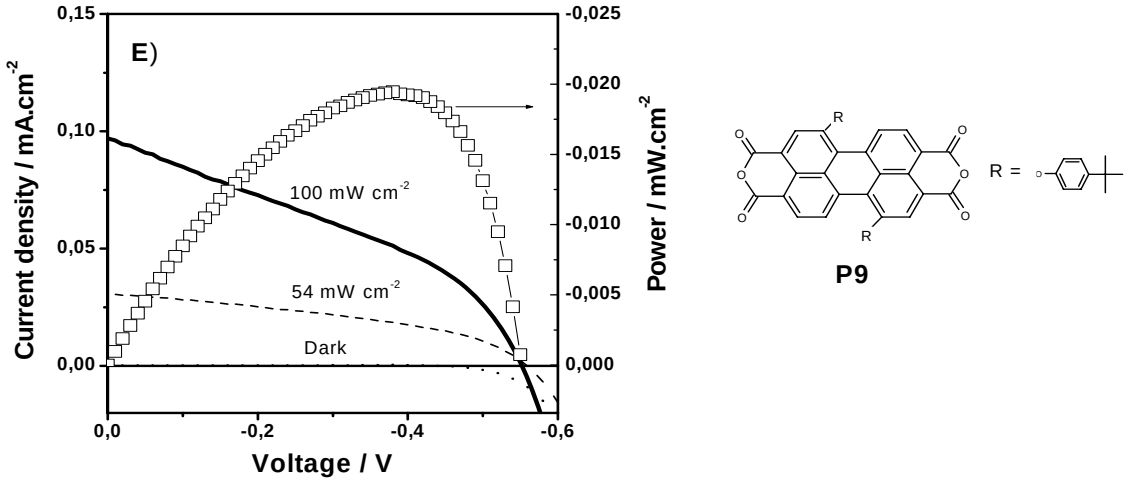

Figure 7.1 Current-Voltage characteristics of solid-state dye-sensitized solar cells based on P7 (a) P4 (b), P8 (c), P10 (d) and P9 (e) at different illumination conditions (1 sun, 0.54 sun and in dark). The hole conductor composition was 0.2 M spiro-MeOTAD, 0.13 mM in $Li(CF_3SO_2)_2N$, 0.18 M in tBP and 0.71 mM in $N(p\text{-}C_6H_4Br)_3SbCl_6$ dissolved in chlorobenzene. TiO_2 film thickness was ~2 µm, the active area 0.15 cm^2. The inset depicts the chemical structure of dyes; the plot of power against voltage is represented by empty squares.

Table 7.1. Summary of device performances extracted from IPCE and IV measurement.

Materials	V_{oc} **[mV]**	J_{sc} **[mA/cm²]**	**FF**	V_m **[mV]**	J_m **[mA/cm²]**	**Pmax [mW/cm²]**	**IPCE [%]**	**η [%]**
P4	476	0.017	0.750	380	0.016	0.006	0.36	0.006
P7	476	0.036	0.641	370	0.030	0.011	1.45	0.011
P8	476	0.033	0.591	330	0.027	0.01	1.76	0.01
P9	552	0.097	0.364	389	0.051	0.019	1.04	0.019
P10	452	0.037	0.618	331	0.033	0.011	2.14	0.011

From Figure 7.1, the open circuit voltage V_{oc}, short circuit current J_{sc}, fill factor FF and efficiency η generated by the devices at 1 sun are 476 mV, 0.017 mA cm^{-2}, 0.750 and 0.006% for P4, 476 mV, 0.036 mA cm^{-2}, 0.641 and 0.01% for P7, 452 mV, 0.033 mA cm^{-2} 0.591, and 0.01% for P8, 552 mV, 0.097 mA cm^{-2}, 0.364, and 0.019% for P9, 452 mV, 0.039 mA cm^{-2}, 0.618 and 0.011% for P10, respectively. Globally, the efficiencies generated by the solid-state devices are lower than their corresponding electrolyte-based cells. (see section 4.1.1). In contrast, V_{oc} in SSDs are higher than in their corresponding electrolyte-based cell. This difference could be explained by the fact that the redox potential of spiro-MeOTAD is by ~0.4V higher than that of I^-/I_3^- couple. However, despite the high V_{oc} in SSD, their low efficiency could be attributed to the poor pore filling of spin-coated spiro-MeOTAD solution into the nanoporous TiO_2 film. In general amorphous films of hole transport materials (HTM) diffuse depending on the environment of the hybrid dye-loaded-TiO_2 nanoporous film [305]. This aspect will be discussed in section 7.3. But it is worth noting that poor pore filling of nanoporous TiO_2 film lead to more recombination sites low J_{sc} and thus a lower efficiency of the device. This could explain the low performance of solid-state devices. The plot of power against voltage at 1 sun (Figure 7.1 plots in empty square) shows that the voltage, current density and the power at the maximum power point are 380 mV, 0.016 mA cm^{-2} and 0.006 mW cm^{-2} for P4, 370 mV, 0.030 mA cm^{-2} and 0.011 mW cm^{-2} for P7, 330 mV, 0.027 mA cm^{-2} and 0.01 mW cm^{-2} for P8, for P10, 389 mV, 0.051 mA cm^{-2} and 0.019 mW cm^{-2} for P9, 331 mV, 0.033 mA cm^{-2} and 0.011 mW cm^{-2}, respectively.

From Figure 7.1 and Table 7.1, the efficiency of the device based on P4 is lower than the values of the other devices (See Table 2.2). Such a difference can be attributed to a low driving force for electron injection from P4 to TiO_2 conduction band. The fill factor of the device is considerably high. This singular behaviour could be likely due to the increase in shunt resistance at the interface TiO_2/P4/spiro-MeOTAD hybrid system. In dye solar cells (DSC) this interface is the place where the shunt resistance is located as described by Han et al. [306]. In fact, the HOMO level of P4 is lower than that of P7 for example and the driving force for P4 regeneration is likely improved.

The efficiency exhibited by P8-SSD is higher than that of P4-SSD described above. This difference in performance is due to the high short-circuit current generated by P8-SSD. In fact, the LUMO level of P8 is 0.06 eV higher than that of P4. Thereby the driving force for electron injection is increased in P8-SSD cells with respect to P4-SSD cells. The electron withdrawing character of the pentafluoro substituent reduces the electron injection capability from P4 to TiO_2 CB. Therefore, the photocurrent generated by P4-SSD is considerably low.

The FF of the P8-SSD cell at 1 sun was found to be 0.591, close to that of typical dye cells where the value is located between 0.6 and 0.8.

The parameters extracted from device P10-SSD (Figure 7.1(d)) are similar to those of P8-SSD cell discussed above. This similarity arises mainly from the similarity in the chemical structure of P10 and P8. However, a slight difference in the performance is to mention. Although their V_{oc} are of the same order, the J_{sc} are slightly different. The J_{sc} generated by P10-SSD device is slightly higher than that of P8-SSD where a short-circuit current density of 0.033 mA cm^{-2} was found. A comparable observation was also made in their corresponding electrolyte cells. However, the shift in J_{sc} in electrolyte cells was found to be $\Delta J_{sc} \approx 0.36$ mA cm^{-2}, which is two orders of magnitude higher than the shift in solid state cells where just $\Delta J_{sc} \approx 0.005$ mA cm^{-2} was observed.

The photocurrent generated by P9-SSD (Figure 7.1(e) and Table 7.1) is slightly higher than that of P4, P7, P8 and P10 solid-state based cells. The improvement in J_{sc} is likely due the electron donation capability of *tert*-butylphenoxy substituents, which by increasing the electron density in the perylene core also increases the electron density in the conduction band of TiO_2. Furthermore, it is worth noting that the presence of bulky *tert*-butylphenoxy groups reduces aggregation of P9 onto TiO_2 surface and thus improves electron injection. The calculated fill factor is very low and far from a classical dye solar cell. This is likely due to the poor pore filling of the spin coated organic semiconductor.

However, the poor pore filling is not to be neglected since it represents until now, the key problem in SSD. It has been established that electron transport in nanocrystalline TiO_2 films is dominated by electron trapping in intraband-gap defect states [307-310]. In a strongly screened environment such as in the electrolyte cell the multiple trapping takes place mainly via thermal activation of trapped electrons [71,72]. As a result of the less efficient screening of photoinduced electric fields in the SSD the electron transport in the TiO_2 may differ significantly from the one in DSSC leading to immobilisation of trapped electrons on the time scale of the experiment. These could likely explain the low short circuit current density generated by solid-state devices with respect for example to electrolyte-based devices.

Furthermore, another problem is the less efficient hole transport in the solid medium as a result of the relatively low hole mobilities in organic semiconductors. Low conductivities imply high resistance causing voltage losses, particularly for high current densities. Slow charge transport is expected to generate charge gradients in the hole conductor matrix. As a consequence an accumulation of holes might build up inside the pores, accompanied by a depletion of holes in the bulk organic semiconductor. This concentration gradient of holes

will lead to a charging of the interface, which will considerably increase the interfacial recombination.

7.1.2. The influence of incident light intensity on the performance of SSDs

7.1.2.1. Influence on the short circuit current density (J_{sc}), fill factor (FF) and efficiency (η)

Figure 7.2 shows the light dependence of P4, P7, P8, P9 and P10-SSD cell parameters and their IPCE. From Figure 7.2(a) one can see that the plot of J_{sc} against incident light intensity for all cell types is nonlinear in the range of light intensity investigated. This behaviour is not the same like in their corresponding electrolyte-based cells and can be attributed to the poor pore filling of spin-coated spiro-MeOTAD into nanoporous hybrid TiO_2/dye film.

The fill factor (FF) varies with incident light intensity (Figure 7.2(b)). FF decreases from 0.751 to 0.641 in P7-SSD, from 0.989 to 0.750 in P4-SSD, from 0.907 to 0.591 P8-SSD, from 0.690 to 0.364 P9-SSD and from 0.900 to 0.618 (P10-SSD), when the light intensity is increased from 25 to 100 mW cm^{-2}. The decrease in FF when the incident light intensity is increased is characteristic of dye solar cells and can be attributed to ohmic losses in the device since the FF depends on series and shunt resistance. The series resistance, Rp reduces drastically when the light intensity increases [311]. However, the fill factors exhibited by these devices at different light intensity remain in the range of ideal dye cells excluding P9-SSD.

Figure 7.2(c) depicts the dependence of efficiency (η) on the incident light intensity. From Figure 7.2(c) one can see that the efficiency is approximately constant between 27.8 and 82 mW cm^{-2} where the average value is close to 0.005 % for P4SSD, 0.007 % for P7-SSD, 0.01 % for P8-SSD, 0.01 % for P9-SSD and 0.01% for P10-SSD. However, the highest efficiency was observed in P9-SSD at 100 mW cm^{-2} where a value of 0.02% was found.

The incident photon-to-electron conversion efficiency (IPCE) for solid-solar cells based on P4, P7, P8, P9 and P10 are shown in Figure 7.2(d). The maximum quantum efficiency generated by the P7-SSD was found to be 1.45% between 425 and 475 nm for a photocurrent density of 3.73 μA cm^{-2}. The IPCE value of 0.36 % generated by P4-SSD is lower than that of P7-SSD. It can be due to low driving force for electron injection in P4-SSD. IPCE generated by the P9-SSD device was found to be 1.04% between 475 and 500 nm for a

current density of 3 μA cm^{-2}. Device P10-SSD exhibits IPCE of 2.12% at 475 nm with a photocurrent density of 6.8 μA cm^{-2}. It is higher than that of P8-SSD (1.75% at 475 nm), likely due to the aggregation hindering by *t*-butyl at position 3 of the phenyl substituent in P10. Globally, these IPCE are very low with respect to electrolyte-based solar cells. As already mentioned, it can be attributed to the poor pore filling of the hybrid nanoporous TiO_2/dye by film by the spin-coated organic HTM, which induces poor dye regeneration and hence low photocurrent.

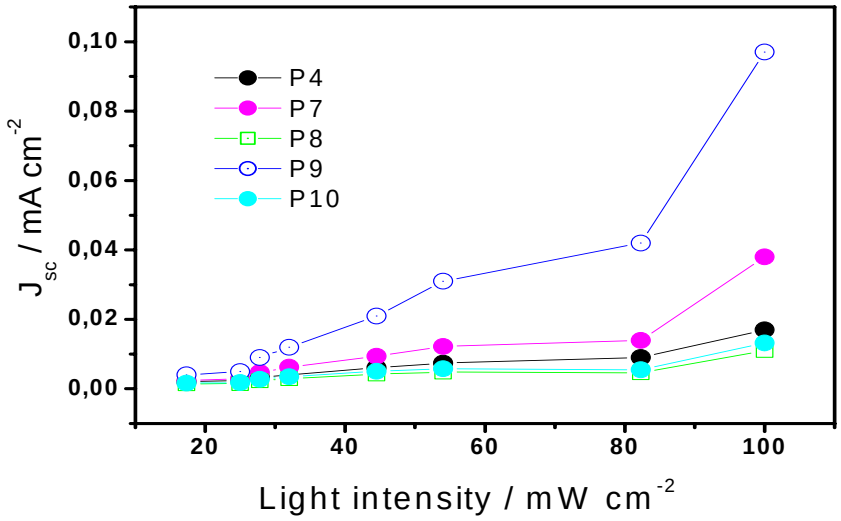

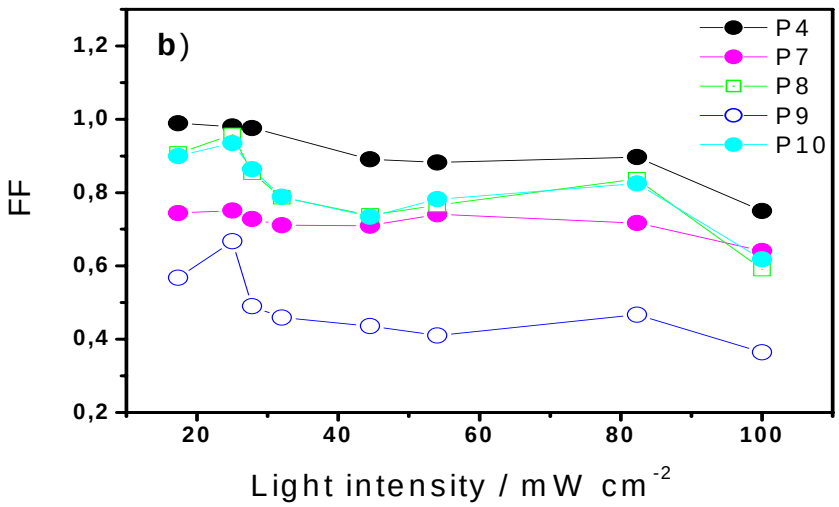

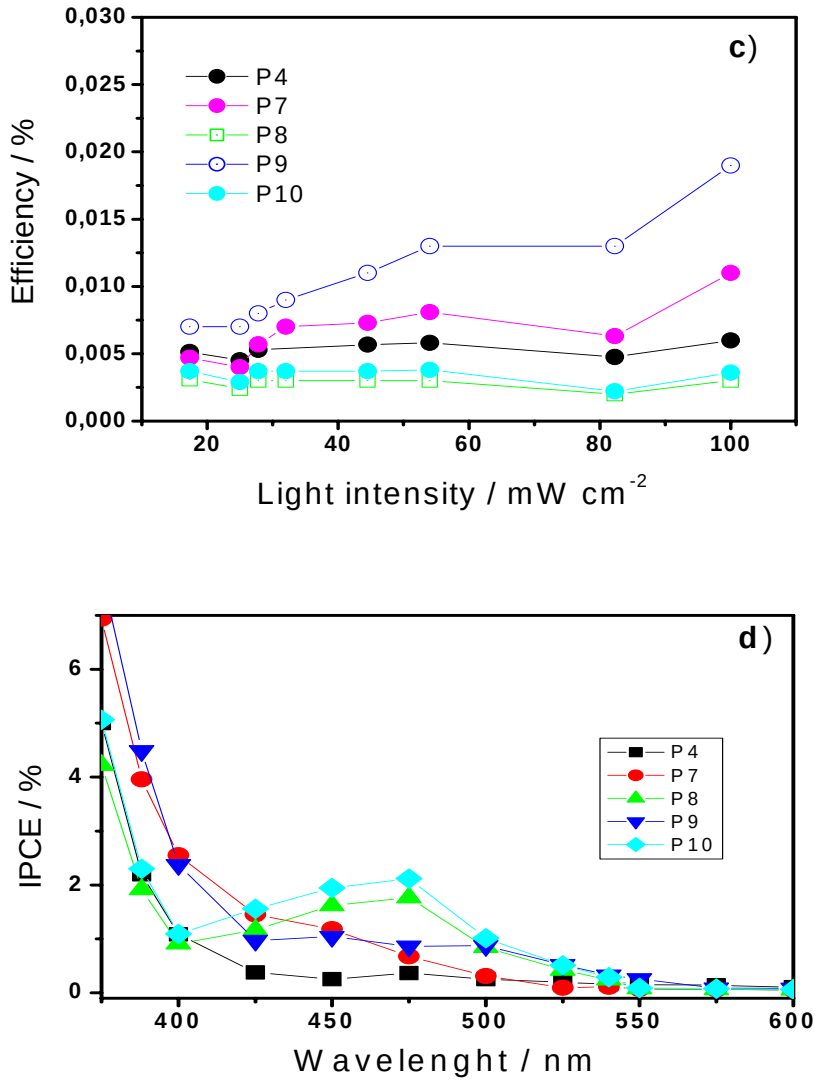

Figure 7.2 Output and characteristics of solid-state dye-sensitized solar cell based on P4, P7, P8, P9, P10 at different light intensities: Light intensity dependence of J_{sc} (a), FF (b) and efficiency (η) (c). Photo action spectra (IPCE) of the corresponding devices (d)

7.1.2.2. **Influence of the incident light intensity on the open circuit voltage (V_{oc})**

The dependence of V_{oc} on incident light intensity was investigated and the results are shown in Figure 7.3.

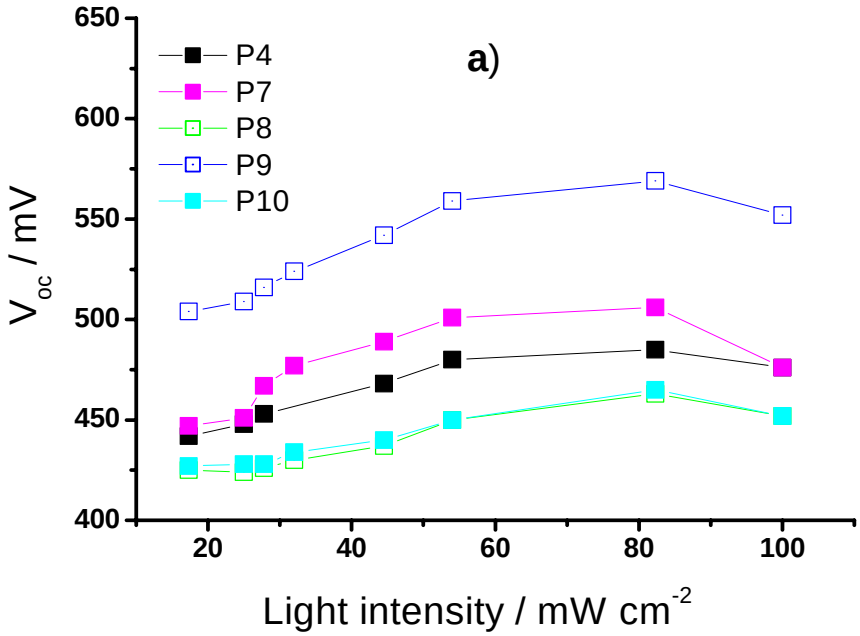

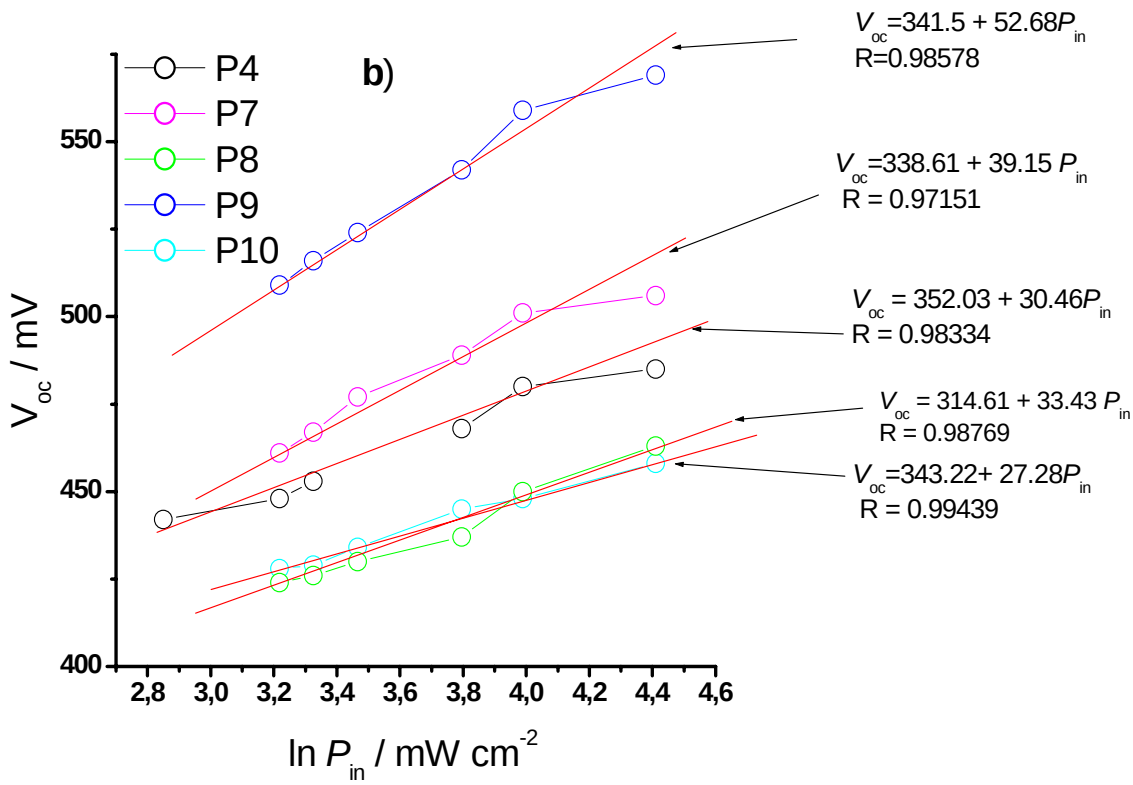

Figure 7.3. Relationship between (a) incident light intensity and the open-circuit voltage, V_{oc}, and (b) the logarithm of the incident light intensity and V_{oc}. The solid red lines denote the linear fit to the experimental data.

From Figure 7.3(a) it can be observed that V_{oc} increases with light intensity and tends to reach a plateau at high light intensity where saturation is observed. In P7-SSD, V_{oc} increases from 447 mV at 17.3 mW cm^{-2} to 489 mV at 54 mW cm^{-2}. Over 54 mW cm^{-2} V_{oc} it remains almost constant until 82.3 mW cm^{-2} where a value of 504 mV was found. All devices show the same behaviour and this is characteristic of dye-sensitized solar cells. The observation is the same as discussed in the case of electrolyte-based cells. The plateau at high light intensity suggests the saturation in the conduction band of TiO_2.

The dependence of V_{oc} with the logarithm of the incidence light intensity is shown in Figure 7.3(b). It can be observed in Figure 7.3(b) that the plot of the V_{oc} against the logarithm of the incident light is almost linear. This linearity, especially at low light intensity for all devices is the consequence of the diode properties of the compact TiO_2 blocking layer. That should also imply that the recombination of the injected electron with holes in the spiro-MeOTAD occurs predominantly via the nanocrystalline TiO_2. The plot in Figure 7.3(b) also shows a slope of 30.5, 39.2, 33.4 52.7 and 27.3 mV/decade for P4, P7, P8, P9 and P10, respectively. These values are lower than that of an ideal diode (59 mV/decade) as reported by Peter et al. [217,312]. This non-ideality probably indicates that the recombination process also occurs via surface states [261]. Interestingly, the deviation from ideality in solid-state cells with respect to electrolyte-based cell can suggest that the rate of electron transfer through surface states is not similar, dye solar cells being complex systems with competing adsorption by dye molecules, solvent, additive and electrolyte ions.

7.2. Solid-State Dye Sensitized Solar Cells based on a spiro-linked compound

Wetting and pore filling

The dye structure has a striking influence on the heterojunction between TiO_2 and the hole conductor. For related organic devices, such as LEDs, the consequences of the introduction of organic molecules on the band energetics, morphology, and stability (hydrophobicity) of organic/inorganic contacts have been studied in detail. Goncalves-Conto et al. [313] have demonstrated that the wettability of ITO substrates by organic semiconductors can be improved by self-assembled monolayers (SAM) of appropriate molecules onto ITO. Similarly spin-coating of the hole conductor leads to films of better quality when the deposition has been established on dye-sensitised TiO_2 instead of pure TiO_2. A dye with organic chains pointing towards the hole conductor might therefore diminish the activation energy for the hole conductor to fill the nanoporous network. This morphology

might also influence the interception kinetics and might shield the TiO_2 surface and therefore affect the recombination kinetics. In P1-SSD devices, the presence of donor moieties structurally similar to the organic hole transport material (spiro-MeOTAD) could improve considerably the wettability of sensitized TiO_2 film by spin-coating organic HTM.

7.2.1. *N*-[2´,7´-Bis-(*N,N*-diphenylamino)-9,9´-spirobifluoren-2-yl]-1,7-bis-(4-*t*-butylphenoxy)-perylene-3,4-dicarboxylic acid anhydride-9,10-imid (P1)

Figure 7.4 shows the current voltage characteristics of solid-state dye solar cells based on *N*-[2´,7´-bis-(*N,N*-diphenylamino)-9,9´-spirobifluoren-2-yl]-1,7-bis-(4-*t*-butylphenoxy)-perylene-3,4-dicarboxylic acid anhydride-9,10-imide (P1-SSD) measured in the dark, at 54 mW cm^{-2} and at 100 mW cm^{-2}. The V_{oc}, J_{sc} and FF generated by P1-SSD cells are 822 mV, 0.48 mA cm^{-2} and 0.504 respectively. This yields to an overall electron conversion efficiency of 0.2% (Figure 7.4(a)). The photovoltage, photocurrent and the power at maximum were found to be 640 mV, 0.311 mA cm^{-2} and 0.2 mW cm^{-2}, respectively (Figure 7.4(b)). The performance of this device is considerably improved with respect to its parent compound based cell (P9-SSD). The efficiency is improved by a factor of 10. This striking improvement in performance was also observed in the corresponding electrolyte based cells described in section 4.2.1. This improvement in performance could be attributed to the chemical structure of P1. The donor units in P1 increase the electron density in the perylene tetracarboxylic core by ”*through space*” charge transfer process and, thus, in the conduction band of TiO_2.

We assume that, once P1 is adsorbed, the spiro-diphenylamine substituent shields the inorganic oxide surface, forming an organic environment which might be advantageous for the filling of pores with the organic hole conductor and therefore for the morphology of the heterojunction. The exact mechanism could be difficult to elucidate, but the similarity in both components characterised by spiro-diphenylamino group could likely improve the diffusion of organic hole conductor in nanoporous network during the preparation. This observation has been also reported by Peter et al. [305] who found that the use of a dual-functional chromophore consisted of triphenylamine antenna groups attached to the dye core improve the wettability and the performance of the device. However, contrary to their ruthenium chromophore in which the intramolecular charge transfer occurs by a push-pull process, a through-space charge transfer governs the charge transfer process in P1. Moreover, the fact that the diphenylamine units in P1 are not in conjugation with perylene core and that the HOMO energy levels for *tert*-butylphenoxy perylene, diphenylamine and spiro-MeOTAD are

-5.92 eV, -4.99 eV and -4.77 eV, respectively, makes the transfer of holes from the dye to the Pt electrode easy via a favourable electrochemical potential cascade process.

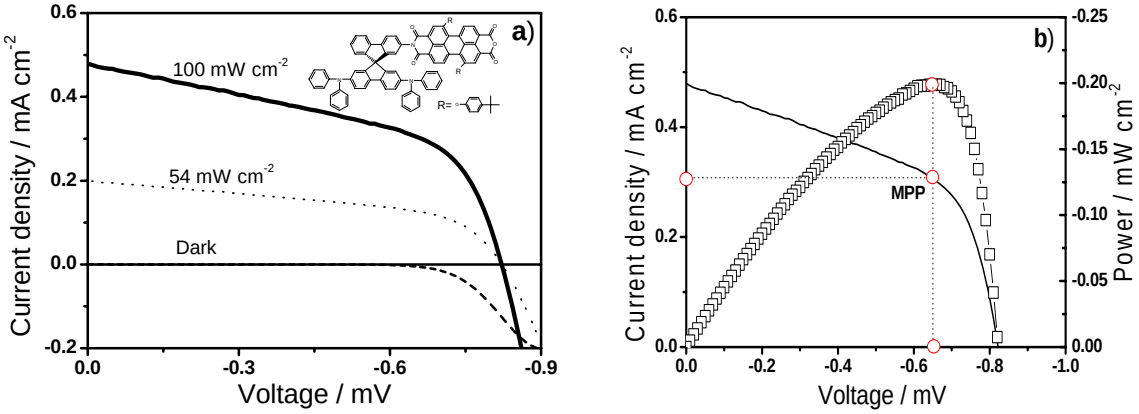

Figure 7.4: (a)**.** Current-Voltage characteristics of solid-state dye-sensitized solar cells based on P1 (P1-SSD) at different illumination conditions (1 sun, 0.54 sun and in dark). The hole conductor composition was 0.2 M spiro-MeOTAD, 0.13 mM in $Li(CF_3SO_2)_2N$, 0.18 M in tBP and 0.71 mM in $N(p\text{-}C_6H_4Br)_3SbCl_6$ dissolved in chlorobenzene. TiO_2 film thickness was ~2 µm, Active area 0.15 cm^2. The inset depicts the chemical structure of P1. (b). The plot of power against voltage: Empty red small circles show the parameters at maximum power point.

The results of the light dependence for P1-SSD cells are shown in Figure 7.5. In Figure 7.5(a), the plot of J_{sc} with light intensity shows linear dependence. This is likely due to easy hole transfer from dye to HTM. However, V_{oc} increases with light intensity and tends to reach a plateau at 100 mW cm^{-2} where a value of 822 mV was found. This behaviour is typical of dye cells. The drop of Voc with the normal logarithm of incident light shows a linear relation with a slope of 72.5 mV/decade. The value is higher than that of ideal diode. Howie et al. [261] reported similar observations when they used some indoline dyes (denoted D102, D131 and D149) where the arylamine moiety act as electron donor and a carboxylic moiety as electron acceptor. Using indoline dyes they found a slope lying in the range from 70 to 80 mV/decade. Since the plot was found to be linear it is evident that back reaction via substrate is negligible as a consequence of the diode properties of a compact TiO_2 blocking layer [312].

Figure 7.5(c) shows the dependence of fill factor and efficiency on the light intensity. It was found that the fill factor decreases when light intensity is increased. The fill factor

decreases from 0.57 to 0.504 when light is changed from 27.8 mW cm^{-2} to 100 mW cm^{-2}. This behaviour is characteristic of dye cells. The efficiency varies slightly with light intensity but remains constant from 54 mW cm^{-2} and 100 mW cm^{-2} with an average value of 0.18%. The highest value is 0.2% at 100 mW cm^{-2}.

The photocurrent action spectrum exhibited by P1-SSD cell is shown in Figure 7.5(d). The incident photon to electron conversion efficiency generated by the device is 7.05% at 475 nm with a current density of 14.32 μA cm^{-2}. This performance is higher than that of its parent P9-SSD.

The improvement of the performance of SSD based on P1 with respect to P9 and to others dyes is a proof that the chemical structure of the dye can improve the wetting the hybrid TiO_2/dye by spin-coated HTM. The nature of dye structure is thereby an important parameter for the quality of SSD.

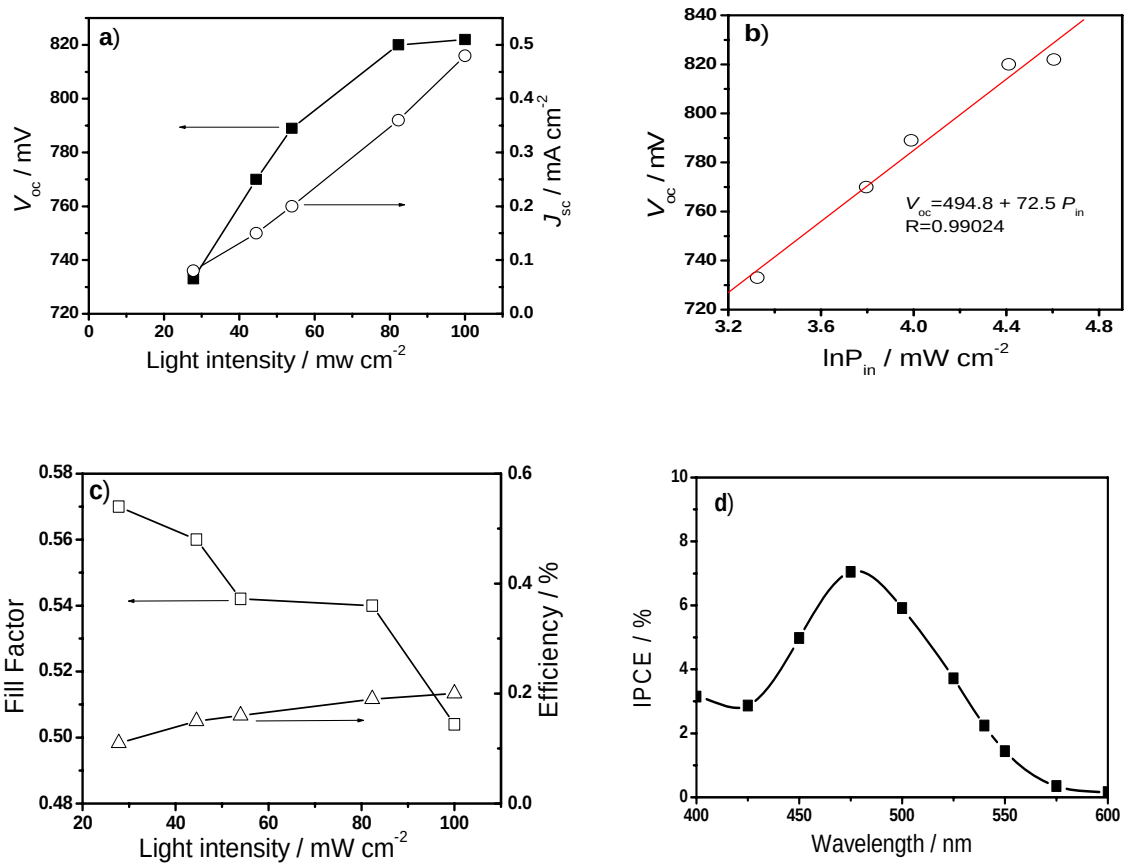

Figure 7.5 Output and characteristics of solid-state dye-sensitized solar cell based on P1 (P1-SSD) at different light intensity: (a). Incident light intensity dependence of V_{oc} and J_{sc}; (b). Relation between the logarithm of incident light and V_{oc}; (c). Light intensity dependence of fill factor and efficiency; (d). The IPCE of P1-SSD.

7.2.2. Long time stability of P1-based cell

High stability under long term exposition at ambient condition is a vital parameter for sustained cell operation, so the J-V curves of P1 sensitized solid state solar cells at different time scales were measured. The performances of P1-SSD were followed during 4 months while keeping the device at ambient condition. The current-voltage characteristics of the device were collected and the results are shown Figure 7.6.

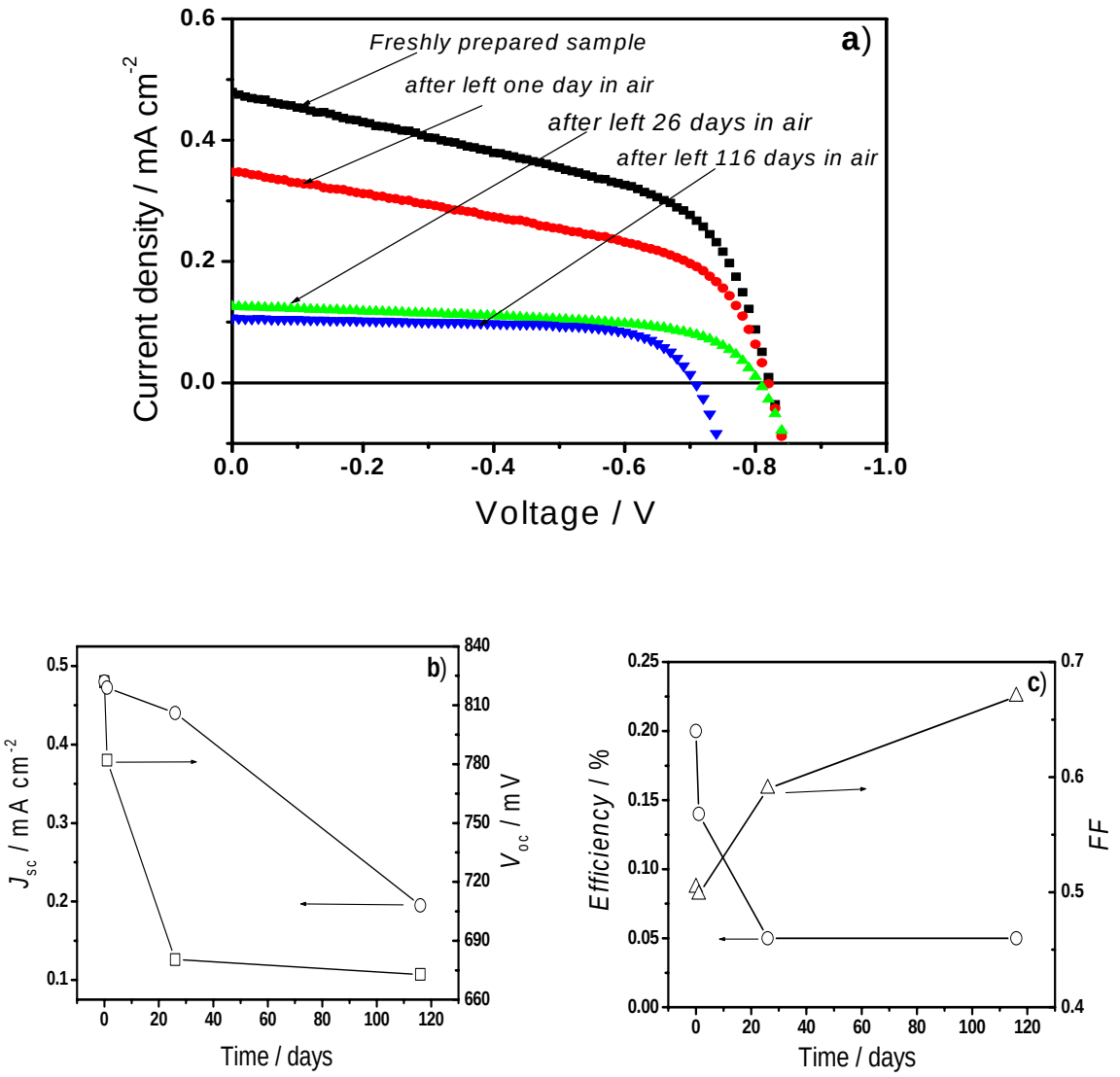

Figure 7.6 Output and characteristics of P1-SSD cell after the device was stored in ambient condition for 116 days. (a) Current voltage characteristics after of P1-SSD, (b) variation of open-circuit photovoltage and short-circuit current density with the time, (c) variation of fill factor and efficiency with the time.

As it can be observed in figure 7.6(a) and (b), the short-circuit current density of the device decreases with the exposure time in ambient condition. It decreases from 0.48 to 0.38 mA cm^{-2} after one day and drops to 0.128 mA cm^{-2} after 26 days. Beyond 26 days the device tends to exhibit its minimum performance, the J_{sc} of 0.107 mA cm^{-2} being observed after 116 days. The decrease in performance could be attributed to the trapping of moisture by the organic hole conductor layer, since the device was not completely sealed.

The open-circuit photovoltage decreases also with time. It decreases slightly from 822 to 819 mV after one day and drops gradually to 806 and 708 mV after 26 days and 116 days, respectively. This behaviour is opposite to its corresponding electrolyte based cell. This change could be due to the denaturing of the amorphous organic hole semiconductor. The crystallisation of organic hole layer could change the redox potential of hole transport mediator.

It was observed that the efficiency of the device also decreases with time (Figure 7.6(c)). This decreases from 0.2 to 0.14% after one day and drops considerably to 0.05% after 26 days from where it becomes stable, an efficiency of 0.05% being obtained after 116 days. In contrast to efficiency, the fill factor increases with the time. FF remains quite stable after the first days with a value around 0.504 and then increases continually to 0.59 and 0.67 after 26 and 116 days, respectively.

The loss in performance observed in the cell after long time exposure upon ambient condition is a hint for side reactions in the device. These side reactions might have diverse origins. Interfacial charge recombination processes have been identified as the main loss mechanism in this type of cell [123]. The recombination processes is accelerated by uncontrolled crystallisation in organic film and by trapping of moisture and O_2 after long time exposure upon ambient condition. In P1-SSD, these phenomena reduce the mobility of hole in organic semiconductor. Low conductivities imply high resistance causing voltage losses [123]. Slow charge transport is expected to generate concentration gradients in the hole conductor matrix. As a consequence an accumulation of holes might build up inside the pores, accompanied by a depletion of holes in the bulk organic semiconductor. This gradient of holes could lead to a charging of the interface, which could considerably increase interfacial recombination and, thus, reduces short circuit photocurrent, open circuit voltage and efficiency.

The increase of fill factor fits with the observation already reported [122,134] although the exact reason is not yet clearly established.

It is worth noting that electron transport in nanocrystalline TiO_2 is dominated by electrons in intraband-gap defect states [307-310]. In a strongly screened environment such as in the electrolyte cell multiple trapping takes place mainly via thermal activation of trapped electrons [71,72]. As a result of the less efficient screening of photoinduced electric fields in the SSD the electron transport in the TiO_2 may significantly differ from the one in DSSCs leading to immobilisation of trapped electrons on the time scale of the experiment. One can suggest that the sensitivity to moiture and O_2 of the organic semiconductor catalyses this phenomenon and reduces the performance of the device.

7.3. Influence of TiO_2 thickness on solid-state dye sensitized solar cells

As observed in DSSCs, the morphology and thickness of TiO_2 film plays an important role on the performance of SSD. In this section the influence of TiO_2 film thickness on the performance of SSD is presented. For this experiment, P1 was used as sensitizer and TiO_2 films were varied between 1.2 and 5 µm thickness. The characteristics of devices under simulated 1.5 AM sunlight (100 mWcm^{-2}) are shown in the Figure 7.7

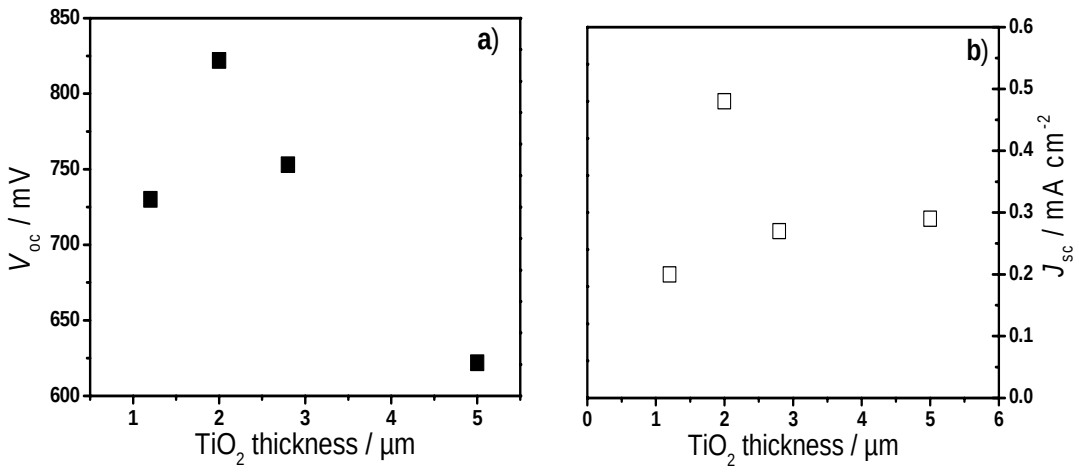

Figure 7.7. Influence of TiO_2 thickness on the performance SSD: (a) dependence of open circuit voltage, $V_{oc,}$ on TiO_2 film thickness (1.2 µm < d < 5 µm) under simulated solar light AM 1.5 (100 mW cm^{-2}); (b) the evolution of short circuit current density.

Figure 7.7 (a) depicts the dependence of V_{oc} with TiO_2 thickness. It can be seen that V_{oc} increases from 730 mV to 822 mV when the thickness of TiO_2 film is changed from 1.2

µm to 2µm. Beyond 2µm, V_{oc} decreases gradually to 753mV for 2.8µm and 622 mV for 5µm TiO_2 film. In my knowledge there is no thermodynamic theory enabling to explain such dependence of V_{oc} on TiO_2 film thickness in SSD as it is the case for DSSCs. However, Hagen et al. [314] used an organic triphenyldiamine (TPD) molecule as hole transport medium and varied the TiO_2 thickness in their cells. While they say nothing about the voltage generated by the devices they just represent a maximum quantum yield at a thickness d = 5 µm. Using spiro-MeOTAD as HTM, Kron [197] varied the TiO_2 film thickness in the range $1.5 < d < 4.5$ µm. An increase of V_{oc} in the range of TiO_2 thickness investigated was observed. These changes were attributed to the increase of Dember voltage.

Dember effect

A Dember potential difference always arises from an inhomogeneous generation of electrons and holes in a semiconductor when these have different mobilities. According to the final expression for the electrical potential difference between the surface (x = 0) and the interior of the semiconductor (x = d) [202] resulting from inhomogeneous light exposure, Dember voltage is expressed as

$$V_D = \frac{kT}{\mathrm{e}} \frac{b_\mathrm{n} - b_\mathrm{p}}{b_\mathrm{n} + b_\mathrm{p}} \ln\left(\frac{\sigma_\mathrm{n}(0) - \sigma_\mathrm{p}(0)}{\sigma_\mathrm{n}(d) + \sigma_\mathrm{p}(d)} \right) \qquad 7.1$$

where b_n is the mobility of electrons in the semiconductor , b_p the mobility of holes in the amorphous organic film , σ_n and σ_p the conductivity of electrons and holes, respectively.

Examining the case in which the electron are mobile and the hole immobile enables to correctly understand the meaning of Dember effect. For this case ($b_\mathrm{h} = 0$, $\sigma_\mathrm{h} = 0$), the Dember potential voltage reaches its maximum possible value

$$V_D = \frac{kT}{\mathrm{e}} \ln\left(\frac{n_n(0)}{n_n(d)} \right) \text{ considering } \sigma_i = q\mu_i n_i \qquad 7.2$$

where n_i is the concentration of the species i and μ_i its mobility..

For the concrete case in which electrons and holes diffuse from the surface of semiconductor, where they are produced, into the interior, with the electrons being more mobile ($b_\mathrm{e} > b_\mathrm{h}$), the

surface then becomes positively charged and assumes a potential, which is more positive than in the interior.

From Eq.7.1, Kron [197] tried to establish a mathematical relationship fitting the case of SSD. The final expression of the Dember voltage V_D obtained was

$$V_D = \frac{kT}{q}\frac{b_1\mu_n - b_2\mu_p}{b_1\mu_n + b_2\mu_p}\ln\left(\frac{\Delta p(0)(b_1\mu_n + b_2\mu_p) + b_2\mu_p N_A}{\Delta p(d)(b_1\mu_n + b_2\mu_p) + b_2\mu_p N_A}\right) \qquad 7.3$$

where b_1 is the half of the TiO_2 thickness column, b_2 the half of the thickness of the hole conductor layer between two TiO_2 columns, N_A the density of acceptors and $\Delta p(0)$ and $\Delta p(d)$ the excess* hole density at x = 0 and x = d [315]. The full description of Eq.7.3 is not presented here since it is not the main objective of this work. These mathematical expressions are used just for the qualitative explanation of my experimental results.

After modelling Eq.7.3 with TiO_2 thickness varying from 1.5 < d < 4.5 µm [197], it was found that the Dember voltage increases by $\Delta V_D \approx 0.04$ V. The modelling was done considering the mobility of electrons in the TiO_2 $\mu_n \approx 2\times10^{-3}$ cm^2 V^{-1} s^{-1} and the mobility of holes in the spiro-MeOTAD $\mu_p \approx 2\times10^{-4}$ cm^2 V^{-1} s^{-1}. The increase of the Dember voltage induces the growth of V_{oc}. However, it has been suggested that the increase of the open circuit voltage is not only due to the Dember voltage. The latter just contributes in part to the increase of V_{oc}.

Another contribution was reported coming from the electric field arising at the interface TiO_2/ HTM [197]. In a dye solar cell under light exposure occurs charge carriers, electrons in TiO_2 and holes in the electrolyte or HTM. A capacitive element namely Helmholtz layer or "double layer" in DSSCs [316] and depletion layer in SSD separates the charge carriers at the interface. Accordingly a potential drop occurs linearly at this interface analogue to an electrical capacitor. Since the thickness of the double layer in DSSCs is in the order of few Ångstroms the corresponding capacitance C = dQ/dV will be considerably high, accordingly the voltage will drop. In the case of SSD, the drop in potential at the interface

* The term *excess carriers* is used for electron and hole that are in excess of their thermal equilibrium values. Excess carriers can be created in semiconductor by variety of processes such as optical excitation, electron bombardment or injection from a contact [315].

TiO_2/HMT due to Helmholtz layer can not be neglected. This additional potential was considered as the additional voltage V_{ad} [197]. This means that at TiO_2/HMT interface in SSD coexist Dember Voltage resulting from the ambipolar diffusion of electron and holes in both side of the interface and the voltage resulting from the Helmholtz layer.

The expression describing the dependence of the additional potential V_{ad} with thickness of TiO_2, d, according to Poisson's law is

$$V_{ad} = \frac{q}{2}\frac{b_1}{b_1\mu_n + b_2\mu_p}\mu_n\left(\frac{b_1^2}{\varepsilon_{TiO2}\varepsilon_0} + \frac{b_2^2}{\varepsilon_{HC}\varepsilon_0}\right)(\Delta p(d) - \Delta p(0)) \qquad 7.4$$

the overall potential V_{total} can be then obtained by adding Eq. 7.3 and Eq. 7.4 which leads to Eq. 7.5

$$V_{total} = V_D + V_{ad} \qquad 7.5$$

where ε_{TiO2}, ε_{HC} are the relative dielectric constants of TiO_2 and hole conductor, respectively. It has been found theoretically [197] with remarkable clarity that the variation of TiO_2 thickness Δd of ~4µm increases the additional voltage V_{ad} of ca. 0.06 V. This leads to an overall variation of 0.1 V close to the experimental value 0.11 V. However, in this work, as it is shown by Figure 7.7(a), the open circuit voltage increases from 730 mV to 822 mV when the TiO_2 thickness is changed from 1.2 µm to 2 µm. This corresponds to a variation ΔV of 92 mV. This change can be attributed to Dember voltage and to the so called additional voltage. In contrast, when the film thickness was changed to 2.8 µm a surprising drop of open circuit voltage V_{oc} = 753 mV occurs. For a thickness of 5 µm the open circuit voltage was found to be V_{oc} = 622 mV. This behaviour doesn't fit any more with theoretical predictions. Although, it is known that the overall voltage V_{total} does not increase indefinitely with TiO_2 film thickness [197], this decrease of open circuit voltage has singular character. According to the simulated curve corresponding to Eq.7.5 a saturation of total voltage V_{total} has been predicted for TiO_2 thickness d ≈10µm. However, it was reported that on the basis of Dember Voltage and additional Voltage, the increase of V_{oc} can not exceed 0.3V [197]. At this stage of my work, a clear explanation of the decrease of V_{oc} for film thickness beyond 2.8 µm can not be given. J_{sc} augments from 0.20 to 0.29 mA cm^{-2} for TiO_2 film thicknesses varying from 1.2 to 5µm (Figure 7.7(b)). A higher value 0.48 mA cm^{-2} is obtained with 2µm of TiO_2 film. The

general increase of J_{sc} with thickness of TiO_2 can be attributed to the light harvesting capability of thicker sensitized layer. However, the increase in TiO_2 film thickness is not always beneficial for the device since the spin-coated organic hole transport layer does not diffuse perfectly until the base of the TiO_2 network. From these results one can suggest that poor pore filling by spiro-MeOTAD limits its contact with hybrid TiO_2/dye interface and hence poor dye regeneration. On the other hand the low mobility of charge carriers in the solid hole transporting medium reduces also the performance of the device when TiO_2 thickness is increased.

7.4. Conclusion

Solid-state dye-sensitized solar cells based on perylene derivatives have been realised and characterized. The current voltage characteristics for the various compounds show varying efficiencies between 0.006% and 0.02%. The SSD based on P4 exhibited the lowest efficiency η = 0.006% likely owing to the presence of an electron withdrawing group (pentafluorophenyl substituent), that reduces the driving forces of charge separation in the hybrid TiO_2/dye system. The potential barrier for charge injection from P4 to TiO_2 CB is the lowest (0.26 eV). However, the performance of devices based on the P8 and P10 with identical LUMO energy levels enabled to conclude that the performance also depends on the position and type of alkyl group bonding to the phenyl substituent. P8-SSD and P10-SSD generate short circuit current densities of ~0.03 mA cm^{-2} and ~0.04 mA cm^{-2}, respectively. This slight difference $\Delta J_{sc} \approx 0.01$ mA cm^{-2} was attributed to the aggregation hindering of *t*-butyl at position 3 of the phenyl substituent.

The use of the bipolar dye molecule P1 based on the spiro concept enabled to realise devices exhibiting efficiency one order of magnitude higher than device based on its parent compound P9. Efficiency up to 0.2% under simulated AM1.5 (100 mW cm^{-2}) was obtained which is the highest result up to now reported with a perylene derivative. These results enable to suggest that, through improved wettability of the nanoporous TiO_2/dye hybrid layer with spin-coated spiro-MeOTAD dye regeneration is facilitated.

The fill factor exhibited by the devices is globally in the range of ideal dye cells. However, it decreases when the incident light intensity is increased because of ohmic losses in the devices. This phenomenon is characteristic of dye-sensitized solar cells.

The investigation of the long term stability of the SSD-P1 cell has shown no noticeable change on the performance of the cell during the first days. After 26 days of

exposure in ambient atmosphere the performance drops strikingly. The change was likely due to a denaturing of the organic hole transport layer inducing more traps and interfacial charge recombinations in the device.

The investigation of the dependence of the device parameters with TiO_2 thickness turned out that the highest performance is obtained with 2μm of TiO_2. It was observed that the open-circuit voltage increases with film thickness in the range 1.2 μm < d < 2 μm and decrease beyond 2 μm. No clear explanation was found for this singular behaviour, however the increase of V_{oc} for thickness of 1.2 μm < d < 2 μm could be attributed to the Dember effect and Helmholtz layer occurring in the device.

Chapter 8
GENERAL CONCLUSION

Electrolyte and solid-state Solar Cells based on of perylene derivatives such as perylene dicarboxylic acid-3,4-anhydride (P7), *N*-(pentafluorphenyl)-perylen-3,4:9,10-tetracarboxylicacid-3,4-anhydrid-9,10- imide (P4) *N*-(diisopropylphenyl)-3,4:9,10-perylene tetracarboxylic acid-3,4-anhydrid-9,10-imide (P8) *N*-(di-*t*-butylphenyl)-3,4:9,10-perylene tetracarboxylic acid-3,4-anhydrid-9,10-imide (P10) 1,7-(4′-*t*-butylphenoxy)-3,4:9,10-perylene tetracarboxylic dianhydride (P9) and bipolar spiro-linked compound, namely, *N*-[2′,7′-bis-(*N,N*-diphenylamino)-9,9′-spirobifluoren-2-yl]-1,7-bis-(4-*t*-butylphenoxy)-perylene-3,4-dicarboxylic acid anhydride-9,10-imide (P1) were realised and characterized under standard conditions (AM1.5, 100 $mWcm^{-2}$ at 25 °C).

The dye structure was found to play an important role in the formation of the heterojunction. The comparison between the performance of devices based on simple perylenes and that of a bipolar compounds show that the use of a bipolar spiro-linked compound improve significantly the performance of electrolyte and solid-state solar cells. P1-based electrolyte cells generated an efficiency 15 times higher than cells from its parent P9 and proves the effect of the spiro concept on the performance of perylene based cells. The presence of bulky groups (alkyl-phenyl) bonded to perylene monoimide (P8 and P10) suppresses dye aggregation and increases electron injection and thereby the efficiency when compared to P7. Electron donating groups turn out to reduce the dark current in device.

Additive in the electrolyte turned out to influence the performance of electrolyte based cells. The results showed that the presence of lithium ion is beneficial for devices. The short circuit current increased remarkably after adding lithium ions to the electrolyte. In contrast, addition of *t*BP was found be disadvantageous despite the fact that it contributed to suppress the dark current by open circuit voltage enhancement. The replacement of I^-/I_3^- by Br^-/Br_3^- as mediator enabled to increase the open circuit voltage considerably. However, a low photocurrent and efficiency was generated by the devices likely due to the slow kinetic of dye regeneration by Br^- since the redox potential Br^-/Br_3^- is more positive than that of I^-/I_3^-.

Experimental results show that the adsorption mode is dissociative with an unidentate configuration, giving rise to free cabonyl at the carboxylate anchoring group. This free C=O was found to be sensitive to electrolyte nature and was found to contribute significantly to the change in V_{oc} in the devices, owing to an in-situ cation coordination. The in-situ cation

coordination prevents cations to reach the TiO_2 surface. P1 containing more coordination sites with respect to P7 has shown a slight invariance in the potential owing to the inhibition of cations to reach TiO_2 surface. Small size cations turned out to generate high J_{sc} and low V_{oc}.

The performance of DSSC depends strongly on light harvesting cross sections. A strategy to enhance adsorption of perylene derivatives by UV pretreatment of TiO_2 surface was demonstrated. Preliminary results show that after UV pretreatment of TiO_2 prior to sensitization the performance of the corresponding device is improved. This improvement is attributed to the enhancement of dye adsorption since the absorbance of the treated photoanode is improved by 3% and 24% for P1 and P7, respectively, after 2 hours of UV pretreatment. This leads to an improvement of the performance of DSSCs without positive shift of the TiO_2 CB and independently on the nature of cation in the electrolyte.

In solid-state devices based on P1, efficiency up to 0.2% under simulated AM1.5 (100 mW cm^{-2}) was obtained which is the highest result up to now reported with a perylene derivative. This result enables to suggest that through this concept the wettability of nanoporous TiO_2/dye hybrid layer with spin-coated spiro-MeOTAD is improved and hence the dye regeneration is facilitated.

The layer thickness of TiO_2, which is an important parameter in order to increase the light harvesting of a device, cannot be increased because of electronic limitations. The electronic limitations are given by the increasing importance of resistive losses for increasing layer thickness. ~7µm TiO_2 thickness was found to be the optimal film thickness for electrolyte based cells ~2µm for the solid-state version.

REFERENCES

[1] Energy Information Administration, *International Energy Outlook 2008*, September **2008** (www.eia.doe.gov/oiaf/ieo/index.html).

[2] BP, *Statistical Review of World Energy*, June 2008.

[3] E. Bequerel, *C. R. Acad. Sci.* **1839**, 9, 145.

[4] M. Grätzel, *Nature* **2001,** 414*,* 338.

[5] E. A. Andrews, *A Latin Dictionary*, p845; Clarendon Press, **1879**, Oxford.

[6] W. Siemens, *Van Nostrand's Eng. Mag.* **1885**, 32, 392.

[7] M. Planck, *Ann. Phys.* **1901**, 4, 553.

[8] A. Einstein, *Ann. Phys.* **1905**, 17, 132.

[9] A. Goldmann, J. Brodsky, *Ann. Phys.* **1914**, 44, 849.

[10] W. Schottky, *Physik. Z.* **1930**, 31, 913.

[11] A. W. Copeland, O. D. Black, A. B. Garrett, *Chem. Rev.* **1942**, 31, 177.

[12] R. Audubert, C. Stora, *Compt. Rend.* **1932**, 194, 1124.

[13] C. Fuller, **10-7-53**, Book 24863, Loc. 123-09-01, *AT&T Archives*, Warren, NJ.

[14] D. Chapin, **1-26-54** & **2-23-54**, Book 29349, Loc. 124-11-02, *AT&T Archives*, Warren, NJ.

[15] "Sunlight Converted to Electricity", Sunday Globe, **Aug. 19, 1973**, Boston.

[16] J. B. Biot, *C. R. Acad. Sci. Paris,* **1839**, 9, 169

[17] R.W. Gurney, N. F. Mott, *Proc. Roy. Soc.* **1938**, A164, 151.

[18] T. H. James, **1977**, *The Theory of the photographic process*. 4th. Ed. Macmillan, New York, USA.

[19] W. West, *Photogr. Sci. Eng.* **1974**, 18, 34.

[20] J. Moser. *Monatsh. Chem.* **1887**, 8, 373.

[21] H. Rigollot, *C. R. Acad. Sci. Paris,* **1893**, 116, 813.

[22] H. Gerischer, H. Tributsch. *Berich. Buns. Gesell.* **1968**, 72, 437.

[23] H. Gerischer, H. R. Schoppel and B. Pettinge. *J. Electrochem. Soc.* **1972**, 119, C230.

[24] H. Tributsch and H. Gerischer. *Berich. Buns. Gesell.* **1969**, 73, 251.

[25] R. Memming. *Faraday Discuss.* **1974**, 261.

[26] R. Memming, F. Schroppel. *Chem. Phys. Lett.* **1979**, 62, 207.

[27] R. Memming, F. Schroppel , U. Bringmann. *J. Electroanal. Chem.* **1979**, 100, 307.

[28] H. Tsubomura, M. Matsumura, Y. Noyamaura, T. Amamyiya, *Nature* **1976**, 261, 402.

[29] W. D. K. Clark, N. Sutin, *J. Am. Chem. Soc.* **1977**, 99, 4676.

[30] S. Anderson, E. C. Constable, M. P. Dare-Edwards, J. B. Goodenough, A. Hamnett, K. R. Seddon, R. D. Wright, *Nature* **1979**, 280, 571.

[31] H. Gerischer, *Electroanal. Chem. Interfac. Electrochem.* **1975**, 58, 263.

[32] H. Gerischer, *Photochem. Photobiol.* **1972**, 16, 243.

[33] R. Memming, *Photochem. Photobiol.* **1972**, 16, 325.

[34] A. Fujishima, T. Watanabe, O. Tatsuoki, K. Honda, *Chem. Lett.* **1975**, 4, 13.

[35] T. S. Jayadevaiah, *Appl. Phys. Lett.* **1974**, 25, 399.

[36] A. Hamnett, M. P. Dare-Edwards, R. D. Wright, K. R. Seddon, J. B. Goodenough, *J. Phys. Chem.,* **1979**, 83, 3280.

[37] M. P. Dare-Edwards, J. B. Goodenough, A. Hamnett, K. R. Seddon, R. D. Wright, *Faraday Discuss. Chem. Soc.* **1980**, 70, 285.

[38] D. Shi, N. Pootrakulchote, R. Li, J. Guo, Y. Wang, S. M. Zakeeruddin, M. Grätzel, P. Wang, *J. Phys. Chem. C* **2008,** 112, No. 44, 17047.

[39] Q. Yu, S. Liu, M. Zhang, N. Cai, Y. wang, P. Wang, *J. Phys. Chem. C* **2009**, 113, 14559

[40] B. O'Regan , M. Grätzel. *Nature* **1991**, 353, 737.

[41] M. K. Nazeeruddin, A. Kay, I. Rodicio, R. Humphry-Baker, E. Müller,P. Liska, N. Vlachopoulos, M. Grätzel, *J. Am. Chem. Soc.* **1993**, 115, 6382.

[42] M. K. Nazeeruddin, P. Pechy, M. Grätzel, *Chem. Commun.* **1997**, 1075.

[43] B. A. Gregg, *J. Phys. Chem. B* **2003**, 107, 4688.

[44] L. M. Peter *J. Phys. Chem. C* **2007**, 111, 6601.

[45] B. A. Gregg, M. C. Hanna, *J. Appl. Phys.* **2003**, 93, 3605.

[46] K. Onken, *PhD. Thesis*, University of Kassel, Germany, **2007**

[47] C. Noumissing-Sao, K. Onken, T.P.I. Saragi, J. Salbeck, DPG-Spring Meeting, **2007**, P.808

[48] C. J. Barbé, F. Arendse, P. Comte, M. Jirousek, F. Lenzmann, V. Shklover, M. Grätzel, *J. Am. Ceram. Soc.* **1997**, 80, 3157.

[49] B. Burfendt, T. Hannappel, W. Storck, F. Willig, *J. Phys. Chem.* **1996**, 100, 16463.

[50] T. Hannappel, B. Burfendt, W. Storck, F. Willig, *J. Phys. Chem.* **1997**, 101B, 6799.

[51] J. R. Durrant, Y. Tachibana, I. Mercer, et al. *Z Phys. Chemie-Int. J. Res. Phys. ChemChem Phys.* **1999**, 212, 93.

[52] J. B. Asbury, E. Hao, Y. Wang, Y. Wang, T. Lian, *J. Phys. Chem. B* **2000**, 104, 11957.

[53] B. T. Langdon, V. J. MacKenzie, D. J. Asunskis, D. F. Kelley *J. Phys. Chem. B* **1999**, 103, 11176.

[54] K. Kalyanasundaram, M. Grätzel, *Coord. Chem. Rev.* **1998**, 77, 347.

[55] H. Gerischer, *Surf. Sci.* **1969**, 18, 97

[56] R. A. Marcus, *J. Chem. Phys.* **1956**, 24, 966.

[57] R. A. Marcus, *Ann. Rev. Phys. Chem.* **1964**, 15, 155.

[58] A. Hagfeldt, M. Grätzel, *Chem. Rev.* **1995**, 95, 49.

[59] http://www.scribd.com/doc/10043326/handbook-of-photovoltaic-science-and-engeneering15

[60] Y. Tachibana J. E. Moser, M. Grätzel, D. R. Klug, J. R. Durrant, *J. Phys. Chem.* **1996**, 100, 20056.

[61] A. Solbrand, H. Lindstrom, H. Rensmo, A. Hagfeldt, S.E. Lindquist, S. Sodergren, *J. Phys. Chem.* B **1997**, 101, 2514.

[62] S. Nakade, S. Kambe, T. Kitamura, Y. Wada, S. Yanagida, *J. Phys. Chem. B* **2001**, 105, 9150.

[63] N.W. Duffy, L.M. Peter, K.G.U. Wijayantha, *Electrochem. Commun*. **2000**, 2, 262.

[64] J. van de Lagemaat, A. J. Frank, *J. Phys. Chem. B* **2001**, 105, 11194.

[65] N. Kopidakis, K. D. Benkstein, J. van de Lagemaat, A. J. Frank, *J. Phys. Chem. B* **2003**, 107, 11307.

[66] J. Nelson, R. E. Chandler, *Coord. Chem. Rev.* **2004**, 248, 1181.

[67] R. Katoh, A. Furube, A.V. Barzykin, H. Arakawa, M. Tachiya*, Coord. Chem. Rev.* **2004**, 248, 1195.

[68] A. Blumen, G. Zumofen, J. Klafter, *Phys. Rev. B* **1984,** 30, 5379.

[69] S.Y. Huang, G. Schlichthörl, A.J. Nozik, M. Grätzel, A.J. Frank, *J. Phys. Chem. B* **1997**, 101, 2576.

[70] S. A. Haque, Y. Tachibana, D. R. Klug, J. R. Durrant, *J. Phys. Chem. B* **1998**, 102, 1745.

[71] J. Nelson, *Phys. Rev. B* **1999**, 59, 15374.

[72] J. Nelson, S. A. Haque, D. R. Klug, J. R. Durrant, *Phys. Rev. B* **2001**, 63, 205321.

[73] G. M. Hasselmann, G. J. Meyer, *J. Phys. Chem. B* **1999**, 103, 7671.

[74] J. Van de Lagemaat, N. G. Park, A. J. Frank, *J. Phys. Chem. B* **2000**, 104, 2044.

[75] C. Bauer, G. Boschloo, E. Mukhtar, A. Hagfeldt, *J. Phys. Chem. B* **2001**, 105, 5585.

[76] A. V. Barzykin, M. Tachiya, *J. Phys. Chem. B* **2002**, 106, 4356.

[77] J. Krüger, R. Plass, M. Grätzel, P. J. Cameron, L. M. Peter *J. Phys. Chem. B* **2003**, 107, 7536.

[78] S. A. Haque, Y. Tachibana, R. L. Willis, J. E. Moser, M. Grätzel, J. R. Durrant, *J. Phys. Chem. B* **2000**, 104, 538.

[79] J. N. Clifford, G. Yahioglu, L. R. Milgrom, J. R. Durrant, *Chem. Commun*. **2002**, 1260.

[80] J. N. Clifford, E. Polares, M. K. Nazeerudin, M. Grätzel, J. Nelson, X. Li, N. Long, J. R. Durrant, *J. Am. Chem. Soc.* **2004**, 126, 5225.

[81] S. Handa, H. Wietasch, M. Thelakkat, J. R. Durrant, S. A. Haque, *Chem. Commun.* **2007**, 1725.

[82] P. Wang, S. M. Zakeeruddin, J. E. Zakeeruddin, T. Sekiguchi, M. Grätzel, *Nat. Mater*. **2003**, 2, 402

[83] V. K. Thorsølle, B. Wenger, J. Teuscher, C. Bauer, J. E. Moser, *Chimia*, **2007**, 61, 631.

[84] Z. Zhang, *PhD Thesis*, EPFL, **2008.**

[85] U. Bach, D. Lupo, P. Comte, J. E. Moser, F. Weissörtel, J. Salbeck, H. Spreitzer, M. Grätzel, *Nature*, **1998**, 395, 583

[86] U. Bach, Y. Tachibana, J.-E. Moser, S. A. Haque, J. R. Durrant, M. Grätzel, D. R. Klug, *J. Am. Chem. Soc.* **1999**, 121, 7445.

[87] J. E. Moser, *Nature Mater*. **2005**, 4, 723

[88] P. Bonhôte, E. Gogniat, S. Tingry, C. Barbe, N. Vlachopoulos, F. Lenzmann, P. Comte, M. Grätzel, *J. Phys. Chem. B* **1998**, 102, 1498.

[89] P. Wang, C. Klein, R. Humphry-Baker, S. M. Zakeeruddin, M. Grätzel, *J. Am. Chem. Soc.* **2005**, 127, 808

[90] M. Grätzel, *J. Photochem. Photobiol. A* **2004**, 164, 3.

[91] P. Wang, C. Klein, R. Humphry-Baker, S. M. Zakeeruddin, M. Grätzel, *Appl. Phys. Letts.* **2005**, 86, 123508

[92] D. Kuang, C. Klein, S. Ito, J. E. Moser, R. Humphry-Baker, S. M. Zakeeruddin, M. Grätzel, *Adv. Func. Mater.* **2007**, 17, 154.

[93] P. Wasserscheid, T. Welton, *Ionic Liquids in Synthesis*; Wiley: Weinheim, Germany, **2002**.

[94] R. D. Dogers, K. R. Seddon, *Science* **2003**, 302, 792.

[95] J. Dupont, R. F. de Souza, P. A. Z. Suarez, *Chem. Rev*. **2002**, 102, 3667.

[96] W. Xu, C. A. Angell, *Science* **2003**, 302, 422.

[97] D. B. Kuang, P. Wang, S. Ito, S. M. Zakeeruddin, M. Grätzel, *J. Am. Chem. Soc.* **2006**, 128, 7732.

[98] W. Kubo, K. Murakoshi, T. Kitamura, Y. Wada, K. Hanabusa, H. Shirai, S. Yanagida, *Chem. Lett*. **1998**, 27, 1241.

[99] W. Kubo, S. Kambe, S. Nakade, Kitamura, T. K. Hanabusa, Y. Wada, S. Yanagida *J. Phys. Chem. B* **2003**, 107, 4374.

[100] P. Wang, S. M. Zakeeruddin, I. Exnar, M. Grätzel, *Chem. Commun.* **2002**, 2972.

[101] F. Cao, G. Oskam, P. C. Searson, *J. Phys. Chem*. **1995**, 99, 17071.

[102] P. Wang, S. M. Zakeeruddin, P. Comte, I. Exnar, M. Grätzel, *J. Am. Chem. Soc.* **2003**, 125, 1166.

[103] A. F. Nogueira, J. R. Durrant, M. A. De Paoli, *Adv. Mater.* **2001**, 13, 826.

[104] C. Longo, A. F. Nogueira, M. De Paoli, H. Cachet, *J. Phys. Chem. B* **2002**, 106, 5925.

[105] P. Wang, Q. Dai, S. M. Zakeeruddin, M. Forsyth, D. R. MacFarlane, M. Grätzel M. *J. Am. Chem. Soc.* **2004**, 126, 13590.

[106] J. Desilvestro, M. Grätzel, L. Kaven, J. Moser, *J. Am. Chem. Soc.* **1985**, 107, 2988.

[107] B. O'Regan, F. Lenzmann, *J. Phys. Phys. Chem. B* **2004**, 108, 4342.

[108] B. O'Regan, F. Lenzmann, R. Muis, J. Wienke, *Chem. Mater.* **2002**, 14, 5023.

[109] B. O'Regan, D. T. Schwartz, S. M. Zakeeruddin, M. Grätzel, *Adv. Mater*. **2000**, 12, 1263.

[110] T. Taguchi, X. T. Zhang, I. Sutanto, K. Tokuhiro, T. N. Rao, H. Watanabe, T. Nakamori, M. Uragami, A. Fujishima, *Chem. Comm.* **2003**, 2480.

[111] A. Konno, T. Kitagawa, H. Kida, G. R. A. Kumara, K. Tennakone, *Cuur. Appl. Phys*. **2005**, 5, 149.

[112] G. R. A. Kumara, A. Konno, K. Shiratsuchi, J. Tsukahara, K. Tennakone, *Chem. Mater.* **2002**, 14, 954.

[113] H. Snaith, S. M. Zakeeruddin, Q. Wang, P. Pechy, M. Grätzel, *Nano Lett.* **2006**, 6, 2000.

[114] D. Gebeyehu, C. J. Brabec, N. S. Sariciftci, *Thin Solid Film* **2002**, 403-404, 271.

[115] S. Tan, J. Zhai, M. Wan, Q. Meng, Y. Li, L. Jiang, D. Zhu, *J. Phys. Chem. B* **2004**, 108, 18693.

[116] L. Schmidt-Mende, J. E. Kroeze, J. R. Durrant, M. K. Nazeeruddin, M. Grätzel, *Nano Lett.* **2005**, 5, 1315.

[117] A. Kay, M. Grätzel, *Sol. Energy Mater. Sol. Cells* **1996**, 44, 99.

[118] H. Lindstrom, A. Holmberg, E. Magnusson, S. E. Lindquist, L. Malmqvist, A. Hagfeld, *Nano Lett.* **2001**, 1, 97.

[119] K. Imoto, K. Takatashi, T. Yamaguchi, T. Komura, J. Nakamura, K. Murata, *Sol. Energy Mater. Sol. Cells* **2003**, 79, 459.

[120] Y. Saito, T. Kitamura, Y. Wada, S. Yanagida, *Chem. Lett.* **2002**, 31, 1060.

[121] Y. Saito, W. Kubo, T. Kitamura, Y. Wada, S. Yanagida, *J. Photochem. Photobiol. A* **2004**, 164, 153.

[122] U. Bach. *Ph.D. Thesis*, EPFL, **2000.**

[123] J. Krüger, *PhD. Thesis*, EPFL, **2003**

[124] M. Probst, R. Haight. *Appl. Phys. Lett.* **1997**, 70, 1420.

[125] R. Willecke, F. Faupel. *J. Polym. Sci. Part B* **1997**, 35, 1043.

[126] R. Willecke, F. Faupel. *Macromol.* **1997**, 30, 567.

[127] A. C. Dürr, F. Schreiber, M. Kelsch, H. D. Carstanjen, H. Dosch *Adv. Mater.* **2002**, 14, 961.

[128] S. Kim, J. K Lee, S.O. Kang, J. Ko, J.H Yum, S. Fantacci, F. De Angelis, D. Di Censo, M. K. Nazeeruddin, M. Grätzel, *J. Am. Chem. Soc.* **2006**, 128*,* 16701.

[129] P. Qin, X. Yang, R. Chen, L.C. Sun, T. Marinado, T. Edvinsson, G. Boschloo, A. Hagfeldt, *J. Phys. Chem. C*, **2007**, 111*,* 1853.

[130] C. A. Bignozzi, R. Argazzi, C. Kleverlaan, *J. Chem. Soc. Rev.* **2000**, 29, 87.

[131] M. K. Nazeeruddin, S. M. Zakeeruddin, R. Humphry-Baker, M. Jirousek, P. Liska, N. Vlachopoulos, V. Shklover, C. H. Fischer, M. Grätzel, *Inorg. Chem.* **1999,** 38, 6298.

[132] M. K. Nazeeruddin; P. Pechy, T. Renouard, S. M. Zakeeruddin, R. Humphry-Baker, P. Comte, P. Liska, L. Cevey, E. Costa, V. Shklover, L. Spiccia, G. B. Deacon, C. A. Bignozzi, M. Grätzel, *J. Am. Chem. Soc.* **2001,** 123, 1613.

[133] M. Grätzel, *Inorg. Chem.* **2005**, 44, 6841.

[134] C. Y. Chen, S. J. Wu, C. G. Wu, J. G. Chen, K. C. Ho, *Angew. Chem. Int. Ed.* **2006**, 45, 5822.

[135] K.J. Jiang, N. Masaki, J. Xia, S. Noda, S. Yanagida, *Chem. Commun.* **2006**, 2460.

[136] K. Hara, H. Sugihara, Y. Tachibana, A. Islam, M. Yanagida, K. Sayama, H. Arakawa, *Langmuir* **2001**, 17, 5992.

[137] D. Kuang, C. Klein, S. Ito, J. E. Moser, R. Humphry-Baker, N. Evans, F. Duriaux, C. Grätzel, S. M. Zakeeruddin, M. Grätzel, *Adv. Mater.* **2007**, 19, 1133.

[138] V. Aranyos, J. Hjelm, A. Hagfeldt, H. Grennberg, *J. Chem. Soc., Dalton Trans.* **2004**, 1319.

[139] K. Sayama, K. Hara, N. Mori, M. Satsuki, S. Suga, S. Tsukagoshi, Y. Abe, H. Sugihara, H. Arakawa, *Chem. Commun.* **2000**, 1173.

[140] T. N. Rao, L. Bahadur, *J. Electrochem. Soc.*, **1997**, 144, 179.

[141] C. Nasr, D. Liu, S. Hotchandani, P. V. Kamat, *J. Phys. Chem*., **1996**, *100*, 11054.

[142] S. Ferrere, A. Zaban, B. A.Gregg, *J. Phys. Chem. B*, **1997**, 101, 4490.

[143] K. Sayama, M. Sugino, H. Sugihara, Y. Abe, H. Arakawa, *Chem. Lett.*, **1998**, 753.

[144] L. Schmidt-Mende, U. Bach, R. Humphry-Baker, T. Horiuchi, H. Miura, S. Ito, S. Uchida, M. Grätzel, *Adv. Mater.* **2005**, 17*,* 813.

[145] K. Hara, K.Sayama, Y. Ohga, A. Shinpo, S. Suga, H. Arakawa, *Chem. Commun.* **2001**, 569.

[146] K. Hara, T. Sato, R. Katoh, A. Furube, Y. Ohga, A. Shinpo, S. Suga, K. Sayama, H. Sugihara, H. Arakawa, *J. Phys. Chem. B* **2003**, 107*,* 597.

[147] Z.S. Wang, Y Cui, K. Hara, Y. Dan-oh, C. Kasada, A. Shinpo, *Adv. Mater.* **2007**, 19*,* 1138.

[148] T. Horiuchi, H. Miura, K. Sumioka, S. Uchida, *J. Am. Chem. Soc.* **2004**, 126*,* 12218.

[149] T. Horiuchi, H. Miura, S. Uchida, *Chem. Commun.* **2003**, 3036.

[150] M. Velusamy, K. R. J. Thomas, J. T. Lin, Y. C. Hsu, K. C. Ho, *Org. Lett.* **2005,** 7, 1899.

[151] T. Kitamura, M. Ikeda, K. Shigaki, T. Inoue, N. A. Andersson, X. Ai, T. Lian, S. Yanagida, *Chem. Mater.* **2004**, *16,* 1806.

[152] I. Jung, J. K. Lee, K. H. Song, K. Song, S. O. Kang, J. Ko, *J. Org. Chem.* **2007**, 72, 3652.

[153] M. Liang, W. Xu, F. Cai, P. Chen, B. Peng, J. Chen, Z. Li, *J. Phys. Chem.C* **2007**, 111, 4465.

[154] N. Koumura, Z. S. Wang, S. Mori, M. Miyashita, E. Suzuki, K. Hara, *J. Am. Chem. Soc.* **2006**, 128, 14256.

[155] S. Ferrere, B. A. Gregg, *New J. Chem*. **2002**, 26, 1155

[156] H. Tian, P.-H. Liu, W. Zhu, E. Gao, D.-J. Wu, S. Cai, *J. Mater. Chem.* **2000**, 10, 2708

[157] C. Zafer, M. Kus, G. Turkmen, H. Dincalp, S. Demic, B. Kuban, Y. Teoman, S. Icli, *Sol. Energy Mater. Sol. Cells* **2007**, 91, 427.

[158] Y. Shibano, T. Umeyama, Y. Matano, H. Imahori, *Org. Lett.* **2007**, 9, 1971.

[159] T. Edvinsson, C. Li, N. Pschirer, J. Schöneboom, F. Eickemeyer, R. Sens, G. Boschloo, A. Herrman, K. Müllen, A. Hagfeldt, *J. Phys. Chem. C* **2007**, 111, 15137.

[160] J. Salbeck, in *Proc. Symp. Inorg. Org. Electroluminescence (EL 1996),Eds : R H Mauch, H E Gumlich*, Wissenschaft und Technik Berlin, **1996**, 243.

[161] R. Pudzich, *Ph.D Thesis*, University of Kassel, **2002**.

[162] T.P.I. Saragi, *Ph.D Thesis*, University of Kassel, **2004**.

[163] C. Noumissing-Sao, K. Onken, Tobat P. I. Saragi, T. Fuhrmann-Lieker, J. Salbeck, *Energy Environ. Sci.* **2009**, to be submitted

[164] F. Würthner, *Chem. Commun.* **2004**, 1564

[165] N. Johansson, D. A. dos Santos, S. Guo, J. Cornil, M. Fahlman, J. Salbeck, H. Schenk, H. Arwin, J. L. Brédas, W. R. Salanek *J. Chem. Phys.* **1997**, 107, 2542

[166] J. Heinze, *Angew. Chem.* **1984**, 96, 823

[167] T. Fuhrmann, J. Salbeck, *Advances in Photochemistry*, Vol 27, 83-166 (Eds: D. C. Neckers, G. von Bünau, W.S. Jenks, Wileys, **2002**)

[168] J. Pommerehne, H. Westweber, W. Guss, R. F. Mahrt, H. Bässler, M. Porsch and J. Daud, *Adv. Mat*. **1995**, 7, 551.

[169] G. Zhou, N. Pschirer, J. C. Schöneboom, F. Eickemeyer, M. Baumgarten, K. Müllen, *Chem. Mater.* In press

[170] H. Quante, *PhD. Thesis*, University of Mainz, Germany, **1994**

[171] W. E. Ford, *J. Photochemistry* **1986**, 34, 43.

[172] J. Krüger, U. Bach, M. Grätzel, *Adv. Mater.* **2000**, 12, 447.

[173] J. E. Kroeze, N. Hirata, L. Schmidt-Mende, C. Orizu, S. D. Ogier, K. Carr, M. Grätzel, J. R. Durrant, *Adv. Funct. Mater*. **2006**, 16, 1832.

[174] J. Salbeck, F. Weissörtel, J. Bauer. *Macromol. Symp.* **1997**, 125, 121.

[175] J. Salbeck, N. Yu, J. Bauer, et al. *Synth. Met.* **1997**, 91, 209.

[176] F. Weissörtel. *Ph. D. Thesis*, University of Regensburg, **1999**.

[177] J. S. Facci, M. Abkowitz, W. Limburg, et al. *J. Phys. Chem.* **1991**, *95*, 7908.

[178] D. Poplavsky, J. Nelson. *J Appl Phys* **2003**, 93, 341.

[179] U. Bach, K. de Cloedt, M. Grätzel. *Adv. Mat.* **2000**, 12, 1060.

[180] H. Bässler. *Phys. Stat. Sol. B* **1993**, 175, 15.

[181] M. Abkowitz, D. M. Pai. *Phil. Mag. B* **1986**, 53, 193.

[182] L. Kavan, M. Gräetzel, *Electrochemica Acta* **1995,** 40, 643.

[183] J. Salbeck, T. Gerloff, *Elektrolumineszenz* - Wissenschaftliche Grundlagen und Highlights, *PdN-ChiS 3/53. Jg*., **2004**, 8.

[184] S. Ngamsinlapasathian, T. Sreethawong, Y. Suzuki, S. Yoshikawa, *Sol. Energy Mater. Sol. Cell* **2005**, 86, 269.

[185] A. Kay, *Ph.D Thesis*, EPLF, **1994**.

[186] IR-spektrometerzubehör für Dispersive und FTIR-Geräte, *Oriel* Laser Optik Technologie, **1997/98**

[187] S. Ferrere, B. A. Gregg, *J. Phys. Chem. B* **2001**, 105, 7602.

[188] N. G. Park, J. van de Langemaat, A. J. Frank, *J. Phys. Chem. B* **2000**, 104, 8989

[189] M. Gómez, E. Magnusson, E. Olsson, A. Hagfeldt, S. E. Lindquist, C. G. Grandqvist, *Sol. Energy Mater. Sol. Cells* **2000**, 62, 259.

[190] S. Chappel, A. Zaban, *Sol. Energy Mater. Sol. Cells*, **2002**, 71**,**141.

[191] J. Ferber, J. Luther, *Sol. Energy Mater. Sol. Cells* **1998**, 54, 265.

[192] Z.-S. Wang, F.-Y. Li, C.-H. Huang, L. Wang, M. Wei, L.-P. Jin, N.-Q. Li, *J. Phys. Chem. B* **2000**, 104, 9676.

[193] Z.-S. Wang, F.-Y. Li, C.-H. Huang, *J. Phys. Chem. B* **2001**, 105, 9210.

[194] M. G. Kang, K. S. Ryu, S. H. Chang, N. G. Park, J. S. Hong, K-J Kim**,** *Bull. Korean Chem. Soc*. **2004**, 25, 742

[195] S. Ito, S. M. Zakeeruddin, R. Humphry-Baker, P. Liska, R. Charvet, P. Comte, M. K. Nazeeruddin, P. Péchy, M. Takata, H. Miura, S. Uchida, M. Grätzel, *Adv. Mater*. **2006**, 18, 1202

[196] Y. Liu, A. Hagfeldt, X-R. Xiao, S-E. Lindquist**,** *Sol. Energy Mater. Sol. Cells* **1998**, 55, 267

[197] Kron Gregor, *Ph.D Thesis*, University of Stuttgart, **2003**

[198] R. Brendel, H. J. Queisser, *Sol. Energy Mater. Sol. Cells* **1993**, 29, 397

[199] H. J. Queisser, *Phisica E* **2002**, 14, 1-10

[200] A. M. Barnett, R. B. Hall, J. A. Rand, W. R. Bottenberg, in *Proc. 6th Int. Photovoltaic Science and Engeneering Conf.* (International Science, New York, **1992**), S. /37.

[201] A. W. Blakes, J. H. Werner, E. Bauser, H. J. Queisser, *Appl. Phys. Lett.* **1992**, 60, 2752

[202] P. Würfel, Physics of Solar Cells: From Principles to new Concepts. Wiley-VCH, Weinhein-Germany **2005**

[203] J. Nelson, The physics of Solar Cells, Imperial College Press, London, **2003**

[204] C. A. Kelly, F. Farzad, D. W. Thompson, et al. *Langmuir* **1999**, 15, 7047.

[205] M. Primet, P. Pichat, M.-V. Mathieu. *J. Phys. Chem.* **1971**, 75, 1221.

[206] F. Bonino, A. Damin, S. Bordiga, et al. *J. Phys. Chem. B* **2003**.

[207] S. Suzuki, H. Onishi, K. Fukui, et al. *Chem. Phys. Lett.* **1999**, 304, 225.

[208] T. Edvisson, C. Li, N. Pschirer, J. Schöneboom, F. Eickemeyer, R. Sens, G. Boschloo, A. Herrman, K. Müllen, A. Hagfeldt, *J. Phys. Chem. C*, **2007**, 42, 15137

[209] P. Suri, R.M. Mehra. *Sol. Energy Mater. Sol. Cells* **2007**, 91, 518.

[210] S.S. Kim, J.H. Yum, Y.E. Yung, *Sol. Energy Mater. Sol. Cells* **2003**, 79, 495.

[211] M. I. Zaki, M. A. Hasan, F.A. Al-Sagheer, et al. *Colloids Surf. A* **2001**, 261.

[212] Special issue on dye-sensitized solar cells: *Coord. Chem. Re*v. **2004**, 248, 1161.

[213] J. R. Durrant, S. A. Haque, E. Palomares, *Chem. Commun.* **2006**, 3279.

[214] Z.S. Wang, T. Yamaguchi, H. Sugihara, H. Arakawa, *Langmuir,* **2005**, 21, 4272.

[215] W. H. Howie, F. Claeyssens, H. Miura. L. M. Peter, J. *Am. Chem. Soc.* **2008**, in press

[216] H. Tributsch, *Coord. Chem. Rev.* **2004**, 248, 1511.

[217] P. J. Cameron, L. M. Peter, *J. Phys. Chem. B* **2005**, 109, 7392.

[218] M. Xu, R. Li, N. Pootrakulchote, D. Shi, J. Guo, Z. Yi, S. M. Zakeeruddin, M. Grätzel, P. Wang, *J. Phys. Chem. C*, **2008**, 112, 19770.

[219] T. W. Hamann, O. K. Farha, J. T. Hupp, *J. Phys. Chem. C*, **2008**, 112, 19756.

[220] D. Zhang, H. Hu, L. Li, D. Shi, *J. Nano.* **2008**

[221] J. Weidmann, Th. Dittrich, E. Konstantinova, I. Lauermann, I. Uhlrndorf, F. Koch, *Sol Energy Mater. Sol. Cells* **1999**, 56, 153.

[222] R. Grünwald and H. Tributsch, *J. Phys. Chem. B* **1997**, 101, 2564.

[223] B. Macht, M. Turrión, A. Barkschat, P. Salvador, K. Ellmer, H. Tributsch, *Sol. Energy Mater. Sol. Cells* , **2002**, 73, 163.

[224] H. Lindström, H. Rensmo, S. Södergren, A. Solbrand, S.-E. Lindquist, *J. Phys. Chem.* **1996**,100, 3084

[225] S. K. Deb, S. Ferrere, A. J. Frank, B. A. Gregg, S. Huang, A. J. Nozik, G. Schlichthörl, A. Zaban, Photochemical solar cells based on dye-sensitization of nanocrystalline TiO_2, *26th IEEE PV Spec. Conf.* **1997**, Anaheim, USA

[226] A. Barkschat, T. Moehl, B. Macht, H. Tributsch, PCCP, submitted for publication.

[227] K. Schwarzburg, R. Ernstorfer, S. Felber, and F. Willig, *Coord. Chem. Rev.* **2004**, 248, 1259.

[228] R. Ernstorfer, S. Felber, W. Storck, E. Galoppini, Q. Wie, F. Willig, *Res. Chem. Intermed.* **2005**, 31, 643.

[229] L. Gundlach, R. Ernstorfer, F. Willig, *Appl. Phys. A* **2007**, 88, 481.

[230] W. West, P. B. Jr. Gilman, *Photogr. Sci. Eng.* **1969**, 13, 221.

[231] P. B. Jr. Gilman, T. D. Koszelak, *J. Photogr. Sci.* **1973**, 21, 53.

[232] F. Nuesch, J. E. Moser, V. Shklover, M. Grätzel, "Merocyanine aggregation in mesoporous networks", *J. Am. Chem. Soc.* **1996,** 118, 5420.

[233] J. B. Asbury, R. J. Ellingson, H. N. Ghosh, S. Ferrere, A. J. Nozik, T. Q. Lian, *J. Phys. Chem. B* **1999,** 103, 3110.

[234] B. Wenger, *Ph.D Thesis*, EPFL, **2006**

[235] H. Tamotsu, H. Miura, S. Uchida, *Chemcomm* **2003,** 3036.

[236] N. W. Dury, K. D. Dobson, K. C. Gordon, B. H. Robinson, A. J. McQuillan, *Chem. Phys. Lett.* **1997**, 266, 451.

[237] K. S. Finnie, J. R. Bartlett, J. L. Woolfrey, *Langmuir* **1998**, 14, 2744.

[238] J. M. Kesselman-Truttmann, S. J. Hug, *Environ. Sci. Technol.* **1999**, 33, 3171.

[239] C. Bauer, G. Boschloo, E. Mukhtar, A. Hagfeldt, *J. Phys. Chem. B* **2002**, 106, 12693.

[240] A. Sasahara, H. Uetsuka, H. Onishi, *Appl. Phys. A* **2001**, 72, 101.

[241] S. A. Chambers, S. Thevuthasan, Y. J. Kim, G. S. Herman, Z. Wang, E. Tober, R. Ynzunza, J. Morais, C. H. F. Peden, K. Ferris, C. S. Fadley, *Chem. Phys. Lett.* **1997**, 267, 51.

[242] S. P. Bates, G. Kresse, M. J. Gillan, *Surf. Sci.* **1998**, 409, 336.

[243] Q. Guo, I. Cocks, E. M. Williams, *Surf. Sci.* **1997,** 393, 1.

[244] L. Patthey, H. Rensmo, P. Persson, K. Westermark, L. Vayssieres, A. Stashans, A. Petersson, B. Bruehwiler, H. Siegbahn, S. Lunell, and N. Martensson, *J. Chem. Phys.* **1999**, 110, 5913.

[245] A. Vittadini, A. Selloni, F. P. Rotzinger, M. Grätzel, *J. Phys. Chem. B* **2000**, 104, 1300.

[246] S. J. Puttock, C. H. Rochester, *J. Chem. Soc. Faraday Trans. 1*, **1986**, 82, 3013.

[247] A. Bertoluzza, M.A.B. Morelli, C. Castellari, *Atti accad. Naz. Lincei. Mem. Cl. Sci. Fis. Mat. Nat. Sez. 2a*, **1965**, 38, 686

[248] M. L. M. Botani, R.W. Joyner, M. Stockenhuber, *Cat. Today* **2003**, 81, 653

[249] H. Ashima, W-J. Chun, K. Asakura, *Surf. Sci.* **2007**, 601, 1822.

[250] C. Noguera, *J. Phys. Condens. Matter.* **2000**, 12 R367

[251] J. W. Eastman, G. M. Androes, and M. Calvin, *J. Chem. Phys.* **1962**, 36, 1197.

[252] J. Szczepanski, C. Chapo, M. Vala, *Chem. Phys. Lett.* **1993**, 205, 434.

[253] K. K. Ong, J. O. Jensen, and H. F. Hameka, *Journal of Molecular Structure (Theochem)* **1999**, 459, 131.

[254] P. Raghunath, M. C. Lin, *J. Phys. Chem. C* **2008**, in press

[255] A. L. Smith, Applied Infrared Spectroscopy, **1979**, John Wiley & Sons

[256] U. Senapati, D. De, B. R. De, *J. Mol. Struct. (Theochem)* **2007**, 808, 157-159

[257] M. J. Kappers, M. Vaarkamp, J.T. Miller, F.S. Modica, M. K. Barr, J.H. van der Maas, D. C. Koningsberger, *Cat. Lett.* **1993**, 21, 235.

[258] D. Kuang, C. Klein, H. J. Snaith, J. E. Moser, R. H. Baker, P. Comte, S. M. Zakeeruddin, M. Grätzel, *Nano Lett.* **2006**, 6, 769.

[259] Z-S. Wang, H. Sugihara, *Langmuir* **2006**, 22, 9718.

[260] Md. K. Nazeeruddin, R. Humphry-Baker. P. Lista, M. Grätzel, *J. Phys. Chem.* B. **2003**, 107, 8981-8987

[261] W. H. Howie, Frederik Claeyssens, H. Miura, L. M. Peter, *J. Am. Chem. Soc.* **2008**, 130, 1367.

[262] G. Redmond, D. Fitzmaurice, *J. Phys. Chem.* **1993**, *97*, 1426.

[263] B. Enright, G. Redmond, D. Fitzmaurice, *J. Phys. Chem.* **1994**, *98*, 6195.

[264] H. Lindstrom, S. Sodergren, A. Solbrand, H. Rensmo, J. Hjelm, A. Hagfeldt, S.E. Lindquist, *J. Phys. Chem. B* **1997**, *101*, 7717.

[265] S. Nakade, T. Kanzaki, W. Kubo, T. Kitamura, Y. Wada, S. Yanagida *J. Phys. Chem.B* **2005**, *109*, 3480.

[266] *CRC Handbook of Chemistry and Physics*, 64th ed.; CRC Press Inc.: Boca Raton, Florida, **1983**.

[267] K. Schwarzburg, F. Willig, *J. Phys. Chem. B* **1999**, 103, 5743.

[268] C. Minero, G. Mariella, V. Maurino, E. Pelizzetti, *Langmuir* **2000**, 16, 2632.

[269] C. Minero, G. Mariella, V. Maurino, D. Vione, E. Pelizzetti, *Langmuir* **2000**, 16, 8964

[270] H. Park, W. Choi, *J. Phys.Chem. B* **2004**, 108, 4086

[271] S. Södergren, H. Siegbahn, H. Rensmo, H. Lindström, A. Hagfeldt, S. J. Lindquist, *J. Phys Chem. B* **1997**, 101, 3087

[272] S. Lunell, A. Stashans, L. Ojamäe, H. Lindström, A. Hagfeldt, *J. Am. Chem. Soc.* **1997**, 119, 7374.

[273] S. Pelet, J. Moser, M. Grätzel, *J. Phys. Chem. B* **2000**, 104, 1791.

[274] S. Kambe, S. Nakade, T. Kitamura, Y. Wada, S. Yanagida, *J. Phys Chem. B* **2002**, 106, 2967

[275] J. Krüger, R. Plass, M. Grätzel, *Appl. Phys. Lett*. **2002**, 81,367.

[276] J. Jiu, S. Isoda, M. Adachi, and F. Wang, *J. Photochem. Photobiol. A* **2007**, **189**, 314

[277] T. V. Nguyen, H. C. Lee, O. Yang, *Sol. Energy Mater. Sol. Cells* **2006**, 90, 967

[278] Z. Wang, H. Kawauchi, T. Kashima, H. Arakawa, *Coord. Chem. Rev.* **2004**, 248, 1381

[279] Y. Saito, S. Kanbe, T. Kitamura, Y. Wada, S. Yanagida, *Sol. Energy Mater. Sol. Cells* **2004**, 83, 1

[280] S. Uchida, R. Chiba, M. Tomiha, N. Masaki, M. Shirai, *in Nanotechnology in Mesostructured Materials*, Vol. 146, lst ed., S.-E. Park, R. Ryoo, W.-S. Ahn, C. W. Lee, and J. S. Chang, Editors, p. 791, Elsevier Science, Amsterdam, **2003**

[281] H. S. Jung, J-K. Lee, S. Lee, K. S. Hong, H. Shin, *J. Phys. Chem. C,* **2008**, 112, 8476.

[282] R. Nakamura, K. Ueda, S. Sato, *Langmuir* **2001**, 17, 2298.

[283] N. Sakai, A. Fujishima, T. Watanabe, K. Hashimoto, *J. Phys. Chem. B* **2003,** 107, 1028.

[284] C. Wang, H. Groenzin, M. J. Shultz, *J. Phys. Chem. B* **2004,** 108, 265.

[285] T. Zubkov, D. Stahl, T: L: Thompson, D. Panayotov, O. Diwald, J. T. Yates, *J. Phys. Chem. B* **2005***,* 109, 15454

[286] V. Rico, C. López, A. Borrás, J.P. Espinós, A.R. González-Elipe, *Sol. Energy Mater. Sol. Cells* **2006**, 90, 2944

[287] N. Sakai, A. Fujishima, T. Watanabe, K. Hashimoto**,** *J. Phys. Chem. B* **2001,** 105, 3023.

[288] F. Hirose, K. Kuribayashi, T. Suzuki, Y. Narita, Y. Kimura, M. Niwano, *electrochem. and Solid-State Letters* **2008**, 11 A109.

[289] N. Tsubokawa, A. Kogure, *J. Polym. Sci. Part A: Polym. Chem.* **1991**, 29, 697.

[290] A. Kitamura, M. Shimohigoshi, T. Watanabe, *Nature* **1997**, 388, 431.

[291] R. Wang, K. Hashimoto, A. Fujishima, M. Chikuni, E. Kojima, A. Kitamura, M. Shimohigoshi, T. Watanabe, *Adv. Mater.* **1998**, 10, 135.

[292] R. Wang, S. Nobuyuki, A. Fujishima, T. Watanabe, K. Hashimoto, *J. Phys. Chem. B* **1999**, 103, 2188.

[293] K. Uosaki, T. Yano, S. Nihonyanagi, *J. Phys. Chem. B* **2004**, 108, 19086.

[294] A. Y. Nosaka, E. Kojima, T. Fujiwara, H. Yagi, H. Akutsu, Y. Nosaka, *J. Phys. Chem. B* **2003**, 107, 12042.

[295] G. Ketteler, S. Yamamoto, H. Bluhm, K. Andersson, D. E. Starr, D. F. Ogletree, H. Ogasawara, A. Nilsson, M. Salmeron, *J. Phys. Chem. C* **2007**, 111, 8278.

[296] G. Caputo, C. Nobile, T. Kipp, L. Blasi, V. Grillo, E. Carlino, L. Manna, R. Cingolani, P. D. Cozzoli, A. Athanassiou, *J. Phys. Chem. C* **2008**, 112, 701.

[297] A. Vittadini, A. Selloni, F. P. Rotzinger, M. Grätzel, *Phys. Rev. Lett.* **1998**, 81, 2954.

[298] G. S. Herman, Z. Dohnalek, N. Ruzycki, U. Diebold, *J. Phys. Chem. B* **2003**, 107, 2788.

[299] Z. Zhang, O. Bondarchuk, B. D. Kay, J. M. White, Z. Dohnalek, *J. Phys. Chem. B* **2006**, 110, 21840.

[300] O. Bikondoa, C. L. Pang, R. Ithnin, C. A. Muryn, H. Onishi, G. Thornton, *Nat. Mater.* **2006**, 5, 189.

[301] F. Hirose, M. Kurita, Y. Kimura, M. Niwano, *Appl. Surf. Sci*. **2006**, 253, 1912.

[302] A. Brian, S. Gregg , S. Chen, S. Ferrere, *J. Phys. Chem. B* **2003**, 107, 3019.

[303] A. Brian, S. Gregg, *Coord. Chem. Rev.* **2004**, 248, 1215.

[304] L. Schmidt-Mende, U. Bach, R. Humphry-Baker, T. Horiuchi, H. Miura, S. Ito, S. Uchida, M. Grätzel, *Adv. Funct. Mater.* **2007**, 17, 154.

[305] K. Peter, H. Wietasch, B. Peng, M. Thelakkat, *Appl. Phys. A* **2004**, 79, 65.

[306] L. Han, N. Koide, Y. Chiba, A. Islam, R. Komiya, N. Fuke, A. Fukui, R. Yamanaka, *Appl. Phys. Lett.* **2005**, 86, 213501.

[307] K. Schwarzburg, F. Willig. *Appl. Phys. Lett.* **1991**, 58, 2520.

[308] R. Könenkamp, R. Henninger, P. Hoyer. *J. Phys. Chem.* **1993**, 97, 7328.

[309] F. Cao, G. Oskam, G. J. Meyer, et al. *J. Phys. Chem.* **1996**, 100, 17021.

[310] P. E. d. Jongh and D. Vanmaekelbergh. *Phys. Rev. Lett.* **1996**, 77, 3427.

[311] W. Brütting, Physic of Organic Semiconductors, **2005**, Wiley-VCH, Weinhein-Germany

[312] P. J. Cameron, L. M. Peter, *J. Phys. Chem*. B **2005**, 109, 930.

[313] S. Goncalves-Conto, M. Carrard, L. Si-Ahmed, et al. *Adv. Mat.* **1999**, 11, 112.

[314] J. Hagen, W. Schaffrath, P. Otschik, R. Fink, A. Bacher, H. W. Schmidt, D. Haarer, *Synth. Met*. **1997**, 89, 215.

[315] M. S. Tyagi, Introduction to Semiconductor materials and Devices, **1991**, John Wiley & Sons, USA

[316] D. Cahen, G. Hode, M. Grätzel, J. F. Guillemoles, I. Riess, *J. Phys. Chem. B* **2000**, 104, 2053.

ACKNOWLEDGEMENTS

The present study was established in the Laboratory of Macromolecular Chemistry and Molecular Materials (Department of Chemistry) at the University of Kassel under the direction of Prof. Josef Salbeck.

First of all I gratefully acknowledge Prof. Josef Salbeck for having given me the opportunity to perform a PhD thesis in his group. I appreciate in particular the autonomy of decision I was provided with during my work, and especially the choice of this exciting and interesting theme, which was totally new for me and was thereby a personal challenge. I am also thankful for believing in myself.

I thank the DAAD for the scholarship. Without your financial support, this work would not have been possible.

I am grateful to PD. Dr. Thomas Fuhrmann-Lieker for having been there at the early stages of my project and for having motivated me at the beginning of my work. With your help and your fruitful advices my dreams became a reality.

I thank Dr. K. Onken for providing some sensitizers used in my work. I thank you also for the illuminating discussion about intramolecular charge transfer and the spiro concept.

I thank Dr. Rainer Bausch for introducing me to the IR instrument and Dr. Manfred Kussler for the fruitful discussions on the IR spectra.

I acknowledge my office colleague Dipl. Chem. T. Gerloff for assisting me with writing some computer program and for the warm atmosphere we shared in our beautiful office. I'll never forget all these marvelous moments we spent together.

I thank Dr. Thiel Gerhard and Dipl. Chem. Th. Ebert and Lothar Weißenborn for helping me with setting up my measurement systems, and Dipl. Chem. A. Siebert for his permanent availability.

Dipl. Chem. Ayna Tsyrenzhapova is acknowledged for electrochemistry measurements.

Dr. T.P.I. Saragi, do you remember this day (during my first days) when you told me how difficult is the writing of a thesis, actually I agree with you. With your advices, I have successfully anticipated some problems far in advance. I would like also to thank you for critically proof-reading my thesis.

Karin Pfaff, find here my thanks for helping me when I had some administrative matters.

I am thankful to all my other colleagues (Dr. Londenberg, Dr. Spehr, Dr. Fetten, Dr. Kucki, Dr. Popova, Dipl. Chem. Tatarov, Dr. Saiju, Dipl. Chem. Arlt, Dipl. Chem. Brendel, Dipl. Chem. Kiurski, Dipl. Chem.Ueberschaer) for their helpful scientific discussions and also for making me always feel at home.

To the people of other research groups:

I thank Dipl. Phys. Kai Ludolph for being a good mentor for AFM,

I thank Dipl. Phys. I. Kommallein for helping me to work in clean room of INA, D. Albert and Kertin Fuchs for depositing gold and Platinum on my samples.

Dr. Clemens Bruhn is acknowledged for the helpful discussion about crystal structure of TiO_2.

I thank Basoene Briggs and Dr. C. Tomla Tanifum who have invested time to read and correct my thesis manuscript.

I sincerely thank all CDD e.V. members “Lah’li” for supporting me morally during my first integration year in Germany.

To the people who always supported me:

I would like to express my deepest gratitude to my *living joy* A. L. Mezop Temgoua and my daughter A. S. Noumissing Mezop for all their love, care and attentions during this period.

To my mother Julienne Tsafack, please find here the outcome of all your sacrifices.

A deepest thought to my late father Jean Sao, who taught me to always work hard towards my goals with a strong sense of discipline, who also taught me to always believe in myself.

To my sisters (M. L. Awountsa and M. Djuazong Sao) and my brothers (S. Temgoua Sao, V. Voufo Sao, R. Sao, L. G. Ateuzem Sao,) I appreciate your support and encouragement throughout my Ph.D. program.

To my syster-in-law C. L. Mezop Keumo, find here all my gratitude for your help.

I thank Families Temgoua, Kaptue, Nkuipou and Sonfack for their support during a critical period of my academic life. Find here all my recognitions.

My greatest thanks go to the Almighty God, for His entire blessing on my family and me.

CURRICULUM VITAE

Chérubin, NOUMISSING SAO

CIVIL STATUS: Born in June 13, 1976 at Bafoussam, Cameroon
Nationality: Cameroonian.
Family status: Married with one Child.

EDUCATION

2004 – 2009 Macromolecular Chemistry and Molecular material, Department of Sciences, University of Kassel- PhD Student under the supervision of Prof. Dr. Josef Salbeck
PhD. Thesis: Dye-Sensitized Solar cells based on perylene derivatives

1999 – 2000 Diplome d' Etude Approfondies **(DEA)**, diploma in Inorganic Chemistry; Specialization in Analytical Chemistry – Electrochemistry, University of Yaounde I, Yaoundé, Cameroon

1997 – 1999 M.Sc. in Inorganic Chemistry Specialization in Analytical Chemistry, University of Dschang, Dschang, Cameroon

1994 – 1997 **B.Sc.** in Chemistry, University of Dschang, Dschang, Cameroon

EXPERIENCE

2007 – 2009 Research Assistant in University of Kassel, Kassel, Germany

2005 – 2009 Teaching Assistant in University of Kassel, Kassel, Germany

2000 – 2003 Teaching Assistant in University of Yaoundé I, Yaoundé, Cameroon

1996 – 1999 Teacher of Physical Sciences at the Albert Camus college of Dschang, Dschang, Cameroon

INTERNSHIPS & OTHER WORK EXPERIENCE

2007 Participation to International School on Organic Photovoltaics ISOPHOS 2007 in Ventotene, Italy (September 23-27, 2007).

2006 Participation to International Summer School in Poland in Krutyn, Poland
Thema: *High Brightness OLEDs for ICT & Next Generation Lighting Applications* (May 26-June 2, 2006).

2002 Seminar on University Pedagogy, University of Yaoundé I, (February 13-14, 2002)

1999 Internship at the laboratory of Soil at the University of Dschang, Cameroon, in the framework of my M.Sc. research works.

AWARDS

2004 – 2007 German Academic Exchange Service scholarship (DAAD)

PUBLICATIONS

- C. Noumissing Sao, K. Onken, T.P.I. Saragi, Thomas Fuhrmann-Lieker, Joseph Salbeck, Dye sensitized solar cells based on a bipolar spiro compound, to be submitted to *Energy Environ. Sci.*
- C. Noumissing Sao, K. Onken, T.P.I. Saragi, Thomas Fuhrmann-Lieker, Joseph Salbeck, New road to improve Light harvesting of the photoanode for Dye-Sensitized Solar Cells based on a bipolar spiro compound, *manuscript in preparation*

Conference papers

- C. Noumissing Sao, K. Onken, T.P.I. Saragi, Joseph Salbeck, Dye sensitized solar cells based on novel bipolar spiro compound. Poster presented at *71st Annual Meeting and DPG-Spring Meeting of the Condensed Matter*, March **2007**, Regensburg, Germany

- C. Noumissing Sao, K. Onken, T.P.I. Saragi, Thomas Fuhrmann-Lieker, Joseph Salbeck, Light induces through-space charge transfer in a bipolar spiro compound unsed as sensitizer in Dye sensitized Solar Cells, Poster presented at the 3rd International Symposium, *Technologies for polymer electronics TPE 08*, May 2008, Rudolstadt, Germany